DOTTORATO DI RICERCA IN INGEGNERIA MECCANICA

XVIII CICLO

SEDE AMMINISTRATIVA

UNIVERSITÀ DEGLI STUDI DI MODENA E REGGIO EMILIA

TESI PER IL CONSEGUIMENTO DEL TITOLO DI

DOTTORE DI RICERCA

DISSERTATION PRESENTED IN PARTIAL FULFILLMENT OF THE REQUIREMENTS FOR THE DEGREE DOCTOR OF PHILOSOPHY IN THE GRADUATE SCHOOL OF THE UNIVERSITY OF MODENA AND REGGIO EMILIA

STATIC AND DYNAMIC MODELLING OF GEAR TRANSMISSIONS

Giorgio Bonori

Adviser: Prof. A.O Andrisano

Anno Accademico 2004 - 2005

Index

Introduction

A gear is a toothed wheel designed to transmit torque to another gear or toothed component. This simple mechanism is well known since humankind started to deal with machineries. Early engineers developed wood gears with cylindrical pegs for cogs to multiply torque and to change speed properties of different shafts. Subsequently cogs were replaced by teeth and many archaeological discoveries had revealed that ancient civilizations (100 b.c.) used gears for a large variety of purposes: from a single spur gear pair in water mill, to differential gear systems in very complex astronomical calculating device (de Solla Price, 1974), such as the Antikythera mechanism, found near the greek island Crete (de Solla Price, 1959).

Although gear systems have such a long history, the most important gear developments took place in the eighteenth century, during the industrial revolution; in this period progresses were made in the use of metallic alloys and in the development of sophisticated teeth shapes. Helical gears were found to be more silent than spur gears, even if a resultant thrust along the rotational axis and a greater sliding friction are produced, beveled and hypoid gears allowed to transmit power between intersecting or non intersecting non parallel axes, while worm gears could assure higher transmission ratios with comparable size. In the first part of nineteenth century, the sudden raise of automotive and aeronautical industries caused the development of particular gears applications; for example: four beveled gear differential systems used in car rear axle; planetary speed reducer systems used in helicopters; the first can transmit power to two axles spinning at different speeds, the latter allows a great speed reduction with small encumbrance and light weight.

In view of the large employ of gears, the main difficulties in designing those systems were related to the strength resistance. Starting from the end of nineteenth century many engineers formulated analytical methods to evaluate the effect of loads on teeth stresses. Two main problems affect tooth resistance: contact pressure fatigue and bending fatigue. In 1892 Lewis (Lewis, 1892) applied a cantilever beam approach to model the behavior of a single tooth with an applied force. In 1937 Almen and Straub (Almen and Straub, 1937) proposed a method to evaluate bending strength. These approaches are still the basic fundamental method to calculate the stress at the root fillet according to standards ((AGMA 2001-B88, 1988), (AGMA 2101-C95, 1995) , (ISO 6336-1, 1996), (ISO 6336-2, 1996), (ISO 6336-3, 1996) and (ISO 6336-5, 1996)) even if many experimental coefficients have been added in order to take

into account: dynamic effects, the load cycle, lubrication and surface treatments. The basic analytical equations used to calculate the contact pressure were developed from Hertz's theory and adapted to tooth profile contact (Johnson, 1985). For many years these simple calculation were the only tools available to predict gears failure. Of course many tests were carried out to support calculations, correct approximations and improve models and knowledge.

In the second half of nineteenth century, the increasing performances of engines and materials involved a necessary improvement of gears calculation (Tuplin,1950) especially with respect to non conventional gear such as spiro-conical gears. The outstanding works of the russian researcher Litvin ((Litvin,1989),(Litvin, 1994)) was able to cover the lack of understanding the geometry of all kind of gears geometry and gears drives. Litvin revised, expanded and unified in a unique compact analytical theory, called the theory of meshing, all the useful equations to design and generate gears starting from all type of manufacturing process. His work covered: spur involute gears, internal involute gears, noncircular gears, cycloidal gearing, involute helical gears with parallel axes, modified involute gears, involute helical gears with crossed axes, new version of Novikov-Wildhaber helical gears, face-gear drives, worm-gear drives with cylindrical worms, double-enveloping worm-gear drives, spiral bevel gears, hypoid gear drives, planetary gear trains, generation of helicoids, design of flyblades and generation of surfaces by CNC machines. For almost any of this sort of gears Litvin proposed calculations for relative velocity, centrodes, axodes, operating pitch surfaces, equations of gears curve/surfaces, curvatures of curves/surfaces, curvature relations, contact ellipse and computerized simulations for meshing and contact.

The contribution given by academic and industrial engineers was gradually collected by important associations founded at the beginning of last century with the objectives of provide organization for the development of gears standards. For example, the American Gear Manufacturers Association (AGMA) was established in 1916 and its executive committee draw up a constitution, which stated that the main intentions of the association were: the advancement and improvement of that industry, the collection and dissemination of statistics and information of value to its members, the standardization of gear design and manufacture and application, and the promotion of a spirit of cooperation among its members for improved production and increased application of gears. In the same way many different associations appeared all over the world: the Verein Deutscher Ingenieure (VDI), established in Germany

in 1856, as well as the Deutsches Institut für Normung established in 1917, the Japanese Gear Manufacturer Association (JGMA) in Japan and the International Federation of the National Standardizing Associations (ISA) established in1926. ISA became the well known International Organization for Standardization (ISO) in 1946 which, nowadays, is a network of the national standards institutes (not only related to gears) of 156 countries, on the basis of one member per country, with a Central Secretariat in Geneva, Switzerland, that coordinates the system.

This brief history shows how much interest have been placed in understanding gears and their applications since many centuries. The main reason of such interest is probably related to the fact that, the full comprehension of gears phenomena is still unknown. In effect the study of the gears involve many complex aspects. In addition many are the applications, since even a simple gear set up can have very different uses and functions, resulting in a completely different behavior. Furthermore, the increased speeds and torques applied in rotating machineries was partially balanced by the introduction of new technologies. In effect new materials and powerful lubricants can be helpful to reduce gear failures but not to avoid vibrations and noise. On the other hand, standards for automotive comfort require lower and lower levels for noise and vibrations, giving very few design suggestions. Nowadays four are the most important issues that must be taken into account by gear engineers: static strength resistance, dynamic behavior, weights-encumbrances and costs.

The ultimate tools to design gears involved very powerful computer tools, which can be classified in two main categories: standard code software, which are able to verify if a gear system is designed according to standard, and finite elements analysis (FEA) and boundary elements analysis (BEA) packages, that can perform very accurate static strength analysis. Each of these pieces of software are very accurate but do not concentrate efforts on solving any vibration problem, despite gear dynamics has been modeled since 1950 ((Tuplin, 1950), (Johnson, 1958)).

On the other hand, there is a vast amount of literature (see (Ozguven and Houser, 1988)) focused on gears dynamics, and many mathematical models have been developed to control gears noise and stability but many of them remained tools to analyze existing systems and not to design them. If a simple spur gear pair is considered, the fundamental problem in gear design is to evaluate the best solution that can offer good dynamic performances, as well as a good static behavior. In other words, it is an optimization problem, which involve both accurate static and dynamics modeling. Torque, speed and macro geometry influence the

behavior as well as the micro geometry, due to profile modification and manufacturing errors. Such detailed analysis must be able to evaluate the influence of all these parameters and be able to calculate their best setting.

The main part of the present work deals with the modeling of a spur gear pair and try to give a unique approach to design gears, joining static and dynamics analyses. At first, a new methodology for the realization of an integrated CAD-FEM model for spur gears is proposed. This CAD-FEM tool provides exact gear geometry, relative positioning and the automatic FEM discretization for a wide family of spur gears. The code generates gear profiles based on parameters describing the cutting tool and particular attention is paid on simulating the enveloping process, when profile modifications exist. In order to provide a FE model, a parametric routine is used to generate automatically the mesh according to the teeth profiles geometry. This tool allows a fast and accurate static analysis of the gear and the calculation of the main source of dynamic excitation, such as the transmission error. The transmission error is strictly related to the variable global mesh stiffness, which depends on the gear position, materials and teeth geometry. A correct FEA can provide the value of the mesh stiffness, i.e. the transmission error.
In the second part of the work a single degree of freedom oscillator with clearance type non-linearity is considered. Such an oscillator represents the simplest model able to analyze a single teeth gear pair, neglecting bearings and shafts stiffness and multi mesh interactions. The model is also able to predict the effect of detailed profile modifications and manufacturing errors on the vibration of the gear pairs. In the case of a preexisting design, a general optimization technique has been also implemented to refine gears geometry in order to improve the dynamic behavior. It must be noticed that comparison to literature and experiments are shown in order to validate some of results.

The main attempt of the work is basically focused in showing and joining together the ultimate modeling techniques and supply useful tools, to predict what happen when two gears are meshing together at various load conditions. All the used mathematical concepts and modeling approaches are well known. The intention is to provide an original way of combining static and dynamic modeling together. In addition to the spur gear modeling, particular attention has been paid to the static modeling of complex systems such as multi-mesh system gear trains. The new FE software packages allow to reproduce very complicated systems and simulate stresses on gears when multiple load conditions occur. The modeling of

such systems requires the knowledge of gears geometry and gears kinematics. A unique modeling of a compound planetary gear system is presented as example of combined multibody / finite elements application.

Chapter 1

In the following sections general analytical equations for spur gear profile are given. The approach focuses on the description of the gear involute geometry generated by a general rack tool profile. In this way the actual cutting process is simulated. The nomenclature and parameters definitions will follow ISO 701 and ISO 1122-1 ((ISO 701, 1998) (ISO 1122-1, 1998)) and subscript 1 and 2 will be related respectively to the pinion and to the gear.

1.1 Basic spur gears geometry: involute profile

A spur gears pairs is the simplest existing gears set. It is constituted by two wheels, named pinion (driver wheel) and gear (driven wheel), with the purpose of transmit rotational motion between two parallel axis and, at the same time, multiplying either speed or torque. If Ω_1 and Ω_2 are respectively the rotational speed of the pinion and of the gear, the transmission ratio is defined has:

$$\tau = \frac{\Omega_2}{\Omega_1} \tag{1.1.1}$$

or:

$$\tau = \frac{T_1}{T_2} \tag{1.1.2}$$

where T_1 and T_2 are torques acting on the pinion and on the gear.

The two wheels are connected through a certain number of teeth, which are engaged each other. In almost all spur gears applications the tooth profile has a peculiar shape called involute, which is generated by means of the enveloping method. This method creates conjugated curves with the property to ensure a constant transmission ratio during motion. If the enveloping method is applied to gears, two tangent circles ζ_1 and ζ_2 and two straight lines ζ_e and ζ_r must be considered. ζ_1 and ζ_2 are primitive circles (also referred as generating pitch circles) relative to pinion and gear, ζ_e is a straight line called epicycle and ζ_r is a straight line rigidly connected with ζ_e as shown in Figure 1. The involute profiles σ_1 and σ_2 are the enveloped curves generated by ζ_r , while ζ_e is rolling without sliding respectively on ζ_1 and ζ_2. It must be noticed that the same profiles σ_1 and σ_2 can be obtained with the same procedure,

using ζ_{b1}, ζ_{b2} and ζ_a instead of ζ_1, ζ_2 and ζ_e. ζ_a is called line of action and it is perpendicular to ζ_r, α is the pressure angle between ζ_e and ζ_a. The two circles ζ_{b1} and ζ_{b2} are called base circles, they are the fundamental geometric entities describing the two gears; in effect there is an unequivocal relationship between them and the teeth profiles σ_1 and σ_2. The base circles represent the evolutes to the teeth profiles, since they are locus of curvatures centers of σ_1 and σ_2. Litvin (Litvin, 1994) distinguished four different types of involute curves depending on the offset, along curve ζ_r , of the involute generating point M with respect to the line of action. A positive offset generate shortened involute curves, a negative offset generate extended involute curves, a null offset generate ordinary involute curves and an offset equal to base radius generate an Archimedes spiral. Figure 1 shows that σ_1 and σ_2 are ordinary involute curves because point M is at the intersection point between the line of action and ζ_r.

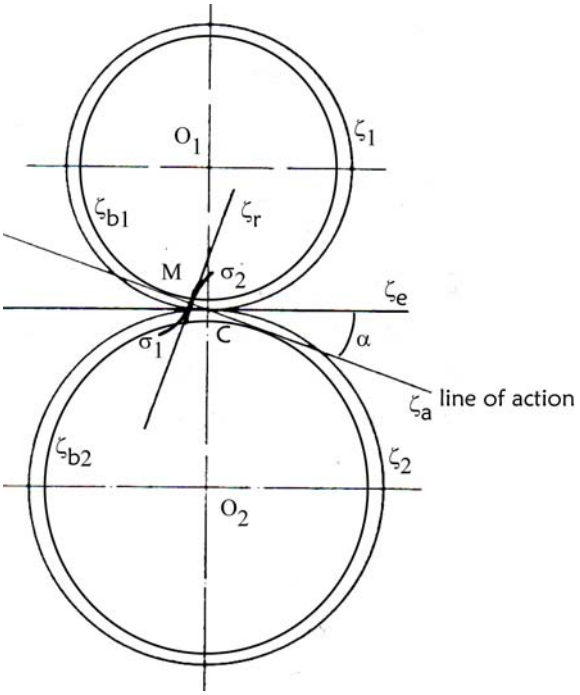

Figure 1: Generation of involute profiles.

As the base circles are tangent to the line of action the following relationships can be written:

$$r_{b1} = r_1 \sin(\alpha); \qquad r_{b2} = r_2 \sin(\alpha) \tag{1.1.3}$$

where r_{b1} and r_{b2} are base circles radii and r_1 and r_2 are primitive circle radii.

In point C of Figure 1 (instantaneous centre of relative rotation between ζ_1 and ζ_2) the tangential speed v of the two wheels must be equal:

$$v_1 = v_2 \tag{1.1.4}$$

where:

$$v_i = \Omega_i r_i \qquad i = 1,2 \tag{1.1.5}$$

Using equation (1.1.1), (1.1.3), (1.1.4) and (1.1.5) the transmission ratio can be calculated with the following relationships:

$$\tau = \frac{r_1}{r_2} = \frac{r_{b1}}{r_{b2}} \tag{1.1.6}$$

In order to give an analytical description of involute curve, the involute function must be defined. Let us consider a current point P on the tooth profile at radius r_p as suggested in Figure 2.

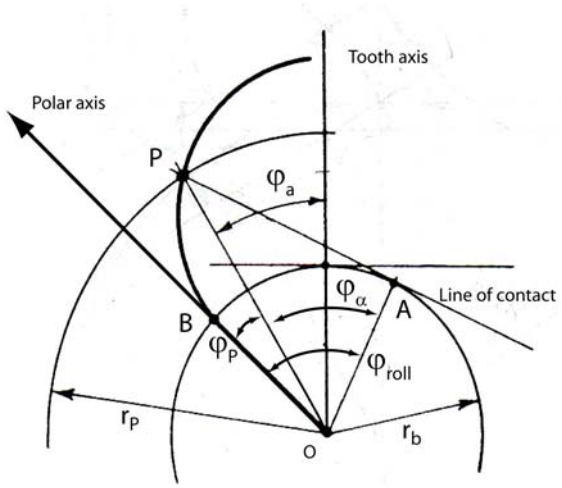

Figure 2: Involute function parameter.

Point A is the tangent point of the line of action ζ_a to the base circle and point B is intersection point between the tooth profile and the base circle. φ_P is the involute polar angle relative to point P. φ_{roll} is called roll angle relative to point P, it is a useful variable to described the involute curve.

Basic vector considerations yield to:

$$\overline{OP} = \overline{OA} + \overline{AP} \tag{1.1.7}$$

where:

$$\overline{OA} = r_b \left[\sin(\varphi_{roll}) \quad \cos(\varphi_{roll})\right]^T \tag{1.1.8}$$

and

$$\overline{AP} = \left|\overline{AP}\right| \left[-\cos(\varphi_{roll}) \quad \sin(\varphi_{roll})\right]^T \tag{1.1.9}$$

For the involute properties, $\left|\overline{AP}\right|$ and $\widehat{AB}$ have the same length and the following equation can be written:

$$\left|\overline{AP}\right| = \widehat{AB} = r_b \varphi_{roll} \tag{1.1.10}$$

Combining equation (1.1.7), (1.1.8), (1.1.9) and (1.1.10) a Cartesian representation of point P can be calculated:

$$\begin{aligned} x_p &= r_b(\sin(\varphi_{roll}) - \varphi_{roll}\cos(\varphi_{roll})) \\ y_p &= r_b(\cos(\varphi_{roll}) + \varphi_{roll}\sin(\varphi_{roll})) \end{aligned} \tag{1.1.11}$$

Different expressions of involute curve can be found using variable parameter φ_{α}; Figure 2 yields:

$$\begin{aligned} x_p &= \frac{r_b \sin(\varphi_P)}{\cos(\varphi_\alpha)} \\ y_p &= \frac{r_b \cos(\varphi_P)}{\cos(\varphi_\alpha)} \end{aligned} \tag{1.1.12}$$

and:

$$\left|\overline{AP}\right| = r_b \tan(\varphi_\alpha) \tag{1.1.13}$$

Equation (1.1.10) and (1.1.13) yield:

$$r_b \varphi_{roll} = r_b \tan(\varphi_\alpha) \rightarrow \varphi_\alpha + \varphi_P = \tan(\varphi_\alpha) \rightarrow \varphi_P = \tan(\varphi_\alpha) - \varphi_\alpha = inv(\varphi_\alpha) \tag{1.1.14}$$

The function $\tan(\varphi)$-φ is called "involute function" and it is usually indicated as *inv(φ)*. The representation of point P with respect to variable parameter φ_α becomes:

$$\begin{aligned} x_p &= \frac{r_b \sin(inv(\varphi_\alpha))}{\cos(\varphi_\alpha)} \\ y_p &= \frac{r_b \cos(inv(\varphi_\alpha))}{\cos(\varphi_\alpha)} \end{aligned} \tag{1.1.15}$$

1.2 Spur gear design parameters

1.2.1 Simple gear

In the following a list of the main spur gear design parameters will be described in order to provide basic knowledge for the design process.

The main design parameter for a spur gear is called normal module m, it is defined as the quotient of the pitch at the reference diameter expressed in millimeters divided by π. Unless otherwise specified, the module refers to the generating pitch circle.

$$m = \frac{\frac{2\pi r}{Z}}{\pi} = \frac{2r}{Z} \tag{1.2.1}$$

Standard values for the module are available in ISO 54 (ISO 54, 1996). According to American nomenclature, values of module can be given in terms of diametral pitch, which is defined as the inverse of the module (AGMA 913-A98, 1998):

$$P_d = \frac{1}{m} \tag{1.2.2}$$

The tooth flank is completely bounded by two circles: the tip circle of radius r_a at the tip and the root circle of radius r_f at the root. The radial distance between the tip circle diameter d_a and the pitch diameter d is called addendum h_a, while the radial distance between the root diameter d_f and the pitch diameter d is called dedendum h_f. Standards values for addendum and dedendum are:

$$h_a = m \qquad h_f = 1.25m \tag{1.2.3}$$

When equations (1.2.3) are respected, the gear is said "normalized", otherwise if addendum modifications are introduced, the gear is said "corrected". The thickness of the tooth at the pitch circle is indicated with s. Figure 3 clarify the meaning of the previous parameters.

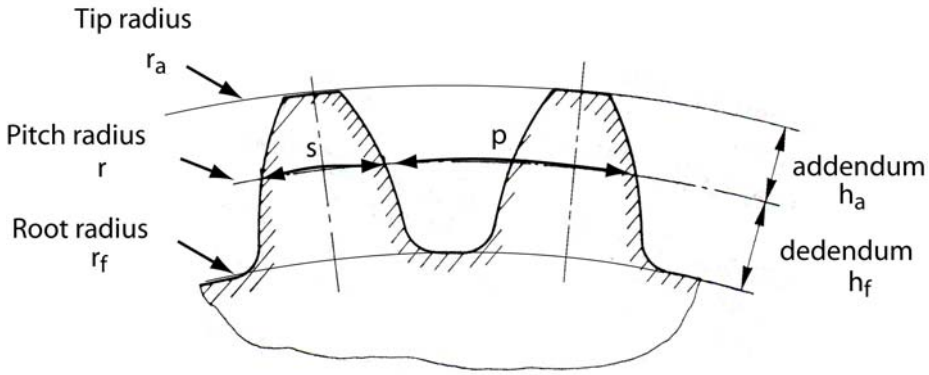

Figure 3: Spur gear design parameter.

Once the generating pitch radius is given, the thickness s at the pitch circle can easily be calculated by taking into account that the thickness of the tooth is equal to the vain:

$$s = \frac{\frac{2\pi r}{Z}}{2} = \frac{m\pi}{2} \tag{1.2.4}$$

Subsequently the thickness s_g at any radius r_g can be calculated with the following simple relationship:

$$\frac{s_g}{2r_g} + (\varphi_{roll,generic} - \tan^{-1}(\varphi_{roll,generic})) = \frac{s}{2r} + (\varphi_{roll,pitchcircle} - \tan^{-1}(\varphi_{roll,pitchcircle})) \tag{1.2.5}$$

Where $\varphi_{roll,generic}$ is the roll angle relative to a current point on the tooth profile at radius r_g and $\varphi_{roll,pitchcircle}$ is the roll angle relative to a point on the tooth profile at radius r. Each roll angle can be calculated from the relative radius value according to the following equation:

$$\varphi_{roll,generic} = \sqrt{\left(\frac{r_g}{r_b}\right)^2 - 1} \tag{1.2.6}$$

Another important parameter is the circular pitch p as indicated in Figure 3. The value of p can be calculated with the following expression:

$$p = \frac{2\pi r}{Z} = \frac{\pi}{m} \tag{1.2.7}$$

1.2.2 Spur gear pair

Figure 4 shows the meshing of two spur gears: the two wheels profile mesh each other along the line of action (also called line of contact). Three different contact points are represented: point N_1, intersection between the line of action and the gear tip circle, is the first point of contact; N_2, intersection between the line of action and the pinion tip circle, is the last point of contact; point C, intersection between the line of action and the center distance line, is the pitch point. The center distance line connects the centers of the two wheels. The part of the line of action between N_1 and N_2 is usually referred as segment of action (contact segment).
During the relative rotation, the contact point moves along the line of action, from N_1 to N_2. At the same time pitch circles ζ_1 and ζ_2 roll without sliding on each other, describing the arcs of action $\widehat{A_1B_1}$ and $\widehat{A_2B_2}$.

In order to assure a smooth continuous tooth action, as one pair of teeth ceases contact, a succeeding pair of teeth must already have to come into engagement. It is desired to have as much overlap as possible; a measure of this overlapping is the involute (or profile) contact ratio ε_α, it is the ratio of the length of the line of action with respect to the base pitch p_b.

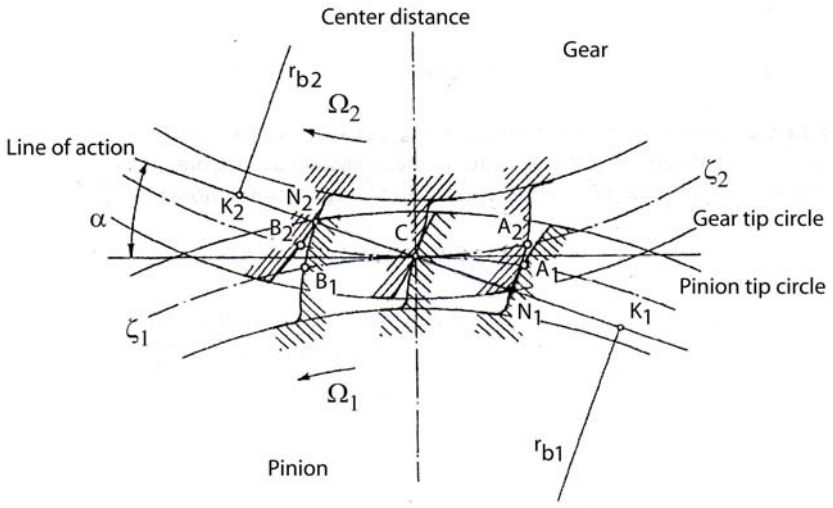

Figure 4: Contact point along line of action.

The length of the contact segment can be calculated when base radii and tip circles radii are known:

$$N_1N_2 = \sqrt{r_{a1}^2 - r_{b1}^2} + \sqrt{r_{a2}^2 - r_{b2}^2} - a\sin(\alpha) \tag{1.2.8}$$

where *a* is the center distance length.

The base pitch is defined as follows:

$$p_b = \frac{2\pi r_{b1}}{Z_1} = \frac{2\pi r_{b2}}{Z_2} \tag{1.2.9}$$

Obviously, the base pitch is the same for two mating gears.

Equations (1.2.8) and (1.2.9) lead to:

$$\varepsilon_\alpha = \frac{\sqrt{r_{a1}^2 - r_{b1}^2} + \sqrt{r_{a2}^2 - r_{b2}^2} - a\sin(\alpha)}{\frac{2\pi r_{b1}}{Z_1}} \tag{1.2.10}$$

The involute contact ratio ε_α is also a useful indicator of the average number of meshing gear teeth during a mesh cycle.

The choice of the involute tooth profile implies that the functionality of a spur gears pair is independent from the value of the center distance. Indeed according to equation (1.1.6) the transmission ratio does not depend from the value of the center distance *a*. In the previous sections, the value of the center distance *a* indicates the distance between the wheels centers, considering that the generating pitch circle are rolling without sliding on each other. Therefore, a new operating center distance *a'* can be considered, i.e. the gears pair is mounted with a different center distance value. Two new pitch circles (operating pitch circles ζ'_1 and

ζ'_2) are rolling without sliding and a new value of the pressure angle can be calculated. According to Figure 5 the following relationship can be written:

$$\alpha' = \cos^{-1}\left(\frac{a\cos(\alpha)}{a'}\right) \tag{1.2.11}$$

$$r'_1 = \frac{r_{b1}}{\cos(\alpha')};\quad r'_2 = \frac{r_{b2}}{\cos(\alpha')} \tag{1.2.12}$$

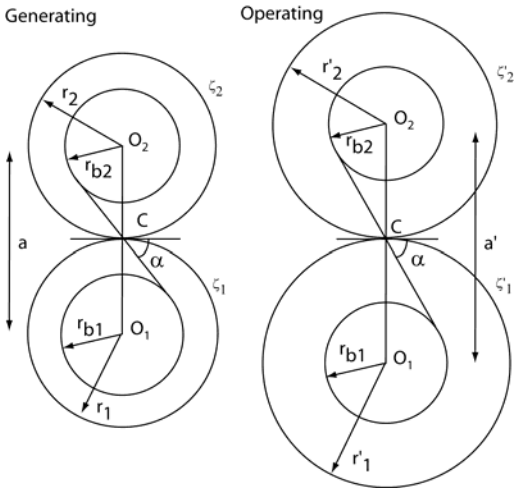

Figure 5: Generating and operating parameters.

Another important parameter in a gears pair, is backlash, which is the difference between the width of a tooth space with respect to the thickness of the engaging tooth on pitch circles. Backlash can also be defined as the distance between mating tooth surfaces at the tightest point of mesh, in a direction normal to the tooth surface, when gears are mounted in their specified positions. The value of backlash along the operating line of contact be calculated as follow:

$$j_n = \frac{s'_1 - \left(\frac{2\pi r'_2}{Z_2} - s'_2\right)}{r'_1} r_{b1} \tag{1.2.13}$$

where s'_1 and s'_2 are the tooth thickness at the operating pitch circle calculated combining expressions (1.2.5) and (1.2.12).

1.2.3 Undercutting

Figure 4 shows that the maximum length of the segment of contact is limited to the length of the common tangent ($N_1N_2 < K_1K_2$). Any tooth addendum that extends beyond the tangent points (K_1 and K_2) interferes with the root fillet area of the mating tooth. This results in the typical undercutted tooth (Figure 6).

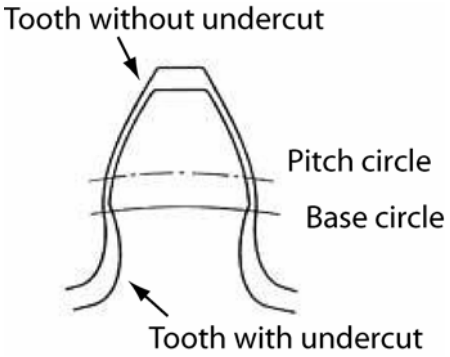

Figure 6: Effect of undercut.

The undercut not only weakens the tooth with a wasp-like waist, but also removes some of the useful involute adjacent to the base circle. The literature (Dudley and Townsend, 1996) (Funaioli et al., 1987) proposed the condition for no undercutting in a standard spur gear by the expressions:

$$\begin{aligned} &\max addendum\ h_a \le \frac{mZ}{2}\sin^2\alpha \\ &\min tooth\ number\ Z \ge \frac{2}{\sin^2\alpha} \end{aligned} \tag{1.2.14}$$

1.2.4 Addendum modifications

In order to explain the application of the involute method to gears manufacturing, a simple rack is considered as cutting tool. The rack is a degenerated gear, with straight line teeth profile, its primitive is a straight line, called pitch line. At the pitch line, the tooth and vain thicknesses are equal. Figure 7 shows a typical rack with normalized addendum (h_{ar}) and dedendum (h_{fr}) (see (ISO 53, 1998) for details). Comparing Figure 1 and Figure 7, the reference pitch line coincides with the epicycle ζ_e and the rack profile with the straight line ζ_r. A normalized rack cuts a normalized gear (see equations (1.2.3)) if the gear primitive circle rolls without sliding on the reference pitch line. In a pair of mating gears, if the cutter is inserted so that the gear pitch circle just touches the cutter reference pitch line (the cutter

tooth thickness is equal to the cutter gap width), this would have zero backlash for a given centre distance. Therefore it is usual to insert the cutter a little deeper to provide backlash. This means to shift up (negative addendum modification) the pitch line with respect to the reference pitch line during the cutting process. Figure 7 shows an example of positive addendum modification, the pitch line is shifted down from the reference pitch line. In both positive and negative addendum modification the gear pitch circle rolls without sliding on a new pitch line shifted from the reference line by an amount $x \cdot m$ called addendum modification (x is the addendum modification coefficient). Basically a positive addendum modification coefficient results in an increase of the gear tooth thickness, a negative addendum modification in a decrease of the gear tooth thickness.

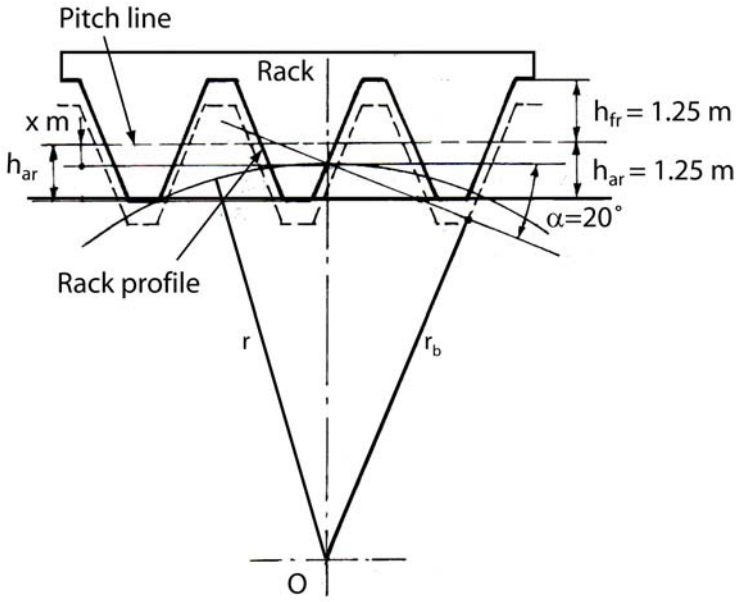

Figure 7: Generation of an involute gear through rack.

Because of this property, the addendum modification is applied to reinforce the gear root, to avoid undercut in gear with small numbers of teeth and also to decrease the relative sliding speed and Hertzian stress of flanks (ISO 4467, 1982), (Henriot, 1987), (Ruggieri and Righettini, 2003). Addendum modification is therefore a simple means for improving the load capacity of gear pairs.

The calculation of the addendum modification coefficient is strictly related to the gears application; the technical report ISO 4467 provides limits of addendum modifications and the distribution of addendum modifications between mating gears, depending on speed regime. The prescriptions have not any restrictive nature and can be applied to gears defined by ISO 53 (ISO 53, 1998). Approximated equation for addendum modification coefficient were proposed by Pedrero ((Pedrero and Artes, 1996), (Pedrero et al., 1996)) and Henriot (Henriot,

1987) for tooth gears with balanced specific sliding and by Arikan (Arikan, 1996) to investigate the effect of addendum modifications on dynamic loads.

When addendum modifications are used the addendum and dedendum values change as follow:

$$h_a = m + xm \qquad h_f = 1.25m - xm \tag{1.2.15}$$

The thickness at the new generating pitch circle becomes:

$$s = \frac{m\pi}{2} + 2xm\tan(\alpha) \tag{1.2.16}$$

1.2.5 Contact point along line of action

In the previous paragraphs the concept of line of action has been introduced as the geometrical locus of the contact point during relative rotation.

In spur gears, the contact point moves from the first point of contact N_1 to the last point of contact N_2 (see Figure 8).

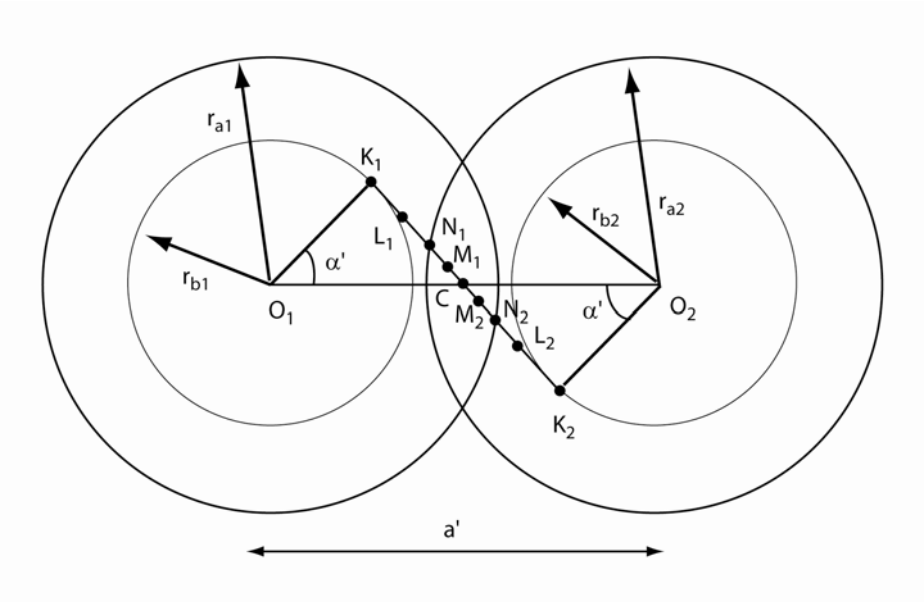

Figure 8: Points along the line of action.

In the case of a contact ratio less than two, simple calculations allow to evaluate the radius r_{N1} (points N_1), with respect to the pinion, and the radius r_{N2} (point N_2) with respect to the gear:

$$K_1N_1 = a'\sin(\alpha') - \sqrt{r_{a2}^2 - r_{b2}^2} \tag{1.2.17}$$

$$r_{N1} = \sqrt{K_1N_1^{\,2} - r_{b1}^2} \tag{1.2.18}$$

$$K_2N_2 = a'\sin(\alpha') - \sqrt{r_{a1}^2 - r_{b1}^2} \tag{1.2.19}$$

$$r_{N2} = \sqrt{K_2N_2{}^2 - r_{b2}^2} \tag{1.2.20}$$

Points M_1 and M_2 represent points at which the number of teeth pairs in contact changes. In effect two pairs of teeth are in contact when the contact point move from N_1 to M_1. Only one pair is in contact from M_1 to M_2 and again two pair are in contact from M_2 to N_2.

The same points can be located along the pinion and gear tooth profile as shown in Figure 9.

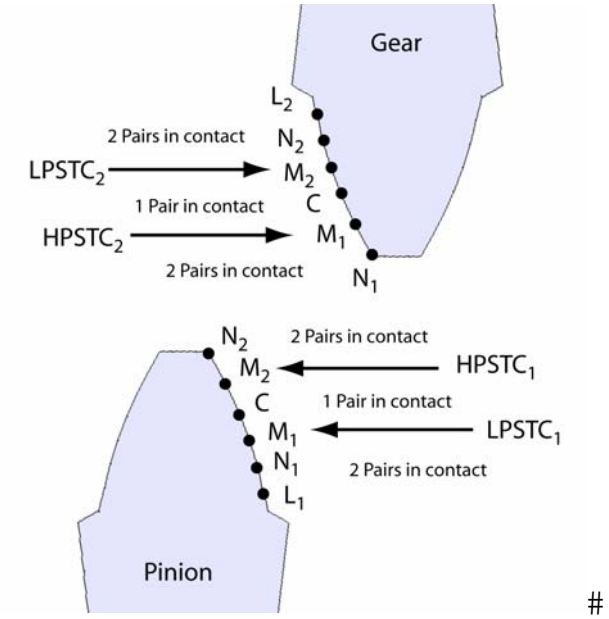

Figure 9: Contact points along teeth profile.

Since points M_1 and M_2 correspond to the largest and smaller radius at which a single tooth is in contact, they are generally referred as the highest point of single tooth contact (HPSTC) and lowest point of single tooth contact (LPSTC), depending on whether pinion or gear profile is chosen as reference. L_1 and L_2 correspond to the minimum radius at which the involute exists (also referred as the start active profile point SAP). Note that in this work no difference exists between the end of active profile radius (EAP) and the tip radius.

The following relationships allow to calculate the radii r_{M1} and r_{M2} with respect to both pinion and gear:

$$K_1M_1 = a'\sin\alpha' - K_2N_2 - \frac{2\pi r_{b1}}{Z_1} \tag{1.2.21}$$

$$r_{LPSTC\,1} = \sqrt{K_1M_1^{\,2} + r_{b1}^2} \tag{1.2.22}$$

$$K_2M_2 = a'\sin\alpha' - K_1N_1 - \frac{2\pi r_{b2}}{Z_2} \tag{1.2.23}$$

$$r_{LPSTC\,2} = \sqrt{K_2M_2^{\,2} + r_{b2}^2} \tag{1.2.24}$$

$$K_1M_2 = K_1N_1 + \frac{2\pi r_{b1}}{Z_1} \tag{1.2.25}$$

$$r_{HPSTC\,1} = \sqrt{K_1M_2^{\,2} + r_{b1}^2} \tag{1.2.26}$$

$$K_2M_1 = K_2N_2 + \frac{2\pi r_{b2}}{Z_2} \tag{1.2.27}$$

$$r_{HPSTC\,2} = \sqrt{K_2M_1^{\,2} + r_{b2}^2} \tag{1.2.28}$$

Equations (1.2.18), (1.2.20), (1.2.22), (1.2.24), (1.2.26) and (1.2.28) can be combined with equation (1.2.6) to obtained relative roll angles $\varphi_{roll,N1}$, $\varphi_{roll,N2}$, $\varphi_{roll,LPSCT1}$, $\varphi_{roll,LPSCT2}$, $\varphi_{roll,HPSCT1}$ and $\varphi_{roll,HPSCT2}$.

1.2.6 Profile modifications

Since gears applications are generally related to motion transmission under load, all teeth can be subjected to deflection. This can results in interference phenomena and the tooth tip can enter contact not in the pure involute position. Manufacturing errors can add to this effect so that it is necessary to relieve the tooth tip to ensure that the corner does not dig in. Correspondingly, at the end of the contact, the tooth tip is relieved to give a gradual removal of force (Smith, 1999).

Both profile modifications can be achieved by removing material from the tooth according to six manufacturing parameters. At the tip: the "start roll angle at tip" $\varphi_{t,s}$ and the "magnitude at tip" mag_t specify the point on the profile at which the relief starts and the amount of the material removed at the tip radius. At the root, the "start roll angle at root" $\varphi_{r,s}$ and the "magnitude at root" mag_r specify the point on the profile at which the relief starts and the

amount of the material removed at the radius corresponding to the "end roll angle at root" $\varphi_{r,e}$ (see Figure 10).

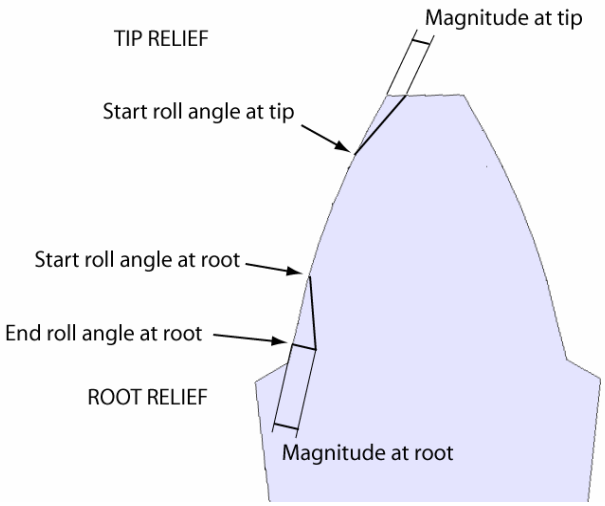

Figure 10: Tip and root relief.

Typical manufacturing gears process, such as grinding, allows to control whether the variation of the removed material is linear or parabolic with respect to the roll angle. Note that the removal of material is measured along the direction normal to the profile. For this reason usual representations of the reliefs are given as deviation from the theoretical involute profile. Figure 11 shows an example with parabolic-type modifications.

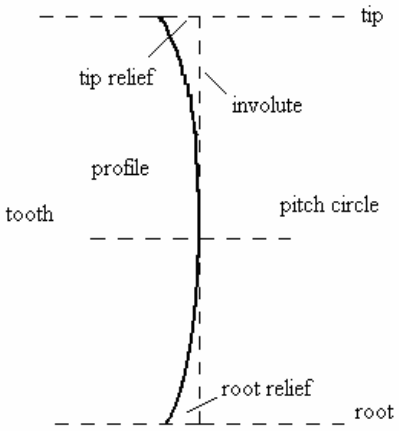

Figure 11: Tip and root relief: deviation from involute profile.

Another design recommendation for spur gears is constituted by crowning. Crowning is a removal of material along the face width direction (Figure 12 a)) to accommodate misalignment. For example, if the shaft is flexible and slender and the gear is not centered between the bearings, the shaft will bend under load and the gear teeth will be at an angle compared to the unloaded case. Crowning compensates misalignment and centers the contact pattern increasing the contact area. Again, the removal of material is measured along the

direction to the normal profile. For this reason, usual representations of the crowning are given as deviation from the theoretical involute profile (Figure 12 b)).

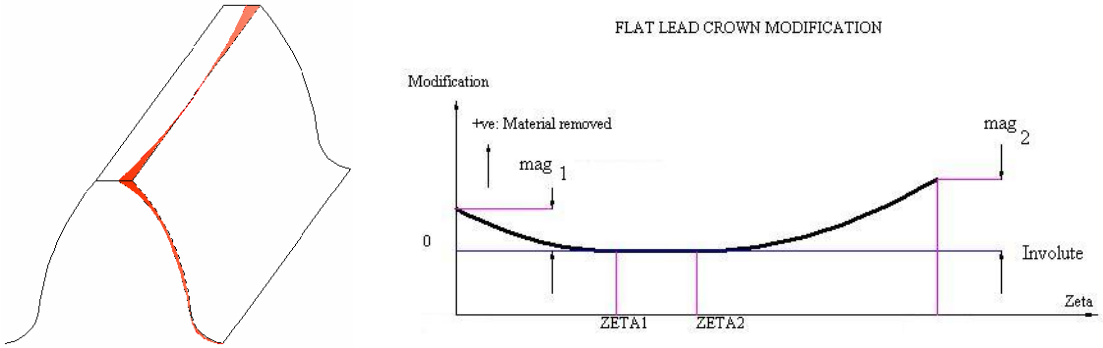

a) b)

Figure 12: Crowning: a) effect of crowning on spur gear tooth; b) crowning parameters.

Four parameters control a common lead crowning: the crowning magnitudes mag_1 and mag_2 at the face width extremes and the face width coordinates *zeta1* and *zeta2* at which the modification start.

1.2.7 Mesh frequency

The gear mesh frequency, also called "tooth mesh frequency", is the rate at which gear teeth mate together. It is equal to the number of teeth on the gear times the rotational frequency of the gear.

$$f_m = \frac{\Omega_1 Z_1}{60} = \frac{\Omega_2 Z_2}{60} \tag{1.2.29}$$

where Ω_1 and Ω_2 are rotational speed expressed in RPM.

From equation (1.2.29) the mesh period T_m and the mesh circular frequency ω_m (in term of radians per seconds) can be evaluated:

$$T_m = \frac{1}{f_m} \tag{1.2.30}$$

$$\omega_m = \frac{2\pi}{T_m} \tag{1.2.31}$$

1.3 Meshing equations

Let us consider the profile generation by means of an envelope of a rack profile ζ_r, see Figure 13. Three references systems are introduced:

-S_f ($O_f x_f y_x$) fixed reference;

-S_1 ($O_1 x_1 y_1$) moving respect to S_f;

-S_2 ($O_2 x_2 y_2$) moving respect to S_f;

where ζ_r is fixed in S_1 and σ_2 is fixed in S_2.

θ is local variable that identify a point on the curve ζ_r and ϕ is local variable that identify a point on the curve σ_2. The parameter ϕ depends on ϕ; P_1 and P_2 are the same point P represented in the reference systems S_1 and S_2.

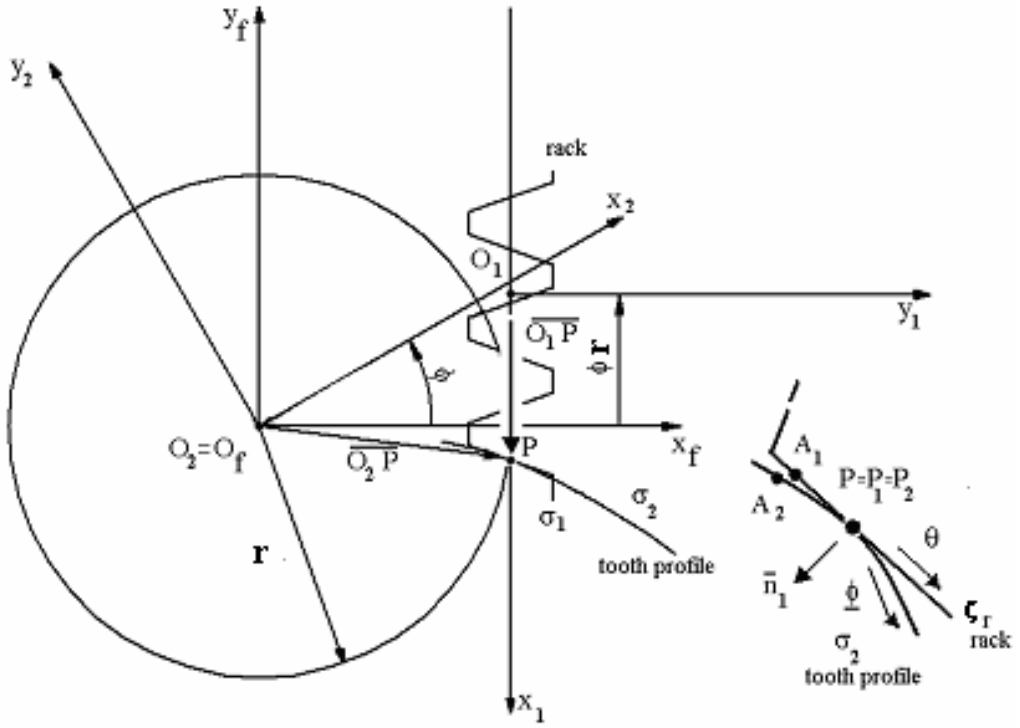

Figure 13: Reference systems.

Let consider a regular plane curve ζ_r describing the rack tooth profile. The tooth profile (σ_2) is described by the meshing equation (Litvin, 1994):

$$f(\theta,\phi) = \overline{n}_1(\theta) \cdot \overline{v}_t(\theta,\phi) = 0 \tag{1.3.1}$$

such equation state that the sliding velocity $\overline{v}_t$, of S_2 with respect to S_1, has to be normal to the enveloping curve ζ_r. Moreover, one can express the normal vector to curve ζ_r as:

$$\overline{n}_1(\theta) = \overline{k}_1 \times \frac{\partial}{\partial \theta} \overline{O_1 P_1}(\theta) \tag{1.3.2}$$

Using homogenous coordinates, P_1 on ζ_r is described by vector $\overline{O_1 P_1}$; the following regularity conditions of the curve are imposed:

$$\overline{O_1 P_1}(\theta) \in C^1, \quad \frac{\partial \overline{O_1 P_1}}{\partial \theta}(\theta) \neq \overline{0} \tag{1.3.3}$$

Assuming that S_1 is fixed and S_2 is moving with respect to S_1, the sliding velocity of P in S_1 becomes:

$$\overline{v}_\tau(P_1) = \frac{d}{dt} \overline{O_1 O_2} + \overline{\omega} \times \overline{O_2 P_1} = \frac{d}{dt} \overline{O_1 O_2} + \overline{\omega} \times (\overline{O_2 O_1} + \overline{O_1 P_1}) \tag{1.3.4}$$

where $\overline{\omega}$ is the angular velocity vector of system S_2.

In order to describe the vector $\overline{O_1 P_1}(\theta)$ in the reference S_2 a transformation matrix $\mathbf{M}_{21}$ must be considered:

$$\overline{O_2 P_2}(\theta, \phi) = M_{21}(\phi) \cdot \overline{O_1 P_1}(\theta) \tag{1.3.5}$$

$\mathbf{M}_{21}$ transforms reference system 1 to 2 by expressing the motion of S_1 and S_2 respect to S_f, using the Lagrangian parameter ϕ. Equation (1.3.5) represents a family of curves, which describe trajectories of the points of ζ_r while θ is varying during the motion with respect to S_2. Equation (1.3.1) allows to reduce the family of curves to a unique curve σ_2, which is the envelope of ζ_r. Equation (1.3.1) and (1.3.5) are sufficient to determinate the tooth profile curve σ_2 as function of ϕ. According to Litvin, (Litvin et al., 2001), the following sufficient conditions for the existence and regularity of the curve must be respected:

1. The family of curves σ_2 must have C^2 regularity for both θ and ϕ parameters:

$$\overline{O_2 P_2}(\theta, \phi) \in C^2, \quad \theta \in E \subseteq R, \quad \phi \in (a, b) \tag{1.3.6}$$

2. ζ_r must be regular:

$$\frac{\partial}{\partial \theta} \overline{O_1 P_1}(\theta_0) \neq \overline{0} \tag{1.3.7}$$

3. If a generic point (θ_0, ϕ_0) verifies equation (1.3.1), then it cannot be a singular point and must verify the following equation:

$$\frac{\partial}{\partial\theta}\overline{O_1P_1}(\theta)\frac{\partial}{\partial\theta}\theta(t_0)+v_\tau(\theta_0,\phi_0)\neq\overline{0} \tag{1.3.8}$$

where $\theta=\theta(t)$ provides the contact point on ζ_r while θ is varying.

1.4 Application of the analytical envelopping method

1.4.1 Rack protuberance parameters

Figure 14 shows the rack and protuberance parameters according to ISO 53 (ISO 53, 1998) and UNI 8862/2 (UNI 8862/2, 1998):

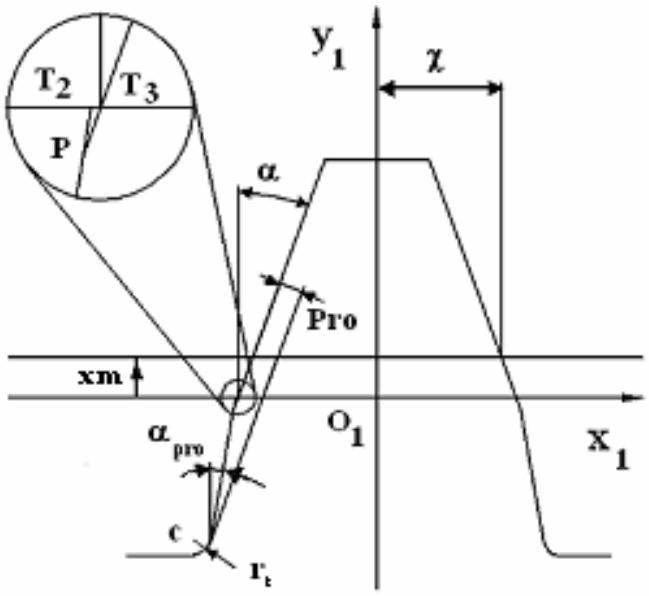

Figure 14: Rack protuberance parameters.

Both tooth profiles are constituted by three regular curves: a circular arc (1r) and two rectilinear segments (2r) and (3r). Such profile is defined by means of the following parametric equations, written in terms of the parameters θ_1, θ_2 and θ_3:

$$(r1)\begin{cases}x_1=x_C+r_t\ \cos\left(\dfrac{\theta_1}{r}\right)\\ y_1=y_C+r_t\ \sin\left(\dfrac{\theta_1}{r}\right)\end{cases};(r2)\begin{cases}x_1=x_{T2}+\theta_2\ \sin(\alpha_{Pro})\\ y_1=\theta_2\ \cos(\alpha_{Pro})\end{cases};(r3)\begin{cases}x_1=x_{T3}+\theta_3\ \sin(\alpha_n)\\ y_1=\theta_3\ \cos(\alpha_n)\end{cases} \tag{1.4.1}$$

where:

$$\chi = \frac{\pi m}{4};$$

$$x_c = -\chi = \frac{P_{ro}}{\cos(\alpha_n)} - \left(hm - r_t + r_t \sin(\alpha_n)\right) tg(\alpha_n) - r_t \cos(\alpha_n);\ \ y_c = -hm + v + r_t \tag{1.4.2}$$

$$x_{T2} = x_c = r_t \cos(\alpha_{Pro}) + \left(hm - v - r_t + r_t \sin(\alpha_{Pro})\right) tg(\alpha_{Pro});\ \ x_{T3} = -\chi - vtg(\alpha_n)$$

are the coordinates of the points C, T_2 and T_3 indicated in Figure 14. The three curves, which constitute the whole rack profile, are defined in the following intervals:

$$(1)\quad \theta_1 \in \left[\theta_{11} = -\frac{\pi}{2} r_t; \theta_{12} = -\alpha_{pro} r_t\right]$$

$$(2)\begin{cases} \theta_2 \in \left[\theta_{21} = \dfrac{-\left(hm - v - r_t + r_t \sin(\alpha_{pro})\right)}{\cos(\alpha_{pro})};\ \ \theta_{22} = \dfrac{x_{T3} - x_{T2}}{\sin(\alpha_{pro}) - \cos(\alpha_{pro}) tg(\alpha_n)}\right] & if\ \alpha_{pro} \neq \alpha_n \\ \theta_2 \in \left[\theta_{21} = \dfrac{-\left(hm - v - r_t + r_t \sin(\alpha_n)\right)}{\cos(\alpha_n)};\ \ \theta_{22} = \dfrac{-\left(hm - v - r_t + r_t \sin(\alpha_n)\right)}{\cos(\alpha_n)}\right] & if\ \alpha_{pro} = \alpha_n \end{cases} \tag{1.4.3}$$

$$(3)\begin{cases} \theta_3 \in \left[\theta_{31} = \dfrac{1}{\cos(\alpha_n)} \dfrac{x_{T3} - x_{T2}}{tg(\alpha_{pro}) - tg(\alpha_n)};\ \ \theta_{32} = \dfrac{hm + v}{\cos(\alpha_n)}\right] & if\ \alpha_{pro} \neq \alpha_n \\ \theta_3 \in \left[\theta_{31} = \dfrac{-\left(hm - v - r_t + r_t \sin(\alpha_n)\right)}{\cos(\alpha_n)};\ \ \theta_{32} = \dfrac{hm + v}{\cos(\alpha_n)}\right] & if\ \alpha_{pro} = \alpha_n \end{cases}$$

1.4.2 Involute profile generated from a rectilinear segment and rack fillet

For the rectilinear segments, using equation (1.4.1-r2) or equation (1.4.1-r3) inserting in (1.3.1) and solving with respect to θ yields to:

$$\theta(\phi) = (r\phi - x_T)\sin(\alpha) \tag{1.4.4}$$

Substituting equation (1.4.4) into (1.3.5) one obtains:

$$\begin{cases} x(\phi) = r\cos(\phi) + (r\phi - x_T)\cos(\alpha)\sin(\alpha + \phi) \\ y(\phi) = -r\sin(\phi) + (r\phi - x_T)\cos(\alpha) co\,s(\alpha + \phi) \end{cases} \tag{1.4.5}$$

for the rack tooth fillet using equation (1.4.1-r1) and (1.3.1) and solving with respect to θ yields to four solutions in the interval $[-\pi;\ \pi]$:

$$\theta_{1,2,3,4} = \pm \arccos\left[\pm \frac{|x_c - r\phi|}{\sqrt{y_c^2 + (x_c - r\phi)^2}}\right] \tag{1.4.6}$$

according to equations (1.4.3) only the following solution is acceptable:

$$\theta = -\arccos\left[\frac{|x_c - r\phi|}{\sqrt{y_c^2 + (x_c - r\phi)^2}}\right] \tag{1.4.7}$$

Substituting equation (1.4.7) into (1.3.5) yields to:

$$\begin{cases} x(\phi) = A\cos(\phi) + B\sin(\phi) \\ y(\phi) = B\sin(\phi) + A\sin(\phi) \end{cases} \tag{1.4.8}$$

with:

$$A = r + y_c - r_t\sqrt{\frac{y_c^2}{y_c^2 + (x_c - r\phi)^2}}; \qquad B = r - y_c - r_t\frac{r\sqrt{(x_c - r\phi)^2}}{\sqrt{y_c^2 + (x_c - r\phi)^2}} \tag{1.4.9}$$

Equations (1.4.5) and (1.4.8) represent the curves which generate the tooth profile from the rack cutter envelope.

1.4.3 Involute profile generated from a rack with semi topping

In the present section a general description of the geometry of a complex rack profile is given when semi topping and protuberance are present. Particular attention is paid to parameters which define non standard tools. Figure 15 a) shows the notation used:

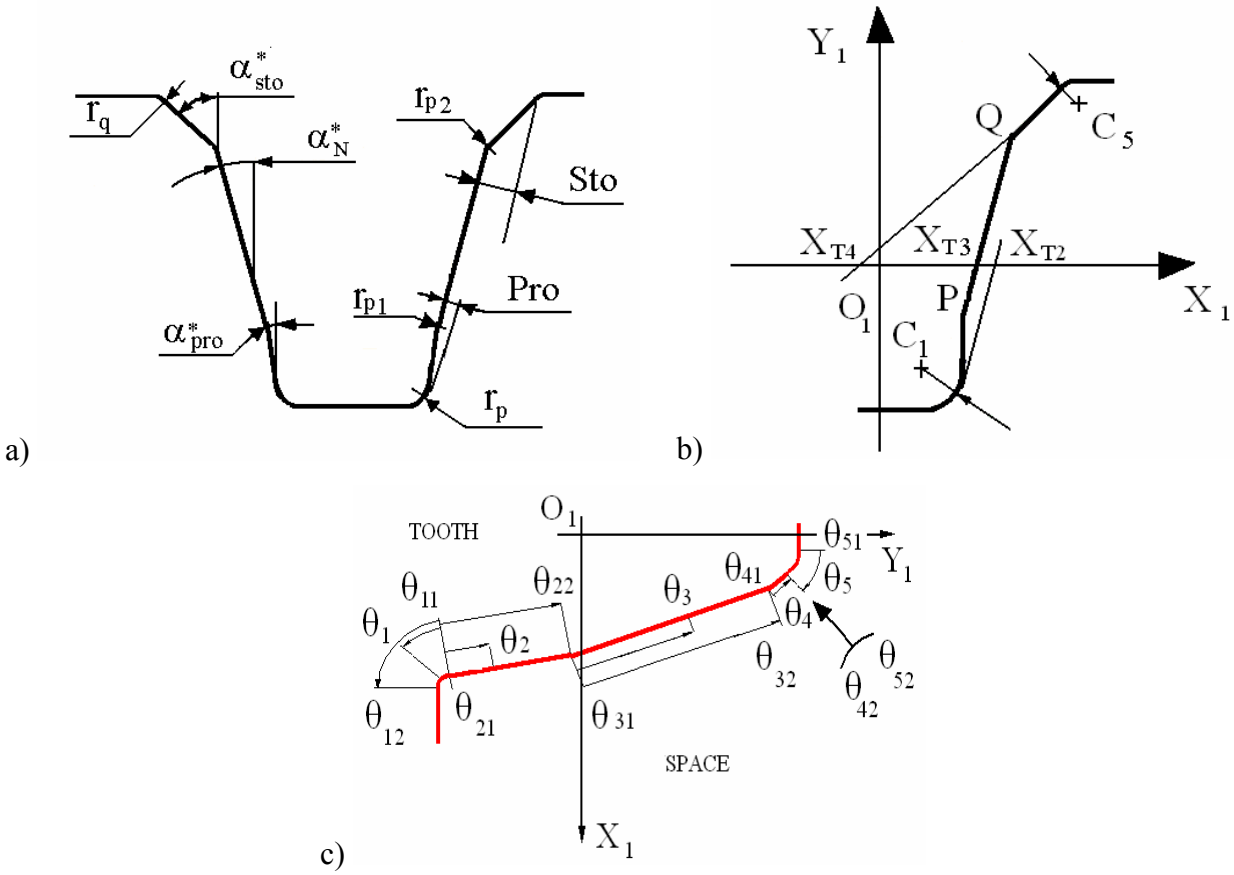

Figure 15: a) Geometrical parameters defining the profile of the rack; b) Point of intersection between different rack segments; c) Lagrange parameters and extreme values.

α^*_n is the pressure angle of the rack, α^*_{pro} is the pressure angle of the protuberance and α^*_{sto} is the pressure angle of semi-topping segment. *Pro* and *Sto* are respectively the protuberance and semi topping magnitude. r_p, r_{p1}, r_{p2} and r_q are fillet radii between generating segments. Introducing a reference frame $O_1x_1y_1$, where y_1 corresponds to the axis of the rack tooth, and Lagrange parameters θ_1, θ_2, θ_3, θ_4 and θ_5 according to figure 1 c), each straight segment of the rack profile can be analytically described as follow:

$$\begin{aligned} x_i &= x_{Ti} + \theta_i \cdot Sin(\alpha_i) \\ y_i &= \theta_i \cdot Cos(\alpha_i) \end{aligned} \tag{1.4.10}$$

where *i* can be 2, 3 and 4 according to Figure 15 b).

With the same approach fillet arcs can be described with the following expression:

$$\begin{aligned} x_j &= x_{cj} + r_{pj} \cdot Cos\left(\theta_j / r_{pj}\right) \\ y_j &= y_{cj} + r_{pj} \cdot Sin\left(\theta_j / r_{pj}\right) \end{aligned} \tag{1.4.11}$$

where *j* can be 1 and 5. Points C_j, and T_i are described by Figure 15 b). Note that radii r_{p1} and r_{p2} were neglected and substituted by a discontinuity at points *P* and *Q*.

Figure 16 shows the enveloped curves along the gear profile in the general case of a cutting tool with both protuberance and semitopping .

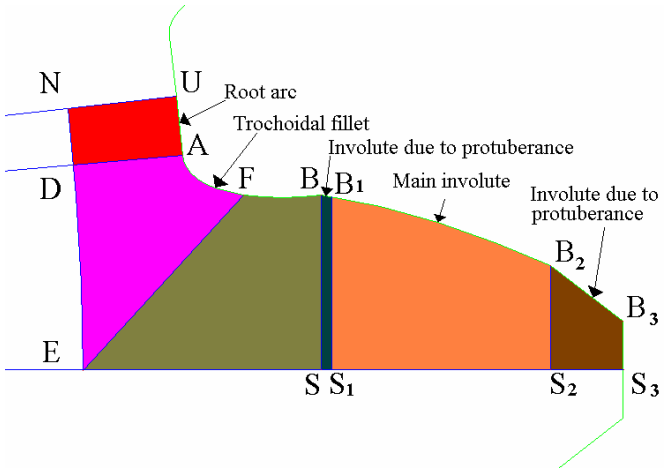

Figure 16: Different enveloped curves along gear profile.

According to previous sections, equations (1.3.1) and (1.3.5) can be applied to equations (1.4.10) and (1.4.11) to generate correspondent profile curves of the gear tooth. The following analytical expressions can be calculated for the enveloped profile:

$$\begin{aligned} x_i &= rCos(\phi_i) + (r\phi_t - x_{Ti})Cos(\alpha_i)Sin(\alpha_i + \phi_i) \\ y_i &= -rSin(\phi_t) + (r\phi_t - x_{Ti})Cos(\alpha_i)Cos(\alpha_i + \phi_i) \end{aligned} \tag{1.4.12}$$

$$\begin{aligned} x_j &= A_j \cdot Cos(\phi_j) + G_j \cdot Sin(\phi_j) \\ y_j &= G_j \cdot Cos(\phi_j) + A_j \cdot Sin(\phi_j) \end{aligned} \tag{1.4.13}$$

where i can be 2, 3 and 4 and j can be 1 and 5 according to Figure 16; R is the pitch radius of the gear; A_j and G_j can be define as follow:

$$\begin{aligned} &(1) \qquad A_j = r \pm y_{cj} - r_{pj}\sqrt{\frac{{y_{cj}}^2}{{y_{cj}}^2 + \left(x_{cj} - \phi_j r\right)^2}} \\ &(2) \qquad G_j = r\phi_j \pm x_{Cj} - r_{pj}\sqrt{\frac{\left(x_{Cj} - \phi_j r\right)^2}{{y_{Cj}}^2 + \left(x_{Cj} - \phi_j r\right)^2}} \end{aligned} \tag{1.4.14}$$

Note that equations (1.4.14) have + for j equal to 1 and – for j equal to 5.

It is clear from Figure 16 that each different parts of the profile can be described as an involute curve (equation (1.4.12)) or a trochoidal curve (equation (1.4.13)), and the existence or extension of these curves depends on the values of rack parameters. No analytical expression exists in literature in order to calculate the intersection points between these curves. Therefore point B, B_1 and B_2 are numerically calculated with a particular modified Newton-Rapson technique which assure convergence in a finite number of step.

1.4.4 Limits Φ values

Let us consider the simple case of a rack with protuberance described in Figure 14. The three curves r1, r2 and r3 generate three profiles t1, t2 and t3, see Figure 17. The boundaries of the curves r1, r2 and r3, in terms of their parameters θ_1, θ_2 and θ_3 are reflected on the boundaries of the envelopes t1, t2 and t3, in terms of ϕ_1, ϕ_2 and ϕ_3.

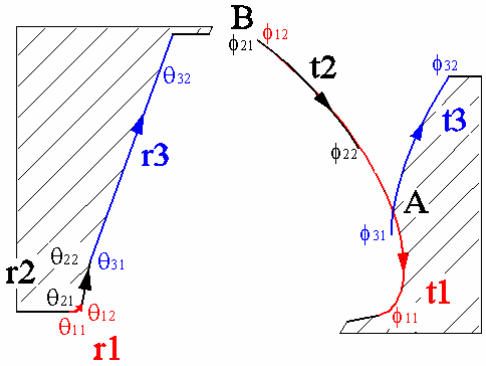

Figure 17: Extremes values of θ and Φ.

Using the mesh equation (1.4.4) and equation (1.4.7); rewritten in terms of ϕ, yields to:

$$\phi_e = \frac{x_T + \theta c\,\mathrm{s}\,c(\alpha)}{r}; \phi_t = \frac{x_C + \theta ctg\left(\frac{\theta}{r_t}\right)}{r} \tag{1.4.15}$$

The first equation is referred to straight line segments r2 and r3 (see Figure 17) of the rack, while the second one is referred to the tooth fillet. Limits ϕ can be obtained substituting in (1.4.15) values for θ found in (1.4.3).

1.4.5 Evaluation of intersection points: a numerical technique

By analyzing Figure 17 one can argue that some parts of the envelope curves can be spurious, because of undercutting, i.e. the theoretical curves cannot be practically built. The actual intersection point A is given by:

$$\begin{cases} x_{t1}(\phi_1) = x_{t3}(\phi_3) \\ y_{t1}(\phi_1) = y_{t3}(\phi_3) \end{cases} \tag{1.4.16}$$

in which x_{t1} and y_{t1} are the expressions (1.4.8) and x_{t3} and y_{t3} are the expressions (1.4.5) applied to segment r3 of the rack. Using the Newton technique equation (1.4.15) can be solved. However, this approach can give rise to numerical troubles. In order to circumvent such problems, equation (1.4.15) can be replaced by considering the distance between two envelope curves; by minimizing such distance one can obtain the intersection point. The Newton technique is used to solve this problem; for what concern first trial value, for the vector $\overline{\phi}^{(0)}$, geometric considerations yield to select:

$$\overline{\phi}^{(0)} = \begin{bmatrix} \phi_{32} \\ \phi_{12} \end{bmatrix} \tag{1.4.17}$$

1.4.6 Limits with undercutting

High values of negative addendum modification give rise to undercutting at the tooth base, i.e. close to the intersection between t1 and t2, see Figure 17. Furthermore the rack can generate spurious envelope branches, if it is too close to the wheel. Singularity happens for:

$$\phi_{32} < \phi_u \tag{1.4.18}$$

The inequality means that the arc profile r3 begins to envelop spurious branch before reaching ϕ_u, at this point the singularity is produced. ϕ_u can be evaluated using equation (1.3.8); In the case of undercutting at least two intersections occur: Figure 18 shows the case of undercutting between curves t1 and t3.

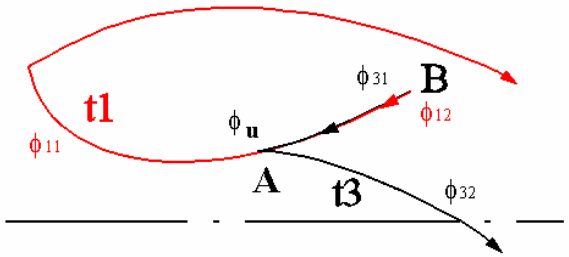

Figure 18: Intersections between curves t1 and t3.

Intersection B is known because it is generated by the limits of the two rack profiles r1 and r3, while the intersection A is evaluated with the previously mentioned numerical method, using ϕ_u instead of ϕ_{12} in equation (1.4.17).

1.4.7 Generation of gear profiles

The approach described in the previous paragraphs has been implemented in a Mathematica®4.1 (Wolfram, S., 1999) routine, which is able to represents the tooth geometry according to a particular rack profile.

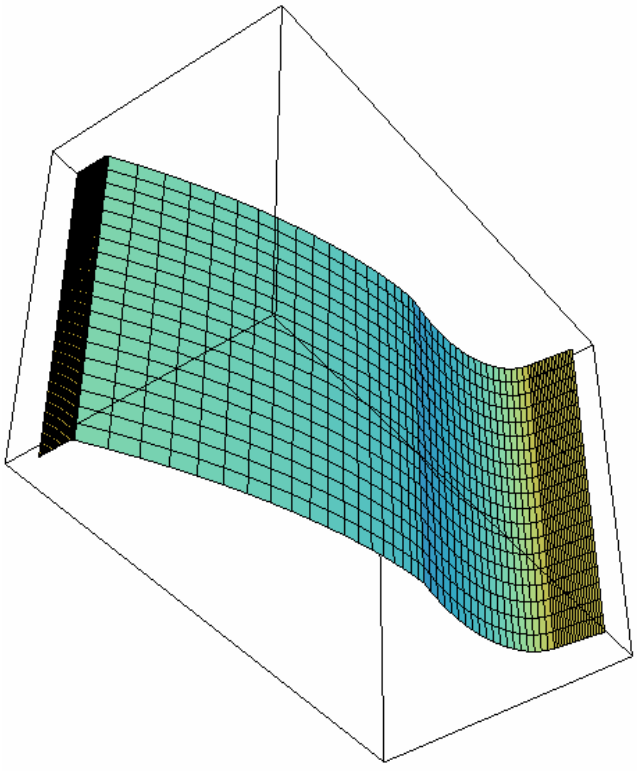

Figure 19: Gear profile.

An example is shown in Figure 19. It is possible to locate the undercutting region on the tooth fillet produced by the protuberance of the rack (Figure 20).

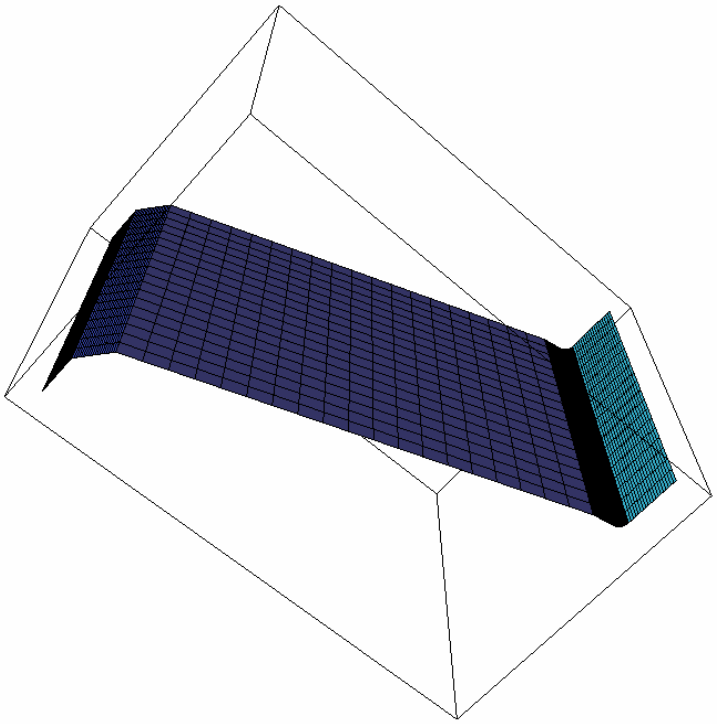

Figure 20: Representation of the gear rack.

Table 1 summarizes the parameter used in the simulation for both gear and rack.

Number of Teeth	20
Module [mm]	5
Normal Pressure Angle [Deg]	20
Face Width [mm]	10
Root gear diameter [mm]	97.5
Outer gear diameter [mm]	110
Rack tip radium r_p [mm]	0.3
α_{pro} [Deg]	10
Rack protuberance [mm]	0.1
α_{sto} [Deg]	50
Rack semitopping [mm]	0.5
r_p [mm]	0.3
r_{p1} [mm]	0.02
r_{p2} [mm]	0.01
r_q [mm]	0.02

Table 1: Rack-gear parameters.

Chapter 2

In this chapter an automatic mesh procedure is described to generate nodes and elements for a spur gear pair for different relative position. Finally two case study are shown.

2.1 Finite element method

The main idea of finite elements is to break up a continuum into a discrete number of smaller elements modeled by a stiffness matrix (Strozzi, 1998). Each element has a certain number of nodes that have a certain number of degrees of freedom. The basic approach is to assume a shape function that describes how the nodal displacements are distributed throughout the element base. If $\overline{H}(x)$ is the shape function matrix and $\overline{\delta}$ the element nodal displacement vector, the displacement anywhere in the element can be calculated as follow:

$$\overline{u}(x) = \overline{H}(x) \cdot \overline{\delta} \tag{2.1.1}$$

The differential operator matrix $\overline{B}$ can be used to convert the displacements vector within the element into the strains vector $\overline{\varepsilon}$.

$$\overline{\varepsilon} = \overline{B}\overline{u} = \overline{B}\overline{H}\overline{\delta} \tag{2.1.2}$$

Using Hooke's law it is possible to obtain stress from strain and therefore:

$$\overline{\sigma} = \overline{E}\overline{\varepsilon} \rightarrow \overline{\sigma} = \overline{E}\overline{B}\overline{H}\overline{\delta} \tag{2.1.3}$$

From equations (2.1.2) and (2.1.3) the strain and stress vectors can be easily calculated once the element nodal displacement vector is known. Calculating the internal and external virtual works and applying the principle of virtual works, the nodal force vector $\overline{f}$ can be expressed in terms of nodal displacements by means of a stiffness matrix $\overline{K}$.

$$\overline{f} = \overline{K}\overline{\delta} \tag{2.1.4}$$

Where

$$\overline{K} = \int_A \overline{B}^T \overline{D}\overline{B} dA \tag{2.1.5}$$

and A indicates integration over the element area.

$\overline{f}$ is known from loading and constraining conditions; the inversion of the stiffness matrix yields to the displacement vector.

Using Finite Elements a very important role is played by the type of element used for the discretization. Many commercial codes (Marc®, ANsys®, NASTRAN®) offer different elements according to applications. In the present work two element types are used: quadrilateral plain strain element and quadrilateral plain stress element.

The first one is a four-node, isoparametric, arbitrary quadrilateral, written for plane strain applications; the second one is a four-node, isoparametric, arbitrary quadrilateral written for plane stress applications. As these elements use bilinear interpolation functions, the strains tend to be constant throughout the element and this results in a poor representation of shear behavior. The stiffness of both elements is formed using four-point Gaussian integration (MSC.Marc, 2003).

The use of plain strain or plane stress is related to the thickness of the structure. In gears analyses, sufficiently accurate results can be obtained using plain strain for a large range of applications. Plain stress is applied only in case of gears with a very thin face width.

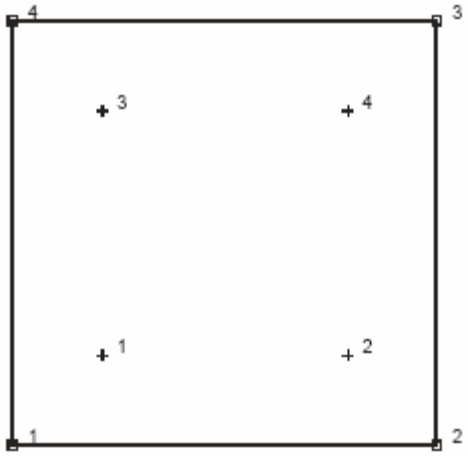

Figure 21: Nodes connectivity for quadrilateral plane strain and plane stress element.

Figure 21 shows the nodes connectivity for both elements. Note that node numbering must be counterclockwise.

2.2 Mesh generation

Finite Elements commercial packages can offer interesting tools capable to simulate the static behavior of a spur gear pair once the shapes and lay out of gear systems are known. For this purpose Finite Elements Method (FEM) are intensively used with regards to bending fatigue, contact pressure and subsurface shear stress, even for very complex gear geometry such as hypoid and bevel gears ((Olakorede and Play, 1991), (Ramamurti et al., 1998), (Vilmos,

2000)). When the dynamic behavior is considered, FEM can be used to evaluate static transmission error (STE), source of parametric excitation into lumped models ((Ming-Haung and Ying-Chien, 1997), (Bonori et al., 2004)). Although the Finite Element Analysis is a very powerful tool, there are some disadvantages in analyzing gears systems; the need of studying different relative positions of the gear bodies, with different contact points, produces a waste of time in creating CAD and FEM models. Furthermore, each configuration requires a different meshing process, which can be very time consuming especially when accuracy is required.

A CAD-FEM procedure capable to create, automatically, FEM models in the simple case of a spur gear pair is developed here. The tool provides exact gear geometry, relative positioning and the automatic mesh for a wide family of gears. Using equations developed in the previous chapter, a specific parametric routine developed to generate the complete mesh (nodes and elements) of a spur gear pair (Bertacchi, 2005). Loads, constraint and contact elements are also imposed automatically without any user involvement in the calculation process. Furthermore, all calculations can be performed for an arbitrary number of relative position within a mesh cycle. All single steps can be run continuously without any loss of time for the user. To validate the model and the tool some case study are presented and the results demonstrate how static analysis can be performed accurately in a very simple way.

In the following paragraphs the basic idea of the automatic mesh procedure to generate nodes and elements is described. Figure 16 shows how each tooth profile can be divided into different parts according to whether the curve is involute, arc or throcoid. Therefore, different methods are proposed for the calculation of nodes coordinates for each segment along a gear tooth (Andrisano et al, 2005-a), (Andrisano et al., 2005-b). Once the coordinates are known a Nastran® script file can be generated in order to describe nodes and elements locations for a complete FE analysis.

2.2.1 Involute profile

A general mesh for a true involute profile is formulated considering *Ie* nodes along the involute profile and *Iss* nodes along the tooth thickness (see Figure 22). All nodes create equally spaced lines of mesh in both radial and circumferential directions. In order to generate a set of equally spaced nodes in the radial direction, the intersection of the involute curve with a generic circumference of radius R_{Ci} is calculated.

$$x_i^2 + y_i^2 = R_{Ci}^2 \tag{2.2.1}$$

Using equation (2.2.1) in equation (1.4.12) yields to:

$$\phi_i = \frac{x_{Ti}}{R} - Tan(\alpha_i) + \sqrt{\left(\frac{R_{Ci}}{RCos(\alpha_t)}\right)^2 - 1} \tag{2.2.2}$$

Using equally spaced values of R_{Ci}, (initial and final values of the radius correspond to radii at point B_l and B_{l+1}) a set of different values of Φ_i (i = 1,..,Ie) can be evaluated. These values are substituted into equation (1.4.12) to obtain Cartesian coordinates of the nodes, for the involute profile. In order to generate nodes along circumferential direction at radius R_{Ci} , the relative value Φ_i is divided by the number of nodes *Iss*. Each series of values allows to calculate Cartesian coordinates for each circumferential line of mesh. Note that points S_l and S_{l+1} are intersection between the tooth axis and the circumference with minimum and maximum radius.

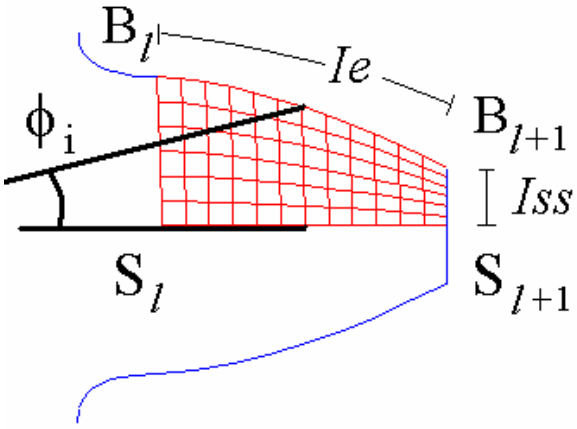

Figure 22: Mesh grid for involute profile.

2.2.2 Trochoidal fillet

Figure 23 shows the mesh grid used for the fillet area. A set of $2{\cdot}Isr{+}1$ nodes ($H_{i,1}$)is considered on the fillet surface from point A to point B. Cartesian coordinates of these points are obtained dividing the angular direction $\zeta_{i,1}$ (from $\zeta_{1,1}$ and $\zeta_{2Isr+1,1}$) into $2{\cdot}Isr$ equal parts and substituting the equivalent Φ_i angular values into equation (1.4.13). Furthermore, the fillet area is divided into two different regions: the right part, from point B to F, and the left part, from F to A. Both parts have *Isr* elements. Point E and point D are defined as intersections between the circumference of radius $R_{ir} = R_{fe} - g_{fe}/2$ (R_{fe} and g_{fe} are respectively radius and tooth thickness at point B) and the tooth axis and the straight line connecting the center of the

gear and point A. Δ_1 and Δ_2 are calculated dividing the length of segment EC and the length of arc DE by *Isr*. Cartesian coordinates of generic internal points $H_{i,j}$ along a vertical line of the mesh can be calculated defining the slope γ of the line of mesh connecting point $H_{i,1}$ with point $H_{i,iss+1}$ and dividing the segment into *Iss* parts of length a_i.

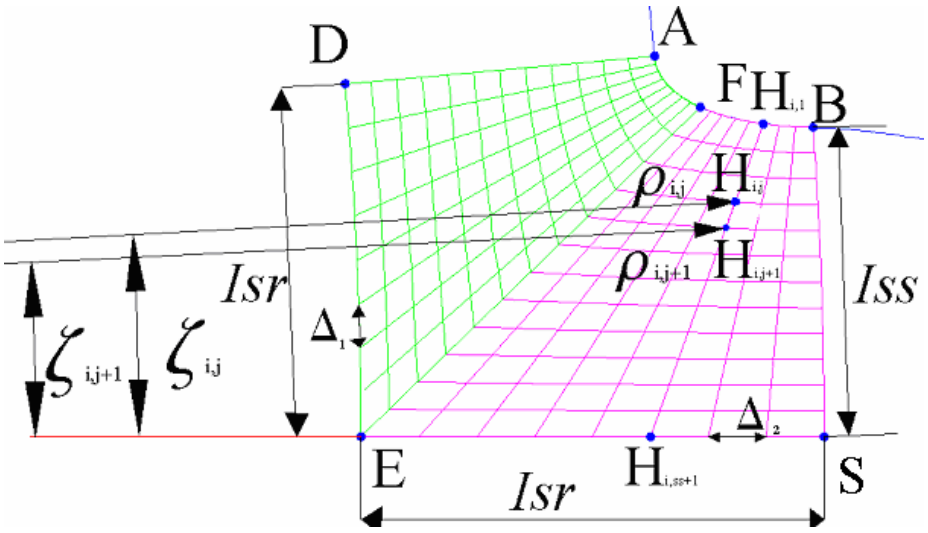

Figure 23: Mesh grid for trochoidal fillet.

A particular procedure is applied to improve computational effort. Polar coordinates of point $H_{i,j+1}$ can be simply evaluated with the following equation, once the polar coordinates of point $H_{i,j}$ are know:

$$\zeta_{i,j+1} = Arctg\left(\frac{\rho_{i,j}Sin\left(\zeta_{i,j}\right) - a_i Cos\left(\gamma_i\right)}{\rho_{i,j}Cos\left(\zeta_{i,j}\right) - a_i Sin\left(\gamma_i\right)}\right) \tag{2.2.3}$$

$$\rho_{i,j+1} = \frac{\rho_{i,j}Cos\left(\zeta_{i,j}\right) - a_i Sin\left(\gamma_i\right)}{Cos\left(Arctg\left(\frac{\rho_{i,j}Sin\left(\zeta_{i,j}\right) - a_i Cos\left(\gamma_i\right)}{\rho_{i,j}Cos\left(\zeta_{i,j}\right) - a_i Sin\left(\gamma_i\right)}\right)\right)} \tag{2.2.4}$$

2.2.3 Arc and rim

Figure 24 a) shows the mesh grid used for the arc below the fillet region. Point N is the intersection between the circumference of radius $R_{ir} = R_{fe} - g_{fe}/2$ and the straight line connecting the center of the gear and point U (point of separation between two contiguous teeth). *Iss* and *Iscp* are number of nodes on the radial and circumferential directions, and which define radius and angular position of each point respectively.

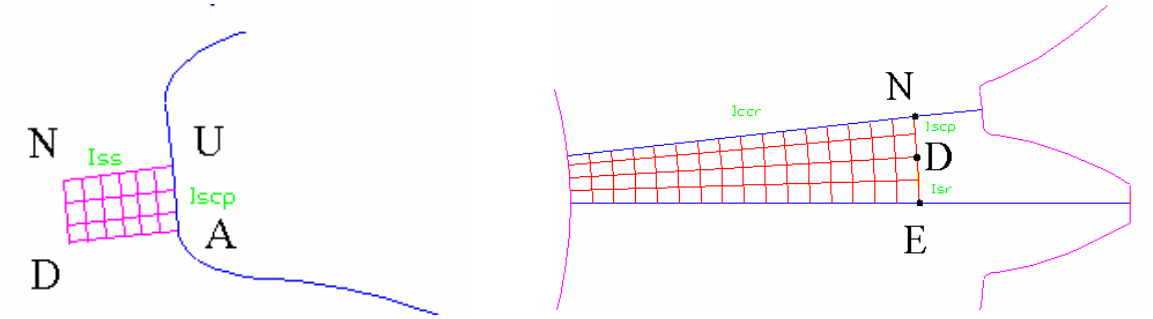

a) b)

Figure 24: Mesh grid for: a) arcs; b) gear rim sector.

A similar approach is used to generate the grid in the rim area, included between circumference of radius R_{ir} and R_{rim}. Note that R_{rim} is the inner radius of the rim. Coordinates of each node are calculated considering *Iccr* and *Iscp+Isr* equally spaced nodes along radial and circumferential directions. Obviously the position of the nodes on the circumference at radius R_{ir} depends upon previous grids for fillet and for root arc.

2.2.4 Shaving

The effect of the shaving process consists in the removal of a stock of material from the profile of the tooth, in order to improve the surfaces finishing (Dudley and Townsend, 1996). In many cases, this cutting process involves only the involute region. For this reason the cutting tool can produce a small step located in the fillet area, which can cause increase in the stress distribution when the load is applied. Figure 25 shows that a typical shape of the step can be mathematically described using two involute curves, one arc and one trochoidal curve. Using the meshing approach, described in the previous sections, a mesh grid for this geometry can be easily generated.

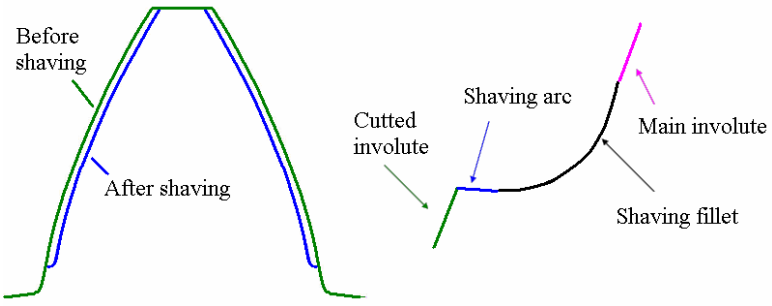

Figure 25: Geometry of the profile after shaving process.

2.2.5 Coordinates rotation

The previous sections show how the first tooth node coordinates are calculated once the total number of elements is provided. In order to calculate node coordinates of all teeth, a coordinate transformation is applied. If Z is the number of teeth in the gear, each different tooth can be generated by rotating the previous by the angle $2\pi / Z$. If the Cartesian coordinates of a node of tooth i are known, the coordinates of the relative node on tooth j can be calculated as follow:

$$\begin{cases} x_j = x_i \cos\left(\dfrac{2\pi}{Z}\right) - y_i \sin\left(\dfrac{2\pi}{Z}\right) \\ y_j = x_i \sin\left(\dfrac{2\pi}{Z}\right) + y_i \cos\left(\dfrac{2\pi}{Z}\right) \\ z_j = z_i \end{cases} \tag{2.2.5}$$

Equation (2.2.5) assumes a counterclockwise rotation of $2\pi / Z$ between tooth i and tooth j.

If a node location is expressed in polar coordinates r_i , α_i and z_i , the rotation of the node is calculated through a simple rotation of the polar angle:

$$\begin{cases} r_j = r_i \\ \alpha_j = \alpha_i + \left(\dfrac{2\pi}{Z}\right) \\ z_j = z_i \end{cases} \tag{2.2.6}$$

2.2.6 Coordinates rotation for the gear pair

In order to complete the previously mentioned procedure, all node coordinates must be subjected to particular rotation due to relative positioning between the pinion and the gear.

A typical example is the analysis of the gear pair when the contact point between mating surface is the pitch point. The pitch point is the intersection between the center distance line and the line of contact, the coordinates of the first generated tooth are expressed with respect to a reference frame whose x-axis is along the tooth axis; then, an appropriate rotation for pinion and gear must be imposed to reach the proper mesh condition. The value of the rotation along z-axis is calculated according to the operating tooth thickness *s'*:

$$\vartheta_{initial,1} = \frac{s'_1}{2r'_1}; \qquad \vartheta_{initial,2} = \frac{s'_2}{2r'_2} \tag{2.2.7}$$

Note that a further rotation must be imposed to both gears, if more then one relative position must be analyzed. Let us consider, for example, the case of *n* different position in a mesh cycle. In terms of rotation, a mesh cycle is the defined as the rotation to be imposed to the gear system such that one tooth reaches the position of the previous one. In order to calculate the coordinates of all nodes at each of the *n* different positions, the following additional rotation must be included to the initial rotation described in equation (2.2.7):

$$\vartheta = step\frac{2\pi}{Z_1 n} \qquad step = 0...n-1 \tag{2.2.8}$$

step indicate each different relative positions.

Equation (2.2.7) and (2.2.8) can be inserted into equation (2.2.5) or (2.2.6) in place of $2\pi / Z$ to calculate the nodes coordinates for whatever relative position between the gears.

2.2.7 Mesh generation

In order to create a Nastran® script file, which can be imported into Marc® environment, two Fortran® applications where developed. The first one is able to numerate nodes and arrange coordinates of each point according to the element description for a single gear, the second one extends the previous procedure at the gears pair with an optimization algorithm, which simplify the ordering and numbering process. The approach is developed for arbitrary quadrilateral isoparametric plain strain and plain stress elements as described in previous sections.

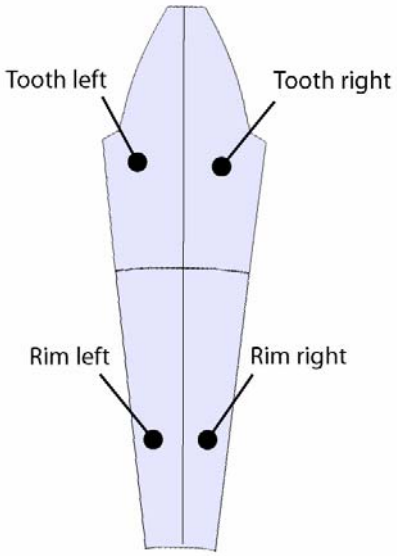

Figure 26: Parts in tooth division.

Each single tooth is divided into four parts: left and right tooth side and the left and right rim side (see Figure 26). For each parts, two main directions are used to number the elements. Elelments of the left side parts are numbered according to the following directions:

Tooth: from left to right along the tooth thickness and from the tip to the root along the gear profile

Rim: from up to down in radial direction and from left to right in circumferential direction. The same approach is used for right sides except that directions go from right to left.

Once the number of elements is known in all directions (this number is specified from the user) the element numbering algorithm for each part can be specified as follows:

$$n_{element} = N \cdot (j-1) + i; \quad i = 1...N, \quad j = 1...M \tag{2.2.9}$$

$$Node_{up}^{left} = (j-1) \cdot (N+1) + i; \quad i = 1...N, \quad j = 1...M \tag{2.2.10}$$

$$Node_{up}^{right} = (j-1) \cdot (N+1) + i + 1; \quad i = 1...N, \quad j = 1...M \tag{2.2.11}$$

$$Node_{down}^{left} = j \cdot (N+1) + i; \quad i = 1...N, \quad j = 1...M \tag{2.2.12}$$

$$Node_{down}^{right} = j \cdot (N+1) + i + 1; \quad i = 1...N, \quad j = 1...M \tag{2.2.13}$$

Where N and M are the number of elements in the first and second directions, and i and j are counter for first and second directions.

For a current element (specified by i and j), equation (2.2.9) provides the element number while equations (2.2.10), (2.2.11), (2.2.12) and (2.2.13) provide the nodes numbers (see Figure 27).

The mesh process of the parts follows the “left to right, up to down” rule. This means that the first part to be meshed is the tooth left part, the second one is the tooth right part, the third one the rim left part and the fourth one is the rim right part. It is important to underline that the meshing process of each part takes into account the number of nodes and elements of the previous part. For example the number of the first element of the tooth right part will be equal to the number of elements of the tooth left part in addition to one. A storing procedure takes also into account that equations (2.2.10), (2.2.11), (2.2.12) and (2.2.13) cannot provide the same number to the nodes at the border lines between each parts. In order to solve the

problem the identification number of nodes at the interface are store during the mesh of the first part. When the second part is meshed the value of the number of nodes at the interface are not calculated through the numbering algorithm but from the stored data. For example, at the interface between tooth left part and tooth right part (see Figure 28), nodes at the interface must have a unique identification number. The procedure stores the number of nodes at the interface during the mesh of tooth left part and uses the stored data in the numbering process of tooth right part.

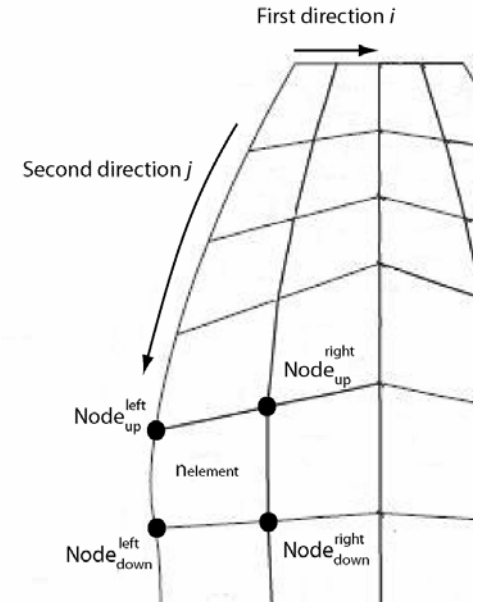

Figure 27: Element numbering.

A similar situation occurs when two different teeth are joint together to create the full gear model. In this case another similar procedure stores the number of identification of each nodes at the interface between teeth and provide a unique identification number for border lines nodes.

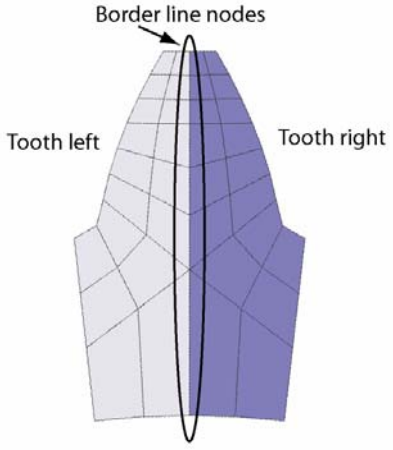

Figure 28: Nodes at border line between tooth left part and tooth right part.

This storing data technique is applied to merge each teeth in a counter clock wise direction until the full gear is completed.

2.2.8 File Nastran

The final step to generate a full FE model for a spur gear pair is writing all the mesh information into an appropriate Nastran script. Marc® user's manual (MSC.Marc, 2003) (Mentat, 2003) indicates the script file must be structured as follows:

BEGIN BULK
Element connectivity
Element nodes coordinates
ENDDATA

The instructions "BEGIN BULK" and "ENDDATA" are used to open and close the file. A short description of the "Element connectivity" and "Element nodes coordinates" is described in the following.

Element connectivity

This item consists in a list of all elements identification numbers followed by +1 or -1, depending on the element orientations (clock wise or counter clock wise), and the list of the relative nodes identification numbers. A specific format instruction must be used to describe the element connectivity according to the number of bit for each piece of information.

The main difficulty is to order all numbers with the first digit on the left column margin. In effect, the number of digits of a number does not depend on the number itself. For example number 10 has 2 digit as well as 20. A simple algorithm based on logarithm function has been used for this purpose. The number of digits for number n is calculated as follow:

$$digits = \text{int}\left(\log_{10}\left(n\right)\right)+1 \tag{2.2.14}$$

where the Fortran function "int" returns the integer smaller number of a real number.

The following lines show how the format instruction has been implemented in Fortran language.

```
 96 format(TL1,'CQUAD4  1',7x,i<int(log10(NUMELEMENT/1.))+1>,
&<7-int(log10(NUMELEMENT/1.))>x,i<int(log10(NODOBASSSX/1.)+1)>,
&<7-int(log10(NODOBASSSX/1.))>x,i<int(log10(NODOBASSDX/1.)+1)>,
&<7-int(log10(NODOBASSDX/1.))>x,i<int(log10(NODOALTODX/1.)+1)>,
&<7-int(log10(NODOALTODX/1.))>x,i<int(log10(NODOALTOSX/1.)+1)>,
                &<7-int(log10(NODOALTOSX/1.))>x)
```

Element nodes coordinates

It consists in a list of all elements identification numbers followed by the relative nodes coordinates. Even for the node coordinates a particular format instruction must be used:

```
 79 format(tl1,'GRID*   ',i<int(log10(NUMNODO/1.))+1>,
&<38-int(log10(NUMNODO/1.))-int(log10(ABS(int(X))+1.))>x,
         &sp,F<INT(log10(ABS(int(X))+1.))+9>.6,
            &<7-int(log10(ABS(INT(Y))+1.))>x,
         &sp,F<INT(log10(ABS(INT(Y))+1.))+9>.6)
 81 format(TL1,'*',<14-int(log10(ABS(int(Z))+1.))>x,
         &sp,F<INT(log10(ABS(INT(Z))+1.))+9>.6)
```

Note that after the word "GRID*" all coordinates are specified with a maximum of six decimal digits and that coordinate on z axis must be specify separately with a second format instruction.

Both "Element connectivity" and "Element nodes coordinates" procedure are repeated for each tooth and for both pinion and gear.

2.2.9 Example of a complete spur gear pair

Using the described technique a batch file can be used to run simultaneously all different script files to analyzed *n* different gear relative positions in a complete mesh cycle.

A Fortran routine creates a .dbf file (file extension for Nastran®, Marc® (MSC.Marc, 2003)) to compute an arbitrary number of relative position, within a mesh cycle in a one step procedure.

A simple case study (case study 1) is carried out to verify the FE approach. Table 2 shows the geometrical data for the spur gear pair:

Data	**Pinion**	**Gear**
Number of teeth	28	43
Module [mm]	3	3
Pressure angle [Deg]	20	20
Base radius [mm]	39.467	60.610
Theoretical pitch radius [mm]	42	64.5
Thickness on theoretical pitch circle [mm]	6.1151	6.7128
Addendum modification [mm]	1.927	2.748
Face width [mm]	27	22.5
Hob tip radius [mm]	0.9	0.9
Outer diameter [mm]	93.1	139.7
Root diameter [mm]	79.1	126.2
Inner diameter [mm]	40	40
Center distance [mm]	111	

Table 2: Geometrical data for the case study 1 (courtesy of CNH Case New Holland).

The first test is carried out to validate the geometry produced with the Fortran routine. The profile created is compared with the same geometry calculated with a commercial software. The comparison between coordinates of the two profiles show errors due to machine precision and the calculation of the maximum error grant a value below 10^9 mm. Figure 29 shows congruity between two profiles for the test case described in Table 2.

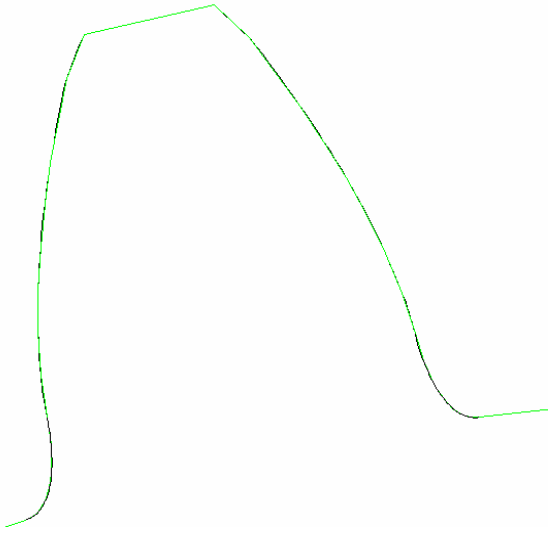

Figure 29: Comparison between generated profile for the pinion: developed technique (green line), commercial software (black line).

A second test (case study 1b) is carried out to check the mesh generation process. Table 3 shows a set of mesh parameters for the gear test study.

Data	Pinion	Gear
Ie	18	19
Isr	5	4
Iss	4	4
Iscp	1	1
Iccr	8	12

Table 3: Mesh parameters for case study 1b.

Figure 30 shows the mesh generated with the previous mesh parameters for both pinion and gear.

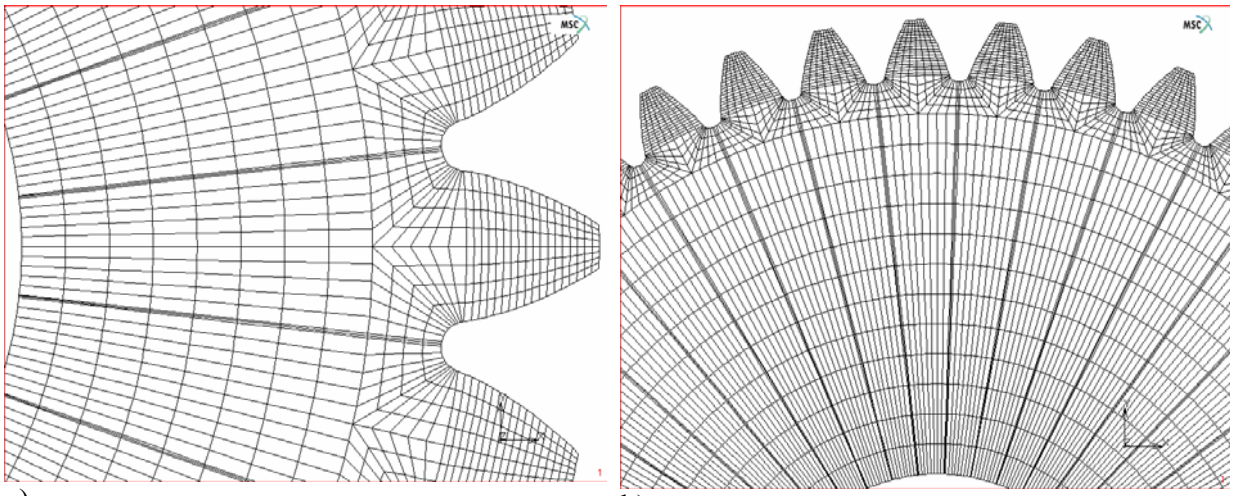

a) b)

Figure 30: Mesh generation: a)Pinion; b) Gear.

Figure 31 and Figure 32 show the complete mesh of pinion and of the gear.

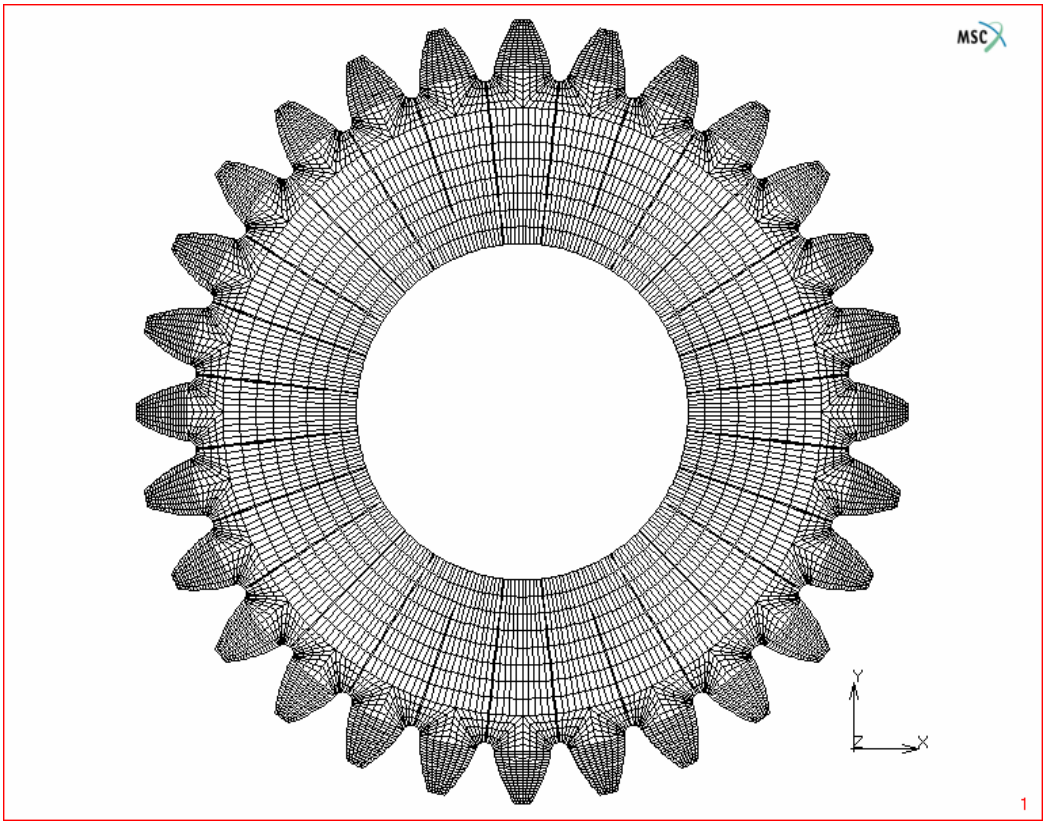

Figure 31: Complete mesh of the pinion.

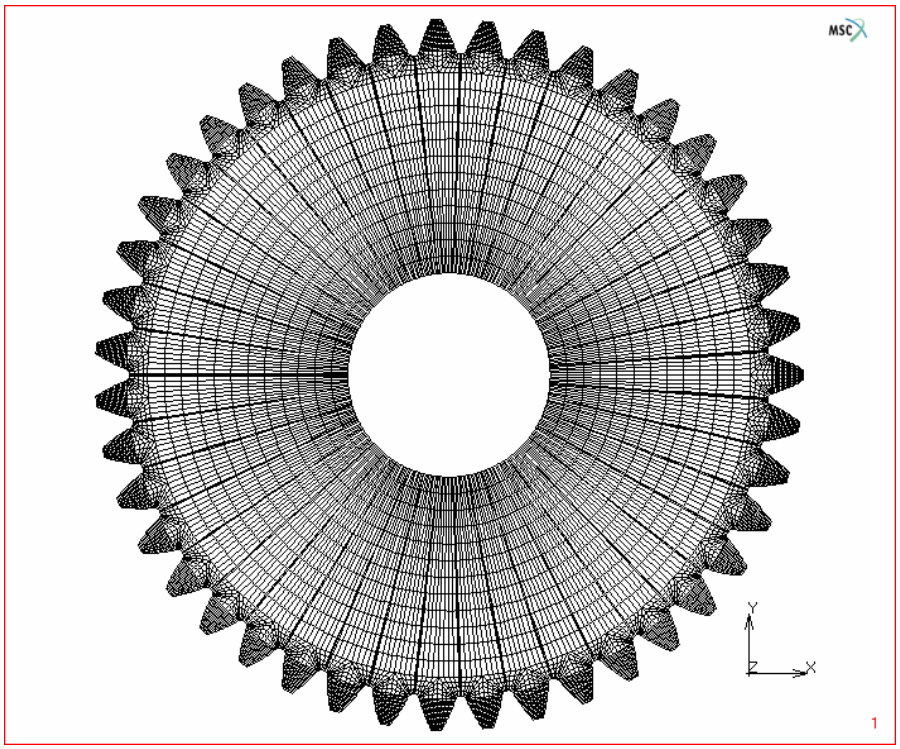

Figure 32: Complete mesh of the gear.

The numbering of nodes and elements is also checked: Figure 33 and Figure 34 show how the numbering process of element and nodes follows the approach described in the previous paragraphs for both pinion and gear.

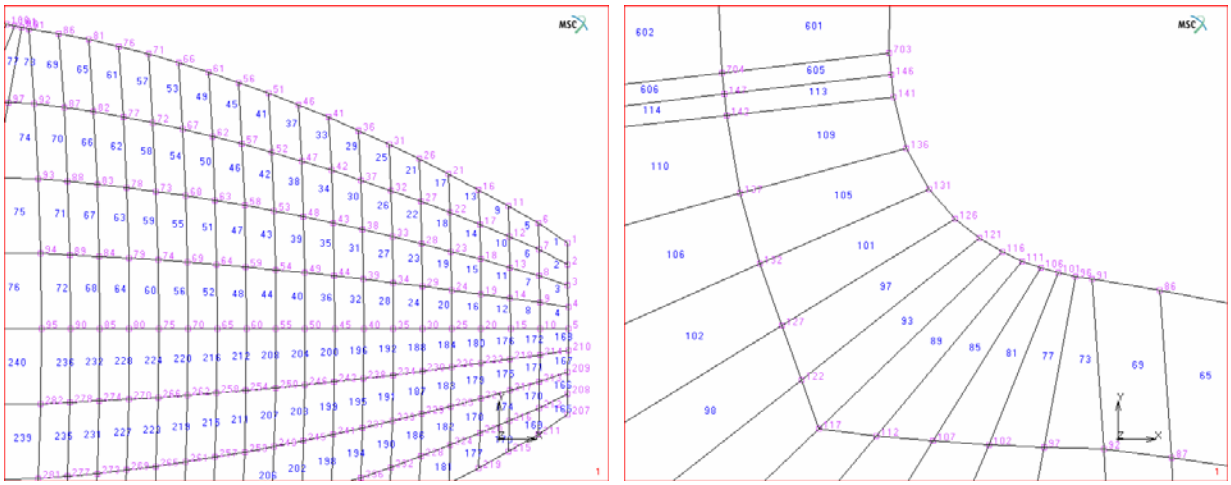

Figure 33: Pinion numeration of node and elements: a) Detail of the tip of tooth 1; b) Detail of the left side fillet of tooth 1.

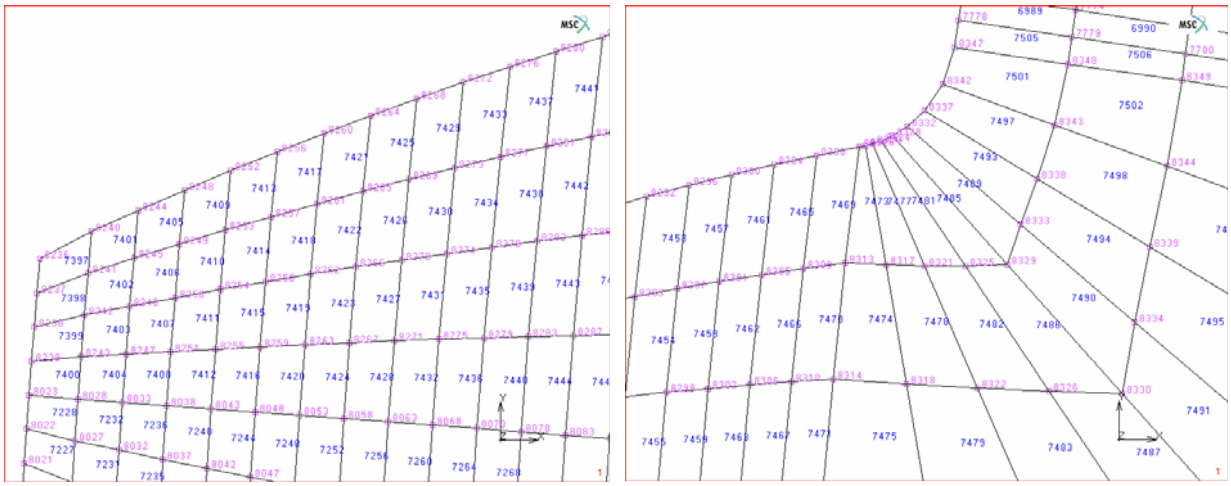

Figure 34: Gear numeration of node and elements: a) Detail of the tip of tooth 22; b) Detail of the right side fillet of tooth 22.

Finally, another test (case study 1c) is carried out to verify the generation of the gears pair model when the contact between the wheel is at the pitch point. The mesh parameters are changed according to Table 4. Figure 35 and Figure 36 show the complete mesh of the spur gear pair and a detail of the mesh at the contact point.

Data	Pinion	Gear
Ie	10	10
Isr	3	3
Iss	3	3
Iscp	3	3
Iccr	3	3

Table 4: Mesh parameters for the case study 1c.

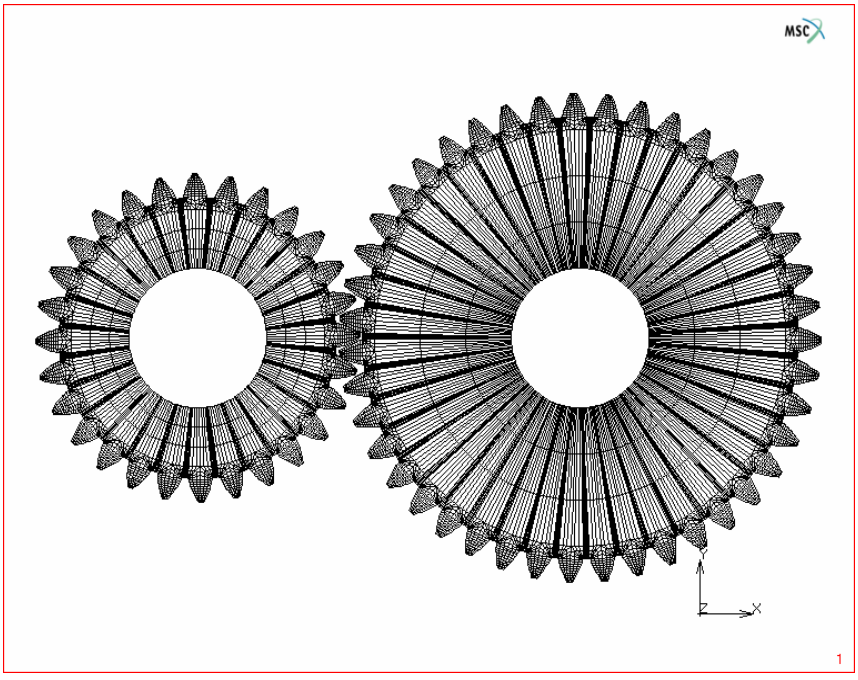

Figure 35: Complete mesh of the gears pair model (case study 1c).

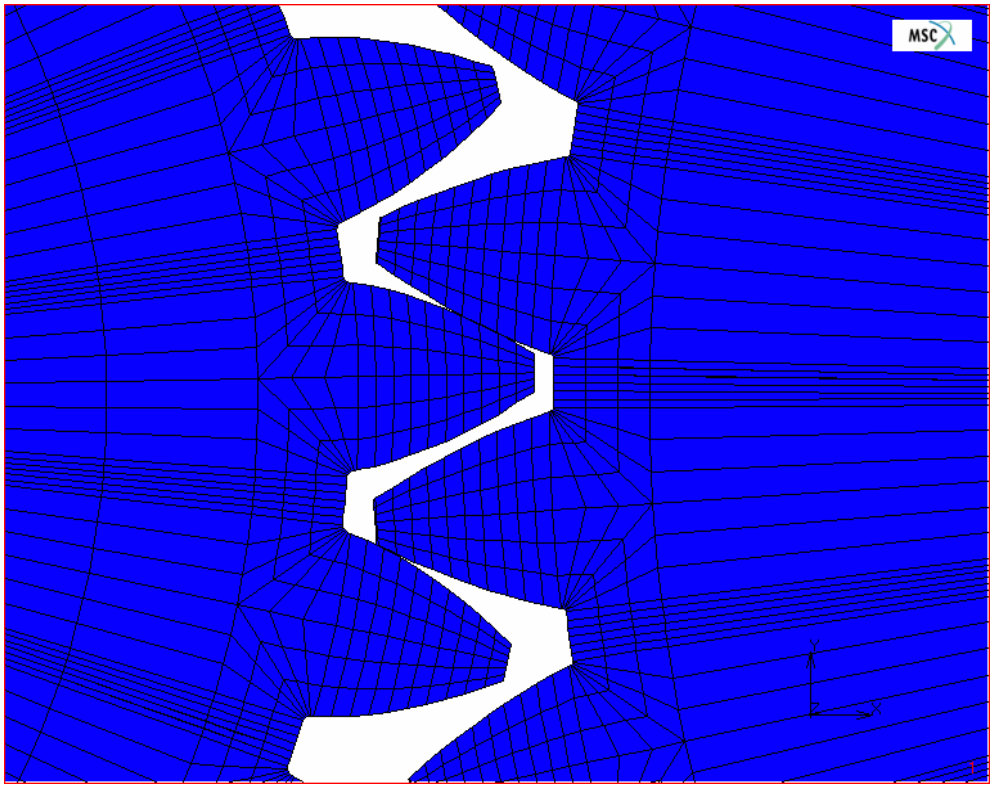

Figure 36: Complete gears pair model: detail of the mesh at the contact point.

2.2.10 Evaluation of static transmission error for a spur gear pair

In the present section the main objective of modeling a spur gears pair with Finite Element consists in the evaluation of the static transmission error. If gears are supposed rigid and with equispaced perfect conjugated teeth, they will transmit exactly uniform angular motion ((Sloane 1941), (Buckingham 1949), (Faires and Keown, 1960), (Funaioli et al., 1987), (Mark,1989)). Real gears are subjected to elastic deformation and the surface profiles are not perfect involute; therefore the relative rotation of the wheels undergoes to a small unsteady component in the transmission of the angular motion. This component is usually referred as the transmission error. ((Walker, 1938), (Harris 1958), (Gregory et al., 1963-1964), (Mark,1989), (Maatar et al., 1995)). Therefore the transmission error is defined as the deviation of the position of the driven gear, for a given angular position of the driving gear, from the position that the driven gear would occupy if the gear were geometrically perfect (Munro, 1969-1970), (Gregory et al., 1963-1964), (Houser and Bolze, 1996). If no dynamics effects are included, such as damping and inertia, the transmission error is effected only by the static deflection of the teeth, the local deformation due to contact pressure and the deviation from the theoretical involute profile due to profile modifications and manufacturing

errors. In this case, the transmission error is always referred as “Static Transmission Error” (STE). On the other hand, when dynamic, effects are taken into account, for example when gears are rotating at a certain speed, the transmission error will be referred as “Dynamic Transmission Error” (DTE) (Bard, 1995).

As the number of teeth pairs in contact within the mesh cycle changes, with the rotation of the gear, the mesh stiffness varies accordingly. For this reason, transmission error does not have a single value, but must be considered as a continuous variable during gears rotations.

If all teeth are equal in both pinion and gear, the static transmission error is periodic with the period of mesh. Therefore the static transmission error can be easily calculated using a FE approach, which can be able to analyze *n* different relative position of the gears within a mesh cycle.

The approach, described in the previous sections, allows to generate the FE model for each of the *n* relative positions in a very easy way. A test case (will be referred as case study 1d) is performed with the spur gear set described in Table 2 with the mesh parameters described in Table 5.

For each relative positions, MSC-MARC® is used to perform the analysis. More than 2400 quadrilateral elements are used for each gear. The driven wheel shaft is considered locked, i.e. the inner circumference of this wheel has zero rotation. This means that the driven wheel can be deformed around its shaft. The shaft elasticity is not considered here. The driver wheel can rotate around its shaft, i.e. its internal circumference has only rigid rotation.

Data	Pinion	Gear
Ie	40	40
Isr	3	3
Iss	5	4
Iscp	1	1
Iccr	6	6

Table 5: Mesh parameters for case study 1d.

A torque of T = 470 Nm is applied to the driver wheel through distributed tangential force applied at all nodes at the inner circumference. The wheel material is an alloy steel with a Young modulus of $2.06*10^{11}$ MPa and Poisson ratio of 0.3.

Using a center distance of 111 mm the contact ratio ε_α becomes 1.2856, with period mesh angle equal to 12.857°. Fifteen, equally spaced, positions are analyzed in order to obtain the driver shaft rotation δ. The contact point between the gears at the first analyzed position is the pitch point. According to the contact ratio, from position 5 to 12 two pairs of teeth are in

contact, while for the remaining positions one pair of teeth is in contact. In addition to the FE model, contact element has been used in the contact regions.

The stiffness k is evaluated for each position by using the following relationship which also transforms the torsion stiffness, T/δ_i, into the linear stiffness by dividing it by the square of the base circle radius of the pinion:

$$k_i = \frac{T}{r_{b1}^2 \delta_i} \quad i = 1...15 \tag{2.2.15}$$

The value of δ_i (usually radians) is calculated as the average circumferential translation of the nodes located at the inner circumference of the pinion at relative position i. The value of the static transmission error along the line of action (usually measured in μm) is calculated for each step with the following expression:

$$STE = r_b \delta_i \quad i = 1...15 \tag{2.2.16}$$

Marc is capable to analyze every single .bdf file and to reliably produce stress result for each single step. Figure 37 shows an example of Von Mises contour for case study 1d.

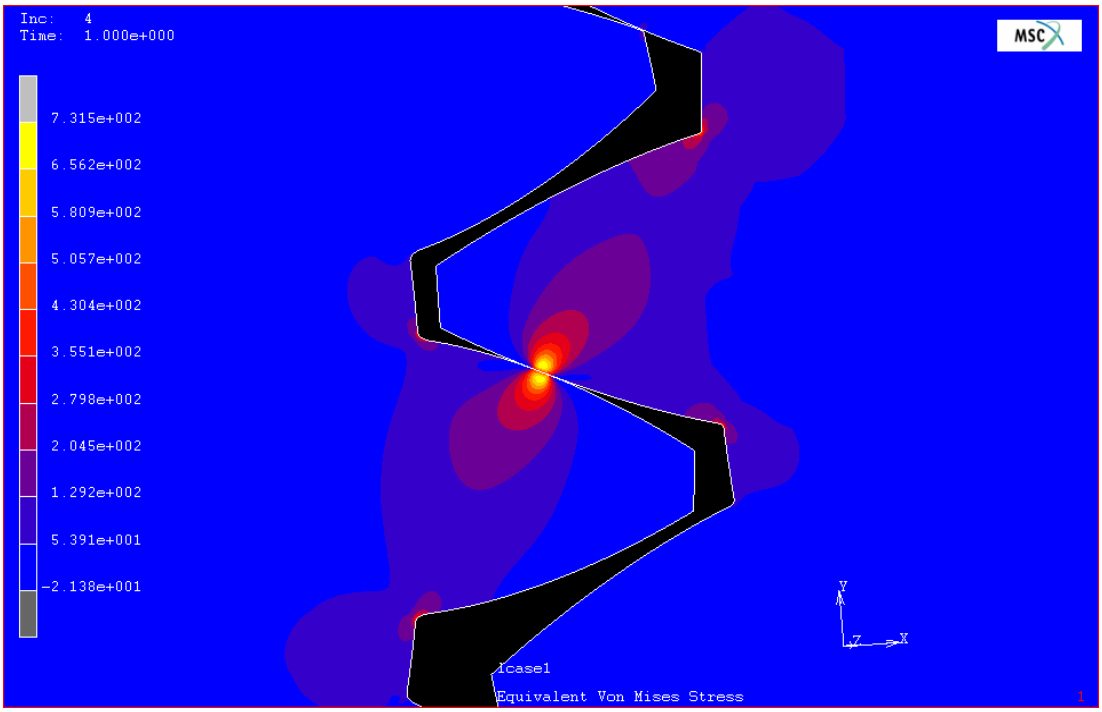

Figure 37: Von Mises stresses contour for case study 1d.

Values of the mesh stiffness are compared with those obtained with the commercial software Calyx®. Figure 38 shows comparisons of the mesh stiffness obtained with MSC Marc and Calyx, the behaviour is similar, even though a certain shift is present (the average is

different), this is due to the fact that in using MSC Marc, plain stress theory has been considered. Figure 39 shows comparisons of the mesh stiffness and the static transmission error, similar comments made for Figure 38 apply.

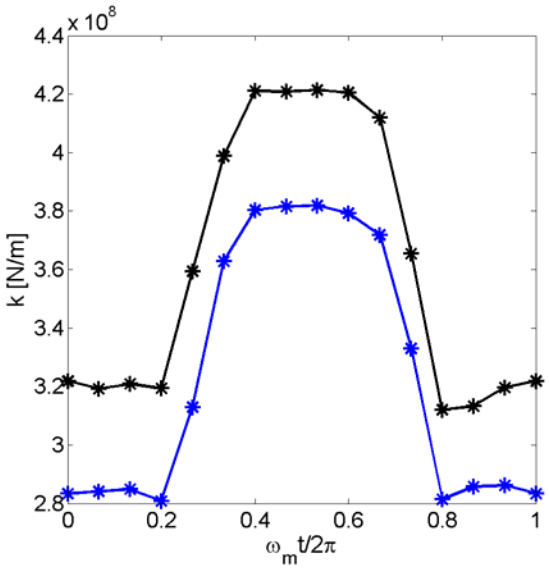

Figure 38: Comparison of mesh stiffness: proposed approach (black); Calyx® (blue).

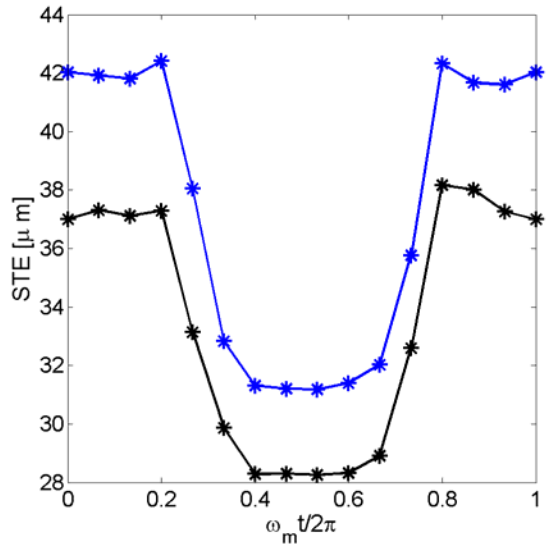

Figure 39: Comparison of static transmission error: proposed approach (black); Calyx® (blue).

Table 6 shows the comparison of the mesh stiffness values plotted in Figure 38. The average percentage error is around 10%.

Proposed approach with MSC-Marc®	Calyx®
3.2189 10^8	2.8332 10^8
3.1918 10^8	2.8407 10^8
3.2085 10^8	2.8483 10^8
3.1937 10^8	2.8078 10^8
3.5941 10^8	3.1296 10^8
3.9875 10^8	3.6280 10^8
4.2103 10^8	3.8034 10^8
4.2081 10^8	3.8161 10^8
4.2140 10^8	3.8192 10^8
4.2051 10^8	3.7931 10^8
4.1195 10^8	3.7185 10^8
3.6545 10^8	3.3298 10^8
3.1200 10^8	2.8139 10^8
3.1328 10^8	2.8576 10^8
3.1963 10^8	2.8621 10^8
3.2189 10^8	2.8332 10^8

Table 6: Comparison between evaluated values on mesh stiffness [N/m].

In order to understand the behavior of the circumferential strain on the pinion rim, depending on the torque applied, one of the fifteen positions for the gear model, is studied with different torque values. Five case with respectively 235 Nm, 470 Nm, 705 Nm, 940 Nm and 1175 Nm are investigated using the same fem approach described previously. The average circumferential strain on the pinion rim is evaluated for each load case. Figure 40 shows an almost linear relationship between the two quantities which allows us to extends the approach used for the evaluation of the stiffness, in a contour of the torque value of 470 Nm.

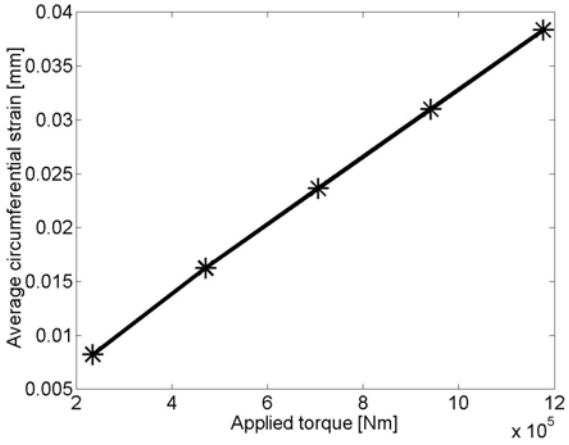

Figure 40: Linear behavior of the circumferential strain depending on torque.

Note that the previous results are calculated when the contact point corresponds to the pitch point. A non-linear behavior can probably occur if the analysis is performed in some

particular point. For example close to the HPSTC, different torque values can involve different number of teeth pair in contact and consequently strong non-linearity behavior.

2.3 Calyx®

In the last few years the Finite Element analysis has become one of the useful tool in engineering design. The increasing power of tools such as faster and multi processor computers allows to model complex system in a reasonable amount of time. Despite these circumstances there are many example of mechanical applications which still are difficult to analyze. One of these application is multi-mesh gears system. For example in planetary gear system or in multi stage speed reducer, the large number of body, the complex kinematics and the effect of gear boxes, shafts and bearings, cannot be neglected when the behavior of the system is simulated.

Calyx® is a computer program meant for the contact analysis of two and three dimensional multi-body system. The analytical technique used in the software combines a unique, semi-analytical finite element approach with detailed contact modeling at the tooth mesh (Vijayakar, 1999) which is specifically developed to examine the mechanics of precisely machined, contacting elastic bodies such as gears. The semi-analytical finite element approach does not require a highly refined mesh at the contacting tooth surfaces which substantially reduces the computational time. With this approach Calyx® is capable to solve many technical difficulties typical of contact pair analysis in complex geared systems (Vijayakar, 2003-c):

Size of the contact zone: The width of the contact zone in typical gearing applications is two orders of magnitude smaller than the dimensions of the gear teeth themselves. In order to model the contact conditions with sufficient accuracy, a general purpose non-linear finite element program needs to have a large number of nodes (a very fine mesh) inside the contact zone. To run such a contact model, the fine mesh in the contact zone has to transition into a much coarser mesh over the rest of the gear. The location of the contact zone, however, changes as the gears move. This means that either the gear finite element model should be re-meshed for each time instant, or that the finite element mesh be highly refined over its entire surface area. Both these alternatives lead to unacceptably high computational costs. Calyx® approach has been to use the finite element models only to compute relative deformation and stresses for points that are away from the contact zones (Vijayakar, 1999). For points within

the contact zone, Calyx® uses semi-analytical techniques to compute the relative deformations and stresses. The "near field" semi-analytical solution and the "far field" finite element solutions are matched at a "matching surface". Such a model is significantly difficult to program on a computer, but once implemented, can provide much better resolution without using a highly refined finite element mesh.

Rigid body degrees of freedom in the system: In multi-mesh gear systems like planetary transmissions, there are many rigid body degrees of freedom or mechanisms that are constrained only by the contact conditions. This means that if a non-linear finite element code with gap elements is used, then the incremental stiffness matrices become singular.

Some manipulations are commonly used, such as adding imaginary linear and torsional springs to make the system stiffness matrices non-singular. The spring stiffness can be made small, but the accuracy of results computed by such almost singular stiffness matrices is questionable. Calyx® approach has been to attach a reference frame to each individual component, and to carry out the finite element computations for each individual component separately in its own reference frame. As long as each finite element mesh is sufficiently well constrained to its reference frame, the stiffness matrices are well behaved (Parker et al, 2000-b). The free mechanisms in the system can be modeled by allowing the reference frames to move freely. The contact solver used is based on the Revised Simplex solver (Vijayakar, 1988). This solver is commonly used to solve quadratic programming problems. It can take into account any free mechanisms in the system while computing the contact loads.

Large number of degrees of freedom: For a typical transmission system models, the total number of finite element degrees of freedom can be extremely large. This is so even with the finite element model refined only as much as is necessary for the far field solution. The total number of finite element degrees of freedom is approximately proportional to the total number of teeth. The amount of CPU time and memory needed to run a finite element analysis with such a large degree of freedom would make it impractical. Calyx® has resorted to using a hierarchical representation of the system, in which the system is built from many substructures, with each substructure in turn being composed of many substructures. The processes of stiffness decomposition and load vector back-substitution now become very complex, and involve multiple recursive traversals of the substructure hierarchy. However, it is now possible to keep CPU requirements within practical limits.

Convergence of conditions at contact interfaces: Poor convergence of contact conditions at interfaces is one of the biggest problems caused by using a general non-linear solver to solve a problem with contact constraints. The constraints imposed by the contact between mating

surfaces are essentially linear inequality constraints. When a general purpose non-linear solver is used to solve this problem, convergence is not guaranteed, and if it does occur, it is usually very slow. The Revised Simplex solver provides a guarantee of convergence within a predetermined number of iterations. Furthermore, ill-posed contact problems can be detected even before the solution process is started (Vijayakar, 1988). The solver is specifically designed for the linear inequality type constraints found in contact problems.

System Kinematics: The nominal position of each individual gear in the system changes with time. The nominal positions of the components are determined by the kinematics of the system. The kinematics of the system affects the nominal sliding velocities and inertial loads. It is very difficult to include this kinematic information into a finite element program. Calyx® has a special purpose programming language into the software in order to specify the details of the kinematics of each component in the system. Important details such as the kinematics effect of assembly errors, runout and misalignments are easy to apply using this approach.

Calyx® communicates with the outside world through a programming language which brings flexibility at the expense of ease of use. It is controlled by the user through instructions in a special purpose programming language (Vijayakar, 2003-a).

In the next paragraphs Calyx® language is used to perform a complex static analysis of a compound two stages planetary gear system using plain strain assumption.

2.4 Compound planetary system

In this section a description of the actual compound planetary system is given. The speed reducer is part of an existing transmission system for aeronautical application. For this reason some data will be indicated using "XXXX". The main purpose of next sections is describe the modeling technique and not data results.

Note that in the next three sections all data are provided in English units.

2.4.1 Example of compound planetary system

The system is a compound planetary gear composed of two planetary stages connected with each other. These components are shown in the schematic of the full transmission as seen in Figure 41. In the first stage, the sun is one piece with the input shaft and meshes with four planets, while in the second stage the sun is connected with a spline to the carrier of the first

stage and meshes with six planets. All planets are supported by bearings that connect them to carriers.

The carrier of the second stage is one piece with the output shaft. The ring gears are connected to each other by a thin ring and bolted to the gear box by multiple circumferential bolts through a radial flange extending from the ring gear.

Two sets of bearings hold the complete structure. The first one, consisting of one spherical roller and a straight roller bearing, supports the input shaft. The second one, consisting of two tapered roller bearings, supports the output shaft. One spherical roller bearing connects the input shaft and the carrier of the first stage to support the carrier and to prevent misalignment.

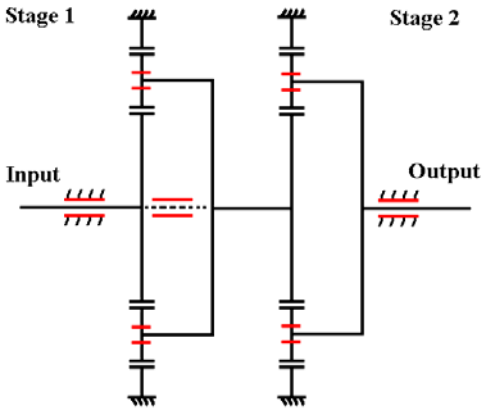

Figure 41: Schematic of the compound planetary system with bearings (red lines).

The 2D model is developed with the following assumptions:

1. All the gears are modeled with their effective tooth profiles as elastic bodies using typical finite element;
2. The input shaft, output shaft and all carriers are considered as rigid bodies;
3. The ring gears are considered as separated bodies;

Particular attention is paid to the connections between bodies. The input shaft and sun of first stage are modeled as a single body constituted by the sun with added input shaft lumped mass and moment of inertia. The carrier of the first stage is rigidly connected to the sun of the second stage, forming a unique body that can deflect along the x and y directions (this two-body assembly will be referred to using one of the component names). The output shaft and the carrier of stage two are a single rigid body, which will now be referred to as carrier of stage two.

Two different sets of spherical roller bearings connect, respectively, the planets and carriers of stages one and two. Figure 41 shows that three different straight roller bearings are modeled

in order to support the structure between input shaft and ground, output shaft and ground, and carrier one and sun one.

Rings one and two have rigid connections to ground, with constraints in all rigid body degrees of freedom. Each can deform elastically as the teeth, rim, and outer diameters are flexible.

All planets are rigidly connected to bearings governing their rigid body degrees of freedom, but each can deform elastically as the inner diameters are flexible.

Because of its large inertia compared to other components, the carrier of the second stage, which is splined to the main rotor, is constrained to have no deviation from its motion based on nominal gear kinematics. Consequently, the bearing that supports the second stage carrier / output shaft is neglected.

The input torque is applied to the first stage sun, meaning the speed of the first stage sun can fluctuate about its nominal value in a dynamic simulation. The boundary condition at the output, as indicated above, is that the second stage carrier has no deviation from its nominal motion (meaning the output torque can vary about its nominal value in a dynamic simulation).

2.4.2 Gear geometry

The first stage is composed of an input shaft, sun, four planets, ring and a carrier. All planets are identical but not equally spaced. Table 7 shows angular positions and center distance of the planet with respect to the sun for stage one. Table 8 shows gear data for stage one.

The second stage is composed of an input sun, six planets, ring, carrier and output shaft. All planets are identical but not equally spaced. Table 9 shows angular positions and center distance of the planet with respect to the sun for stage two. Table 10 shows gear data for stage two.

Quadratic (parabolic) profile modifications are applied according to Table 11 and Table 12. These modifications are the same on both sides of a given tooth. The tip modification extends from the specified roll angle to the end of the tooth. The amount of modification is in the table. The root modification extends from the pitch point to the specified root roll angle with no modification at the pitch point and specified value as given at the ending root roll angle.

Planet number	1	2	3	4
Angular position [deg]	XXXX	XXXX	XXXX	XXXX
Center distance sun-planets XXXX in				

Table 7: Angular position and center distance planets first stage.

Data	Sun	Planet	Ring
Number of teeth	28	39	106
Diametral pitch [1/in]	4.75	4.75	4.75
Pressure angle [Deg]	25	25	25
Base radius [in]	2.671222	3.720632	10.112487
Theoretical pitch diameter [in]	5.894736	8.210526	22.31579
Thickness [in]	XXXX	XXXX	XXXX
Face width [in]	XXXX	XXXX	XXXX
Hob tip radius [in]	XXXX	XXXX	XXXX
Fillet radius [in]	XXXX	XXXX	XXXX
Outer diameter [in]	XXXX	XXXX	XXXX
Root diameter [in]	XXXX	XXXX	XXXX
Inner diameter [in]	XXXX	XXXX	XXXX
Minor diameter [in]	XXXX	XXXX	XXXX
Young modulus [lbf/in^2]	2.9 10^7	2.9 10^7	2.9 10^7
Poisson ratio	0.29	0.29	0.29
Density [lbf·s^2/in^4]	7.3533 10^{-4}	7.3533 10^{-4}	7.3533 10^{-4}

Table 8: Gear data stage one.

Planet number	1	2	3	4	5	6
Position [Deg]	XXXX	XXXX	XXXX	XXXX	XXXX	XXXX
Center distance sun-planets [in] XXXX						

Table 9: Angular position and center distance planets second stage.

Data	Sun	Planet	Ring
Number of teeth	40	33	106
Diametral pitch [1/in]	4.75	4.75	4.75
Pressure angle [Deg]	25	25	25
Base radius [in]	3.816033	3.148226	10.112487
Theoretical pitch diameter [in]	8.421054	6.947368	22.31579
Thickness [in]	XXXX	XXXX	XXXX
Face width [in]	XXXX	XXXX	XXXX
Hob tip radius [in]	XXXX	XXXX	XXXX
Fillet radius [in]	XXXX	XXXX	XXXX
Outer diameter [in]	XXXX	XXXX	XXXX
Root diameter [in]	XXXX	XXXX	XXXX
Inner diameter [in]	XXXX	XXXX	XXXX
Minor diameter [in]	XXXX	XXXX	XXXX
Young modulus [lbf/in^2]	2.9 10^7	2.9 10^7	2.9 10^7
Poisson ratio	0.29	0.29	0.29
Density [lbf·s^2/in^4]	7.3533 10^{-4}	7.3533 10^{-4}	7.3533 10^{-4}

Table 10: Gear data stage two.

Quadratic (parabolic) profile modifications are applied according to Table 11 and Table 12. These modifications are the same on both sides of a given tooth. The tip modification extends from the specified roll angle to the end of the tooth. The amount of modification is in the table. The root modification extends from the pitch point to the specified root roll angle with no modification at the pitch point and specified value as given at the ending root roll angle.

Stage 1	Tip		Pitch		Root	
Gear	Roll Angle	Magnitude [in]	Roll Angle	Magnitude [in]	Roll Angle	Magnitude [in]
Pinion	33.44	-0.001	26.72	0	18.80	-0.00035
Sun	37.06	-0.0008	26.72	0	16.61	-0.00055
Ring	24.06	-0.0006	26.72	0	29.37	-0.00045

Table 11: Profile modification on stage 1.

Stage 2	Tip		Pitch		Root	
Gear	Roll Angle	Magnitude [in]	Roll Angle	Magnitude [in]	Roll Angle	Magnitude [in]
Pinion	34.91	-0.0009	26.72	0	17.57	-0.00045
Sun	33.59	-0.0008	26.72	0	19.49	-0.00055
Ring	24.06	-0.0006	26.72	0	29.37	-0.00045

Table 12: Profile modification on stage 2.

All data in Table 7, Table 8, Table 9 and Table 10 are collected from nominal values from the drawings provided by Boeing. In case of multiple versions of a part in the drawings, the value was chosen from the most recent drawing. The hob tip radii for all the external gears (as required by Multyx) were evaluated by inverting the following formula (Dudley and Townsend, 1996):

$$\rho_{fillet} = r_{hob} + \frac{(b - r_{hob})^2}{\frac{d_{pitch}}{2} + b - r_{hob}} \tag{2.4.1}$$

where ρ_{fillet} is the minimum radius of curvature in the generated trochoidal fillet, r_{hob} is the tip radius of the hob or of the grinding tool, d_{pitch} is the pitch diameter and b is the dedendum value. Boeing provided values for the minimum value of ρ_{fillet} and the inverted formula from equation (2.4.1) becomes:

$$r_{hob} = \frac{-2b^2 - 2b\rho_{fillet} + d_{pitch}\rho_{fillet}}{-2b + d_{pitch} + 2\rho_{fillet}} \tag{2.4.2}$$

2.4.3 Dimensional gear ring modeling

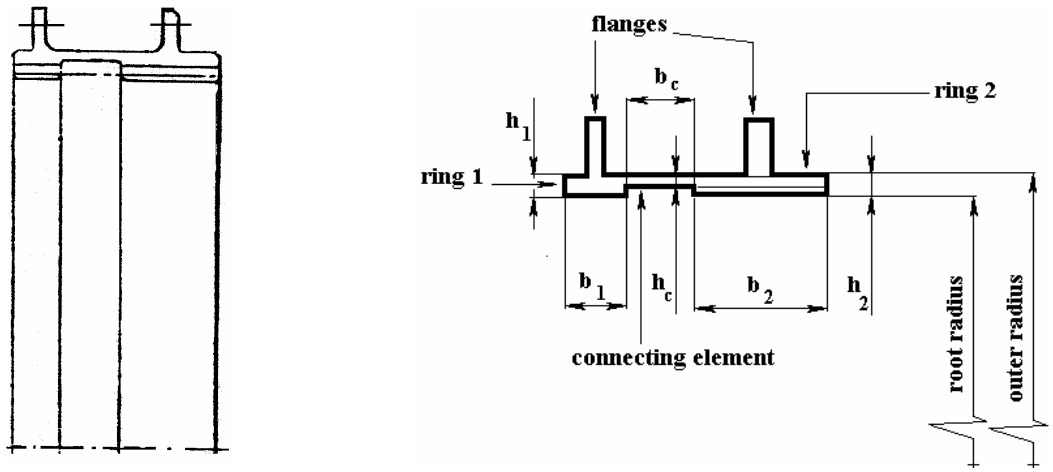

a) b)

Figure 42: Ring section and nomenclature.

Figure 42 a) shows the actual layout of the ring cross-section. The connecting element and flanges change the thickness of the rings in a direction along the axis of rotation of the planetary system. Because the finite element model is two-dimensional, this must be reduced to an equivalent uniform ring gear radial thickness.

A comprehensive 3D model provided simulated displacement values of two particular points along the outer diameter when two diametrically opposed forces are applied to both to rings. The load and deflection points are collocated. The evaluated deflection of the bottom gear at the load point for a 1.0 lbf load is XXXX in. while the deflection of the top gear at the load point for a 1.0 lbf load is XXXX in.

To produce the same displacement for 1 lbf radial loads at the outer diameter in a physically justifiable 2-dimensional model, two finite element analysis using MARC were performed on the system shown in Figure 43.

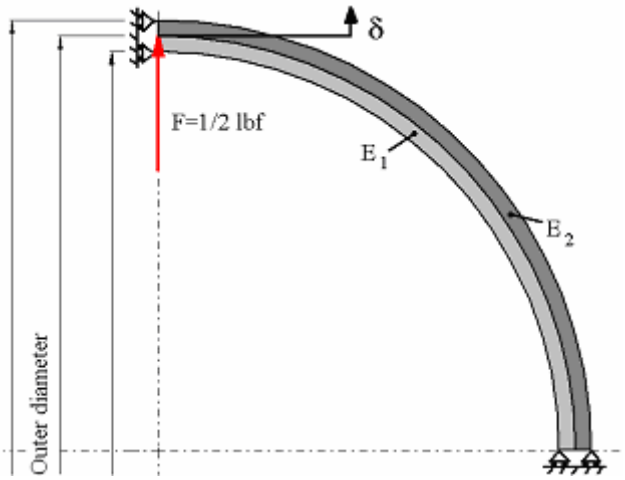

Figure 43: Finite element model to evaluate equivalent ring thickness.

The actual ring thickness was doubled and two different Young's moduli E_1 and E_2 were used for the inner and outer parts of the ring. While E_1 was equal to the nominal value of 2.9 10^7 lbf/in^2 to ensure the teeth are modeled with the correct value, E_2 was changed until the displacement equaled the one provided by the comprehensive 3D model. The same procedure was applied to both rings.

	Young Modulus E_2
Ring stage 1	1.08 10^{10}
Ring stage 2	0.826 10^{10}

Table 13: Evaluated Young modulus.

Table 13 shows the calculated Young modulus E_2 that yields the provided displacement values for both rings. The radial thickness of each of the two concentric rings is 0.455 *in* (Figure 43). Consequently doubling the actual thickness of both rings and using E_2 for the outer part approximates the effective ring stiffness from the full system model. This process incorporates the effective stiffness of the ring and housing. The inertia is increased as well from the doubling of the thickness. This captures, in an ad hoc estimate, the additional inertia of the housing.

2.4.4 Dimensional gear ring modeling: alternative approach

In this section a different approach to calculate the effective outer diameter of the ring is presented (in contrast to method above using two rings of different moduli correlated with Penn State FE data). This method was developed when data presented in the previous correspondent paragraph were not available.

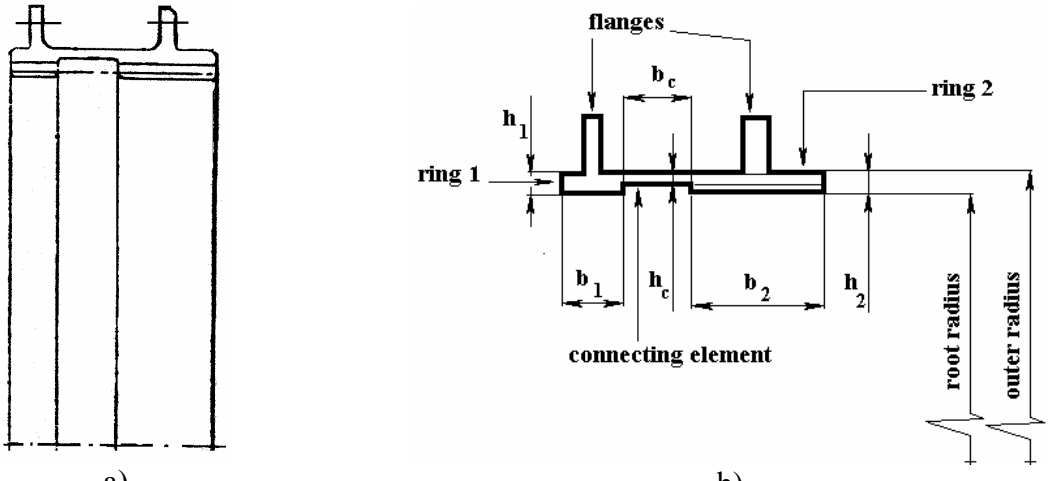

Figure 44: Schematic of ring section.

Figure 44 a) shows a cross-section of the rings for the two stages while Figure 44 b) labels the dimensions used below. As previously mentioned the two rings are modeled separately neglecting the flanges and the connecting element. To accommodate this approximation the values of the outer diameters for the two parts was changed from nominal values.

The connecting element was split into two parts (Figure 45 step 1) divided between the two rings. Each ring was remodeled as a unique rectangular section (Figure 45 step 2) with thickness h_{ef1} and h_{ef2}. To calculate these values the bending stiffness for thin ring was taken into account.

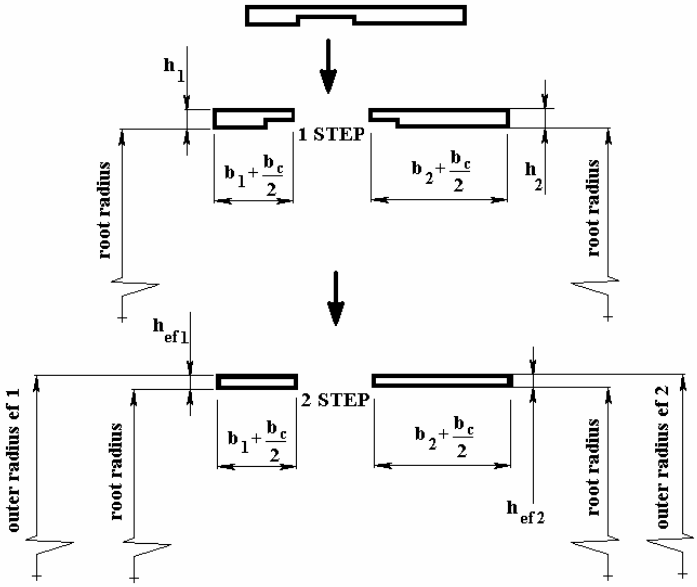

Figure 45: Step for the approximation of sections.

Assuming both rings are thin (thickness/mean radius ratio <<1) and inextensible, the following formula gives the bending stiffness for a ring with rectangular section (Love, 1944):

$$k = \frac{Ebh^3}{12\left(1-\nu^2\right)R_m^3} \tag{2.4.3}$$

where b and h are width and thickness of the rectangular section of the ring, E and ν are Young modulus and Poisson ratio and R_m is the radius of the section from the ring center to the neutral axis.

Every different section in step 1 can be seen as one ring with two different thickness $h_1$or h_2 and h_c. whose stiffness is given by:

$$k_{tot,n} = \frac{Eb_n h_n^{\,3}}{12\left(1-\nu^2\right)R_{m,n}^3} + \frac{E\frac{b_c}{2}h_c^{\,3}}{12\left(1-\nu^2\right)R_{m,c}^3} \tag{2.4.4}$$

where n can be 1 or 2 according to the part considered.

The equivalent total stiffness of the approximate rectangular section of step 2 in Figure 45 are respectively k_{ef1} and k_{ef2} and are given by:

$$k_{ef,n} = \frac{E\left(b_n + \frac{b_c}{2}\right)h_{ef,n}^{\,3}}{12\left(1-\nu^2\right)R_{mef,n}^3} \tag{2.4.5}$$

where n can be 1 or 2.

To evaluate the dimension of the approximated section of step 2 the following equation were imposed:

$$k_{ef,1} = k_{tot,1}; \qquad k_{ef,2} = k_{tot,2} \tag{2.4.6}$$

Equations (2.4.6) yield:

$$\frac{\left(b_n + \frac{b_c}{2}\right)h_{ef,n}^{\,3}}{R_{mef,n}^3} = \frac{b_n h_n^{\,3}}{R_{m,n}^3} + \frac{\frac{b_c}{2}h_c^{\,3}}{R_{m,c}^3} \tag{2.4.7}$$

where the unknowns are $h_{ef,n}$ and $R_{mef,n}$.

To evaluate the dimensions of each equivalent section another equation is needed. This equation is given by the following system:

$$\begin{cases} h_{ef,n} = \mathrm{R}_{out,ef2} - R_{root} \\ R_{mef,n} = \dfrac{\mathrm{R}_{out,ef2} + R_{root}}{2} \end{cases} \rightarrow R_{mef,n} = \frac{h_{ef,n} + 2R_{root}}{2} \tag{2.4.8}$$

Finally the values of $h_{ef,1}$ and $h_{ef,2}$ can be evaluated inserting equation (2.4.8) into equation (2.4.7) as follows:

$$\frac{\left(b_n + \frac{b_c}{2}\right)h_{ef,n}^{\,3}}{\left(\frac{h_{ef,n} + 2R_{root}}{2}\right)^3} = \frac{b_n h_n^{\,3}}{R_{m,n}^3} + \frac{\frac{b_c}{2}h_c^{\,3}}{R_{m,c}^3} \tag{2.4.9}$$

To accommodate the increasing of stiffness due to ring flanges an additional 5% of the effective stiffness, evaluated solving equation (2.4.9) with respect to $h_{ef,n}$, was added to the ring thickness for the both stages.

2.4.5 Lumped bodies

The carriers and shafts are considered as rigid bodies. Values of mass and moment of inertia with respect to z axes were evaluated using CAD software that approximates the real geometries of the structures. shows physical data computed from the CAD modelling.

Structure	Input shaft	Carrier 1	Carrier 2 – Output shaft
Young Modulus [lbf/in^2]	2.9 10^7	2.97 10^7	2.9 10^7
Poisson ratio	0.29	0.29	0.29
Density [lbf·s^2/in^4]	7.3533 10^{-4}	7.3533 10^{-4}	7.3533 10^{-4}

Table 14: Physical data of lumped bodies.

Input shaft

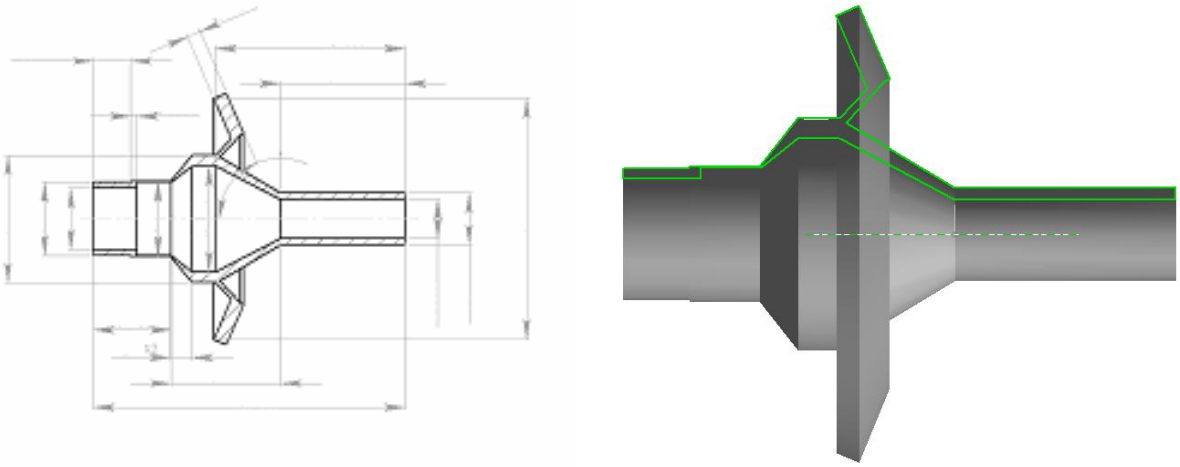

a) b)

Figure 46: CAD model of the input shaft.

Figure 46 a) shows how the input shaft section was approximated while Figure 46 b) shows the three dimensional model used to evaluate mass and moment of inertia with respect to the z axis.

Carrier 1

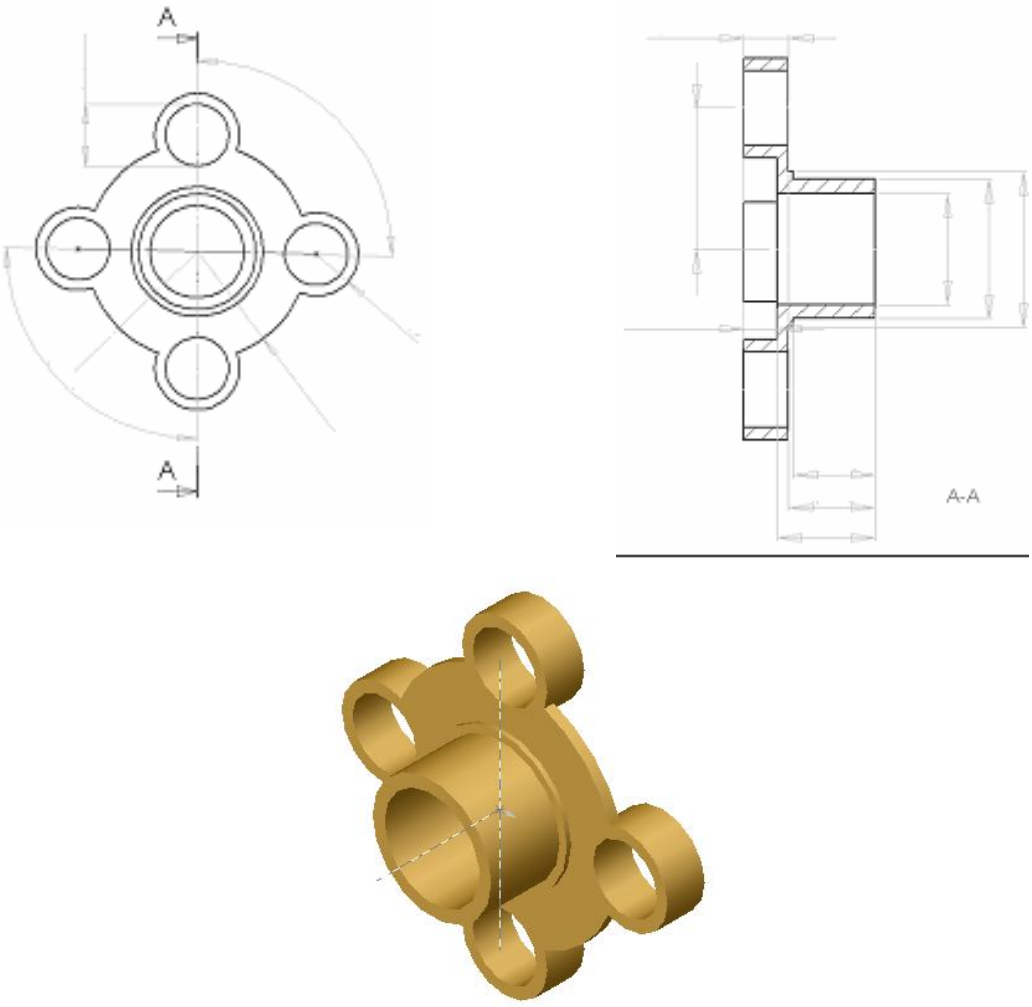

Figure 47: CAD model of the first stage carrier.

Figure 47 shows how the first stage carrier sections were approximated and the three dimensional CAD model used to evaluate mass and moment of inertia with respect to the z axis.

Carrier 2- Output shaft

Figure 48 shows how the second stage carrier sections were approximated and the three dimensional CAD model used to evaluate the mass and moment of inertia with respect to the z axis.

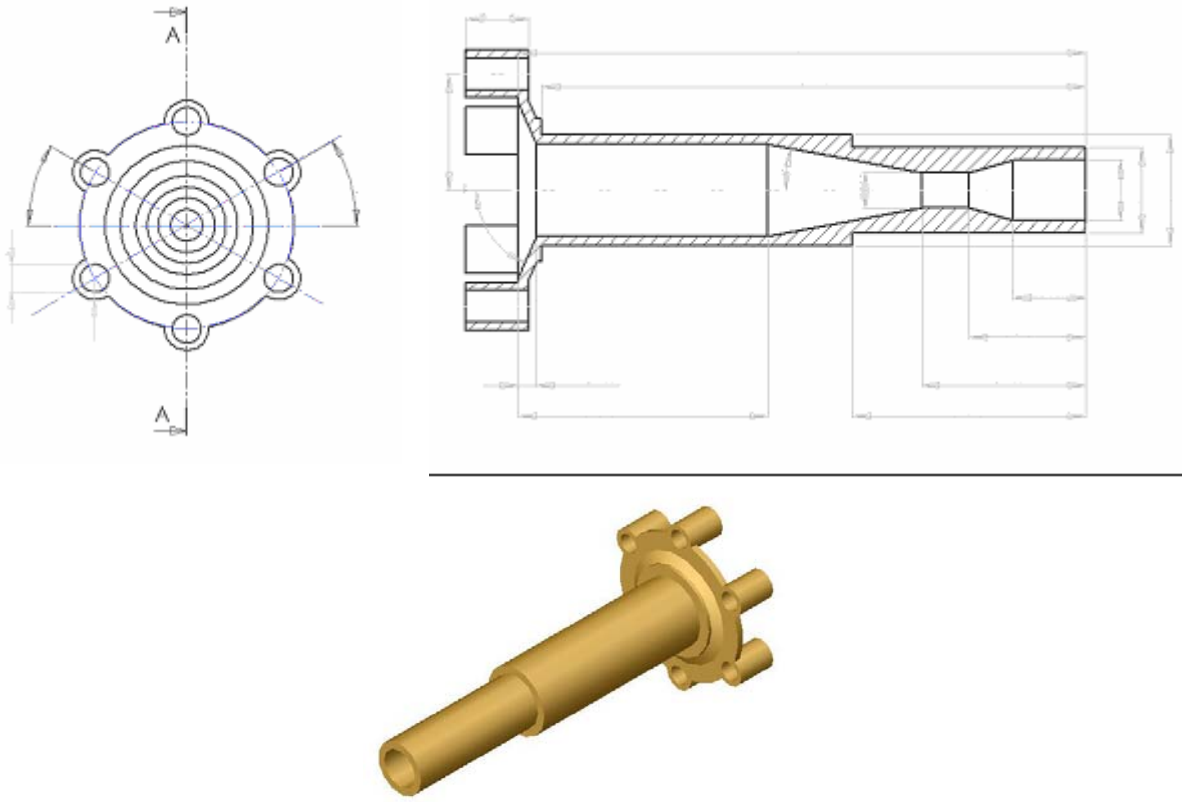

Figure 48: CAD model of the second stage carrier.

Structure	Input shaft	Carrier 1	Carrier 2 – Output shaft
Mass [lbf·s^2/in]	0.11708205	0.13491552	0.55940157
Moment of inertia [lbf·s^2·in]	2.65433221	4.27140614	10.57692223

Table 15: Physical data of the 3D CAD modeled structures.

Table 15 shows the obtained data for the 3D CAD modeled structures, while Table 16 shows a comparison between real masses and the same data evaluated by the 3D model and the finite element software.

Real bodies		Model		
Body	Mass [lbf·s^2/in]	Body	Mass [lbf·s^2/in]	Moment Inertia [lbf in^2]
Sun 1 In shaft	0.13463812	Sun 1 In shaft	0.1344618187	2.771325216
Planet 1	0.0279633	Planet 1	0.02755318199	0.379638858
Ring 1 +Ring 2	0.27341896	Ring 1	0.09192841661	12.70521348
		Ring 2	0.1958201203	27.06384516
Carrier 1	0.11521916	Carrier 1 Sun 2	0.1835942725	5.00399012
Sun 2	0.06110499			
Planet 2	0.04453415	Planet 2	0.04396713697	0.428008048
Carrier 2	N.A.	Carrier 2 Out shaft	0.55940157	10.57692223

Table 16: Comparison between data evaluated with 3D model and real data.

Gear

The lumped mass and moment of inertia with respect to the z axis of all gears are evaluated automatically by Calyx® using the provided geometry and physical data.

2.4.6 Mesh stiffness

In order to have detailed information on the meshing stiffness all gear pairs are modeled separately and the linear stiffness (stiffness along the line of action) is evaluated. 30 positions along one mesh cycle are considered and an average value is calculated.

Every gear pair is modeled using the same approach which consists in locking the driven wheel, i.e. the inner circumference of this wheel has zero rotation. The shaft elasticity is not considered here. The driver wheel can obviously rotate around its shaft, i.e. its internal circumference has only rigid rotation. The finite element program gives values of the circumferential rotation of the driver gear for every position along the mesh cycle and (2.4.10) is used to compute the linear mesh stiffness.

$$k_{mesh} = \frac{T}{\delta r_b^2} \tag{2.4.10}$$

Where T is the torque, δ and r_b are respectively the average circumferential rotation of the internal nodes and the base radius of the driver gear.

In order to compute these mesh stiffness values, a 2D model is developed for every single gear pairs. For each model a particular calculation is used to model the face width of the gear pairs and the applied torques. For all pairs an average between the face width of the meshing gear (sun- planet and ring-planet for both stages) is considered and the applied torque is equal to the nominal torque divided by the number of the planets and divided by the average face width of the considered pairs.

Figure 49 and Figure 50 show the linear mesh stiffness on a mesh cycle for all gear pairs:

Table 17 shows average values of the linear mesh stiffness computed considering a complete mesh cycle.

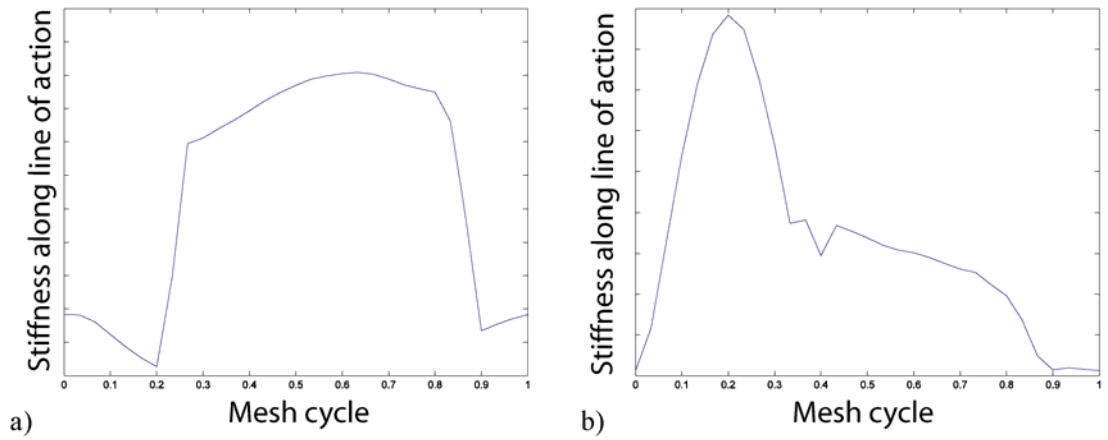

Figure 49: Linear mesh stiffness for a) Sun – Planet of stage 1, b) Ring – Planet of stage 1.

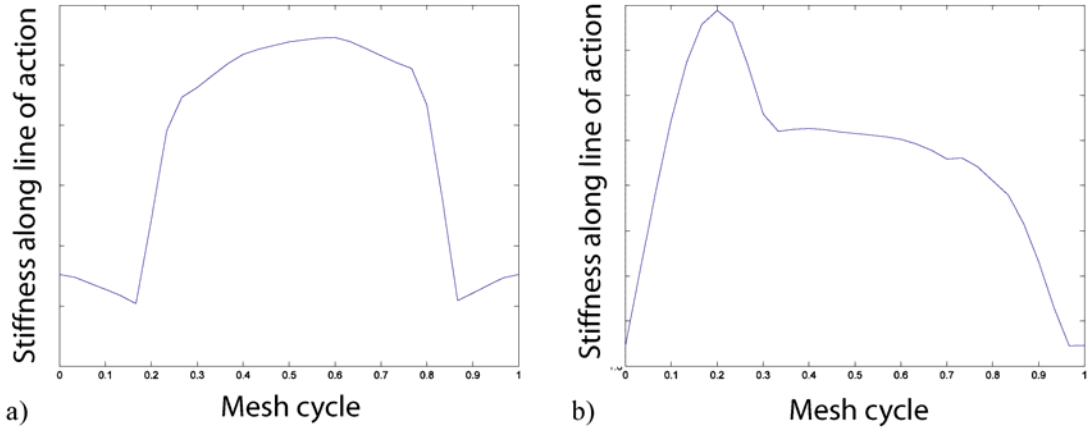

Figure 50: Linear mesh stiffness for a) Sun – Planet of stage 2, b) Ring – Planet of stage 2.

	Stage 1		Stage 2	
	Sun-Planet	Ring-Planet	Sun-Planet	Ring-Planet
Linear mesh	3.1671e+006	4.0897e+006	3.3252e+006	2.0633e+006

Table 17: Average values of the linear mesh stiffness.

2.4.7 Kinematics

Transmission ratio

The transmission ratio for a planetary system with fixed ring is given by (Lynwander, P., 1983):

$$\tau = \frac{r_{pitch,sun} + r_{pitch,ring}}{r_{pitch,sun}} \tag{2.4.11}$$

where $r_{pitch,sun}$ and $r_{pitch,ring}$ are the cutting pitch diameter of the sun and of the ring. In the case of a compound system as in Figure 41, equation (2.4.11) has to be applied to each stage and

the total transmission ratio can be evaluated according to the following equation (Lynwander, P., 1983):

$$\tau_{tot} = \tau_1 \tau_2 \tag{2.4.12}$$

where τ_1 and τ_2 are the transmission ratio of respectively stage 1 and stage 2. The following equations show the relations between input and output torque and rotational speeds:

$$\tau_1 = \frac{T_m}{T_{input}}; \quad \tau_2 = \frac{T_{output}}{T_m}; \quad \tau_{tot} = \tau_1 \tau_2 = \frac{T_{output}}{T_{input}} \tag{2.4.13}$$

$$\tau_1 = \frac{\Omega_{input}}{\Omega_m}; \quad \tau_2 = \frac{\Omega_m}{\Omega_{output}}; \quad \tau_{tot} = \tau_1 \tau_2 = \frac{\Omega_{input}}{\Omega_{output}} \tag{2.4.14}$$

The following figure shows the meaning of symbols used in the preceding equation, note that T_m and Ω_m represent the torque and the speed at the intermediate step between the stages.

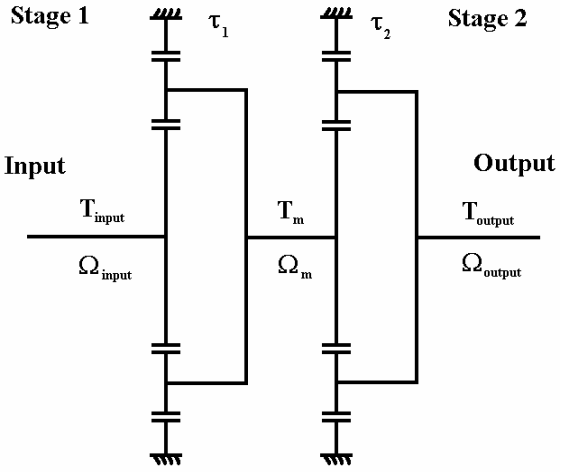

Figure 51: Transmission ratio scheme.

For the present system equations (2.4.11) and (2.4.12) give the following values:

$$\tau_1 = \frac{r_{pitch,sun1} + r_{pitch,ring1}}{r_{pitch,sun1}}$$

$$\tau_2 = \frac{r_{pitch,sun2} + r_{pitch,ring2}}{r_{pitch,sun2}}$$

$$\tau_{tot} = \tau_1 \tau_2$$

The provided values for the output torque and speed are:

$$T_{output} = 1.2 \cdot 10^6 in \cdot lb \qquad \Omega_{output} = 225 RPM = 23.561945 rad/s$$

From these,

$$T_{input} = \frac{T_{output}}{\tau_{tot}} = 68697.5\, in \cdot lb$$

$$\Omega_{input} = \tau_{tot}\Omega_{output} = 3930.27 RPM = 411.577\ rad/s$$

$$T_m = \frac{T_{output}}{\tau_2} = 328767.1564\ in \cdot lb$$

$$\Omega_m = \tau_2\Omega_{output} = 821.25\, RPM = 86.0011\ rad/s$$

Mesh frequencies

The mesh frequency for a planetary system with fixed ring is given by:

$$\omega = \frac{Z_S Z_R}{Z_S + Z_R}\Omega_S \qquad (2.4.15)$$

where Z_S and Z_R are the number of teeth of sun and ring and Ω_S is the speed of the sun. In the present system this equation can be applied to both stages using Ω_{input} and Ω_m as values for Ω_S to obtain

$$\omega_1 = \frac{Z_{S,1} Z_{R,1}}{Z_{S,1} + Z_{R,1}}\Omega_{input} = 9116.12\, rad/s \rightarrow 1450.87\, Hz \qquad (2.4.16)$$

$$\omega_2 = \frac{Z_{S,2} Z_{R,2}}{Z_{S,2} + Z_{R,2}}\Omega_m = 2497.56\ rad/s \rightarrow 397.49\, Hz \qquad (2.4.17)$$

In this case subscripts 1 and 2 indicate the corresponding stage.

2.4.8 Bearing stiffness

All bearing were modeled as stiffness matrix and Table 18 summarizes the stiffness values used in the finite element model:

Bearing	Along y [lbf/in]	Along z [lbf/in]
Input shaft	XXXX	XXXX
Planet Stage 1	XXXX	XXXX
Sun 1 – Carrier 1	XXXX	XXXX
Planet Stage 2	XXXX	XXXX
Output rotor shaft	XXXX	XXXX

Table 18: Bearing stiffness values for the finite element model.

2.4.9 Bearing stiffness: alternative approach

In this section a different approach to calculate the bearings stiffness is presented. It is based on formulae given by Gargiulo (Gargiulo, 1980). This method can be used if bearing data on connections between planets and carriers are not available.

In order to evaluate the stiffness of bearings that connect planets to carriers, the load acting on each bearing must be calculated. First, four simplifying assumptions are made: 1) assume that the system is at a steady state speed (not accelerating); 2) assume that all planets are equally spaced; 3) assume that all planets share load equally; and 4) neglect friction.

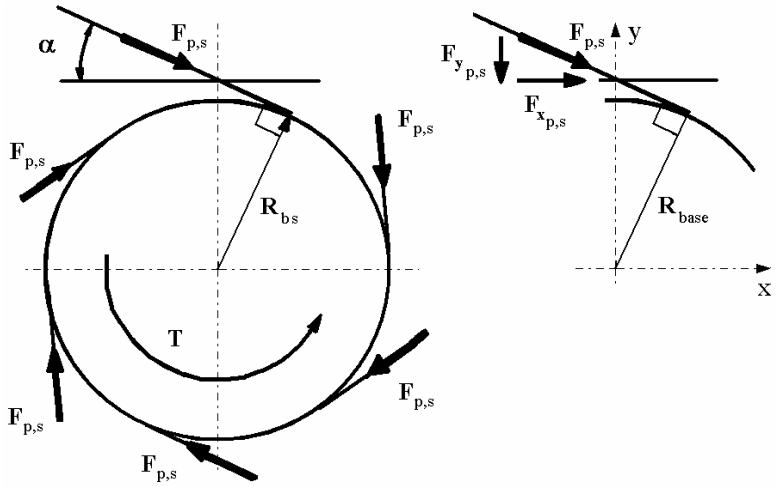

Figure 52: Free body diagram of the sun.

Figure 52 shows the free body diagram of the sun of a general planetary system with fixed ring and n planets where $F_{x\ p,s}$ and $F_{y\ p,s}$ designate the x and y components of mesh force $F_{p,s}$ acting from planet to sun, T designates torque on the sun, R_{bs} designates base radius of the sun and α designates sun-planet pressure angle. Considering rotational equilibrium yields:

$$T = n\left(F_{p,s}R_{base}\right) \rightarrow F_{p,s} = \frac{T}{nR_{base}} \qquad (2.4.18)$$

Figure 53 shows the free body diagram of the planet where β designates ring-planet pressure angle, $F_{s,p}$ and $F_{r,p}$ are the mesh forces acting on the planet from respectively the sun and the ring, $F_{x\ B}$ and $F_{y\ B}$ designate the x and y components of the reaction of the bearing F_B,and F_C is the centrifugal force due to the rotation of the bearing on z axes of the planetary system with the carrier angular velocity Ω_C.

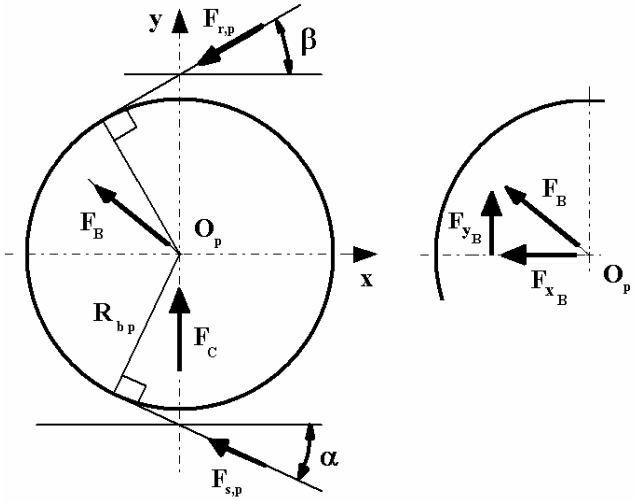

Figure 53: Free body diagram of the planet.

The translation and rotational equilibrium can be obtained applying Newton's 2nd law.

$$x) \qquad F_{x_{s,p}} + F_{x_{r,p}} + F_{x_B} = 0 \tag{2.4.19}$$

$$y) \qquad F_{y_{s,p}} - F_{y_{r,p}} + F_{y_B} + F_C = 0 \tag{2.4.20}$$

$$Rot.O_p \qquad F_{r,p}R_{bp} - F_{s,p}R_{bp} = 0 \rightarrow F_{r,p} = F_{s,p} \tag{2.4.21}$$

Combining these equations with equation (2.4.18) and the fact that:

$$\begin{aligned} F_{x_{s,p}} &= F_{s,p}\cos(\alpha); \quad F_{y_{s,p}} = F_{s,p}\sin(\alpha); \\ F_{x_{r,p}} &= F_{r,p}\cos(\beta); \quad F_{y_{r,p}} = F_{r,p}\sin(\beta); \\ F_C &= m_p\Omega_C^2 I \end{aligned} \tag{2.4.22}$$

where m_p mass of the planet and I planet center distance, yields:

$$F_{x_B} = -\frac{T}{nR_{bs}}\left(\cos(\alpha)+\cos(\beta)\right); \quad F_{y_B} = \frac{T}{nR_{bs}}\left(\sin(\beta)+\sin(\alpha)\right) - m_p\Omega_C^2 I \tag{2.4.23}$$

The reaction force of the bearing is:

$$F_B = \sqrt{F_{x_B}^2 + F_{y_B}^2} = \sqrt{\left(-\frac{T}{nR_{bs}}\left(\cos(\alpha)+\cos(\beta)\right)\right)^2 + \left(\frac{T}{nR_{bs}}\left(\sin(\beta)+\sin(\alpha)\right) - m_p\Omega_C^2 I\right)^2} \tag{2.4.24}$$

The magnitude of this force equals the force acting on the bearing by the planet.

Planet bearing	F_B [lb]
Stage 1	575167.54
Stage 2	384068.4

Table 19: Evaluated forces acting on planet bearings.

Table 19 shows values of evaluated forces acting on planet bearing for the two stages.
A simple way to estimate stiffness of the planet bearings is by using the following formula that is valid for spherical roller bearings (Gargiulo, 1980):

$$k_{bearing} = 0.0921 \cdot 10^6 \sqrt[4]{F_B l^2 n_{rol}^3 cos^7(\varphi)} \qquad (2.4.25)$$

where l is the roller effective length, n_{rol} is the number of the rolling elements and φ is the contact angle.

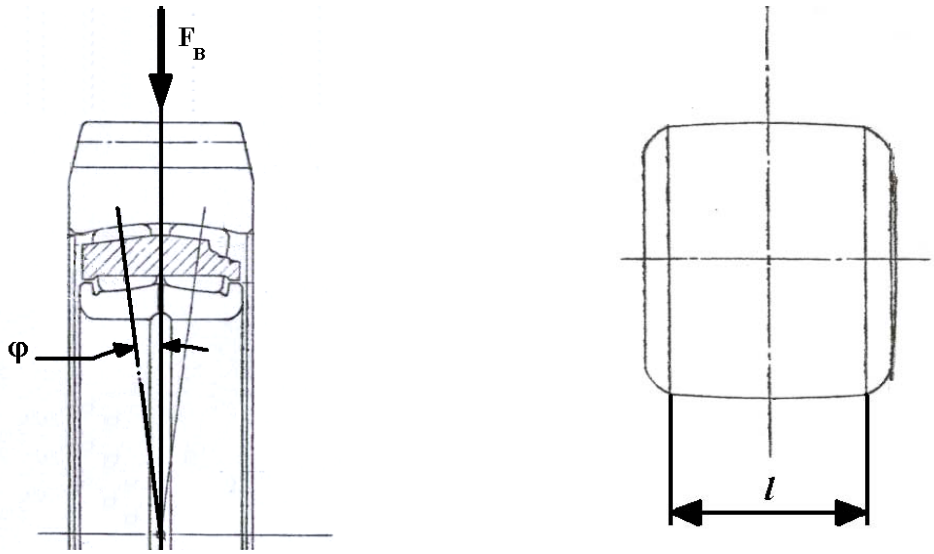

Figure 54: Bearing parameters.

Only half of the bearing force F_B from equation (2.4.24) is used in equation (2.4.25) to take into account the presence in all planet bearing of the double row of spherical rollers, as shown in Figure 54. The value of stiffness is then multiplied by two to obtain the total stiffness of the bearing.

2.5 Modeling of compound planetary system

In the past many authors simulated static and dynamic behaviors of planetary systems using finite elements. Drago and Margasahayam (1987-a) performed a stress analysis of planetary gears with integral bearings as well as a full planetary system for aeronautical applications (Drago and Margasahayam, 1987-b). Valco (1992) calculated stresses, strains and

deformations in the gears for a planetary system using a non-linear finite element model under static load conditions. Better results were achieved in 2003 by Vijayakar (Vijayakar, 2003-b) who was able to perform a very accurate analysis for an helicopter planetary stage. The application of his unique, semi-analytical finite element approach (Vijayakar, 1999) gave stress at the fillet region almost identical to the actual stress recorded by Krantz (Krantz, 1992) in an actual planetary system. The same semi-analytical finite element technique was also employed by Parker et al. (2000-b) to analyze the dynamic behavior of a simple spur gears pair and the dynamic response of a planetary gear system (Parker et al., 2000-a). In Parker et al. (2000-b) the effect of non-linearity due to loss of contact between gears was taken into account and good agreements between simulation and experimental data were shown. Parker et al. (2000-a) showed excellent agreement with analytical models (Lin and Parker, 1999-a) (Lin and Parker, 1999-b) for what concern the evaluation of the natural frequencies and vibration modes. Good agreements were found also for the expected excitation of resonance, at speeds where the mesh frequency or its harmonics coincide with a natural frequency. In the next sections the same approach used by Vijayakar (Vijayakar, 2003-b) is applied in order to model the compound planetary system described previously. For this purpose a Calyx® model is created and deeply discussed to show the modeling technique.

2.5.1 Calyx model

The model consists in twenty files built up using Calyx® language (Vijayakar, 2003-a). Table 20 summarizes and lists all files and their contents:

File name	Contents
Compound.cfg	System geometry and kinematics
Compoundan.cmd	Set up of the analysis and post processing of data
Sun1.msh	Mesh of 1 tooth of the 1st stage sun
Pinion1.msh	Mesh of 1 tooth of the 1st stage planet
Ring1.msh	Mesh of 1 tooth of the 1st stage ring
Ringrim1.msh	Mesh of 1 segment of the ring rim of the 1st stage
Carrierlump1.msh	Inertia and mass of the added lumped mass for the Carrier of 1st stage
Sun2.msh	Mesh of 1 tooth of the 2nd stage sun
Pinion2.msh	Mesh of 1 tooth of the 2nd stage planet
Ring2.msh	Mesh of 1 tooth of the 2nd stage ring
Ringrim2.msh	Mesh of 1 segment of the ring rim of the 2nd stage
Carrierlump2.msh	Inertia and mass of the added lumped mass for the Carrier of 2nd stage
Sun1.brg	Stiffness matrix for Ground-Sun bearing of 1st stage
Pinion1.brg	Stiffness matrix for Planets-Carrier bearings of 1st stage
Carrier1Sun1.brg	Stiffness matrix for Sun-Carrier bearing of 1st stage
Pinion2.brg	Stiffness matrix for Planets-Carrier bearings of 2nd stage
Carrier2.brg	Stiffness matrix for Ground-Carrier bearing of 2nd stage

Table 20: Files index for the compound model.

Two basic files are called Compound.cfg and Compoundan.cmd. The first file is the pre-processing file, it contains the description of the model with both geometry and kinematics. As Calyx® is a multibody-FEM tools, a certain amount of reference systems and bodies must be created according to the system to be modeled. Kinematics relationship must be described to impose a consistent kinematics to the system. Phasing relationships between bodies must be clarified in order to join and mesh bodies properly. All these information are inserted in the Compound.cfg file by means of variable, function, equations and relationships. Except few data (independent parameters) all information will be automatically calculated once this file is compiled.

The second file Compoundan.cmd contains all the set up and post processing information for the analysis. Value of torque, speed, and the data to be stored and calculated during the analysis are specified in this file.

The mesh file (with ".msh" extension) contains the gear mesh property of the relative gear. For example Sun1.msh contains mesh data on the first stage sun. The mesh file is structured in different records, which contains information on nodal coordinates, elements types and enumeration, material properties, constraints and contact element. It must be underlined that each ".msh" file includes only the mesh of a single tooth of the relative wheel. Indeed Calyx® will create the complete gear mesh by taking advantage of repetitive symmetry and use recursive sub-structuring. This approach allows to improve the computational effort for the decomposition of the stiffness matrix during calculation. The number of recursive steps will decrease from Z^3 to $\log_2(Z)$, where Z is the number of teeth in the gear (Vijayakar, 2003-a). The sub structuring technique considers each single tooth as a sub structure that must be joined with the others to create the complete gear structure.

The bearing ".brg" files are text files containing the stiffness and damping matrices, which describe the spring type connection between two bodies.

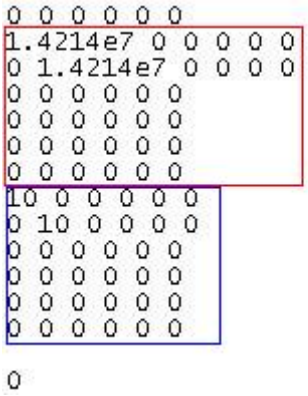

Figure 55: Example of ".brg files" with the stiffness (red) and damping (blue) matrices.

Calyx® creates bodies by assigning a reference system to a structure and imposing to the body its own kinematics. Of course each body must be constrained by means of bearing, and contact constraints.

In order to explain the complexity of the model a simple description of the content of the most important files listed in Table 20 will be discussed. Each code line will be presented with the relative comment and the progression will facilitate the comprehension of the code.

COMPOUND.CFG

The first step in creating the model is to specify the basic data information of the system. The basic data are the essential and independent values that Calyx® cannot evaluate from other specified parameters. Typical example are center distance, number of teeth, number of gears, etc.

```
// System parameters STAGE 1:

Cent_Dist_Planet_Sun_1 :=XXXX;
Planet_Number_of_Teeth_1 := XXXX;
Sun_Number_of_Teeth_1    := XXXX;
Ring_Number_of_Teeth_1   := XXXX;
Number_of_Planets_1:= XXXX;

//Calculated parameters:
dTheta_Sun_1   :=   2*Pi/Sun_Number_of_Teeth_1;
dTheta_Ring_1  :=  -2*Pi/Ring_Number_of_Teeth_1;
dTheta_Planet_1:= 2*Pi/Planet_Number_of_Teeth_1;

// Phasing position between planets:
dTheta_Pia2_1   :=XXXX;
dTheta_Pia3_1   :=XXXX;
dTheta_Pia4_1   :=XXXX;

Ring_Outer_Radius_1     := XXXX;
Interface_Radius_Ring_1 := XXXX;
Planet_Inner_Radius_1   := XXXX;

//Tooth geometry dependent initial rotation value:
Generating_Sun_Tooth_Thickness_1   := XXXX;
Generating_Planet_Tooth_Thickness_1:= XXXX;
Generating_Ring_Tooth_Thickness_1  := XXXX;

Sun_Generating_Diametral_Pitch_1   := XXXX;
Planet_Generating_Diametral_Pitch_1:= XXXX;
Ring_Generating_Diametral_Pitch_1  := XXXX;

Generating_Sun_Pressure_Angle_1   := XXXX;
Generating_Planet_Pressure_Angle_1:= XXXX;
Generating_Ring_Pressure_Angle_1  := XXXX;
```

```
// System parameters STAGE 2:

Cent_Dist_Planet_Sun_2 := XXXX;
Planet_Number_of_Teeth_2 := XXXX;
Sun_Number_of_Teeth_2    := XXXX;
Ring_Number_of_Teeth_2   := XXXX;
Number_of_Planets_2:= XXXX;

//Calculated Parameters:
dTheta_Sun_2   :=   2*Pi/Sun_Number_of_Teeth_2;
dTheta_Ring_2  :=  -2*Pi/Ring_Number_of_Teeth_2;
dTheta_Planet_2:= 2*Pi/Planet_Number_of_Teeth_2;

// Phasing position between planets:
dTheta_Pia2_2   := XXXX;
dTheta_Pia3_2   := XXXX;
dTheta_Pia4_2   := XXXX;
dTheta_Pia5_2   := XXXX;
dTheta_Pia6_2   := XXXX;

Ring_Outer_Radius_2     := XXXX;
Interface_Radius_Ring_2 := XXXX;
Planet_Inner_Radius_2   := XXXX;

//Tooth geometry dependent initial rotation value:
Generating_Sun_Tooth_Thickness_2   := XXXX;
Generating_Planet_Tooth_Thickness_2:= XXXX;
Generating_Ring_Tooth_Thickness_2  := XXXX;

Sun_Generating_Diametral_Pitch_2   := XXXX;
Planet_Generating_Diametral_Pitch_2:= XXXX;
Ring_Generating_Diametral_Pitch_2  := XXXX;

Generating_Sun_Pressure_Angle_2   := XXXX;
Generating_Planet_Pressure_Angle_2:= XXXX;
Generating_Ring_Pressure_Angle_2  := XXXX;
```

```
Omega_Carrier_2 := XXXX*2*Pi/60; // XXXX is RPM
```

Once the main parameters are specified the calculation of the most important gears data can be easily calculated.

1. The generating pitch radii:

$$r = \frac{Z}{2P_d} \qquad (2.5.1)$$

```
STAGE 1
Sun_Generating_Pitch_Rad_1=0.5*Sun_Number_of_Teeth_1/Sun_Generating_Diametral_Pitch_1;
Planet_Generating_Pitch_Rad_1=0.5*Planet_Number_of_Teeth_1/Planet_Generating_Diametral_Pitch_1;
Ring_Generating_Pitch_Rad_1=0.5*Ring_Number_of_Teeth_1/Ring_Generating_Diametral_Pitch_1;

STAGE 2
Sun_Generating_Pitch_Rad_2=0.5*Sun_Number_of_Teeth_2/Sun_Generating_Diametral_Pitch_2;
Planet_Generating_Pitch_Rad_2=0.5*Planet_Number_of_Teeth_2/Planet_Generating_Diametral_Pitch_2;
Ring_Generating_Pitch_Rad_2=0.5*Ring_Number_of_Teeth_2/Ring_Generating_Diametral_Pitch_2;
```

2. The operating pitch radii:

$$r_S' = \frac{Z_S}{Z_P + Z_S} a'; \qquad r_R' = \frac{Z_P}{Z_R - Z_S} a' \qquad (2.5.2)$$

$$Planet\ at\ sun\ mesh:\ r_P' = \frac{Z_P}{Z_P + Z_S} a'; \qquad Planet\ at\ ring\ mesh:\ r_P' = \frac{Z_P}{Z_R - Z_P} a' \qquad (2.5.3)$$

```
STAGE 1
Sun_Operating_Pitch_Rad_1=Cent_Dist_Planet_Sun_1*Sun_Number_of_Teeth_1/
                                    (Planet_Number_of_Teeth_1+Sun_Number_of_Teeth_1);
Ring_Operating_Pitch_Rad_1=Cent_Dist_Planet_Sun_1*Ring_Number_of_Teeth_1/
                                    (Ring_Number_of_Teeth_1-Planet_Number_of_Teeth_1);
Planet_Operating_Pitch_Rad_At_Sun_1=Cent_Dist_Planet_Sun_1*Planet_Number_of_Teeth_1/
                                    (Planet_Number_of_Teeth_1+Sun_Number_of_Teeth_1);
Planet_Operating_Pitch_Rad_At_Ring_1=Cent_Dist_Planet_Sun_1*Planet_Number_of_Teeth_1/
                                    (Ring_Number_of_Teeth_1-Planet_Number_of_Teeth_1);

STAGE2
Sun_Operating_Pitch_Rad_2=Cent_Dist_Planet_Sun_2*Sun_Number_of_Teeth_2/
                                    (Planet_Number_of_Teeth_2+Sun_Number_of_Teeth_2);
Planet_Operating_Pitch_Rad_At_Sun_2=Cent_Dist_Planet_Sun_2*Planet_Number_of_Teeth_2/
                                    (Planet_Number_of_Teeth_2+Sun_Number_of_Teeth_2);
Planet_Operating_Pitch_Rad_At_Ring_2=Cent_Dist_Planet_Sun_2*Planet_Number_of_Teeth_2/
                                    (Ring_Number_of_Teeth_2-Planet_Number_of_Teeth_2);
Ring_Operating_Pitch_Rad_2=Cent_Dist_Planet_Sun_2*Ring_Number_of_Teeth_2/
                                    (Ring_Number_of_Teeth_2-Planet_Number_of_Teeth_2);
```

3. The base radii for each gears:

$$r_b = r\cos(\alpha) \qquad (2.5.4)$$

```
STAGE1
Sun_BasePitch_Rad_1=Sun_Generating_Pitch_Rad_1*cos(Generating_Sun_Pressure_Angle_1*pi/180);
Planet_BasePitch_Rad_1=Planet_Generating_Pitch_Rad_1*cos(Generating_Planet_Pressure_Angle_1*pi/180);
Ring_BasePitch_Rad_1=Ring_Generating_Pitch_Rad_1*cos(Generating_Ring_Pressure_Angle_1*pi/180);

STAGE2
Sun_BasePitch_Rad_2=Sun_Generating_Pitch_Rad_2*cos(Generating_Sun_Pressure_Angle_2*pi/180);
Planet_BasePitch_Rad_2=Planet_Generating_Pitch_Rad_2*cos(Generating_Planet_Pressure_Angle_2*pi/180);
Ring_BasePitch_Rad_2=Ring_Generating_Pitch_Rad_2*cos(Generating_Ring_Pressure_Angle_2*pi/180);
```

4. The operating tooth thickness:

$$s' = 2r'\left(\frac{s}{2r} + \left(\tan(\alpha) - \alpha\right) - \left(\tan(\alpha') - \alpha'\right)\right) \qquad (2.5.5)$$

```
STAGE1
Sun_Operating_Tooth_Thickness_1=2*Sun_Operating_Pitch_Rad_1*(Generating_Sun_Tooth_Thickness_1/(2*
                                Sun_Generating_Pitch_Rad_1)+(Sun_Generating_Involute_Angle_Pitch_1-
                                atan(Sun_Generating_Involute_Angle_Pitch_1))-
                                (Sun_Operating_Involute_Angle_Pitch_1-
                                atan(Sun_Operating_Involute_Angle_Pitch_1)));

Planet_Operating_Tooth_Thickness_At_Sun_1= 2*Planet_Operating_Pitch_Rad_At_Sun_1*
                            (Generating_Planet_Tooth_Thickness_1/(2*Planet_Generating_Pitch_Rad_1)+
                            (Planet_Generating_Involute_Angle_Pitch_1-
                            atan(Planet_Generating_Involute_Angle_Pitch_1))-
                            (Planet_Operating_Involute_Angle_Pitch_At_Sun_1-
                            atan(Planet_Operating_Involute_Angle_Pitch_At_Sun_1)));

Planet_Operating_Tooth_Thickness_At_Ring_1=2*Planet_Operating_Pitch_Rad_At_Ring_1*
                            (Generating_Planet_Tooth_Thickness_1/(2*Planet_Generating_Pitch_Rad_1)+
                            (Planet_Generating_Involute_Angle_Pitch_1-
                            atan(Planet_Generating_Involute_Angle_Pitch_1))-
                            (Planet_Operating_Involute_Angle_Pitch_At_Ring_1-
                            atan(Planet_Operating_Involute_Angle_Pitch_At_Ring_1)));

Ring_Operating_Tooth_Thickness_1=2*Ring_Operating_Pitch_Rad_1*(Generating_Ring_Tooth_Thickness_1/
                            (2*Ring_Generating_Pitch_Rad_1)+
                    (Ring_Operating_Involute_Angle_Pitch_1-
                            atan(Ring_Operating_Involute_Angle_Pitch_1))-
                            (Ring_Generating_Involute_Angle_Pitch_1-
                            atan(Ring_Generating_Involute_Angle_Pitch_1)));

STAGE2
Sun_Operating_Tooth_Thickness_2=2*Sun_Operating_Pitch_Rad_2*(Generating_Sun_Tooth_Thickness_2/(2*
                                Sun_Generating_Pitch_Rad_2)+(Sun_Generating_Involute_Angle_Pitch_2-
                                atan(Sun_Generating_Involute_Angle_Pitch_2))-
                                (Sun_Operating_Involute_Angle_Pitch_2-
                                atan(Sun_Operating_Involute_Angle_Pitch_2)));
Planet_Operating_Tooth_Thickness_At_Sun_2= 2*Planet_Operating_Pitch_Rad_At_Sun_2*
                            (Generating_Planet_Tooth_Thickness_2/(2*Planet_Generating_Pitch_Rad_2)+
                            (Planet_Generating_Involute_Angle_Pitch_2-
                            atan(Planet_Generating_Involute_Angle_Pitch_2))-
```

```
                    (Planet_Operating_Involute_Angle_Pitch_At_Sun_2-
                    atan(Planet_Operating_Involute_Angle_Pitch_At_Sun_2)));
Planet_Operating_Tooth_Thickness_At_Ring_2=2*Planet_Operating_Pitch_Rad_At_Ring_2*
                    (Generating_Planet_Tooth_Thickness_2/(2*Planet_Generating_Pitch_Rad_2)+
                    (Planet_Generating_Involute_Angle_Pitch_2-
                    atan(Planet_Generating_Involute_Angle_Pitch_2))-
                    (Planet_Operating_Involute_Angle_Pitch_At_Ring_2-
                    atan(Planet_Operating_Involute_Angle_Pitch_At_Ring_2)));
Ring_Operating_Tooth_Thickness_2= 2*Ring_Operating_Pitch_Rad_2*(Generating_Ring_Tooth_Thickness_2/
                    (2*Ring_Generating_Pitch_Rad_2)+
                    (Ring_Operating_Involute_Angle_Pitch_2-
                    atan(Ring_Operating_Involute_Angle_Pitch_2))-
                    (Ring_Generating_Involute_Angle_Pitch_2-
                    atan(Ring_Generating_Involute_Angle_Pitch_2)));
```

The previous formula contain value of the generating and operating involute angle calculated as follows:

$$\tan(\alpha) = \sqrt{\left(\frac{r}{r_b}\right)^2 - 1} \qquad (2.5.6)$$

```
STAGE1
Sun_Generating_Involute_Angle_Pitch_1=((Sun_Generating_Pitch_Rad_1/Sun_BasePitch_Rad_1)^2-1)^0.5;
Planet_Generating_Involute_Angle_Pitch_1=((Planet_Generating_Pitch_Rad_1/Planet_BasePitch_Rad_1)^2
                                    -1)^0.5;
Ring_Generating_Involute_Angle_Pitch_1=((Ring_Generating_Pitch_Rad_1/Ring_BasePitch_Rad_1)^2-1)^0.5;

STAGE2
Sun_Generating_Involute_Angle_Pitch_2=((Sun_Generating_Pitch_Rad_2/Sun_BasePitch_Rad_2)^2-1)^0.5;
Planet_Generating_Involute_Angle_Pitch_2=((Planet_Generating_Pitch_Rad_2/Planet_BasePitch_Rad_2)^2
                                    -1)^0.5;
Ring_Generating_Involute_Angle_Pitch_2=((Ring_Generating_Pitch_Rad_2/Ring_BasePitch_Rad_2)^2-1)^0.5;
```

$$\tan(\alpha') = \sqrt{\left(\frac{r'}{r_b}\right)^2 - 1} \qquad (2.5.7)$$

```
STAGE1
Sun_Operating_Involute_Angle_Pitch_1=((Sun_Operating_Pitch_Rad_1/Sun_BasePitch_Rad_1)^2-1)^0.5;
Planet_Operating_Involute_Angle_Pitch_At_Sun_1=((Planet_Operating_Pitch_Rad_At_Sun_1/
                                                Planet_BasePitch_Rad_1)^2-1)^0.5;
Planet_Operating_Involute_Angle_Pitch_At_Ring_1=((Planet_Operating_Pitch_Rad_At_Ring_1/
                                                Planet_BasePitch_Rad_1)^2-1)^0.5;
Ring_Operating_Involute_Angle_Pitch_1=((Ring_Operating_Pitch_Rad_1/Ring_BasePitch_Rad_1)^2-1)^0.5;

STAGE2
Sun_Operating_Involute_Angle_Pitch_2=((Sun_Operating_Pitch_Rad_2/Sun_BasePitch_Rad_2)^2-1)^0.5;
Planet_Operating_Involute_Angle_Pitch_At_Sun_2=((Planet_Operating_Pitch_Rad_At_Sun_2/
                                                Planet_BasePitch_Rad_2)^2-1)^0.5;
Planet_Operating_Involute_Angle_Pitch_At_Ring_2=((Planet_Operating_Pitch_Rad_At_Ring_2/
                                                Planet_BasePitch_Rad_2)^2-1)^0.5;
Ring_Operating_Involute_Angle_Pitch_2=((Ring_Operating_Pitch_Rad_2/Ring_BasePitch_Rad_2)^2-1)^0.5;
```

5. Initial rotations of gears:

In a multi mesh system a very important task is to calculate the relative motion between gears. In order to have a proper mesh between the gears the initial position of every tooth must calculated. If the initial position of a gear is zero, Calyx® will create the gear with the first tooth's axis coincident with the vertical axis, i.e. tooth number 1 of the gear will point according to y axis of the fixed reference frame. In order to mesh properly the gears, an initial rotation must be calculated and imposed to each gear. Figure 56 shows the situation between sun and planet 1. In order to reach the correct mesh position, both sun and planet are rotated by the angle corresponding to half of the tooth thickness at operating pitch circle. The sun initial rotation is negative, while the planet initial rotation is positive.

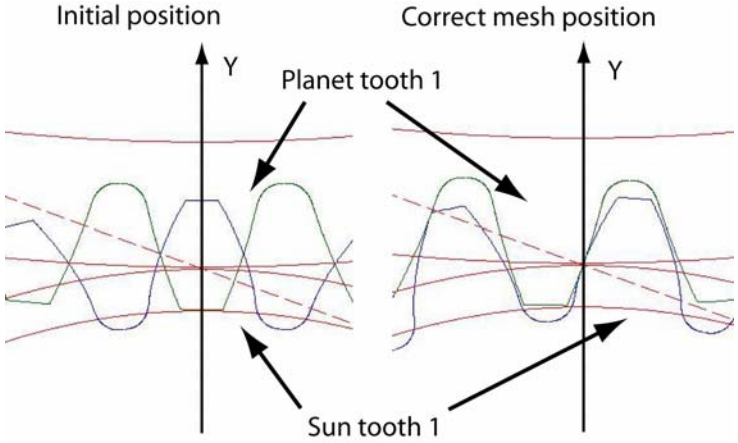

Figure 56: Teeth alignment.

The same problem is solved for all gears.

Initial rotation for the sun:

$$\vartheta_{initial,sun} = \frac{s_S'}{2r_S'} \qquad (2.5.8)$$

Initial rotation for the ring:

$$\vartheta_{initial,ring} = \frac{s_R'}{2r_R'} \qquad (2.5.9)$$

Initial rotation for the planet 1 (the π value is due to allow tooth 1 of planet 1 to point in the opposite direction with respect to the y direction of the fixed reference frame) at sun mesh:

$$Planet\,1\ at\ sun\ mesh\quad \vartheta_{initial,planet1} = \pi - \frac{s_{P1at\,sun}'}{2r_{P1at\,sun}'} \qquad (2.5.10)$$

Initial rotation for the planet 1 at ring mesh (this rotation allows to recuperate at ring the previous planet initial rotation at sun) :

$$Planet\,1\ at\ ring\ mesh\quad \vartheta_{initial,planet1,ring} = \frac{s_{P1at\,ring}'}{2r_{P1at\,ring}'} \qquad (2.5.11)$$

```
STAGE1
Sun_Initial_Rotn_1:=-Sun_Operating_Tooth_Thickness_1/(2*Sun_Operating_Pitch_Rad_1);
Ring_Initial_Rotn_1:=-Ring_Operating_Tooth_Thickness_1/(2*Ring_Operating_Pitch_Rad_1);
Planet_Initial_Rotn_At_Sun_1:=pi-Planet_Operating_Tooth_Thickness_At_Sun_1/
                                        (2*Planet_Operating_Pitch_Rad_At_Sun_1);
Planet_Initial_Rotn_At_Ring_1:=Planet_Operating_Tooth_Thickness_At_Ring_1/
                                        (2*Planet_Operating_Pitch_Rad_At_Ring_1);

STAGE2
Sun_Initial_Rotn_2:=-Sun_Operating_Tooth_Thickness_2/(2*Sun_Operating_Pitch_Rad_2);
Ring_Initial_Rotn_2 := -Ring_Operating_Tooth_Thickness_2/(2*Ring_Operating_Pitch_Rad_2);
Planet_Initial_Rotn_At_Sun_2 := pi-Planet_Operating_Tooth_Thickness_At_Sun_2/
                                        (2*Planet_Operating_Pitch_Rad_At_Sun_2);
Planet_Initial_Rotn_At_Ring_2:=Planet_Operating_Tooth_Thickness_At_Ring_2/
                                        (2*Planet_Operating_Pitch_Rad_At_Ring_2);
```

More complicated is the calculation of the initial rotation for planets 2, 3 and 4 of stage 1 and 2, 3, 4, 5 and 6 of stage 2. In fact the kinematics of the planetary system must be implemented. Using Willis formula, the speed of a planet Ω_P can be calculated with respect to the carrier speed Ω_C.

$$\Omega_P = \Omega_C\left(1+\frac{Z_S}{Z_P}\right) \qquad (2.5.12)$$

Using equation (2.5.12) the angular position of a planet around its own axis can be calculated with respect to the angular position of the planet α_P with respect to the carrier axis α_C.

$$\alpha_P = \alpha_C\left(1+\frac{Z_S}{Z_P}\right) \qquad (2.5.13)$$

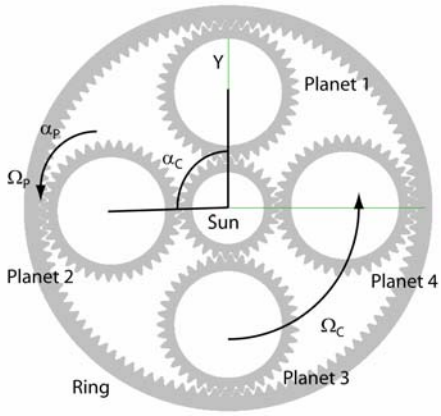

Figure 57: Phase angles for planet 2.

If planet 1 is properly meshed with sun and ring, and α_C corresponds to the phase angles between planet 1 and planet 2 (see Figure 57), equation (2.5.13) allows to calculate the further rotation to be added, which assures the proper mesh of planet 2 at its own location. The following equation summarize the previous concepts.

$$\vartheta_{initial,planet2} = \vartheta_{initial,planet1} + \alpha_C \left(1 + \frac{Z_S}{Z_P}\right) \tag{2.5.14}$$

The same approaches can be used for planet 3 and 4 of stage 1 and for planet 2, 3, 4, 5 and 6 of stage 2.

```
STAGE 1
Planet_1_Initial_Rotn_1  := Planet_Initial_Rotn_At_Sun_1;
Planet_2_Initial_Rotn_1  := Planet_1_Initial_Rotn_1 +
                            (dTheta_Pia2_1)*(1+Sun_Number_of_Teeth_1/Planet_Number_of_Teeth_1);
Planet_3_Initial_Rotn_1  := Planet_1_Initial_Rotn_1 +
                            (dTheta_Pia3_1)*(1+Sun_Number_of_Teeth_1/Planet_Number_of_Teeth_1);
Planet_4_Initial_Rotn_1  := Planet_1_Initial_Rotn_1 +
                            (dTheta_Pia4_1)*(1+Sun_Number_of_Teeth_1/Planet_Number_of_Teeth_1);

STAGE2
Planet_1_Initial_Rotn_2  := Planet_Initial_Rotn_At_Sun_2;
Planet_2_Initial_Rotn_2  := Planet_1_Initial_Rotn_2 +
                            (dTheta_Pia2_2)*(1+Sun_Number_of_Teeth_2/Planet_Number_of_Teeth_2);
Planet_3_Initial_Rotn_2  := Planet_1_Initial_Rotn_2 +
                            (dTheta_Pia3_2)*(1+Sun_Number_of_Teeth_2/Planet_Number_of_Teeth_2);
Planet_4_Initial_Rotn_2  := Planet_1_Initial_Rotn_2 +
                            (dTheta_Pia4_2)*(1+Sun_Number_of_Teeth_2/Planet_Number_of_Teeth_2);
Planet_5_Initial_Rotn_2  := Planet_1_Initial_Rotn_2 +
                            (dTheta_Pia5_2)*(1+Sun_Number_of_Teeth_2/Planet_Number_of_Teeth_2);
Planet_6_Initial_Rotn_2  := Planet_1_Initial_Rotn_2 +
                            (dTheta_Pia6_2)*(1+Sun_Number_of_Teeth_2/Planet_Number_of_Teeth_2);
```

6. Speeds of gears:

All speeds in the model are calculated from the speed of the second stage carrier. For a planetary system with fixed rings ($\Omega_R=0$) the formula of Willis yields:

$$\Omega_P = \Omega_C \left(\frac{Z_P - Z_R}{Z_P}\right) \tag{2.5.15}$$

$$\Omega_S = \Omega_C \left(\frac{Z_S + Z_R}{Z_S}\right) \tag{2.5.16}$$

```
// Define speeds stage 2
Omega_Planet_2 := (Planet_Number_of_Teeth_2-Ring_Number_of_Teeth_2)/(Planet_Number_of_Teeth_2)*
                                                                    Omega_Carrier_2;
Omega_Sun_2 := (Sun_Number_of_Teeth_2+Ring_Number_of_Teeth_2)/(Sun_Number_of_Teeth_2)*
                                                                    Omega_Carrier_2;
Omega_Ring_2 := 0;

// Define speeds stage 1
Omega_Carrier_1 := Omega_Sun_2;
Omega_Planet_1  := (Planet_Number_of_Teeth_1-Ring_Number_of_Teeth_1)/(Planet_Number_of_Teeth_1)*
                                                                    Omega_Carrier_1;
Omega_Sun_1     := (Sun_Number_of_Teeth_1+Ring_Number_of_Teeth_1)/(Sun_Number_of_Teeth_1)*
                                                                    Omega_Carrier_1;
Omega_Ring_1    := 0;
```

Note that in a compound planetary system the speed of the first stage carrier must be equal to the second stage sun.

7. Angular rotations of gears:

Calyx® reserves a particular variable called "time" (also refereed as *t*) value during calculations. The initial value of time must be imposed at the beginning of the analysis and a delta step value can be imposed to specify the current value of time. Calyx® will calculate the position of gears using variable "time" and the described kinematics as principal references. In this way it is possible to perform both static and dynamic analyses of the system. For example, a static analysis can be performed for 10 step in a mesh cycle, speed and time will be used to calculate relative position of the gears at each step.

The following line simply defines relationships between the speed and the angular rotation for stage 1 and 2 using the variable time.

```
// Define angular rotations stage 2
Sun_theta_1     :=  Omega_Sun_1*Time;
Carrier_theta_1 :=  Omega_Carrier_1*Time;
Planet_theta_1  :=  Omega_Planet_1*Time;
Ring_theta_1    :=  Omega_Ring_1*Time;

// Define angular rotations stage 2
Sun_theta_2     :=  Omega_Sun_2*Time;
Carrier_theta_2 :=  Omega_Carrier_2*Time;
Planet_theta_2  :=  Omega_Planet_2*Time;
Ring_theta_2    :=  Omega_Ring_2*Time;
```

Variable "Time" is automatically calculated using a time increment value:

```
time_increment := XXXX;
Set_Time_Increment(time_increment); // Set the value of the delta time between each step
Initialize(0);   // Set to 0 the initial time value
```

Note that using equation (2.4.15) the mesh frequency for each stage can be calculated as follow:

```
Mesh_freq_1:=Omega_Sun_1*(Ring_Number_of_Teeth_1*Sun_Number_of_Teeth_1)/
                                        (Ring_Number_of_Teeth_1+Sun_Number_of_Teeth_1);
Mesh_freq_2:=Omega_Sun_2*(Ring_Number_of_Teeth_2*Sun_Number_of_Teeth_2)/
                                        (Ring_Number_of_Teeth_2+Sun_Number_of_Teeth_2);
```

8. Reference frame:

In order to define the kinematics of the system, a reference frame must be defined for each gear. Figure 58 shows the gears reference frame for the first stage with respect to the fixed reference frame, z-axes of all frame point (not represented) according to right hand rule. The description of the reference is based to the kinematics of the relative wheel and the initial positions calculated previously to have a proper mesh. All references are defined by means of "translate" and "rotate" operators, which translate and rotate each reference frame with respect to the fixed frame or to the carrier reference frame. The reference frame has origin at (0,0,0) and versors e1, e2 and e3, which are uniquely defined using right hand rule.

The amount by which the fixed reference frame is translated and rotated, to create the sun, ring and carrier reference frames, is reported in the following chart:

Body	Translation on x (e1)	Translation on y (e2)	Rotation on z (e3)
Sun	-	-	$\vartheta_{initial,sun,stage1} + \Omega_{S,stage1} t$
Ring	-	-	$\Omega_{R,stage1} t + \vartheta_{initial,ring,stage1} + \left(\vartheta_{initial,planet1,stage1} - \vartheta_{initial,planet1,ring,stage1}\right) \frac{Z_{P,stage1}}{Z_{R,stage1}}$
Carrier 1st stage	-	-	$\Omega_{C,stage1} t$

Table 21: Translations and rotations for stage 1 with respect to fixed frame.

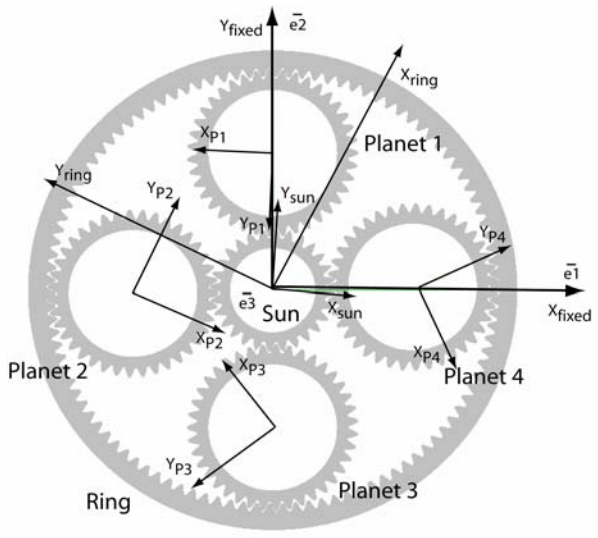

Figure 58: Reference frame for the first stage gears.

The amount by which the carrier reference frame is translated and rotated, to create the planets reference frames, is reported in Table 21:

Body	Translation on x (e1)	Translation on y (e2)	Rotation on z (e3)
Planet 1	-	$a_{PS,stage1}$'	$\vartheta_{initial,planet1,stage1} + \Omega_{P,stage1}t - \Omega_{C,stage1}t$
Planet 2	$-a_{PS,stage1}$'$\sin(\varphi_{P2,stage1})$	$a_{PS,stage1}$'$\cos(\varphi_{P2,stage1})$	$\vartheta_{initial,planet2,stage1} + \Omega_{P,stage1}t - \Omega_{C,stage1}t$
Planet 3	$-a_{PS,stage1}$'$\sin(\varphi_{P3,stage1})$	$a_{PS,stage1}$'$\cos(\varphi_{P3,stage1})$	$\vartheta_{initial,planet3,stage1} + \Omega_{P,stage1}t - \Omega_{C,stage1}t$
Planet 4	$-a_{PS,stage1}$'$\sin(\varphi_{P4,stage1})$	$a_{PS,stage1}$'$\cos(\varphi_{P4,stage1})$	$\vartheta_{initial,planet4,stage1} + \Omega_{P,stage1}t - \Omega_{C,stage1}t$

Table 22: Translations and rotations for stage 1 with respect to the first stage carrier reference frame.

```
// Define reference frames stage 1:
XSun_1 :=Rotate(Sun_theta_1+Sun_Initial_Rotn_1,e3)*Fixed_Frame;
XRing_1:=Rotate(Ring_theta_1+Ring_Initial_Rotn_1+
                                (Planet_Initial_Rotn_At_Sun_1-Planet_Initial_Rotn_At_Ring_1)*
                                Planet_Number_of_Teeth_1/Ring_Number_of_Teeth_1,e3)*Fixed_Frame;
XCarrier_1:=Rotate(Carrier_theta_1,e3)*Fixed_Frame;
XPlanet_1_1:=Rotate(Planet_theta_1-Carrier_theta_1+Planet_1_Initial_Rotn_1,e3)*
                                                Translate(Cent_Dist_Planet_Sun_1*e2)*XCarrier_1;
XPlanet_2_1:=Rotate(Planet_theta_1 - Carrier_theta_1+Planet_2_Initial_Rotn_1,e3)*
                                        Translate(-Cent_Dist_Planet_Sun_1*sin(dTheta_Pia2_1)*e1+
                                        Cent_Dist_Planet_Sun_1*cos(dTheta_Pia2_1)*e2)*XCarrier_1;
XPlanet_3_1:=Rotate(Planet_theta_1 - Carrier_theta_1+Planet_3_Initial_Rotn_1,e3)*
                                        Translate(-Cent_Dist_Planet_Sun_1*sin(dTheta_Pia3_1)*e1+
                                        Cent_Dist_Planet_Sun_1*cos(dTheta_Pia3_1)*e2)*XCarrier_1;
XPlanet_4_1:=Rotate(Planet_theta_1 - Carrier_theta_1+Planet_4_Initial_Rotn_1,e3)*
                                        Translate(-Cent_Dist_Planet_Sun_1*sin(dTheta_Pia4_1)*e1+
                                         Cent_Dist_Planet_Sun_1*cos(dTheta_Pia4_1)*e2)*XCarrier_1;
```

The same approach apply to stage 2 yield to Table 22:

Body	Translation on x (e1)	Translation on y (e2)	Rotation on z (e3)
Sun	-	-	$\vartheta_{initial,sun,stage2} + \Omega_{S,stage2}t$
Ring	-	-	$\Omega_{R,stage2}t + \vartheta_{initial,ring,stage2} + \left(\vartheta_{initial,planet1,stage2} - \vartheta_{initial,planet1,ring,stage2}\right)\frac{Z_{P,stage2}}{Z_{R,stage2}}$
Carrier 2nd stage	-	-	$\Omega_{C,stage2}t$

Table 23: Translations and rotations for stage 2 with respect to fixed frame.

Body	Translation on x (e1)	Translation on y (e2)	Rotation on z (e3)
Planet 1	-	$a_{PS,stage2}$'	$\vartheta_{initial,planet1,stage2} + \Omega_{P,stage2}t - \Omega_{C,stage2}t$
Planet 2	$-a_{PS,stage1}$'$\sin(\varphi_{P2,stage1})$	$a_{PS,stage1}$'$\cos(\varphi_{P2,stage1})$	$\vartheta_{initial,planet2,stage2} + \Omega_{P,stage2}t - \Omega_{C,stage2}t$
Planet 3	$-a_{PS,stage2}$'$\sin(\varphi_{P3,stage2})$	$a_{PS,stage2}$'$\cos(\varphi_{P3,stage2})$	$\vartheta_{initial,planet3,stage2} + \Omega_{P,stage2}t - \Omega_{C,stage2}t$
Planet 4	$-a_{PS,stage2}$'$\sin(\varphi_{P4,stage2})$	$a_{PS,stage2}$'$\cos(\varphi_{P4,stage2})$	$\vartheta_{initial,planet4,stage2} + \Omega_{P,stage2}t - \Omega_{C,stage2}t$
Planet 5	$-a_{PS,stage2}$'$\sin(\varphi_{P5,stage2})$	$a_{PS,stage2}$'$\cos(\varphi_{P5,stage2})$	$\vartheta_{initial,planet5,stage2} + \Omega_{P,stage2}t - \Omega_{C,stage2}t$
Planet 6	$-a_{PS,stage2}$'$\sin(\varphi_{P6,stage2})$	$a_{PS,stage2}$'$\cos(\varphi_{P6,stage2})$	$\vartheta_{initial,planet6,stage2} + \Omega_{P,stage2}t - \Omega_{C,stage2}t$

Table 24: Translations and rotations for stage 2 with respect to the first stage carrier.

```
// Define reference frames stage 2:
XSun_2 :=Rotate(Sun_theta_2+Sun_Initial_Rotn_2,e3)*Fixed_Frame;
XRing_2:=Rotate(Ring_theta_2+Ring_Initial_Rotn_2 +
                                (Planet_Initial_Rotn_At_Sun_2- Planet_Initial_Rotn_At_Ring_2)*
                                Planet_Number_of_Teeth_2/Ring_Number_of_Teeth_2,e3)*Fixed_Frame;
XCarrier_2 := Rotate(Carrier_theta_2,e3)*Fixed_Frame;
XPlanet_1_2:=Rotate(Planet_theta_2-Carrier_theta_2+Planet_1_Initial_Rotn_2,e3)*
                                Translate(Cent_Dist_Planet_Sun_2*e2)* XCarrier_2;

XPlanet_2_2:=Rotate(Planet_theta_2 - Carrier_theta_2+Planet_2_Initial_Rotn_2,e3)*
                                Translate(-Cent_Dist_Planet_Sun_2*sin(dTheta_Pia2_2)*e1+
                                Cent_Dist_Planet_Sun_2*cos(dTheta_Pia2_2)*e2)* XCarrier_2;

XPlanet_3_2:=Rotate(Planet_theta_2 - Carrier_theta_2+Planet_3_Initial_Rotn_2,e3)*
                                Translate(-Cent_Dist_Planet_Sun_2*sin(dTheta_Pia3_2)*e1+
                                Cent_Dist_Planet_Sun_2*cos(dTheta_Pia3_2)*e2)*XCarrier_2;

XPlanet_4_2:=Rotate(Planet_theta_2 - Carrier_theta_2+Planet_4_Initial_Rotn_2,e3)*
                                Translate(-Cent_Dist_Planet_Sun_2*sin(dTheta_Pia4_2)*e1+
                                Cent_Dist_Planet_Sun_2*cos(dTheta_Pia4_2)*e2)*XCarrier_2;

XPlanet_5_2:=Rotate(Planet_theta_2 - Carrier_theta_2+Planet_5_Initial_Rotn_2,e3)*
                                Translate(-Cent_Dist_Planet_Sun_2*sin(dTheta_Pia5_2)*e1+
                                Cent_Dist_Planet_Sun_2*cos(dTheta_Pia5_2)*e2)* XCarrier_2;

XPlanet_6_2:=Rotate(Planet_theta_2 - Carrier_theta_2+Planet_6_Initial_Rotn_2,e3)*
                                Translate(-Cent_Dist_Planet_Sun_2*sin(dTheta_Pia6_2)*e1+
                                Cent_Dist_Planet_Sun_2*cos(dTheta_Pia6_2)*e2)*XCarrier_2;
```

9. Build the structure hierarchy:

The creation of each gear structure requires the assembling of different tooth substructure. The main idea is to load the tooth mesh information from a ".msh" file to create the first substructure and merge the same substructure many times to compose the full gear final structure. Calyx® provides a particular condensed substructure instruction for this purpose. In this paragraph the building of the first stage sun structure is explain.

The first step is to load the sun1.msh file and declare 4 set of nodes contained in the sun1.msh file. This set are called Left side, Right side, Base and Slave. Each set contains the list of nodes according to Figure 59. The Slave nodes set contains all remaining nodes. Note that only the base nodes will be used as constrained nodes.

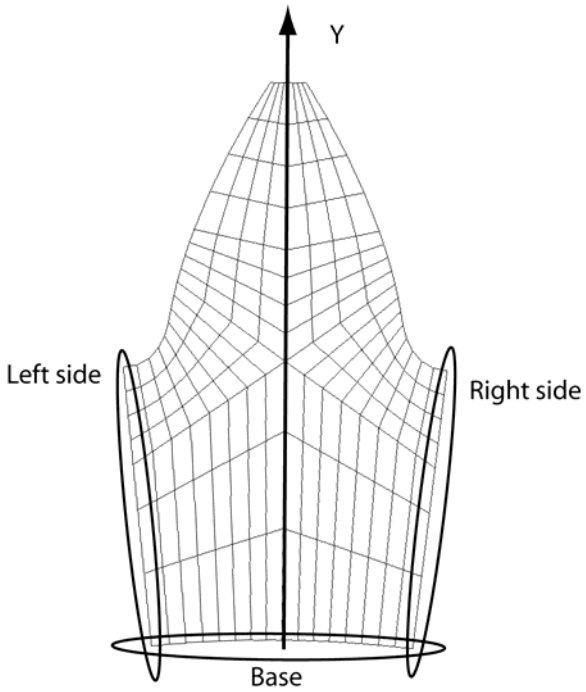

Figure 59: Nodes sets for the first substructure of the first stage sun.

The following code line are used to condensate all information and generate the first tooth substructure (called "Sun_1_Tooth_1") from the sun1.msh file.

```
// Sun 1
Sun_1_Tooth_1:=Condense_Substructures(
  [[ "Sun_Tooth_Mesh","Meshfiles\sun1.msh",Identity_Transformation, TwoDFEM]],
  // New Dofsets:
  [[ "Left_Side" ,Master,[["Left_Side" ]]], [ "Right_Side",Master,[["Right_Side"]]],
            [ "Base", Slave ,     [["Base"      ]]], [ "Slave"     ,Slave ,[["Slave"     ]]] ],
  // Constrained Dofsets:
  [ "Base" ],
  // Label:
  "Sun 1 Tooth 1"
);
```

The second step is to generate a second substructure (called “Sun_2_Tooth_1”) using two times the “Sun_1_Tooth_1” structure. Two structures “Sun_1_Tooth_1” are used, and a rotation of (-dTheta_Sun_1) is used to calculate nodes coordinates for the second tooth. New sets of nodes are created merging the pre existing sets (see Figure 60). No sets are specified as constrained sets, because the constrained set is automatically composed using the constrained Base sets previously defined for “Sun_1_Tooth_1”.

```
Sun_2_Tooth_1:=Condense_Substructures(
  [["Left", Sun_1_Tooth_1,Identity_Transformation], ["Right",Sun_1_Tooth_1,Rotate(-dTheta_Sun_1,e3)]  ],
  // New Dofsets:
  [["Left_Side" ,Master,[["Left_Side"] ,[ ]]],
   ["Right_Side",Master,[[ ],["Right_Side"]]],
   ["Middle",Slave,[["Right_Side"],["Left_Side"]]]
  ],
  // Constrained Dofsets:
  [],
  // Label:
  "Sun 2 Tooth 1"
);
```

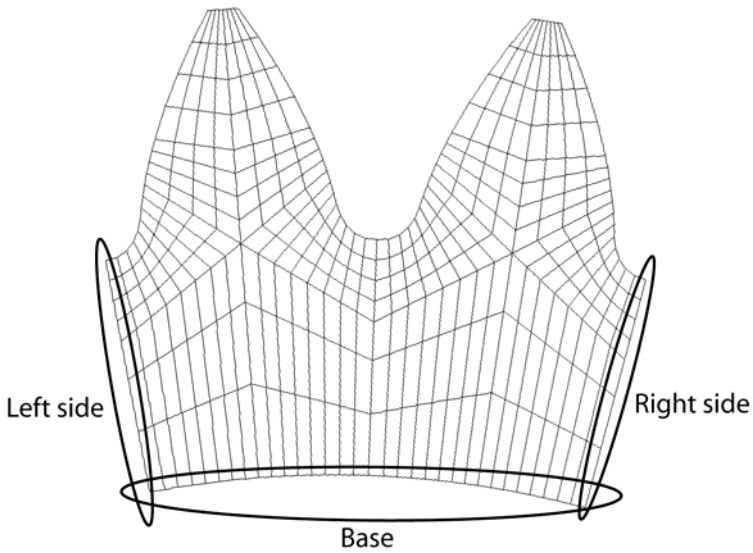

Figure 60: Nodes sets for the second substructure of the first stage sun.

The same technique is repeated many time using combinations of all created substructures until the full gear is generated.

```
Sun_4_Tooth_1:=Condense_Substructures(
 [["Left", Sun_2_Tooth_1,Identity_Transformation],
  ["Right",Sun_2_Tooth_1,Rotate(-2*dTheta_Sun_1,e3)]
 ],
 [["Left_Side" ,Master,[["Left_Side"] ,[]]],
  ["Right_Side",Master,[[],["Right_Side"]]],
  ["Middle",Slave,[["Right_Side"],["Left_Side"]]]
 ],
 // Constrained Dofsets:
 [],
 // Label:
 "Sun 4 Tooth 1"
);

Sun_5_Tooth_1:=Condense_Substructures(
 [["Left", Sun_4_Tooth_1,Identity_Transformation],
  ["Right",Sun_1_Tooth_1,Rotate(-4*dTheta_Sun_1,e3)]
 ],
 [["Left_Side" ,Master,[["Left_Side"] ,[]]],
  ["Right_Side",Master,[[],["Right_Side"]]],
  ["Middle",Slave,[["Right_Side"],["Left_Side"]]]
 ],
 // Constrained Dofsets:
 [],
 // Label:
 "Sun 5 Tooth 1"
);

Sun_10_Tooth_1:=Condense_Substructures(
 [["Left", Sun_5_Tooth_1,Identity_Transformation],
  ["Right",Sun_5_Tooth_1,Rotate(-5*dTheta_Sun_1,e3)]
 ],
 [["Left_Side" ,Master,[["Left_Side"] ,[]]],
  ["Right_Side",Master,[[],["Right_Side"]]],
  ["Middle",Slave,[["Right_Side"],["Left_Side"]]]
 ],
 // Constrained Dofsets:
 [],
 // Label:
 "Sun 10 Tooth 1"
);
);
Sun_20_Tooth_1:=Condense_Substructures(
 [["Left", Sun_10_Tooth_1,Identity_Transformation],
  ["Right",Sun_10_Tooth_1,Rotate(-10*dTheta_Sun_1,e3)]
 ],
 [["Left_Side" ,Master,[["Left_Side"] ,[]]],
  ["Right_Side",Master,[[],["Right_Side"]]],
  ["Middle",Slave,[["Right_Side"],["Left_Side"]]]
 ],
 // Constrained Dofsets:
 [],
 // Label:
 "Sun 20 Tooth 1"
);
```

```
Sun_25_Tooth_1:=Condense_Substructures(
 [["Left", Sun_20_Tooth_1,Identity_Transformation],
  ["Right",Sun_5_Tooth_1,Rotate(-20*dTheta_Sun_1,e3)]
 ],
 [["Left_Side" ,Master,[["Left_Side"] ,[]]],
  ["Right_Side",Master,[[],["Right_Side"]]],
  ["Middle",Slave,[["Right_Side"],["Left_Side"]]]
 ],
 // Constrained Dofsets:
 [],
 // Label:
 "Sun 20 Tooth 1"
);

Sun_26_Tooth_1:=Condense_Substructures(
 [["Left", Sun_25_Tooth_1,Identity_Transformation],
  ["Right",Sun_1_Tooth_1,Rotate(-25*dTheta_Sun_1,e3)]
 ],
 [["Left_Side" ,Master,[["Left_Side"] ,[]]],
  ["Right_Side",Master,[[],["Right_Side"]]],
  ["Middle",Slave,[["Right_Side"],["Left_Side"]]]
 ],
 // Constrained Dofsets:
 [],
 // Label:
 "Sun 26 Tooth 1"
);

Sun_27_Tooth_1:=Condense_Substructures(
 [["Left", Sun_26_Tooth_1,Identity_Transformation],
  ["Right",Sun_1_Tooth_1,Rotate(-26*dTheta_Sun_1,e3)]
 ],
 [["Left_Side" ,Master,[["Left_Side"] ,[]]],
  ["Right_Side",Master,[[],["Right_Side"]]],
  ["Middle",Slave,[["Right_Side"],["Left_Side"]]]
 ],
 // Constrained Dofsets:
 [],
 // Label:
 "Sun 27 Tooth 1"
);

Sun_28_Tooth_1:=Condense_Substructures(
 [["Left",Sun_27_Tooth_1,Identity_Transformation],
  ["Right",Sun_1_Tooth_1,Rotate(-27*dTheta_Sun_1,e3)]
 ],

[["Middle",Slave,[["Left_Side","Right_Side"],["Left_Side","Right_Sid
e"]]]
 ],
 // Constrained Dofsets:
 [],
 // Label:
 "Sun 28 Tooth 1"
```

The same condensing instructions are used to generate all gear structures required to model the full compound planetary system.

A different situation occurs to the carriers structure. In effect for the carrier are not modeled as deformable bodies, the condensing instruction will use a ".mesh" file containing a simple matrix with masses and moment of inertia information. For example the carrier of the first stage is joined with the full structure of the second stage sun to create a unique structure called "Carrier_Sun_2_Structure".

```
Carrier_1_Sun_2_Structure := Condense_Substructures(
    [["Carrier_lump_Mesh_1","Meshfiles\carrierlump1.msh",Identity_Transformation,TwoDFEM],
     ["Rigidelement2_Mesh","Meshfiles\rigidelement2.msh",Identity_Transformation,TwoDFEM],
     ["Sun_2_Mesh",Sun_40_Tooth_2,Identity_Transformation]],
    // New Dofsets:
    [["Connect_dof",Slave,[["lump"],["lump"],[]]]],
    // Constrained Dofsets:
    ["Connect_dof"],
    // Label:
    "Carrier_1_Sun_2_Structure"
   );
```

10. Create bodies consisting of reference frames and structures:

A body is created by connecting a structure to a reference frame. The Calyx® instruction is "Define_Body" and allows to specify the value of the constraint on the structure constrained set of nodes. For example the "Sun_1_Structure_Body" body is created connecting the structure "Sun_1_Structure with the "XSun_1" reference frame. The constrained are given (using the value 1) on z direction (translation) and on x and y axis (rotation). The torque "Sun_Torque_1" is applied to the rotation on z axis.

```
Sun_1_Structure_Body := Define_Body("Sun_1_Structure",    XSun_1,    Sun_1_Structure,
                                                          [0,0,1,1,1,0],[0,0,0,0,0,Sun_Torque_1]);
```

The next lines shows the creations of all bodies:

```
STAGE1
Ring_Body_1    := Define_Body("Ring_1",    XRing_1,    Ring_106_Tooth_1,
                                                          [1,1,1,1,1,1],[0,0,0,0,0,0]);
Planet_1_Body_1:= Define_Body("Planet_1_1",XPlanet_1_1,Planet_39_Tooth_1,
                                                          [0,0,1,1,1,0],[0,0,0,0,0,0]); //Crack
Planet_2_Body_1:= Define_Body("Planet_2_1",XPlanet_2_1,Planet_39_Tooth_1,
                                                          [0,0,1,1,1,0],[0,0,0,0,0,0]);
Planet_3_Body_1:= Define_Body("Planet_3_1",XPlanet_3_1,Planet_39_Tooth_1,
                                                          [0,0,1,1,1,0],[0,0,0,0,0,0]);
Planet_4_Body_1:= Define_Body("Planet_4_1",XPlanet_4_1,Planet_39_Tooth_1,
                                                          [0,0,1,1,1,0],[0,0,0,0,0,0]);

STAGE2
Carrier_1_Sun_2_Body := Define_Body("Carrier_1_Sun_2",    XSun_2,    Carrier_1_Sun_2_Structure,
                                                          [0,0,1,1,1,0],[0,0,0,0,0,0]);
Ring_Body_2    := Define_Body("Ring_2",    XRing_2,    Ring_106_Tooth_2,
                                                          [1,1,1,1,1,1],[0,0,0,0,0,0]);
Carrier_Body_2 := Define_Body("Carrier_2", XCarrier_2, Carrier_Structure_2,
                                                          [0,0,1,1,1,1],[0,0,0,0,0,0]);
Planet_1_Body_2:= Define_Body("Planet_1_2",XPlanet_1_2,Planet_33_Tooth_2,
                                                          [0,0,1,1,1,0],[0,0,0,0,0,0]);
Planet_2_Body_2:= Define_Body("Planet_2_2",XPlanet_2_2,Planet_33_Tooth_2,
                                                          [0,0,1,1,1,0],[0,0,0,0,0,0]);
Planet_3_Body_2:= Define_Body("Planet_3_2",XPlanet_3_2,Planet_33_Tooth_2,
                                                          [0,0,1,1,1,0],[0,0,0,0,0,0]);
```

```
Planet_4_Body_2:= Define_Body("Planet_4_2",XPlanet_4_2,Planet_33_Tooth_2,
                                                    [0,0,1,1,1,0],[0,0,0,0,0,0]);
Planet_5_Body_2:= Define_Body("Planet_5_2",XPlanet_5_2,Planet_33_Tooth_2,
                                                    [0,0,1,1,1,0],[0,0,0,0,0,0]);
Planet_6_Body_2:= Define_Body("Planet_6_2",XPlanet_6_2,Planet_33_Tooth_2,
                                                    [0,0,1,1,1,0],[0,0,0,0,0,0]);
```

According to previous lines all bodies are constrained on translation along z direction and on rotation around x and y axes except the second stage carrier which is constrained also in the rotation around z axis and rings which are constrained in all 6 degrees of freedom.

11. Bearing modeling:

According to Figure 41 all bodies are connected with the ground or each other thought stiffness matrix bearings. The used instruction is “Assemble_Bearing”. This instruction allows to connect different bodies using the contains of a “.brg” file. In the example a bearing between “Sun_1_Structure_Body” and the “Fixed_Body” is created using the stiffness matrix specified trough “sun1.brg” file. The “Fixed_Body” is a default body which simulate the ground.

```
Sun_Bearing_1 := Assemble_Bearing(
  // Label:
  "Sun_Bearing_1",
  // File:
  "Meshfiles\sun1.brg",
  [Sun_1_Structure_Body,Constrained,Identity_Transformation],
  [Fixed_Body,Identity_Transformation]);
```

12. Pairs of surfaces that may come into contact:

The contact constrain are created by means of the imposition of mating surface between bodies. In the example a set of non conformal surface pairs are set between the bodies “Planet_1_Body_1” and “Sun_1_Structure_Body”. Calyx® will perform a contact analysis between the surface of the teeth using the specified contact parameters (friction coefficient, separation tolerance between surface, etc..). Note that two mating surface are created between the bodies to consider the possibility of back side contact.

```
Set_Surface_Pairs(
   [Nonconformal,[Planet_1_Body_1,"SURFACE1",Disjoint_Surface],
            [Sun_1_Structure_Body,"SURFACE1",Disjoint_Surface],
    Friction_Coeff,Separation_Tolerance,Contact_Patch_Width_SP_1,
    nContact_Patches_Across_Width,nContact_Patches_Across_Length,
    x1,x2,x3,Fixed_Frame],                                          //1

   [Nonconformal,[Planet_1_Body_1,"SURFACE2",Disjoint_Surface],
            [Sun_1_Structure_Body,"SURFACE2",Disjoint_Surface],
    Friction_Coeff,Separation_Tolerance,Contact_Patch_Width_SP_1,
    nContact_Patches_Across_Width,nContact_Patches_Across_Length,
    x1,x2,x3,Fixed_Frame],                                          //2
);
```

Similar instructions are used for all mating pairs within the compound planetary system.

COMPOUNDAN.CMD

The "compoundan.cmd" file is used to set the analysis and post process the data after the analysis. In the first part values of the applied loads are given. In the compound planetary system the only load that need to be specify is the torque on the first stage sun. Secondly parameters for the contact analysis must be specified. These parameters will affect the analysis of each pairs of surface that may come into contact (see (Vijayakar, 2003-a) for details on each parameter).

```
// Applied loads
Sun_Torque_1 := XXXX;

//Contact parameters
Friction_Coeff := XXXX;
Separation_Tolerance := XXXX;
Contact_Patch_Width_RP_1 := XXXX;
Contact_Patch_Width_SP_1 := XXXX;
Contact_Patch_Width_RP_2 := XXXX;
Contact_Patch_Width_SP_2 := XXXX;
nContact_Patches_Across_Width := XXXX;
nContact_Patches_Across_Length := XXXX;
```

The remaining part of the file is composed by the definition of the solution method, a "for" loop which analyze every single step and a certain number of standard Calyx® instruction that allows to print into ".dat" files all the data required. In the following an example shows how the bearing reactions are store into a file called "Bearing_React_Stage1.dat". The first lines set the analysis to "Static" and enable stress calculation. Then the ".dat" file is opened to be ready to store data. The "for" loop automatically increase the value of time to reach different system configuration at each step. Once the configuration is ready the instruction Analyze() runs the analysis at the current step. The instruction "Out_to_file" prints the values of bearing

reactions into the “Bearing_React_Stage1.dat” file. The “.dat” file is closed at the end of the “for” loop just before the end of all calculation.

```
//Set analysis
Set_Solution_Method(Static);
Enable_Stress_Calculation();


// Opening file .dat
var  Bearing_React_Stage1 := Open_Output_File("StaticResult\Bearing_React_Stage1.dat");
// Starting “for” loop
for(var i=0;i<Number_of_Timesteps;i=i+1){
   Analyze();
    // writing data into .dat file
   Out_To_File(Bearing_React_Stage1,
            Eval(Time),"\t",
            Eval(Bearing_React_Vector(Sun_Bearing_1)[1]),"\t",
            Eval(Bearing_React_Vector(Sun_Bearing_1)[2]),"\t",
            Eval(Bearing_React_Vector(Sun_Bearing_1)[6]),"\t",
            Eval(Bearing_React_Vector(Planet_1_Bearing_1)[1]),"\t",
            Eval(Bearing_React_Vector(Planet_1_Bearing_1)[2]),"\t",
            Eval(Bearing_React_Vector(Planet_1_Bearing_1)[6]),"\t",
            Eval(Bearing_React_Vector(Planet_2_Bearing_1)[1]),"\t",
            Eval(Bearing_React_Vector(Planet_2_Bearing_1)[2]),"\t",
            Eval(Bearing_React_Vector(Planet_2_Bearing_1)[6]),"\t",
            Eval(Bearing_React_Vector(Planet_3_Bearing_1)[1]),"\t",
            Eval(Bearing_React_Vector(Planet_3_Bearing_1)[2]),"\t",
            Eval(Bearing_React_Vector(Planet_3_Bearing_1)[6]),"\t",
            Eval(Bearing_React_Vector(Planet_4_Bearing_1)[1]),"\t",
            Eval(Bearing_React_Vector(Planet_4_Bearing_1)[2]),"\t",
            Eval(Bearing_React_Vector(Planet_4_Bearing_1)[6])
           );

}; // ending of for loop

// Close .dat file
Close_File(Bearing_React_Stage1);

End;
```

MESH FILE .MSH

Table 20 shows that a “.msh” is required for each gear modeled as deformable body. Calyx® provides separate tools ((Vijayakar, 2003-b), (Vijayakar, 2004), (Vijayakar, 2005)) to create each of these mesh file according to the gear manufacturing process. Basically the application generate the “.msh” file from both macro and micro geometric gear information. The value of module, pressure angle, number of teeth, radii, material properties and cutting tool parameters as well as profile modifications on the gear are used to calculate the tooth profile geometry. The user can also specify a mesh template trough which an automatic mesh of the tooth is also generated using particular Calyx® elements. The “.msh” file contains information about nodes coordinates, normal nodes coordinates, elements location, contact surface and the tooth set of

nodes used by the “compound.cfg” file to build and constrain the full gear structure. In order to show the structure of a “.msh” file, the first stage sun “.msh” is listed below:

```
Mesh File Version No.:1.03
374
987
176
4
3
0
0
1.92
0.2987156240198202  2.651174490384677
0.1119644761033078  0.9937122098932424
0.2860296211540961  2.652596937556581
0.1339803582117775  0.9909839875666227
…….
…….
-0.2885670239502212  2.56110317353969
-0.2936413239850207  2.606138831962184
0 0 0 1 0 0 1 0 0
0 0 0 1 0 0 1 0 0
…….
…….
0 0 0 1 0 0 1 0 0
0 0 0 1 0 0 1 0 0
0 4 204 197 198 205
4 41 1 2 42
29000000 0.29 0.0007353300000000002 0 0
…….
…….
0 16 297 294 99 100 101 102 103 104 105 106 107 108 109
110 111 112
4 509 505 506 510
29000000 0.29 0.0007353300000000002 0 0
SURFACE1
49
1 2 3 4 5 6 7 8 9 10
11 12 13 14 15 16 17 18 19 20
21 22 23 24 25 26 27 28 29 30
31 32 33 34 35 36 37 38 39 40
41 42 43 44 45 46 47 48 49 50
51 52 53 54 55 56 57 58 59 60
61 62 63 64 65 66 67 68 69 70
71 72 73 74 75 76 77 78 79 80
81 82 83 84 85 86 87 88 89 90
91 92 93 94 95 96 97 98
SURFACE2
49
99 100 101 102 103 104 105 106 107 108
109 110 111 112 113 114 115 116 117 118
119 120 121 122 123 124 125 126 127 128
129 130 131 132 133 134 135 136 137 138
139 140 141 142 143 144 145 146 147 148
149 150 151 152 153 154 155 156 157 158
159 160 161 162 163 164 165 166 167 168
169 170 171 172 173 174 175 176 177 178
179 180 181 182 183 184 185 186 187 188
189 190 191 192 193 194 195 196
FILLET1
16
1 2 3 4 5 6 7 8 9 10
11 12 13 14 15 16 17 18 19 20
21 22 23 24 25 26 27 28 29 30
31 32
FILLET2
16
165 166 167 168 169 170 171 172 173 174
175 176 177 178 179 180 181 182 183 184
185 186 187 188 189 190 191 192 193 194
195 196
Right_Side
30
2 1 2 2
3 1 3 2
4 1 4 2
5 1 5 2
6 1 6 2
7 1 7 2
8 1 8 2
9 1 9 2
10 1 10 2
11 1 11 2
12 1 12 2
13 1 13 2
14 1 14 2
15 1 15 2
16 1 16 2
Left_Side
30
973 1 973 2
974 1 974 2
975 1 975 2
976 1 976 2
977 1 977 2
978 1 978 2
979 1 979 2
980 1 980 2
981 1 981 2
982 1 982 2
983 1 983 2
984 1 984 2
985 1 985 2
986 1 986 2
987 1 987 2
Base
34
1 1 1 2
41 1 41 2
81 1 81 2
121 1 121 2
161 1 161 2
201 1 201 2
241 1 241 2
281 1 281 2
486 1 486 2
692 1 692 2
732 1 732 2
772 1 772 2
812 1 812 2
852 1 852 2
892 1 892 2
932 1 932 2
972 1 972 2
0
```

2.6 Results

In this section an application of the previously described model for the static analysis of a compound planetary system is presented.

Since the model contains the kinematics of the system, the analysis of more then one relative position between the gears results very easy. Therefore a total of 106 mesh cycles on the second stage were considered adequate to analyze the static stress behavior of the system during rotation. For each mesh cycle 80 steps where considered. Therefore a total of 8480 different analyses are performed to evaluate the variation of stresses for each body for a complete revolution of second stage carrier. Since the second stage is the slower stage, the number of mesh cycles analyzed for first stage results less accurate with 22 steps of analysis in around 385 mesh cycle.

The main goal of the analysis is the description of the hoop stress on the two rings. Another interesting result is related to the ring deformation shape due to the applied constraint and rim thickness. No particular attention is paid to contact pressure between gears. The torque applied at the first stage sun has a typical value for this application.

Note that in the following paragraphs some stress data will be plotted. All values are calculated in the fillet region of a particular tooth for each gear body on the same side of the contact surface (see figure above).

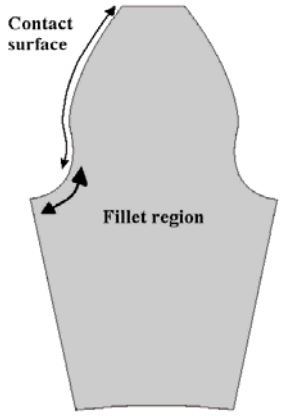

Figure 61: Fillet region and contact surface of a gear tooth.

The stress values are not evaluated in a specific point on the fillet region. This means that the values recorded are the maximum or minimum values of the specific stress (Principal, Shear, Von Mises etc.) found all along the fillet region.

When the x-axis of the plots shows a time value, the data must be considered plotted with respect to the system rotation. Since the analysis is purely static, the use of a time variable does not involve any dynamical meaning and is merely related to the hypothetic speed of rotation through which relative position of the gears are evaluated.

2.6.1 Model connections and finite element mesh

The full model is first presented to show how it appears; this allows to check the location and relative position between the bodies. Also connections and mesh refinement can be controlled. The first stage, the second stage and the compound planetary models are shown respectively in Figure 62 a), Figure 62 b) and Figure 62 c). Bearings, lumped added masses and rigid bodies (such as carriers) are not shown in the pictures.

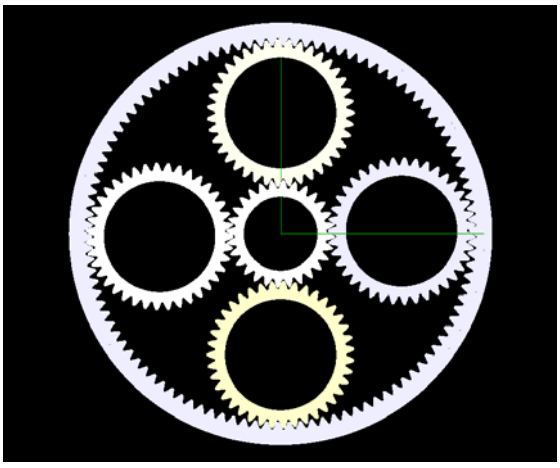

a)

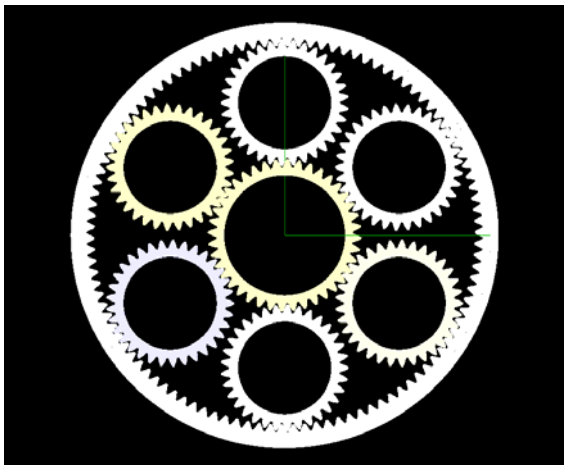

b)

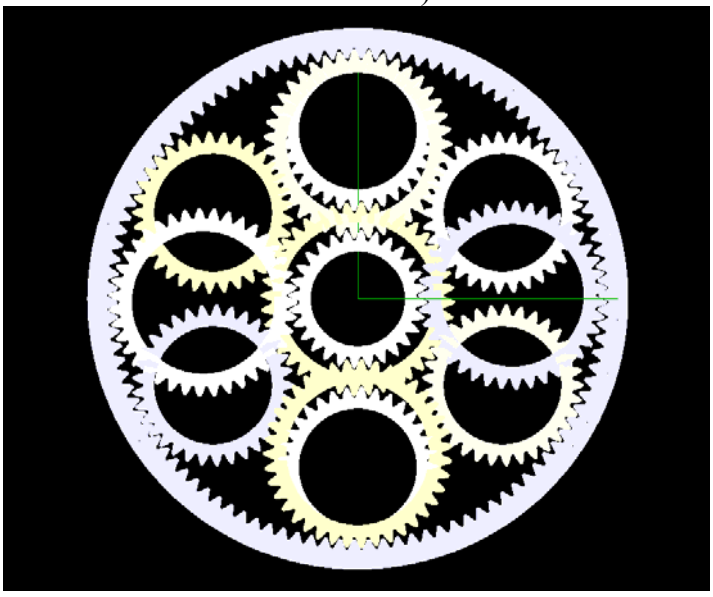

c)

Figure 62: Model of planetary system: a) First stage; b) Second stage; c) Full system.

Figure 63 shows details of the mesh at planet 1 sun and planet 1 ring interface for stage 2. Note that the mesh appears coarse at the gears contact interface. This is due to the particular formulation (Vijayakar, 1999) used to solve the contact problem.

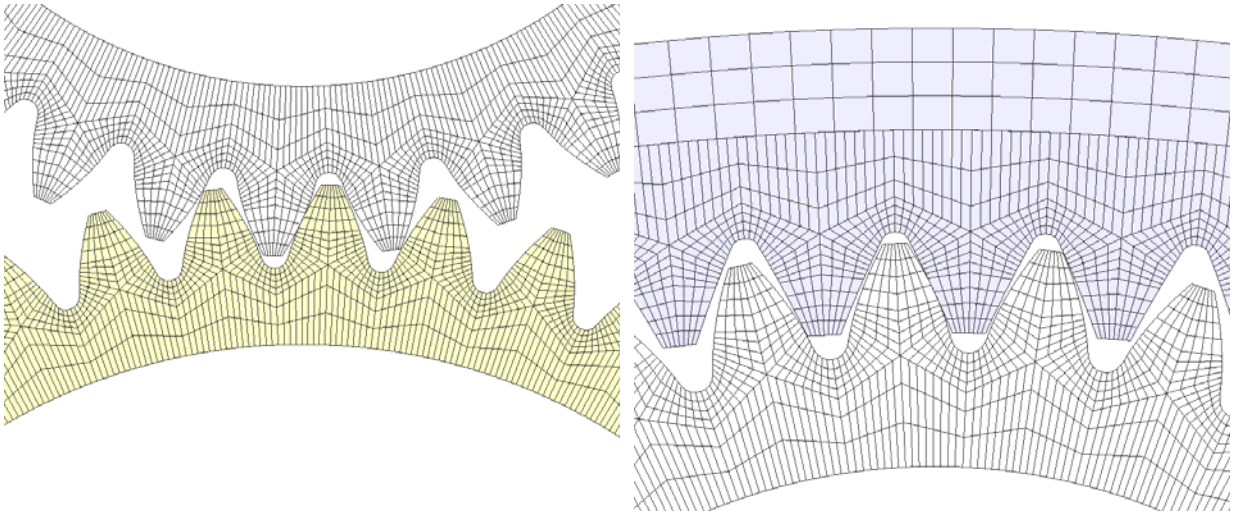

Figure 63: Details of the mesh on planet 1 for stage 2: a) Planet 1-Sun; b) Planet 1-Ring.

2.6.2 Stress analysis results

Figure 64 shows relative rotations between gears for stage 1 used for the analysis. Stresses are calculated at tooth 1 for planet 1, at tooth 90 for the ring and at tooth 28 for the sun. Bending stresses are evaluated in the fillet region on the active side of each tooth. Only the contact side between planet 1 and sun is considered for tooth 1.

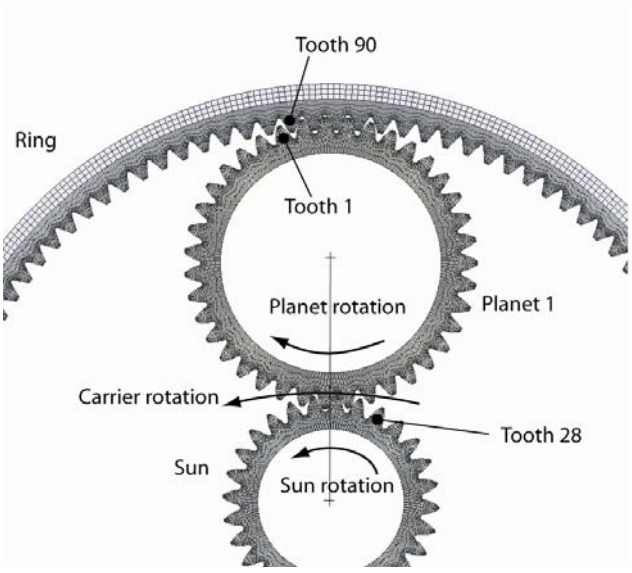

Figure 64: Relative rotations between gears for stage 1.

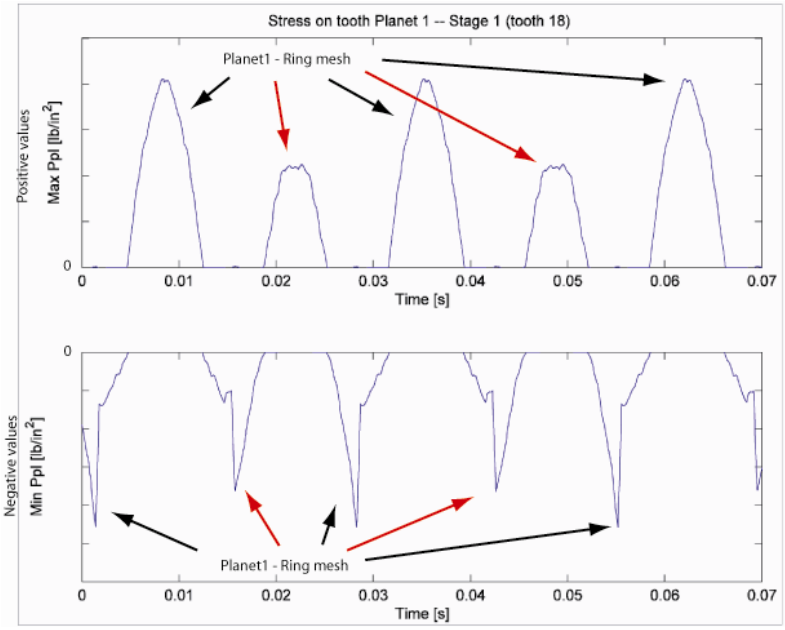

Figure 65: Maximum and minimum principal stresses in fillet region on Planet 1 (tooth 18) for stage 1.

Figure 65 shows the maximum and minimum principal stresses in fillet region on planet 1. According to Figure 65, the positive tensile peaks are recorded when the planet meshes with the sun, while the negative compressive peaks are recorded when the planet meshes with the ring. The analysis shows different values of the peaks according to the position of the planet during the rotation (black or red flags). This is due to different phase angles between the four planets (the planets are not equally spaced).

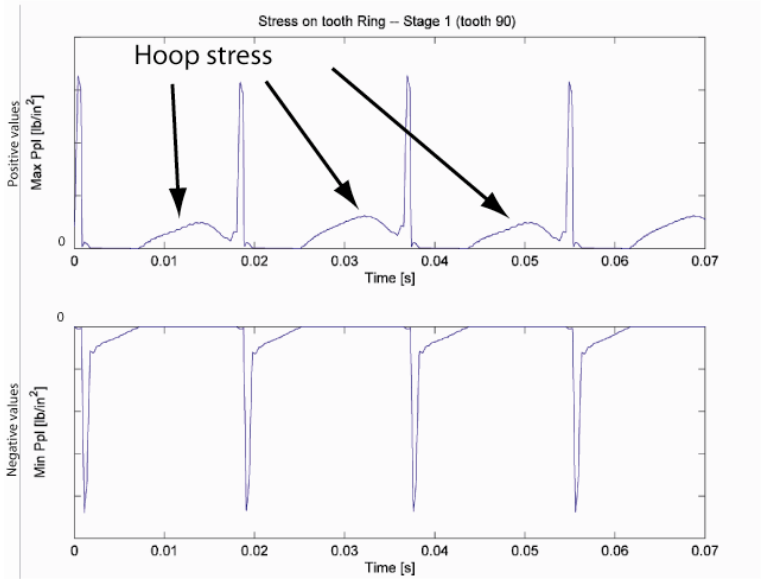

Figure 66: Maximum and minimum principal stresses in fillet region on Ring (tooth 90) for stage 1.

Figure 66 shows the maximum and minimum principal stresses in fillet region on the ring. The most interesting result consists in the evaluation of the hoop stress in region far away from the contact zone. Figure 67 clarify that the ring ovalization causes hoop stresses on the ring between planets. The small bump in Figure 66 between peaks corresponds to step of analysis at which the hoop effect occurs on tooth 90.

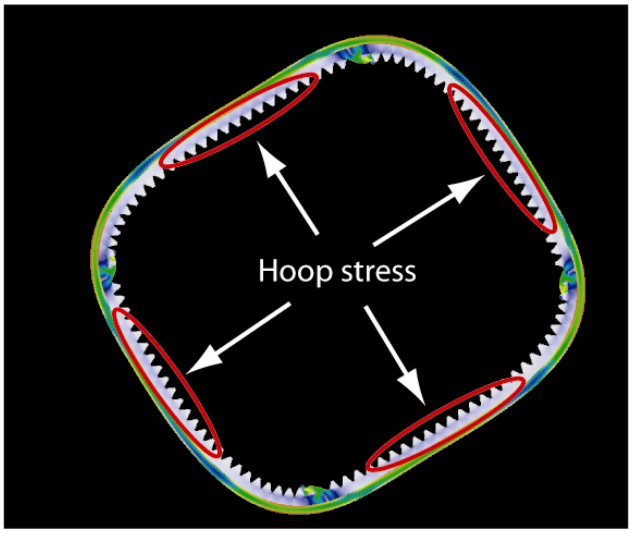

Figure 67: Ovalization of the first stage ring and locations of the hoop stress.

It is very important to control the value of the hoop stress especially when the ring thickness is thin. When the ring is very thin, such as in aeronautical applications, the peak in the hoop stress can become higher then the peak due to bending effect, and can causes unexpected failures.

In this particular application, an additional external rim is modeled to simulate the constraints of the ring. In order to give the model the exact boundary conditions, the Young' modulus of this rim is much higher then the ring. This rigid effect limits the peak value of the hoop stresses as shown in Figure 66.

2.6.3 Displacement of planet

Another important result, obtained through the planetary model, is the displacement of planets with respect to the theoretical position. The radial and tangential displacement of the center position due to deformation is calculated for each step of the analysis. Displacements take also into account the effect due to the stiffness matrix type bearings included in the model.

For example Figure 68 show the tangential displacement of planet 1 of the second stage and the relative spectrum.

It is very interesting to underline that the tangential displacements spectrum show harmonics which depend on both first and second stages mesh frequencies.

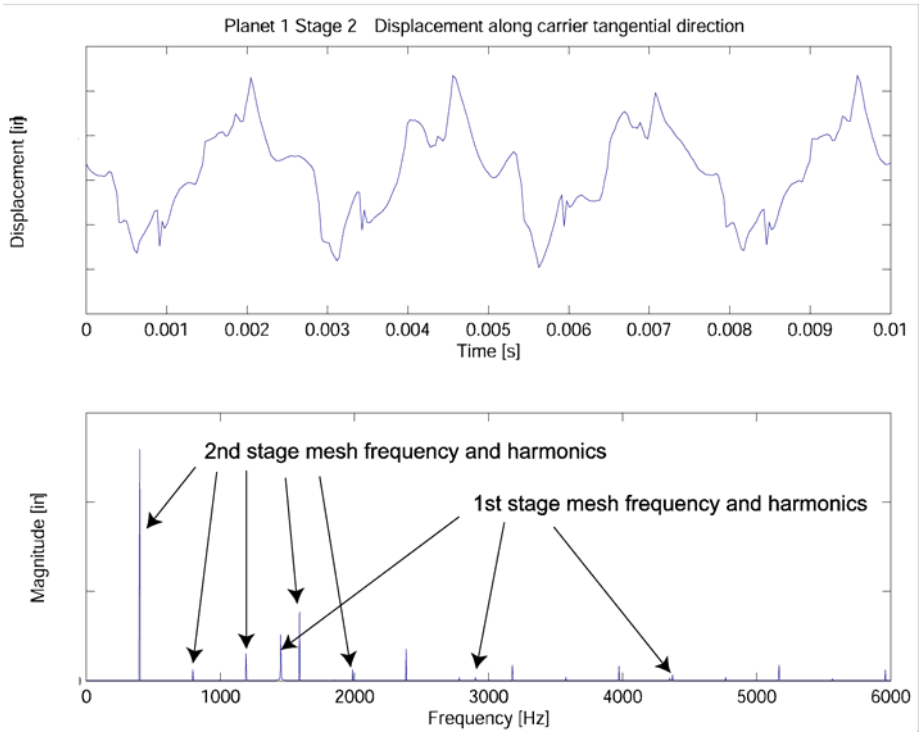

Figure 68: Displacement along tangential direction and spectrum of Planet 1 of stage 2.

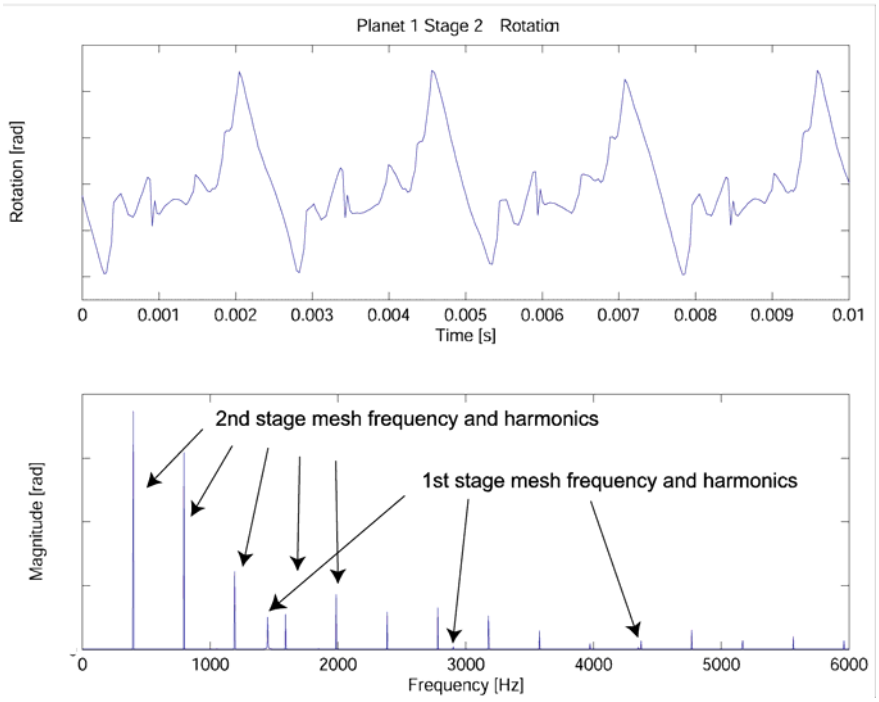

Figure 69: a)Rotation and spectrum of Planet 1 of the stage 2.

Figure 69 shows the same effect on the planet also for the rotational degree of freedom.

2.6.4 Bearings reactions

Since all bearings in the system are modeled, the value of the reactions at their locations can be evaluated. Figure 70 shows reactions exerted by the bearing, which connects planet 1 and the carrier for the first stage. The tangential and radial reactions are plotted with respect to the system rotation. The relative spectra show periodicity depending from the first and second stage mesh frequencies:

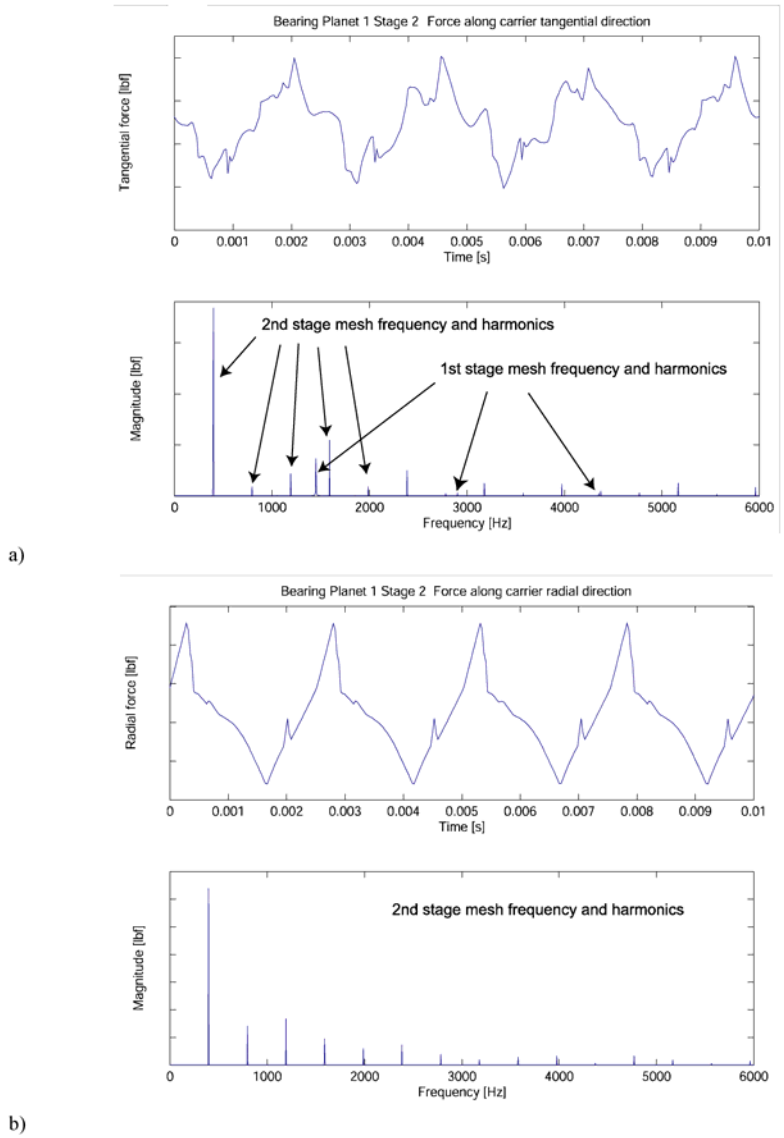

Figure 70: a) Bearing reaction force along carrier tangential direction on Planet 1 of stage 1 and its spectrum; b) Bearing reaction force along carrier radial direction on Planet 1 of stage 1 and its spectrum.

2.6.5 General deformation

As final result, some pictures of the magnified deformed shape of the two rings are presented and compared with respect to the undeformed system.

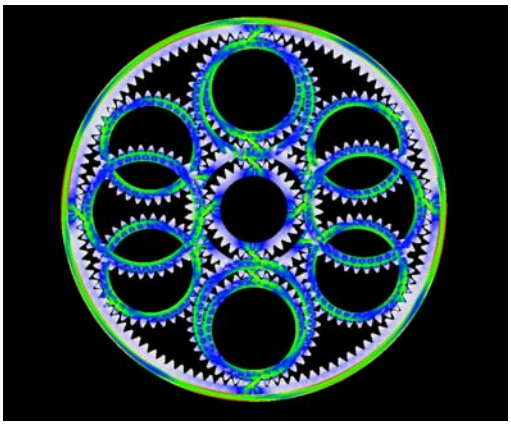

a)

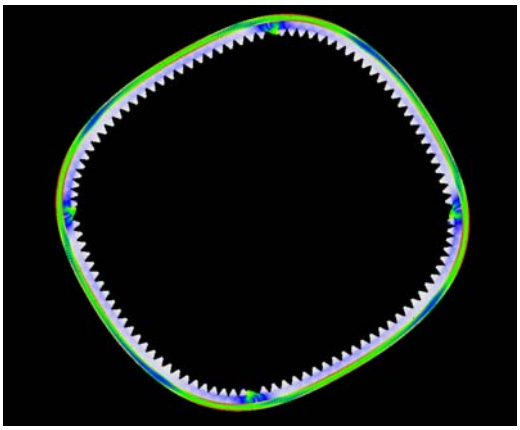

b)

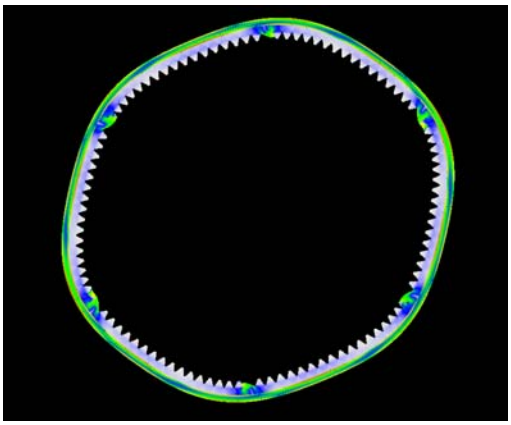

c)

Figure 71: Ovalization of the rings: a) Undeformed shape; b) Deformed shape for ring of stage 1; c) Deformed shape for ring of stage 2.

Two main effects can be seen:

1. The typical ovalized shape of the two rings depends on the different number of planet and hoop stresses are visible between planet locations for both rings.
2. The deformed shape is not perfectly symmetric with respect to the rotation axis. The reason of this behavior are the direction of the line of action between planets and rings and the phase angle between each planets (planets are not equally spaced).

Chapter 3

The present chapter is concerned with vibration problems in a spur gears pair. A single degree of freedom oscillator with clearance type non-linearity is considered. Such an oscillator represents the simplest model able to analyze a single teeth gear pair, neglecting: bearings and shafts stiffness; multi mesh interactions. Some test cases considered in the following sections represent an actual gear pair that belongs to a gear box of an agricultural vehicle; such gear pair gave rise to noise problems.

The main gear pair characteristics (mesh stiffness and inertia) are evaluated after an accurate geometrical modeling and a finite element analysis, including contact mechanics. Values for the mesh stiffness are evaluated for different positions along one mesh cycle and a Fourier expansion of the time varying stiffness is carried out. The gear modeling includes the presence of manufacturing errors.

The dynamical model presents a piecewise linear periodic stiffness and a constant viscous damping. A direct numerical integration approach and a smoothing technique have been considered to obtain the dynamic scenario, following periodic responses and detect instabilities and dynamic bifurcations.

3.1 Brief review

The problem of gear noise has been intensively studied in the past; however, recently the interest about this problem grew because of great restrictions in the laws regarding noise level and the increase of international competition with particular attention to automotive. One of the most important vibration and noise sources is the transmission error that excites the gearbox, the gearbox surfaces, and connected components. This results in noise radiated by the external box. Figure 72 shows noise path on a gears unit with bearings and housing.

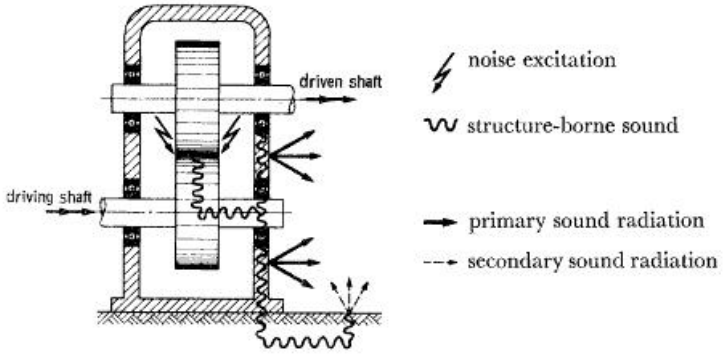

Figure 72: Noise path in gear transmission.

Despite the main strong interaction between noise and static transmission error has been clearly proved (Chung et al., 1999), number of experiments on gear systems has shown that several nonlinear phenomena occur when the dynamic transmission error is present: multiple coexisting stable motions, sub and super harmonic resonances, fold bifurcations, long period subharmonic and chaotic motions have been clearly demonstrated experimentally (Kahraman and Blankenship, 1997). Even though there is a general agreement about the nature of the phenomenon, the current understanding of gear vibration remains incomplete.

In the dynamic analysis of a gear system, an important role is played by the load conditions. Two main phenomena are described in literature (Dudley and Townsend, 1996), rattle and whine. Rattling occurs at low load condition while whine is related to higher loads and speeds (Pfeiffer and Kunert, 1990).

The literature suggests that many different models have been developed in the past sixty years. In effect the first mass-spring approach to gear dynamics was to created by Tuplin in 1953 (Tuplin, 1953) and intensive studies were conducted by Harris (Harris, 1958), Munro (Munro, 1962) and Gregory (Gregory et al., 1963-1964) in the sixties. An interesting literature overview can be found in (Ozguven and Houser, 1988), where the mathematical models used in gear dynamics were classified by considering: the evaluation of simple dynamic factor; tooth compliance; gear dynamics; geared motor dynamics; and torsion vibration. The previous paper shows how the interest on gear vibrations grew up continuosly from the seventies.

Important papers were published by Hsu and Cheng (1974), Benton and Seireg (1978) and Mark (1978). The first two papers concentrated their attention on the steady state response of a spur gear system to detect the effect of parametric excitations on resonances and instabilities. On the other hand Mark (1978) focused on the harmonic components of the static transmission error.

In the eighties important contributions were given by Bahgat et al. (1983), who presented a dynamic procedure based on Hert'z impact formula for two cylinders in contact, by Yang et al. ((Yang and Sun, 1985), (Yang and Lin, 1987)), who proposed two different models to take into account energy dissipation, hertzian damping and tooth friction, and by Umezawa et al. ((Umezawa et al., 1984-a), (Umezawa et al., 1985-b), who developed approximated equation to simulate rotational vibrations of both spur and helical gears.

In the last twenty years the most of dynamic models were focused on non-linear aspects. Kahraman and Singh (1990) considered the effect of backlash and time varying mesh stiffness using harmonic balance method and digital simulation. A similar model was developed by Theodossiades and Natsiavas (2000) who predicted chaotic behavior by means of numerical integration: such intermitted chaos and boundary crises. Ozguven (1991) extended the non linear spur gear model considering both shaft and bearing dynamics. Cai and Hayashi (1994) proposed a linear approximation for a pair of spur gears and compared the analytical solution with the numerically calculated result by the nonlinear equation. Amabili and Rivola (1997) obtained a continuous closed form solution for any rotational speed and computed the transition curves, stable and unstable regions, by means of the Hill infinite determinant. Parker et al. (2000-b) studied the nonlinear dynamic response of a spur gear pair using a semi-analytical approach and two single degrees of freedom models. Andersson and Vedmar (2003) studied the dynamics of helical gears including the contribution of elliptic distributed tooth load.

All previous papers agree in considering the following sources of vibrations for gears system: torsion resonance, impulsive or cyclic fluctuations in drive torque, gear mesh transmission error, local component vibration responses and fluctuations in the output torque demand. The concept of a vibrating system made of two gears is generally modeled through two wheels linked by the teeth mesh stiffness. In its simplest form, this model can simulate the classical linear resonance, i.e. the resonant frequency of the system. However, more complex phenomena such as parametric instabilities can be an important source of noise.

In the present chapter a single degree of freedom oscillator with clearance type non-linearity simulates the dynamics of a simple spur gear pair. The model takes into account a time variable mesh stiffness and a constant viscous damping. Bearings and shafts stiffness are neglected. The main gear pair characteristics (mesh stiffness and inertia) have been evaluated after an accurate geometrical modeling and a finite element analysis, including contact mechanics. Values for the mesh stiffness are evaluated for different positions along one mesh cycle and a Fourier expansion of the time varying stiffness is carried out. Backlash is also modeled by means of a smoothing technique. This approach is able to approximate the piecewise linear displacement function, typical for systems with clearance. A random technique capable to evaluate composite deviation from a perfect involute profile according to manufacturing process quality is also given. Some simple case studies are considered in order to analyze the effect of manufacturing processes and profile modifications, on the dynamic

behavior of the spur gear. An adaptive step-size numerical algorithms is considered. The accuracy of the direct numerical integration of the non-smooth system is checked by means of comparisons with the existent literature and the efficiency of the integration algorithms is evaluated.

Semi-amplitude/frequency and bifurcation diagrams of Poincaré maps are given in order to show the effect of variable mesh stiffness and deviation from the perfect involute profile on dynamic behavior.

3.2 Equation of Motion

The theoretical model considers the spur gear pair as a single degree of freedom lumped system. Each gear is represented by a rigid disk coupled along the line of action through a time varying mesh stiffness *k(t)* and a constant mesh damping *c* (see Figure 73).

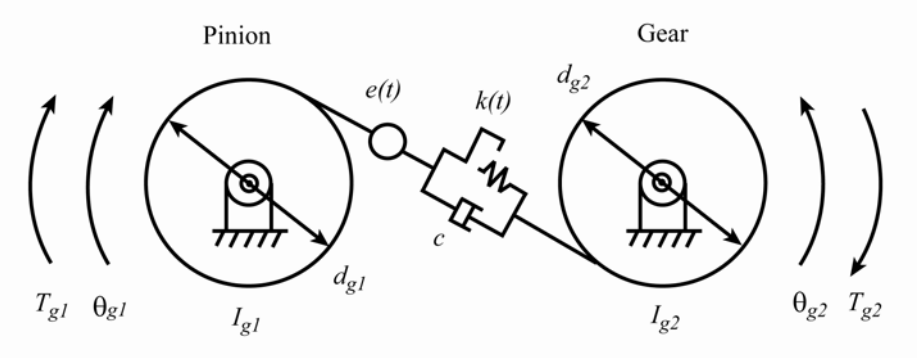

Figure 73: Dynamic spur gears model.

Diameters of disks are base gear diameters d_{g1} and d_{g2} ; the angular position of the driver tooth wheel (pinion) is θ_{g1}, while the angular position of the driven wheel (gear) is θ_{g2}; the rotary inertia are I_{g1} and I_{g2}; the driver torque is $T_{g1}(t)$, while the breaking torque is $T_{g2}(t)$. Shafts and bearings are supposed to be rigid. A time varying excitation *e(t)* is included in the model, which considers both manufacturing errors and profile modifications. When *e(t)* is positive a lack of material is considered (see Figure 74).

A backlash function is included in order to simulate clearances:

$$f(t) = f\left(\frac{d_{g1}}{2}\theta_{g1}(t) - \frac{d_{g2}}{2}\theta_{g2}(t) - e(t)\right) \tag{3.2.1}$$

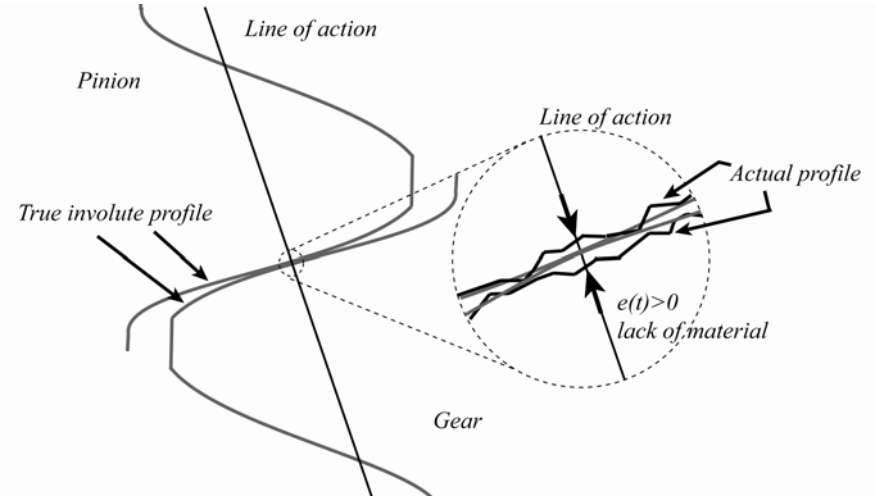

Figure 74: Manufacturing errors: lack of material along the line of action.

Equations of motions for the gear pair read:

$$I_{g1}\ddot{\theta}_{g1} + c\frac{d_{g1}}{2}\left(\frac{d_{g1}}{2}\dot{\theta}_{g1} - \frac{d_{g2}}{2}\dot{\theta}_{g2} - \dot{e}(t)\right) + \frac{d_{g1}}{2}k(t)f\left(\frac{d_{g1}}{2}\theta_{g1} - \frac{d_{g2}}{2}\theta_{g2} - e(t)\right) = T_{g1}(t) \tag{3.2.2}$$

$$I_{g2}\ddot{\theta}_{g2} + c\frac{d_{g2}}{2}\left(-\frac{d_{g1}}{2}\dot{\theta}_{g1} + \frac{d_{g2}}{2}\dot{\theta}_{g2} + \dot{e}(t)\right) + \frac{d_{g2}}{2}k(t)f\left(-\frac{d_{g1}}{2}\theta_{g1} + \frac{d_{g2}}{2}\theta_{g2} + e(t)\right) = -T_{g2}(t) \tag{3.2.3}$$

where $(\cdot)^{\cdot} = \mathrm{d}(\cdot)/\mathrm{d}t$.

The dynamic transmission error (DTE) x along the line of action is defined as in the following:

$$x(t) = \frac{d_{g1}}{2}\theta_{g1}(t) - \frac{d_{g2}}{2}\theta_{g2}(t) \tag{3.2.4}$$

Note that the actual transmission error will be $x(t) - e(t)$.

Using equation (3.2.4) and equations (3.2.3), equation (3.2.2) and (3.2.1) can be reduced to the following equation:

$$m_e\ddot{x}(t) + c(\dot{x}(t) - \dot{e}(t)) + k(t)f(x(t) - e(t)) = T_g(t) \tag{3.2.5}$$

where m_e is the equivalent mass:

$$m_e = \frac{1}{\left\{\left(d_{g1}^2/4I_{g1}\right) + \left(d_{g2}^2/4I_{g2}\right)\right\}} \tag{3.2.6}$$

T_g is the equivalent applied preload:

$$T_g(t) = m_e\left(\frac{d_{g1}T_{g1}(t)}{2I_{g1}} + \frac{d_{g2}T_{g2}(t)}{2I_{g2}}\right) \tag{3.2.7}$$

and we assume $T_{g2}(t) = T_{g1} d_{g2} / d_{g1}$; in the following T_g will be assumed constant. Equation (3.2.5) represents the relative dynamics along the line of action.

Note that some authors (Barber et al., 2003) stated that since the stiffness of the system changes with time, a conventional Newtonian statement of the equations of motion will generally lead to solutions that violate the fundamental principle of the mechanics "the work done by the external forces must be equal to the increase in total energy of the system". Barber stated theat "to obtain a correct statement of the governing differential equations, it is necessary to allow for the local deformation of the components in determining the direction of the contact forces or tractions. This result, which is a generalization of the ''Timoshenko paradox'' (Timoshenko et al., 1974) applies even in small strain problems where the problem statement is conventionally referred to the undeformed configuration". Despite this controversy the author also confirmed that, since the stiffness variation is periodic "We cannot emphasize too strongly that such equations of motion are therefore incorrect".

3.2.1 Modeling backlash: smoothing techniques

When the clearance is present between two mating teeth, in a gear pair, non-linear phenomena take place (Kahraman and Blankenship, 1997). In the past years many author proposed different way in order to model the dynamic effect of clearance in gear systems. Wang (Wang, 1978) (Wang, 1981) defines a backlash function as the angular distance between reverse tooth flanks, while the forward active tooth flank remains in contact. Since backlash depends on gear angular position, the backlash function was considered as a time varying function. Cai (Cai, 1995) used a nonlinear model, where dynamic loads are forced to zero when the relative tooth pair is separated from each other. The most of authors (Yang an Sun, 1985), (Kahraman and Singh, 1990), (Kahraman and Singh, 1992), (Blankenship and Kahraman, 1995), (Kahraman and Blankenship, 1996-a), (Amabili and Rivola, 1996), (Theodossiades and Natsiavas, 2000) consider a non-linear displacement function *f(t)* that can be used to describe the change of stiffness, which is related to the loosing of contact and the back side low impacts. Tomlinson and Lam (1984) mathematically shows an application to this technique also to asymmetrical clearance element.

In this work the gear pair is considered equivalent to a simple 1dof oscillator (see Figure 75).

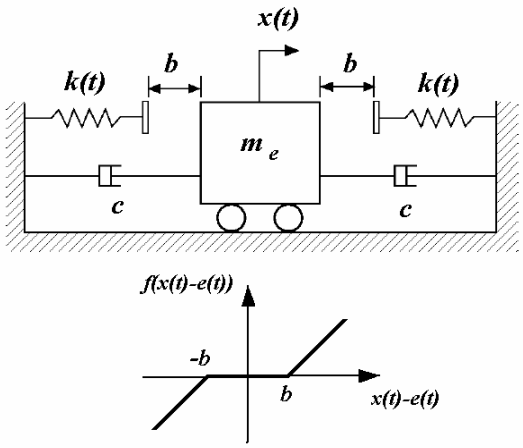

Figure 75: Equivalent gear model and backlash function.

In this model the gear mesh has a constant clearance equal to *2b*; the displacement function, for which concern the restoring force, assumes the following expression:

$$f\left(x(t)-e(t)\right)=\begin{cases} x(t)-e(t)-b & x(t)-e(t)\geq b \\ 0 & \left|x(t)-e(t)\right|\leq b \\ x(t)-e(t)+b & x(t)-e(t)\leq -b \end{cases} \tag{3.2.8}$$

The displacement function returns 0 when $\left|x(t)-e(t)\right|\leq b$ to simulate loss of contact between gears.

Inserting equation (3.2.8) into equation (3.2.5) a second order piecewise linear time varying differential equation is obtained.

$$\begin{cases} m_e\ddot{x}(t)+c(\dot{x}(t)-\dot{e}(t))+k(t)(x(t)-e(t)-b)=T_g(t) & x(t)-e(t)\geq b \\ m_e\ddot{x}(t)+c(\dot{x}(t)-\dot{e}(t))=T_g(t) & \left|x(t)-e(t)\right|\leq b \\ m_e\ddot{x}(t)+c(\dot{x}(t)-\dot{e}(t))+k(t)(x(t)-e(t)+b)=T_g(t) & x(t)-e(t)\leq -b \end{cases} \tag{3.2.9}$$

In order to apply a standard numerical approach to integrate the differential equation (3.2.9) some authors (see eg. Kim et al., 2003) suggest the use of smoothing techniques. The main idea is to approximate the piecewise linear displacement function given by equation (3.2.8) and illustrated in Figure 75 with a continuous function. This involve the substitution of a zero class $C^0\left(\mathbb{R}\right)$ function with a function of class $C^\infty\left(\mathbb{R}\right)$.

For example, using a polynomial interpolation it is possible to approximate a given function *f* defined on a certain interval, imposing that the interpolation function assumes vaues of *f* for a set of *M=n+1* points x_i in this interval: the polynomial *p(x)* of degree *n*, reads.

$$p(x)=p_1x^n+p_2x^{n-1}+p_3x^{n-2}+\ldots+p_nx^n+p_{n+1} \tag{3.2.10}$$

The most common techniques calculate the polynomial coefficients p_i such as the following quantity is minimized:

$$\sum_{i=1}^{M}\left(u_i-\widehat{u_i}\right)^2 \tag{3.2.11}$$

where:

$$\widehat{u_i}=f(x_i)=p_1x_i^{\,n}+p_2x_i^{\,n-1}+p_3x_i^{\,n-2}+\ldots+p_nx_i^{\,n}+p_{n+1} \tag{3.2.12}$$

200 equispaced samples are calculate for equation (3.2.8) with a backlash value of 2*b*=2 in order to check the behavior of polynomial interpolation with respect to the backlash function. Figure 76 and Figure 77 plot the polynomial approximated function when different degree of interpolation functions are used. Low values of the degree yield to bad approximation of the backlash function both inside and outside the non contact domain. Using a higher degree, yields to good approximation except fro the discontinuity points and the boundaries of the domain.

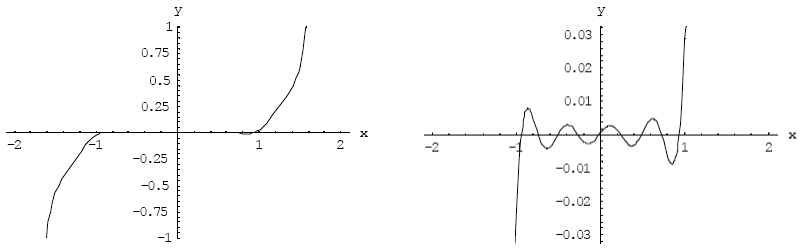

a) b)

Figure 76:Backlash polynomial interpolation functions: a) Degree 21; b) Degree 21 (zoom).

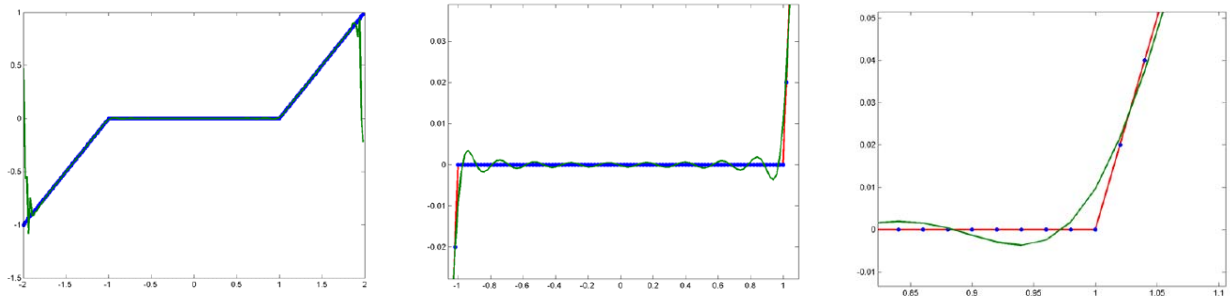

a) b) c)

Figure 77:Backlash polynomial interpolation functions: a) Degree 61; b) Degree 61 (zoom); c) Degree 61 (zoom on discontinuity);

For example the percentage of error at point *x*=1 is around 0.8% when the degree of the polynomial function is 61. Higher value of the degree yields similar behaviors with values of percentage error not admissible in gear dynamics simulations.

Kim et al. (2003) suggests the following smothering functions:

1. Arc-tangent type

$$f(x) = \arctan(\alpha x) \tag{3.2.13}$$

2. Hyperbolic tangent type

$$f(x) = \tanh(\alpha x) \tag{3.2.14}$$

3. Hyperbolic-cosine type

$$f(x) = \frac{1}{\alpha}\ln(2\cosh(\alpha x)) \tag{3.2.15}$$

4. Quintic spline type (here $y = x/\varepsilon$ and $\varepsilon = b/\alpha$)

$$f(x) = \begin{cases} \frac{\varepsilon}{8}(3 + 6y^2 - 1y^4), & |y| \le 1 \\ |x|, & |y| > 1 \end{cases} \tag{3.2.16}$$

where α is the shape parameter.

Kim also concludes that:

1. All functions (such as hyperbolic tangent and arc-tangent types) can be employed in both direct time domain numerical integration and semi-analytical methods though these must be handled with some care;
2. Hyperbolic-cosine type, when coupled with friction or impact damping, cannot be applied because of a singularity involved;
3. The quintic spline type localized smoothening function provides advantages only in semi-analytical methods.

In the following only the first two smothering functions are discussed and the application of each function to the backlash function (3.2.8) is described.

Let us consider the following backlash function:

$$f(\chi) = f_1(\chi) + f_2(\chi) \tag{3.2.17}$$

where:

$$\chi = x(t) - e(t) \tag{3.2.18}$$

$f(\chi)$ is assumed composed by $f_1(\chi)$ and $f_2(\chi)$ which represent the left and right side of the backlash function.

Arc-tangent type

According to the arc-tangent type approach, $f_1(\chi)$ and $f_2(\chi)$ are expressed in term of the arc-tangent functions (3.2.13).

A simple normalization term $1/\pi$ allows to transform the codomains of the function $f_1(\chi)$ from $[-\pi/2; +\pi/2]$ to $[-1/2; +1/2]$. Subsequently two translations shift the asymptotes to y=0 and y=1 and the symmetry axis to $\chi = b$, the result is multiplied by $(\chi\text{-}b)$ and a shape parameter α is inserted to controls the accuracy of the approximation. A similar procedure is applied to function $f_2(\chi)$. Equation (3.2.17) becomes:

$$f(\chi) = f_1(\chi) + f_2(\chi) = \left[(\chi - b)\left\{\frac{1}{2} + \frac{1}{\pi}\arctan[\alpha(\chi - b)]\right\}\right] + \left[(\chi + b)\left\{\frac{1}{2} - \frac{1}{\pi}\arctan[\alpha(\chi + b)]\right\}\right] \quad (3.2.19)$$

Figure 78 shows f_1 and a f_2 when $2b$=2 and $e(t)$=0:

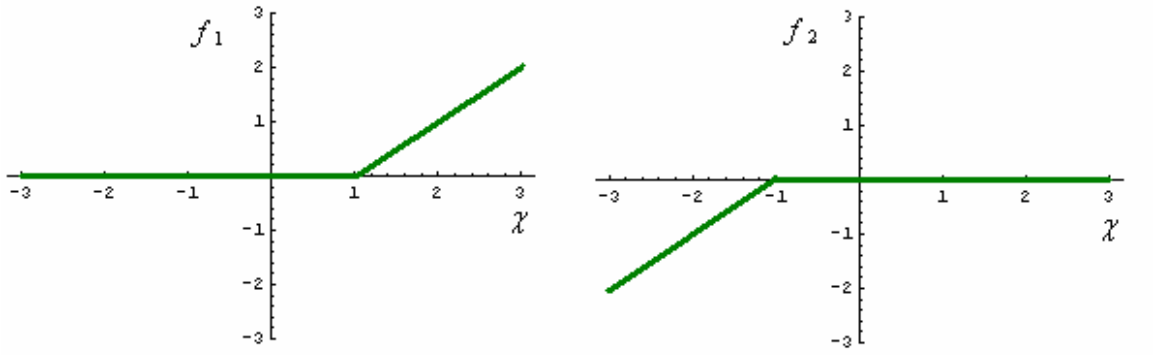

Figure 78: Arc-tangent approach: plots of $f_1(\chi)$ and $f_2(\chi)$.

Figure 79 shows the effect of the shape parameter α on the smoothing function in the proximity of the discontinuity point for the same case of Figure 78. A value of $\alpha = 10^8$ drastically reduce the percentage of the error and allows enough accuracy for dynamics numerical simulation.

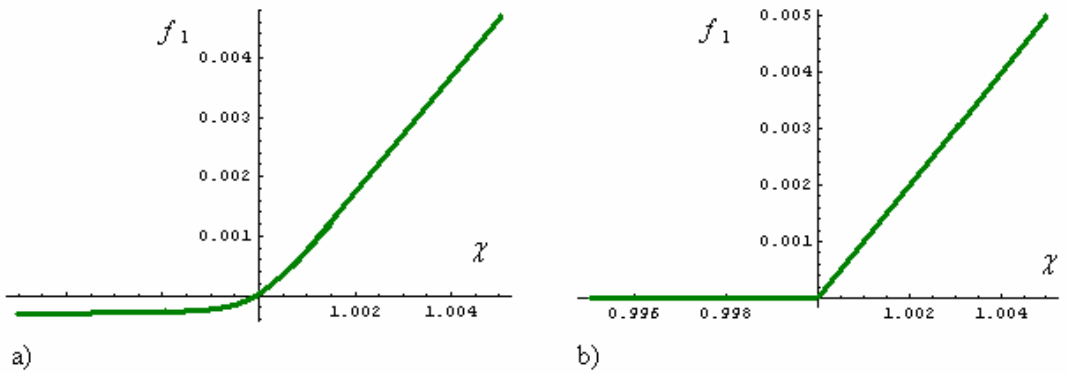

Figure 79: Effect of α on arc-tangent function: a) $\alpha=10^3$; b) $\alpha=10^6$.

Hyperbolic tangent type

According to the hyperbolic tangent type approach, $f_1(\chi)$ and $f_2(\chi)$ are expressed in term of the hyperbolic tangent functions (3.2.14).

Adding 1 to the first term of equation (3.2.17) and multiplying by $1/2$ allows to transform the codomains of the function $f_1(\chi)$ from $[-1; +1]$ to $[0; +1]$. Subsequently a translations of b shift the symmetry axis to $\chi = b$. The obtained function is multiply by $(\chi\text{-}b)$ and a shape parameter α is inserted to controls the accuracy of the approximation. A similar procedure is applied to function $f_2(\chi)$. Equation (3.2.17) becomes:

$$f(\chi) = f_1(\chi) + f_2(\chi) = \left[\frac{1}{2}(\chi - b)\{1 + \tanh[\alpha(\chi - b)]\}\right] + \left[\frac{1}{2}(\chi + b)\{1 + \tanh[-\alpha(\chi + b)]\}\right] \tag{3.2.20}$$

Figure 80 shows a plot of the two obtained function when $2b$=2 and $e(t)$=0:

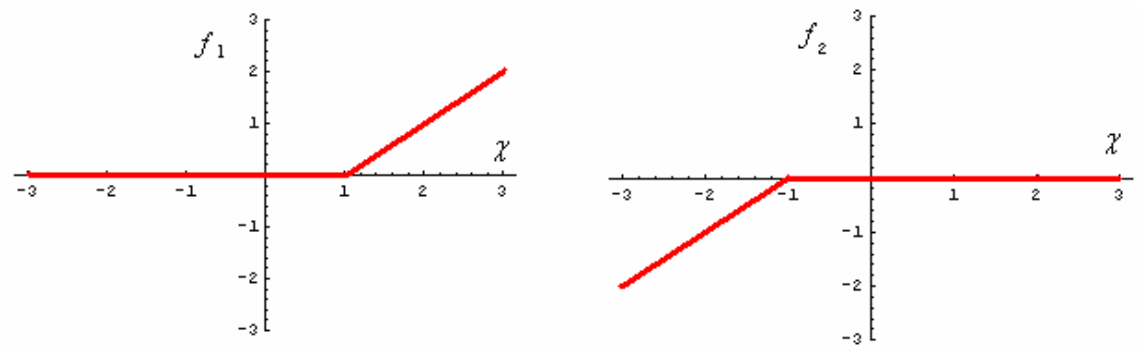

Figure 80: Hyperbolic tangent approach: plots of $f_1(\chi)$ and $f_2(\chi)$.

Figure 81 shows the effect of the shape parameter α on the smoothing function in the proximity of the discontinuity point. Even for the hyperbolic tangent approach, a value of α =10^6 drastically reduce the percentage of the error and consents enough accuracy for dynamics numerical simulation.

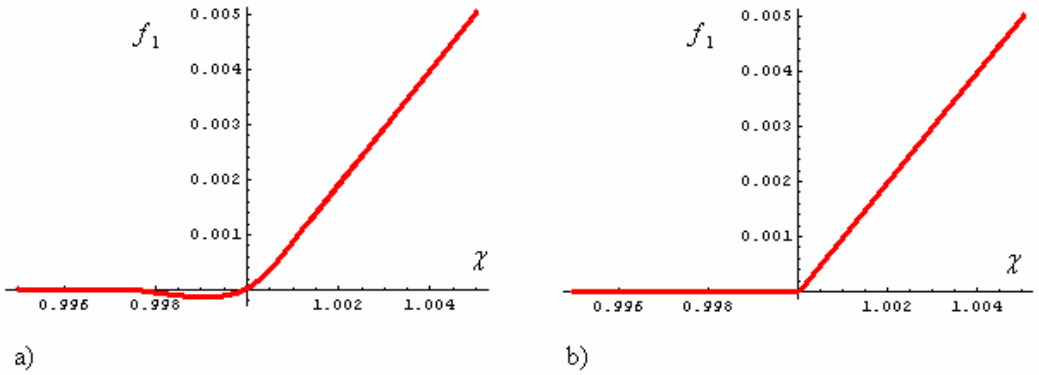

Figure 81: Effect of α on hyperbolic tangent function: a) $\alpha=10^3$; b) $\alpha=10^6$.

Comparison of smoothing functions

In order to choose the best smoothing function for the spur gear application, some detailed comparisons are performed. Due to symmetry, only the right side of the backlash function f_1 is taken into account.

Figure 82 shows a first comparison for $2b$=2, $e(t)$=0 and α=10. Functions are plotted in proximity of χ = 1. The blue line represents the approximated piece wise linear function described in (3.2.8). The comparison shows that the hyperbolic tangent approach has better accuracy with respect to the arc-tangent function. Similar results are obtained when α is increased.

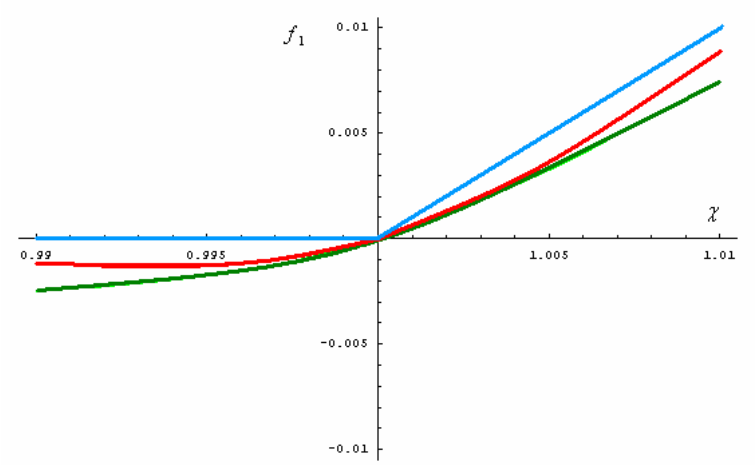

Figure 82: Comparison between smoothing functions (α=10): hyperbolic tangent (red), arc-tangent (green), piece wise linear (blue).

A further investigation analyzes the error distribution Δf_1 with respect to χ between the approximated piece wise linear function and the two smoothing functions for the previous case but with different values of α.

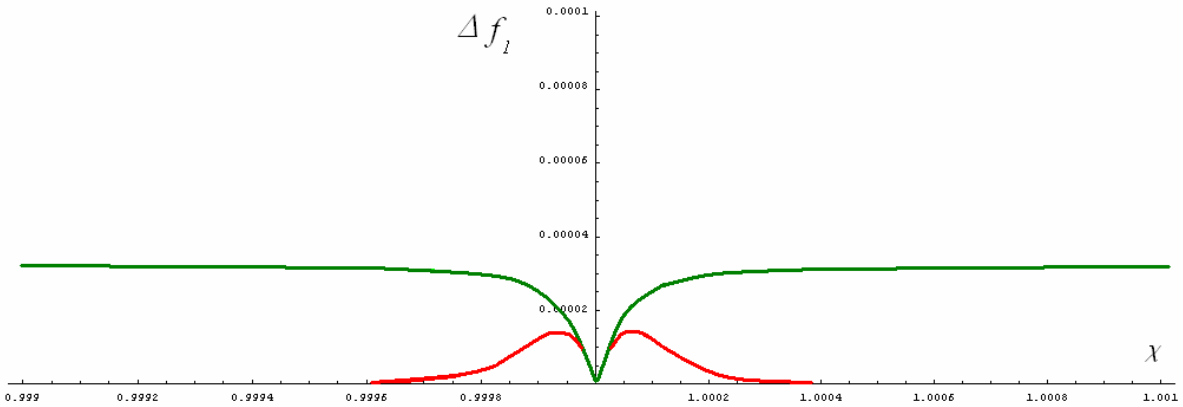

Figure 83: Difference between smoothing functions and the approximated backlash function: $\alpha=10^4$: hyper tangent (red), arc-tangent (green).

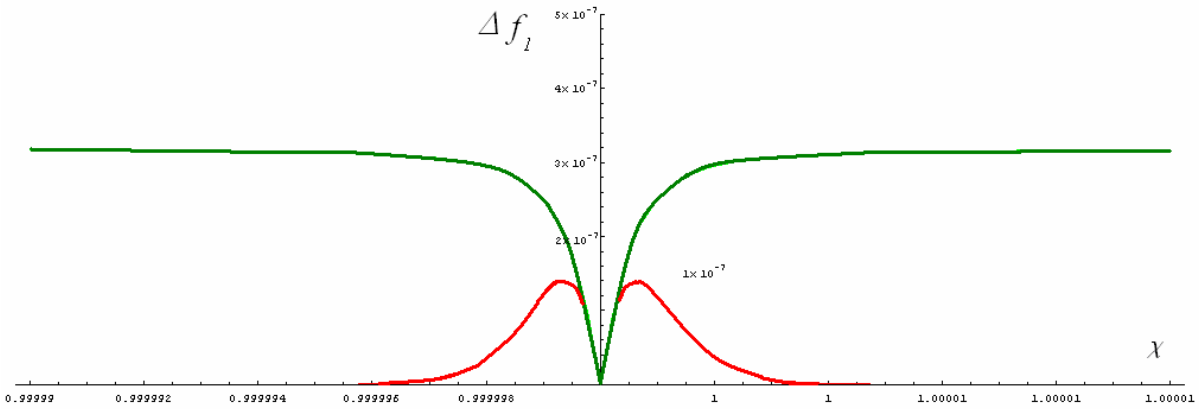

Figure 84: Difference between smoothing functions and the approximated backlash functionfor $\alpha=10^6$: hyper tangent (red), arc-tangent (green).

Figure 83 and Figure 84 allows to write the following considerations:

1. Increasing the shape coefficient α results in a drastically reduction of the error distribution;
2. An error magnitude lower then 10^{-6} is reached for $\alpha=10^6$ and guarantees enough accuracy in the numerical simulation for both smoothing function;
3. The hyperbolic function has peaks value of the error close to the discontinuity and decrease to zero far away from it;
4. The error distribution for the arc-tangent smoothing function has similar behavior to the hyperbolic tangent function close to the discontinuity but a completely different asymptotic behavior far away from it;
5. For a current value of the shape parameter α, the hyperbolic tangent function approximates the piece wise backlash function better then the arc-tangent function.

The analysis of the maximum amplitude of Δf_1 with respect to χ shows that increasing α results in decreasing of the maximum of the error distribution. Furthermore the following relationships can be obtained:

$$\text{for hyperbolic tangent: } \alpha \cdot ErrMax = 13 \div 17 \tag{3.2.21}$$

$$\text{for arc-tangent: } \alpha \cdot ErrMax = 28 \div 32 \tag{3.2.22}$$

where $ErrMax = \max\left\{\left|\Delta f_1\right|\right\}_{\chi \in \mathbb{R}}$.

Relationships (3.2.21) and (3.2.22) estimates that the same error accuracy can be obtained if the value of α used for the arc-tangent function is 2-5 time times the value of α used for the hyperbolic tangent function.

A final analysis takes into account the first derivative of the smoothing functions $\dot{f}_1$.

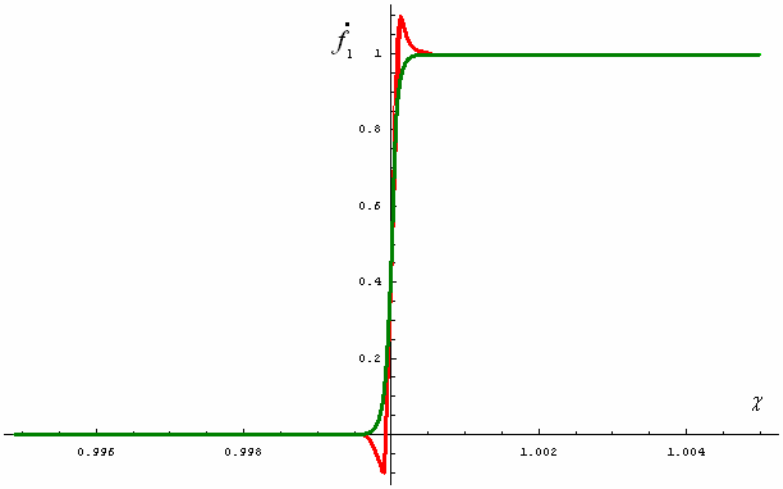

Figure 85: Comparison between first derivative of the smoothing functions for $\alpha=10^4$: hyper tangent (red), arc-tangent (green).

Figure 85 shows that Gibbs-like phenomena occurs for the hyperbolic tangent smoothing function at the point of discontinuity (for example for $\alpha=10^4$). This results in a better behavior of arc-tangent function for what concern the first derivative. Since the current gear pairs model does not include any explicit effect depending on the first derivative of the backlash function, this effect can be neglected.

The full smoothing equations are presented including profile errors:

$$f(t)=(x(t)-e(t))-\frac{1}{\pi}\left\{(x(t)-e(t)+b)\arctan\left[\alpha(x(t)-e(t)+b)\right]-(x(t)-e(t)-b)\arctan\left[\alpha(x(t)-e(t)-b)\right]\right\} \quad (3.2.23)$$

$$f(t)=\frac{1}{2}\left[(x(t)-e(t)-b)\{1+\tanh[\alpha(x(t)-e(t)-b)]\}\right]+\frac{1}{2}\left[(x(t)-e(t)+b)\{1+\tanh[-\alpha(x(t)-e(t)+b)]\}\right] \quad (3.2.24)$$

In the following, equation (3.2.24) is selected as smoothing function with a value of α of 10^8.

3.2.2 Mesh stiffness reconstruction

The unsteady component of the relative angular motion of pairs of meshing gears is well recognized as one of the main source of gear noise. Since 1938 the concept of transmission error was used to describes this displacement-type vibration excitation (Walker, 1938),

(Harris 1958), (Gregory et al., 1963-1964). Mark (1978) described the basic theory to provide analytical expression of the static transmission error which was considered the main parameter to control the dynamic of gears. Since the number of teeth pairs in contact within the mesh cycle changes, with the rotation of the gear, the mesh stiffness varies accordingly. For this reason transmission error does not have a single value but must be considered as a continuous variable during gears rotations.

The described effect generates a continuous variation of the deflection of the teeth and therefore of the angular transmission error during gears rotation which results in noise emission. In order to prove the relationship between transmission error and gear noise, many experiments was conducted in the last twenty years. Chung et al. (1999) found a direct proportional relationship between measured transmission error and generated sound levels emitted by an actual gears system.

In the previous sections the connection between static transmission error and mesh stiffness has been shown. For this reason a 2D finite elements analysis is applied to calculate stiffness. Calyx® (see previous chapters) is used to perform the analysis. If all teeth are equal in both pinion and gear, the static transmission error is periodic with the period of mesh. Therefore, the static transmission error can be easily calculated using a FE approach which can be able to analyze *n* different relative position of the gears within a mesh cycle.

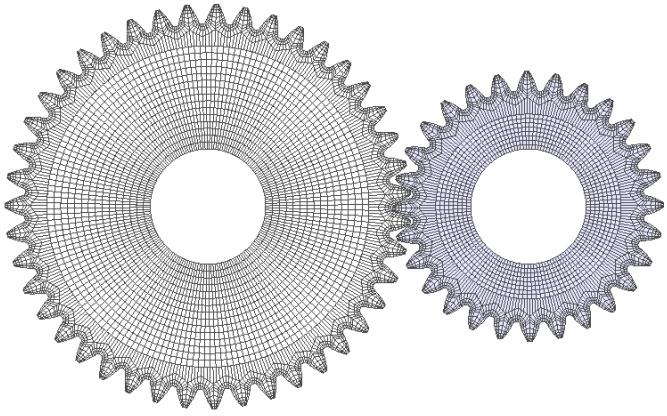

Figure 86: Mesh of the fem model.

The stiffness *k* is evaluated for each position by using equation (2.2.15). Since the stiffness is periodic with the mesh frequency, its analytical formulation can be obtained by means of :

$$k(t) = k_0 + \sum_i k_i \cos(i\omega_m t - \varphi_i) \tag{3.2.25}$$

where:

$$k_0 = c_0 \quad ; \quad k_i = 2\sqrt{c_i\, c_{-i}} \quad ; \quad \varphi_i = \arg\left(c_{-i}\right) \tag{3.2.26}$$

$$c_i = \sum_{h=0}^{n-1} \hat{f}\left(x_h\right) e^{-ji x_h} \tag{3.2.27}$$

where j is the imaginary unit, $\hat{f}\left(x_h\right)$ represents the stiffness value at the sample points x_h .All terms c_i are obtained by means of the Discrete Fourier Transform algorithm. Since k_i must become real values, c_{-i} results the complex conjugate of c_i.

Note that it is preferable to have an odd number of sample n within the mesh cycle and the n+1 sample must correspond to the end of the mesh cycle. In this way the number of harmonics terms in (3.2.25) is equal to (n-1)/2.

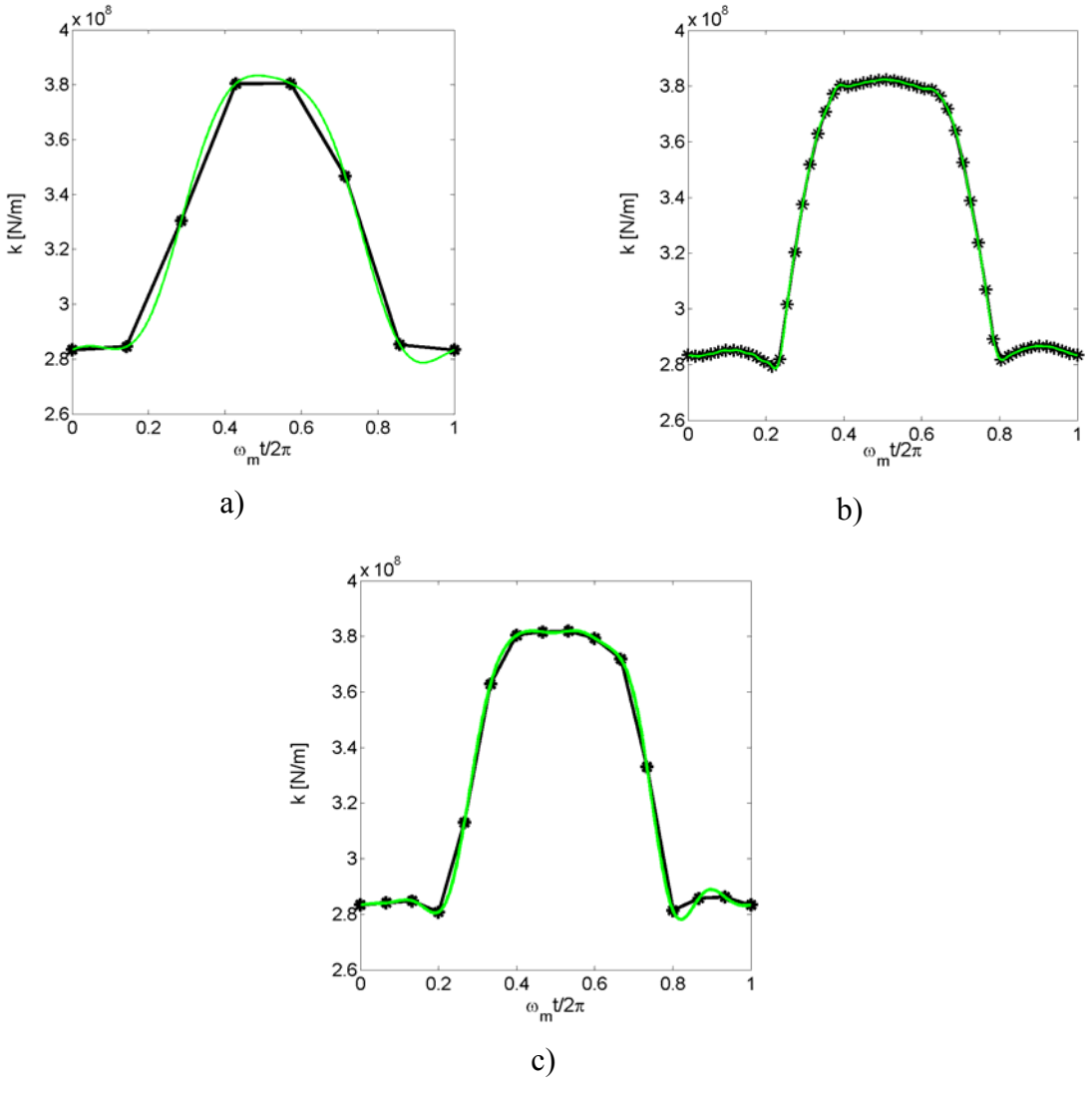

Figure 87: Comparison between analytical function of k(t) (green) and numerical values of k (-- black): a) 7 samples and 3 harmonics; b) 51 samples and 25 harmonics; c) 15 samples and 7 harmonics.*

Figure 87 shows analytical reconstructions of the mesh stiffness for case study 1 (see Table 2) with different parameters. A small number of samples (Figure 87 a)) results in a coarse reconstruction while a large number (Figure 87 b)) can cost computational effort. A good compromise (Figure 87 c)) is to select 15 positions within the mesh cycle for the Finite Element analysis and 7 harmonics for the stiffness analytical reconstruction.

3.2.3 Composite profile errors

Any process used to manufacture gears results in a certain amount of deviation from the theoretical involute profile. Furthermore the literature (see following sections), suggests tip and root relief to reduce the vibration of the system for a designed nominal torque. This profile modification introduce additional deviation from the perfect involute profile.

Many authors identify in manufacturing errors a possible source of rotational vibration. For example, Nielsen (1960) proposed simple analytical equations for angular errors in gears, and provided the theoretical effect of seven key factors that can have influence on angular accuracy. The first attempt to consider geometrical imperfections have been made by Walker (1938). Walker mostly concentrates his attention on the effect of intentional profile modification, applied to compensate tooth deflection. In 1969 Munro (Munro, 1969) described how geometrical imperfections in gears can alter significantly the ways in which load and motion are transmitted through the analysis of the transmission error. Umezawa et al. (1984-b, 1985-a) extended the analysis to understand the influence of pressure angle, normal pitch, waved profile errors on the rotational vibrations of spur gears. A similar work was proposed by Velex and Maatar (1996), with a comprehensive mathematical model, which was able to verify the influence of shape deviation and mounting errors for a spur or helical gears pair.

A particular transfer function approach was proposed by Mark (1979). His model was able to separate the effects of gears tooth errors and gear design parameters and give detailed description of how different classes of error affect different regions of the static transmission error spectrum.

The importance of considering the manufacturing errors in gears dynamics is proved by the possibility of predicting gear quality by means of vibration analysis (Ognjanovic and Subic, 1993) and by the number of vibrational models in which a profile errors term is included (Hayashi and Hayashi, 1976) (Cai and Hayashi, 1994), (Kahraman and Singh, 1990).

In the present section an iterative routine is developed to create a random profile within specified tolerance values. The estimation of an actual profile errors, is generally measured using sophisticated and expensive experimental rigs; therefore, few data are available.

In order to simulate profile errors it is important to define the profile tolerance (also referred to involute tolerance) which is the permissible amount of profile variation with respect to the theoretical involute profile. Since the profile geometry can be modified using tip or/and root relief, a particular chart, called "K" chart is commonly used to specify the tolerance values along the tooth profile projected on the line of action. An example of "K" chart with both tip and root parabolic relief is shown in Figure 88. The chart provides a tolerance value for each single profile segment with respect to a coordinate (roll angle or diameter) along the profile. Three segments are visible: the tip relief segment starting at the start roll angle tip $\varphi_{t,s}$ with tolerance Δ_t, the root relief segment included between the start roll angle root $\varphi_{r,s}$ and the end roll angle root $\varphi_{r,e}$ with tolerance Δ_r and the involute segment with tolerance Δ_i.

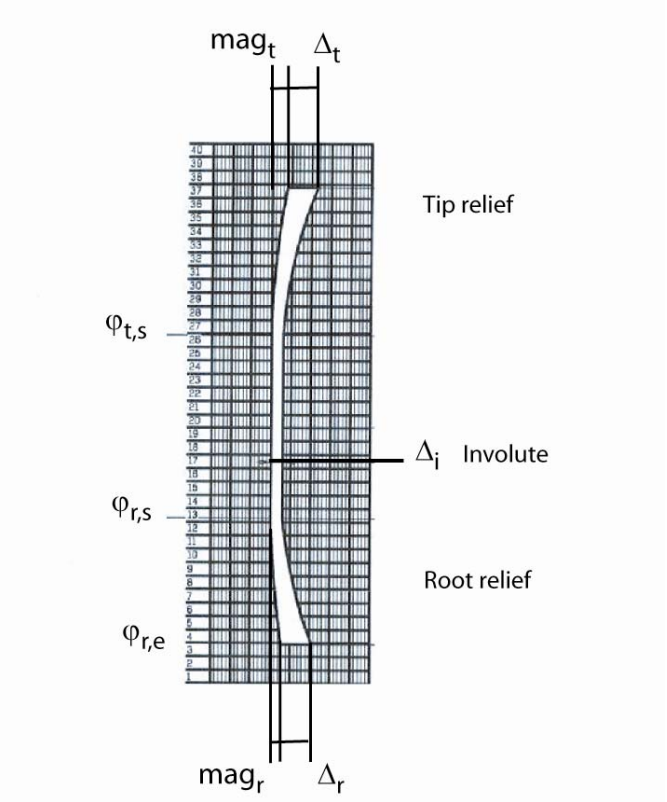

Figure 88: Example of "K" chart.

The quality inspection accepts tooth profile when the measured tooth profile lies between the lower allowance curve and the upper allowance curve. For very accurate application a further restriction on profile curvature is also imposed. Note that at least one measured point must lie on the lower allowance curve to avoid the superimposition of pitch error.

A particular manufacturing process quality can be simulated, according to "K" chart, in case of both linear or parabolic profile modification by generating a random profile which fit the "K" chart. Figure 89 shows an example of random generated profile fitting tolerance in case of a parabolic tip relief..

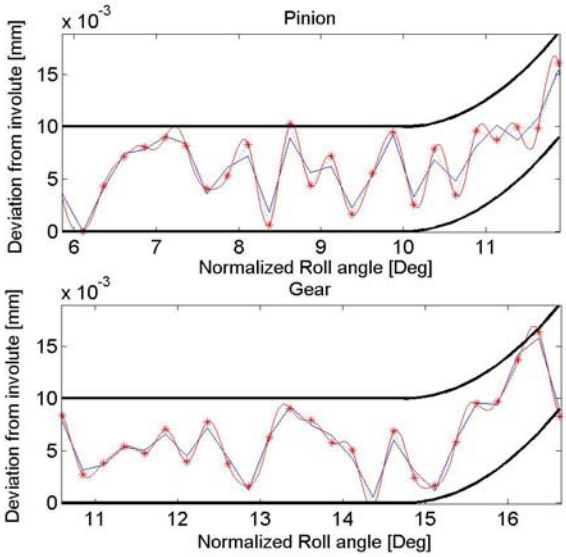

Figure 89: Random generation of pinion and gear profile according to "K" chart parabolic tip relief; (blue) random profile; (red) Fourier expansion reconstruction.

The deviation from the actual involute profile is provided with respect to normalized roll angle ($\varphi_{nroll} = 360(\varphi_{roll} / \varphi_{roll\,p})$), where φ_{roll} is the roll angle and $\varphi_{roll\,p}$ is the difference between the values of the roll angle at the lowest and the highest point of contact along the tooth profile (Dudley and Townsend, 1996).

Positive values of deviation means lack of material. The same approach is repeated to generate random profiles for all pinion and gear teeth.

An analytical formulation of the shape of each tooth profile error is developed by means of a Fourier expansion (see Figure 89). The analytical formulation allows to evaluate the composite profile error, during a mesh cycle, as a sum between deviation on meshing teeth, according to the transmission ratio. This approach is repeated $Z_1 \times Z_2$ times in order to perform a complete fundamental rotation (Z_1 and Z_2 are number of teeth on pinion and on gear). The fundamental rotation is the rotation required for the same tooth pair to reach contact in the same position. During such rotation all possible relative teeth contact combinations take place, then the process is repeated periodically. The composite profile error is approximated again by means of a Fourier series:

$$e(t) = \sum_i E_i \cos(i\tilde{\omega}_m t - \gamma_i) \tag{3.2.28}$$

where: $\tilde{\omega}_m = \omega_m / (Z_1 Z_2)$ and E_i and γ_i are amplitude and phase values evaluated through the FFT algorithm.

The previous methodology is tested by means of the "K" chart parameters described in Table 25:

		Pinion	**Gear**
Involute			
	Tolerance [mm]	0.008	0.008
Tip relief			
	Type of modification	Linear	Linear
	Roll angle at start of relief [Deg]	30.1569	29.2127
	Magnitude of relief [mm]	0.016	0.018
	Tolerance [mm]	0.02	0.02
Root relief			
	Type of modification	Linear	Linear
	Roll angle at start of relief [Deg]	23.4706	25.2079
	Roll angle at end of relief [Deg]	14.4334	20.5764
	Magnitude of relief [mm]	0.016	0.018
	Tolerance [mm]	0.02	0.02
Crowning			
	Magnitude [mm]	None	None

Table 25: Example of "K" chart parameters.

Figure 90 shows a simulation of the manufacturing error for the first tooth of the pinion and of the gear. Eighteen measurements are considers from the SAP radius to EAP radius and the black piece wise line represents simulates a possible machine measurement process. Trough the Fourier analytical formulation ten points are used to calculate the combined profile deviation from involute profile (blue line in Figure 90). Note that the extension of the blue line, with respect to roll angle, does not always coincide with the extension of the black line. This is due to two reasons:

1. The SAP radius can be different to the radius of the first point of contact on the tooth profile;
2. In the simulation the combined error for a single pair of teeth in contact, is calculated in a mesh cycle, therefore the last point considered the HPSTC.

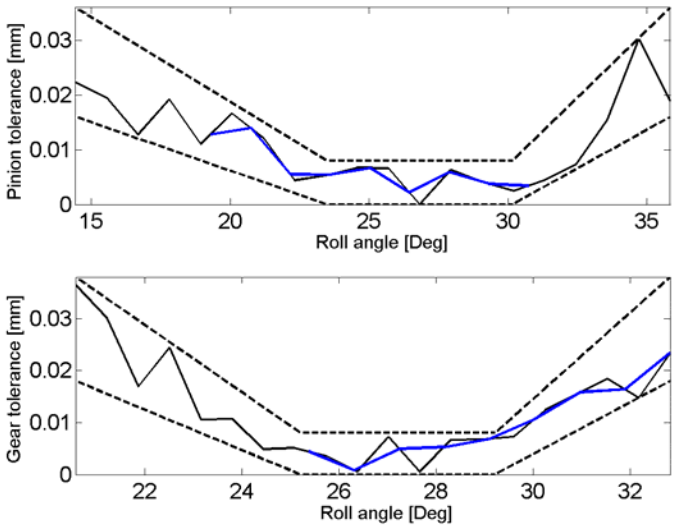

Figure 90: Simulation of manufacturing errors according to "K" chart.

Once the complete combined profile errors is calculated for $Z_1 \times Z_2$ different mesh cycles, the FFT algorithm provides the value of coefficients and phases for equation (3.2.28). The approach is similar to the one used with equations (3.2.25), (3.2.26) and (3.2.27).

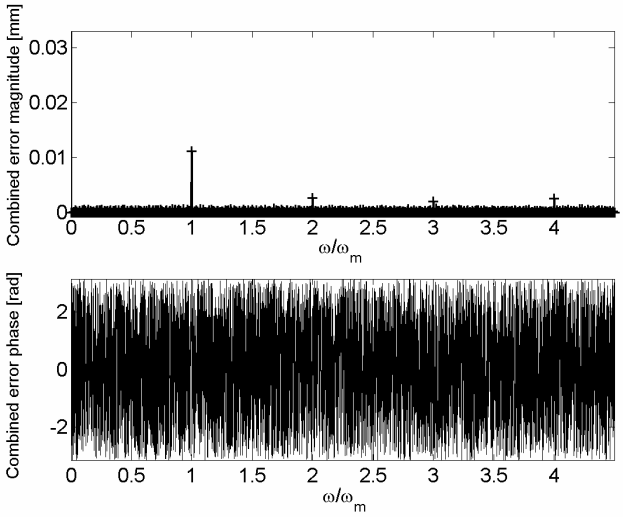

Figure 91: FFT spectrum of the combined profile error.

Figure 91 shows an example of the spectrum obtained from a composite profile error for a gear pair with profile errors. In the present plot, all frequencies are normalized according to the mesh frequency ω_m. The effect of profile errors results in a excitation having ω_m has fundamental frequency.

3.2.4 Back-side contact

Another important source of noise in spur gears is the possibility of having impact between the gear flank. When the relative amplitude of vibration between mating gears becomes high, a loss of contact and impacts between the mating flank can occur. A typical example is the so called “gear rattle”, a noise phenomena which takes place when gears are rotating with low applied torque (Pfeiffer and Kunert, 1990). Usually, in modeling gear rattle, an important role is played by the amount of dissipated energy when the impact occurs (Azar and Crossley, 1977), (Luo, 2005).

According to literature (Kahraman and Singh, 1990) two are the possibilities when impact effects are considered:

1. Single side impact (front side contact): when impact occurs between active mating flanks;
2. Double side impact (also referred as back-side contact): when impact occurs on the non active flanks of a mating teeth pair.
3.

Figure 92 illustrates the meaning of the front side contact and back side contact with respect to gears rotation. In normal condition the pinion transmits motion to the gear with a contact point moving on the line of action. When a back-side contact occurs the line of action change direction instantaneously according to the inverse motion (see Figure 93). Furthermore the change of the direction of the line of action can results in a different number of teeth pairs in contact. For example it is possible that during direct motion only one pair of teeth is in contact while during inverse motion two are the number of teeth pairs in contact.

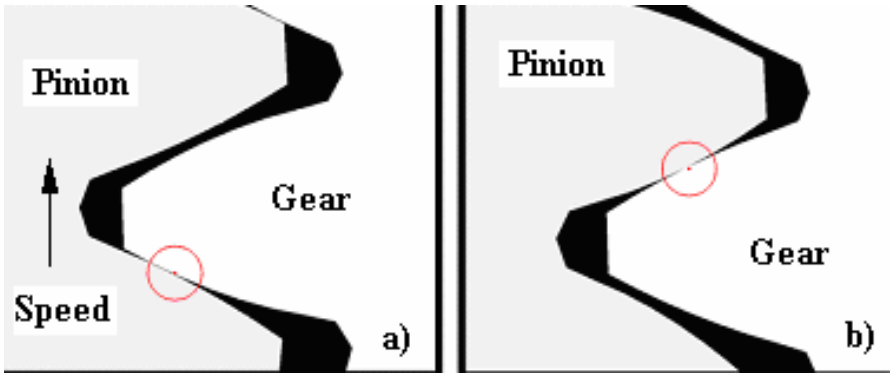

Figure 92: Contact between gears: a) front side contact; b) back-side contact.

Despite some authors predict the possibility of both typology of impact (Kahraman and Singh, 1990), no double side have never been recorded in a test facility for high speed spur gears system (Kahraman and Blankenship, 1997).

Nevertheless, the present work the possibility of back-side contact is taken into account through a change of the instantaneous stiffness value.

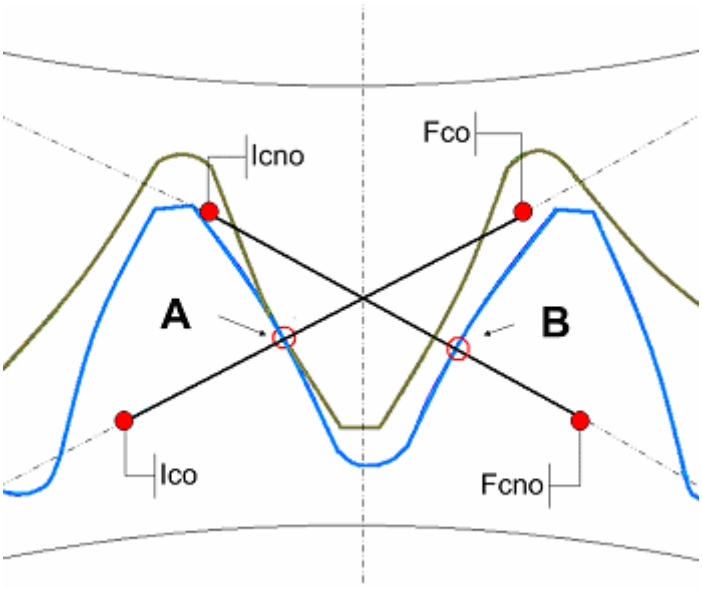

Figure 93: Different lines of action according to teeth contact.

The following assumptions are considered:

1. The gears are considered perfectly rigid and no manufacturing, mounting and geometrical errors are included;
2. The backlash is evaluated through equation (1.2.13);

Let us consider Figure 93. Ico and Fco are respectively the first and the last contact point along the line of action of the direct motion. Icno and Fcno are the equivalent points along the line of action of the inverse motion. If A is a current contact point during direct motion and back-side contact occurs, B will become instantaneously the new contact point.

Points A and B will be referred in the following as non-homologous points. Homologous points have the property of having the same mesh stiffness value, despite the direction of the line of action. Example of homologous points are Ico and Fcno and Fco and Icno..

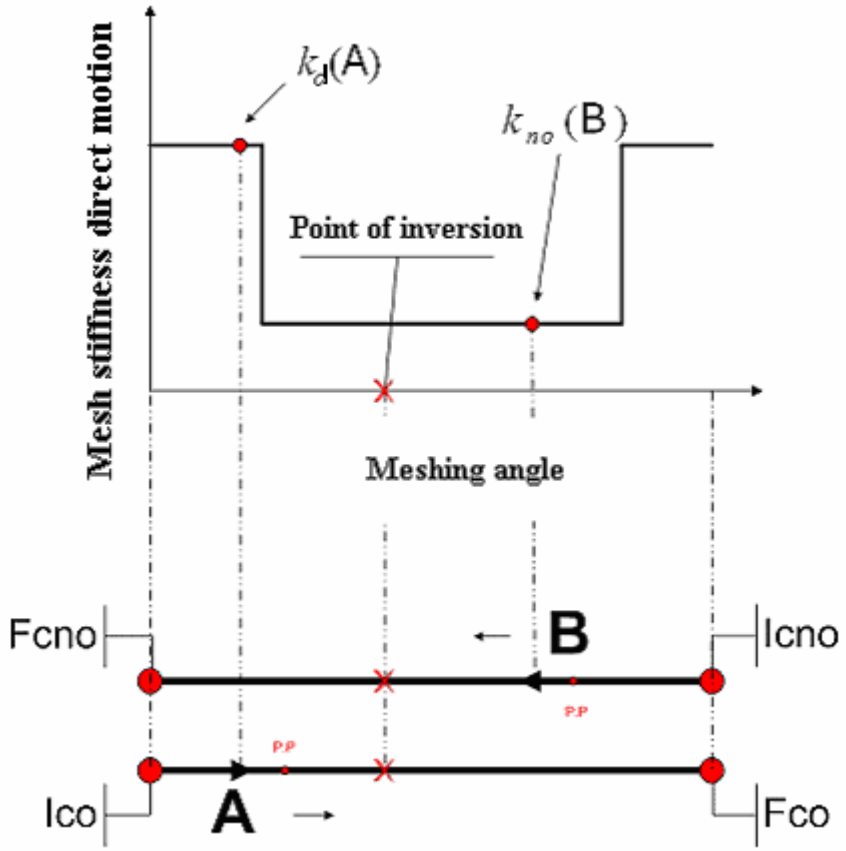

Figure 94: Schematic representation of the stiffness during direct and inverse motion.

Figure 94 shows a schematic representation of homologous points with respect to a generic stiffness curve considering direct motion; P.P. indicates the position of the pitch point.

Since point A and B are not homologous points, the projection of the points on the mesh stiffness curve yields to different stiffness values $k_d(A)$ and $k_{no}(B)$.

Simple kinematics consideration yield to calculate that A and B have the same speed along the relative line of action:

$$\left|\overline{v_A}\right| = \left|\overline{v_B}\right| \tag{3.2.29}$$

This relationship stands that the contact points for direct motion and inverse motion, are moving on the corresponding contact lines with the same speed. This allows to evaluate the value of the back-side contact mesh stiffness, once it is know the stiffness curve of the direct motion. The mesh stiffness of the front side contact $k_d(t)$ (note that $k_d(t)$ is equivalent to equation (3.2.25)) and the correspondent mesh stiffness in case of back-side contact $k_{no}(t)$ are related trough a simple transformation *T*.

$$k_{no} = T(k_d(\theta)) = k_d(-(\theta + \varphi)) \tag{3.2.30}$$

This transformation is composed of a translation and an inversion with respect to a point. The results of the transformation of the stiffness curve of the direct motion $k_d(t)$ produces a new stiffness function for the inverse motion $k_{no}(t)$. This two function have a different phase φ and a inverse orientation of the x-axis.

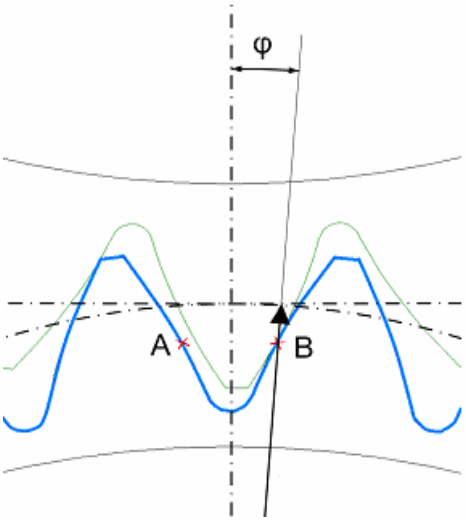

Figure 95: Evaluation of the phase angle φ.

The evaluation of the phase angle φ is performed through simple geometrical considerations. Figure 95 shows as A and B becomes homologous points when the centre line coincides with the symmetry axis of a vane of the pinion. This configuration is described in Figure 94 as the point of inversion for the transformation *T*. The value of the phase can be calculated as follow:

$$\varphi = \frac{1}{2r_{b1}} s_{vain} \tag{3.2.31}$$

where s_{vane} is the thickness of the pinion vain.

Once the point of inversion and the phase angle is calculated the new stiffness function can be described analytically as follows:

$$k_{no}(t) = k_0 + \sum_i k_i \cos(-(i\omega_m t - \varphi_i + \frac{1}{2r_{b1}} s_{vane})) \tag{3.2.32}$$

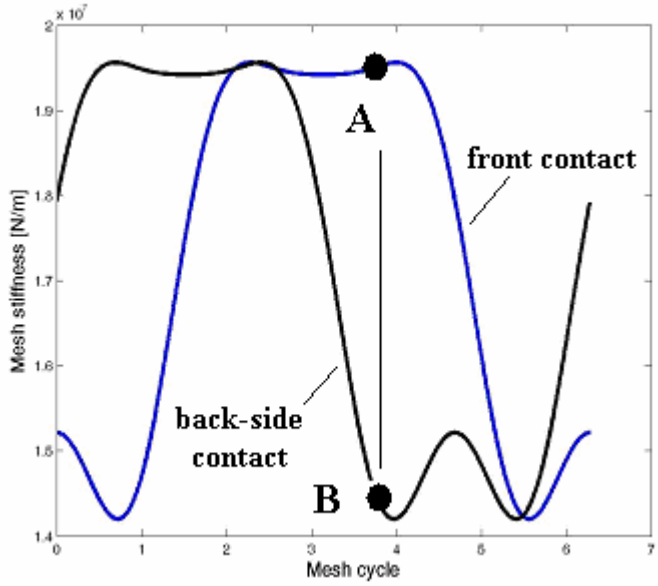

Figure 96: Comparison between mesh stiffness: direct motion (black), inverse motion (blue).

Figure 96 shows an example of comparison between the stiffness curve $k_d(t)$ and the obtained $k_{no}(t)$ along a mesh cycle. Note that if back-side contact occurs in point A, the difference between the two stiffness value (A compared with B) is almost equivalent to the peak to peak value. This effect cannot be neglected for an accurate dynamic simulation.

According to the previous consideration the equation of motion defined in (3.2.5) becomes:

$$m_e\ddot{x}(t) + c(\dot{x}(t) - \dot{e}(t)) + k_d(t) f_1(x(t) - e(t)) + k_{no}(t) f_2(x(t) - e(t)) = T_g(t) \qquad (3.2.33)$$

where f_1 and f_2 depends on the selected smoothing function (see relative sections).

3.3 Normalization

A dimensionless form of equation (3.2.5) is obtained by letting:

$$\omega_n = \sqrt{\frac{k_0}{m_e}};\ \ \zeta = \frac{c}{2m_e\omega_n};\ \ \tau = \omega_n t;\ \ \bar{T}_g = \frac{T_g}{bm_e\omega_n^2};\ \ \bar{x} = \frac{x}{b};\ \ \bar{e} = \frac{e}{b}$$

$$\bar{f}\left(\frac{x(\tau)-e(\tau)}{b}\right) = \bar{f}\left(\bar{x}(\tau)-\bar{e}(\tau)\right) = \begin{cases} \bar{x}(\tau)-\bar{e}(\tau)-1 & \bar{x}(\tau)-\bar{e}(\tau) \geq 1 \\ 0 & \left|\bar{x}(\tau)-\bar{e}(\tau)\right| \leq 1 \\ \bar{x}(\tau)-\bar{e}(\tau)+1 & \bar{x}(\tau)-\bar{e}(\tau) \leq -1 \end{cases}; \tag{3.3.1}$$

and:

$$\bar{k}_i = \frac{k_i}{m_e\omega_n^2};\qquad \bar{k}(t) = 1+\sum\nolimits_i \bar{k}_i \cos\left(i\frac{\omega_m}{\omega_n}\tau - \varphi_i\right);$$

$$\bar{E}_j = \frac{E_j}{b}\ ;\qquad \bar{e}(\tau) = \sum\nolimits_j \bar{E}_j \cos\left(j\frac{\omega_m}{Z_1Z_2\omega_n}\tau - \gamma_j\right) \tag{3.3.2}$$

Equation (3.2.5) assumes the following form:

$$\bar{x}''(\tau) + 2\zeta(\bar{x}'(\tau)-\bar{e}'(\tau)) + \bar{k}(\tau)\bar{f}(\bar{x}(\tau)-\bar{e}(\tau)) = \bar{T}_g \tag{3.3.3}$$

where $(\cdot)' = d(\cdot)/d\tau$.

Using smoothing techniques, the normalized backlash functions become:

$$\bar{f}(\tau) = \bar{f}_1(\tau) + \bar{f}_2(\tau) = \left(\bar{x}(\tau)-\bar{e}(\tau)\right) - \frac{1}{\pi}\left\{\left(\bar{x}(\tau)-\bar{e}(\tau)+1\right)\arctan\left[\alpha\left(\bar{x}(\tau)-\bar{e}(\tau)+1\right)\right] - \left(\bar{x}(\tau)-\bar{e}(\tau)-1\right)\arctan\left[\alpha\left(\bar{x}(\tau)-\bar{e}(\tau)-1\right)\right]\right\} \tag{3.3.4}$$

$$\bar{f}(\tau) = \bar{f}_1(\tau) + \bar{f}_2(\tau) = \frac{1}{2}\left[(x(t)-e(t)-b)\left\{1+\tanh[\alpha(x(t)-e(t)-b)]\right\}\right] + \frac{1}{2}\left[(x(t)-e(t)+b)\left\{1+\tanh[-\alpha(x(t)-e(t)+b)]\right\}\right] \tag{3.3.5}$$

The back-side effect can be considered with the following equations:

$$\begin{aligned} \bar{k}_{d,i} &= \frac{k_{d,i}}{m_e \omega_n^2}; \qquad \bar{k}_d(t) = 1 + \sum\nolimits_i \bar{k}_i \cos\left(i \frac{\omega_m}{\omega_n} \tau - \varphi_i \right); \\ \bar{k}_{no,i} &= \frac{k_{no,i}}{m_e \omega_n^2}; \qquad \bar{k}_{no}(t) = 1 + \sum\nolimits_i \bar{k}_i \cos\left(i \frac{\omega_m}{\omega_n} \tau - \varphi_i + \frac{1}{2 r_{b1}} s_{vane} \right); \end{aligned} \tag{3.3.6}$$

Equation (3.2.33) assumes the following form:

$$\bar{x}''(\tau) + 2\zeta(\bar{x}'(\tau) - \bar{e}'(\tau)) + \bar{k}_d(\tau) \bar{f}_1(\bar{x}(\tau) - \bar{e}(\tau)) + \bar{k}_{no}(\tau) \bar{f}_2(\bar{x}(\tau) - \bar{e}(\tau)) = \bar{T}_g \tag{3.3.7}$$

Note that in the following chapter an important role will be played be the parameter ω_n. This value will be referred as the natural frequency of the system described by equation (3.3.3) or (3.3.7). In effect it corresponds to the circular frequency of the relative the time-invariant linearized system.

3.4 Perturbation solution

Neglecting damping, backlash function, back-side contact effect and the transmitted load and introducing equation (3.2.25) into equation (3.2.5) yields to:

$$\ddot{x} + \left(\tilde{k}_0 + \sum_{i=1}^{+\infty} \tilde{k}_i \cos(i\omega_m t + \varphi_i \right) x = 0 \tag{3.4.1}$$

Where $\tilde{k}_i = k_i / m_e$.

Equation (3.4.1) is a second order differential equation with time depending coefficients, no exact closed form solutions are available. In this section the method of multiple scale is used in order to obtain an approximate solution, which furnishes instability regions of the system. The solution is expanded in power series of a small parameter ε; moreover, multiple time scales are introduced in order to consider fast and slow time variations (Nayfeh and Mook, 1979). Following the procedure described by Nayfeh and Mook (1979) let introduce a set of new independent variable T_i (fast and slow scales) is introduced:

$$T_0 = t; \;\; T_1 = \varepsilon t; \;\; T_2 = \varepsilon^2 t \tag{3.4.2}$$

The derivatives with respect to *t* become:

$$\begin{aligned}\frac{d}{dt} &= D_0 + \varepsilon D_1 + \varepsilon^2 D_2 \\ \frac{d^2}{dt^2} &= D_0{}^2 + 2\varepsilon D_0 D_1 + \varepsilon^2 (D_1{}^2 + 2D_0 D_2)\end{aligned} \tag{3.4.3}$$

where D_i are partial derivatives respect to T_i.

Let us expand now the solution x as power series of ε:

$$x(t,\varepsilon) = x_0(T_0, T_1, T_2) + \varepsilon x_1(T_0, T_1, T_2) + \varepsilon^2 x_2(T_0, T_1, T_2) + \varepsilon^3 x_3(T_0, T_1, T_2) + O(\varepsilon^3) \tag{3.4.4}$$

substituting equation (3.4.3) and (3.4.4) into equation (3.4.1), neglecting φ_i with i=1,..,4, yields to:

$$D_0{}^2 x_0 + \tilde{k}_0 x_0 = 0 \tag{3.4.5}$$

$$D_0{}^2 x_1 + \tilde{k}_0 x_1 = -2D_0 D_1 x_0 - P x_0 \tag{3.4.6}$$

$$D_0{}^2 x_2 + \tilde{k}_0 x_2 = -2D_0 D_1 x_1 - P x_1 - (D_1{}^2 + 2D_0 D_2) x_0 \tag{3.4.7}$$

$$D_0{}^2 x_3 + \tilde{k}_0 x_3 = -2D_0 D_1 x_2 - P x_2 - (D_1{}^2 + 2D_0 D_2) x_1 - (2D_0 D_3 + 2D_1 D_2) x_0 \tag{3.4.8}$$

where P is:

$$P = \cos(\omega_m t) + \alpha \cos(2\omega_m t) + \beta \cos(3\omega_m t) + \gamma \cos(4\omega_m t) \tag{3.4.9}$$

with:

$$\varepsilon = \tilde{k}_1;\ \alpha = \frac{\tilde{k}_2}{\tilde{k}_1};\ \beta = \frac{\tilde{k}_3}{\tilde{k}_1};\ \gamma = \frac{\tilde{k}_4}{\tilde{k}_1} \tag{3.4.10}$$

Equations (3.4.5), (3.4.6), (3.4.7) and (3.4.8) are obtained equating the coefficients of ε^0, ε^1, ε^2 and ε^3 to zero. The solution of equation (3.4.5) is:

$$x_0(T_0, T_1, T_2) = A(T_1, T_2) e^{j\omega_n T_0} + \overline{A}(T_1, T_2) e^{-j\omega_n T_0} \tag{3.4.11}$$

where: $\tilde{k}_0 = \omega_n^2$, $\overline{\mathrm{A}}$ is the complex conjugate of A. Inserting equation (3.4.11) into (3.4.6) we have:

$$\begin{aligned}&D_0^2 x_1 + \tilde{k}_0 x_1 = -2jD_1 A e^{j\omega_n T_0} \\ &-\frac{1}{2}(A e^{j(\omega_m+\omega_n)T_0} + A e^{j(2\omega_m+\omega_n)T_0} + A e^{j(3\omega_m+\omega_n)T_0} + A e^{j(4\omega_m+\omega_n)T_0} + \\ &\overline{A} e^{j(\omega_m-\omega_n)T_0} + \overline{A} e^{j(2\omega_m-\omega_n)T_0} + \overline{A} e^{j(3\omega_m-\omega_n)T_0} + \overline{A} e^{j(4\omega_m-\omega_n)T_0}) + C.C.\end{aligned} \tag{3.4.12}$$

where *C.C.* means complex conjugates terms.

At ε^1 level every harmonic generates two forcing terms whose frequencies are ($n\omega_m$–ω_n) and ($n\omega_m$+ω_n).

The previous consideration allows to consider each harmonic contribution separately.

Secular terms:

In equation (3.4.12) the following secular term is identified:

$$-2j\omega_n D_1 A e^{j\omega_n T_0} \tag{3.4.13}$$

such term gives rise to spurious divergent solutions and must be removed. Depending on the value of ω_n four cases are possible:

$\omega_m - \omega_n = \omega_n$ $\rightarrow \omega_m = 2\omega_n$;

$2\omega_m - \omega_n = \omega_n$ $\rightarrow \omega_m = \omega_n$;

$3\omega_m - \omega_n = \omega_n$ $\rightarrow \omega_m = \frac{2}{3}\omega_n$;

$4\omega_m - \omega_n = \omega_n$ $\rightarrow \omega_m = \frac{\omega_n}{2}$;

Case 1

Eliminating secular terms gives:

$$-2j\omega_n D_1 A e^{j\omega_n T_0} - \frac{1}{2}\overline{A} e^{j(\omega_m - \omega_n)T_0} = 0 \tag{3.4.14}$$

Assuming $\omega_m = \omega_n + \varepsilon\sigma$, where σ is a detuning parameter, and $D_1 A = A'$ and considering that $T_1 = \varepsilon T_0$, equation (3.4.14) becomes:

$$-2j\omega_n A' - \frac{1}{2}\overline{A} e^{j\sigma T_1} = 0 \tag{3.4.15}$$

Since A is a complex number depending on T_1, it can be express as follow:

$$A(T_1) = B(T_1) e^{j\frac{\sigma}{2}T_1} \tag{3.4.16}$$

where $B(T_1)$ is complex function, equation (3.4.15) becomes:

$$-2j\omega_n B' + \omega_n \sigma B - \frac{\overline{B}}{2} = 0 \tag{3.4.17}$$

Equation (3.4.17) can be decomposed in its real and imaginary part:

$$\begin{cases} 2\omega_n B_I' + \omega_n \sigma B_R - \frac{B_R}{2} = 0 \\ -2\omega_n B_R' + \omega_n \sigma B_I + \frac{B_I}{2} = 0 \end{cases} \tag{3.4.18}$$

where $B = B_I + jB_R$.

Assuming that $B(T_1) = \left(G_R(T_1) + jG_I(T_1)\right) e^{\xi T_1}$ we can write equation (3.4.18) in a matrix form:

$$\xi\begin{bmatrix} 0 & 2\omega_n \\ -2\omega_n & 0 \end{bmatrix}\begin{bmatrix} G_R \\ G_I \end{bmatrix}+\begin{bmatrix} \omega_n\sigma-\frac{1}{2} & 0 \\ 0 & \omega_n\sigma+\frac{1}{2} \end{bmatrix}\begin{bmatrix} G_R \\ G_I \end{bmatrix}=\begin{bmatrix} 0 \\ 0 \end{bmatrix} \tag{3.4.19}$$

System (3.4.18) and (3.4.19) are equivalent and the solution can be found imposing:

$$\left(\xi\begin{bmatrix} 0 & 2\omega_n \\ -2\omega_n & 0 \end{bmatrix}+\begin{bmatrix} \omega_n\sigma-\frac{1}{2} & 0 \\ 0 & \omega_n\sigma+\frac{1}{2} \end{bmatrix}\right)\begin{bmatrix} G_R \\ G_I \end{bmatrix}=\begin{bmatrix} 0 \\ 0 \end{bmatrix} \tag{3.4.20}$$

this equation has non trivial solution if the determinant of its matrix is equal to zero, which means:

$$\xi^2=\frac{1}{4\omega_n{}^2}\left(\frac{1}{4}-\omega_n{}^2\sigma^2\right) \tag{3.4.21}$$

Instability occurs when $\xi^2 > 0$, i.e. when:

$$\left(\frac{1}{4}-\omega_n{}^2\sigma^2\right)>0 \tag{3.4.22}$$

Remembering that $\varepsilon=d_1$ and substituting $\sigma=\frac{\omega_m-2\omega_n}{\varepsilon}$ into (3.4.22) yields:

$$2\sqrt{\widetilde{k}_0}-\frac{\widetilde{k}_1}{2\sqrt{\widetilde{k}_0}}<\omega_m<2\sqrt{\widetilde{k}_0}+\frac{\widetilde{k}_1}{2\sqrt{\widetilde{k}_0}} \tag{3.4.23}$$

The same approach is applied to the cases 2, 3, and 4.

Case 2

In this case the detuning parameter σ is:

$$\sigma=\frac{2\omega_m-2\omega_n}{\varepsilon} \tag{3.4.24}$$

which leads to the following instability region:

$$\sqrt{\widetilde{k}_0}-\frac{\widetilde{k}_1}{4\sqrt{\widetilde{k}_0}}<\omega_m<\sqrt{\widetilde{k}_0}+\frac{\widetilde{k}_1}{4\sqrt{\widetilde{k}_0}} \tag{3.4.25}$$

Case 3

In this case the detuning parameter σ is:

$$\sigma=\frac{3\omega_m-2\omega_n}{\varepsilon} \tag{3.4.26}$$

which leads to the following instability region:

$$\frac{2}{3}\sqrt{\widetilde{k}_0}-\frac{\widetilde{k}_1}{6\sqrt{\widetilde{k}_0}}<\omega_m<\frac{2}{3}\sqrt{\widetilde{k}_0}+\frac{\widetilde{k}_1}{6\sqrt{\widetilde{k}_0}} \tag{3.4.27}$$

Case 4

In this case the detuning parameter σ is:

$$\sigma=\frac{2\omega_m-\omega_n}{\varepsilon} \tag{3.4.28}$$

which leads to the following instability region:

$$\frac{1}{2}\sqrt{\widetilde{k}_0}-\frac{\widetilde{k}_1}{8\sqrt{\widetilde{k}_0}}<\omega_m<\frac{1}{2}\sqrt{\widetilde{k}_0}+\frac{\widetilde{k}_1}{8\sqrt{\widetilde{k}_0}} \tag{3.4.29}$$

Case study

The previous perturbation technique is applied to the case study 1 presented in Table 2. By means of the described finite element analysis the following results are obtained:

Component	Stiffness component [N/m]
$\widetilde{k}_0$	9.9605 10^8
$\widetilde{k}_1$	1.7820 10^8
$\widetilde{k}_2$	3.4220 10^7
$\widetilde{k}_3$	3.9132 10^7
$\widetilde{k}_4$	1.8414 10^7

Table 26: Stiffness component of case study 1 used for the perturbation method.

Table 27 shows the instability regions calculated for case study 1, using the stiffness values presented in Table 26:

Case	Instability region [rad/s]
1	$60297<\omega_m<65943$
2	$31289<\omega_m<31831$
3	$20833<\omega_m<21246$
4	$15707<\omega_m<15853$

Table 27: Instability regions expressed on meshing frequency ω_m.

Considering that $\Omega_1=60\omega_m/\left(2\pi Z_1\right)$, the instability regions are reported in Table 28 in terms of the driver gear velocity Ω_1.

Case	Instability region [rpm]	$\Delta\Omega_1$ [rpm]
1	$20564 < \Omega_1 < 22489$	1925
2	$10671 < \Omega_1 < 10855$	184
3	$7105 < \Omega_1 < 7246$	140
4	$5356 < \Omega_1 < 5406$	49

Table 28: Instability regions expressed on driver gear velocity Ω_1.

Table 28 shows that four instability regions occur at about 21500, 10700, 7100 and 5300 rpm. Such high values can be justified by the assumption of neglecting shafts and bearings effects on the meshing stiffness.

3.5 Numerical solution

A numerical solution of equations (3.3.3) and (3.3.7) can be obtained by the use of different numerical integration techniques. Since both equations are differential equations of the second order, it is convenient to transform them into a system of two equations of the first order:

$$\begin{cases} \dot{v}_1 = v_2 \\ \dot{v}_2 = \ddot{\bar{x}} \end{cases} \tag{3.5.1}$$

with the following initial condition:

$$\begin{cases} \dot{v}_1(0) = \dot{v}_{1,0} \\ \dot{v}_2(0) = \dot{v}_{2,0} \end{cases} \tag{3.5.2}$$

Once equations are in the form of equation (3.5.1), a direct numerical integration method (i.e. an adaptive step-size Runge-Kutta (Press, 1992)), is first considered for the piecewise linear system (equations (3.3.3)). In the case of smoothing approach (equations (3.3.7)), in addition to the Runge-Kutta method, an adaptive step-size Gear algorithms is used (IMSL®, 2003). In particular, the Gear approach is used because it is suitable for stiff problems (IMSL®, 2003). Since each numerical approach is able to solve equation (3.3.3) and (3.3.7) for a given value of the pinion speed, three important plots will be used in the following:

1. Time history and spectrum: shows the solution of the equation with respect to normalized time τ and allows to analyze the amount of relative vibration of the gears. An example of time history is reported in Figure 97.

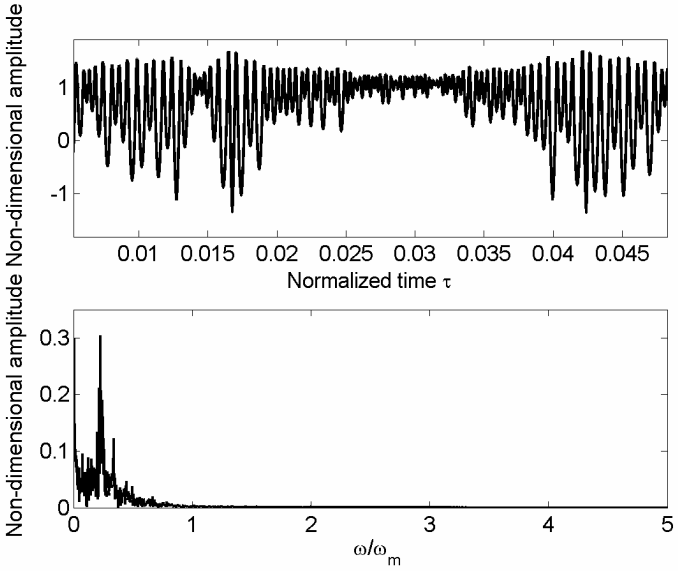

Figure 97: Example of time history.

In this example the value of the non-dimensional amplitude oscillates between 1 and -1 and clarify that double side contact is occurring.

2. Bifurcation diagrams: shows dynamic scenario of different solutions with respect to pinion speed (the pinion speed is usually referred as ω_m/ω_n). In this case, a time history is calculated for each value of the pinion speed. Each time history is sampled with frequency equal to the relative mesh frequency ω_m for an arbitrary number of mesh cycles. The amplitude of the samples is stored and plotted. Figure 98 shows an example of bifurcation diagram. For a given value of ω_m/ω_n two cases take place in this example: the solution has frequency equal to the mesh frequency ω_m , the solution has frequency equal to one half of the mesh frequency. The bifurcation diagram presents one dot for a given value of ω_m/ω_n for the first case (underlined by blue line), two dots for a given value of ω_m/ω_n for the second case (underlined by red line). Point A represents the point at which the change between the two different behavior occurs. Such point is a period doubling (PD) bifurcation point.

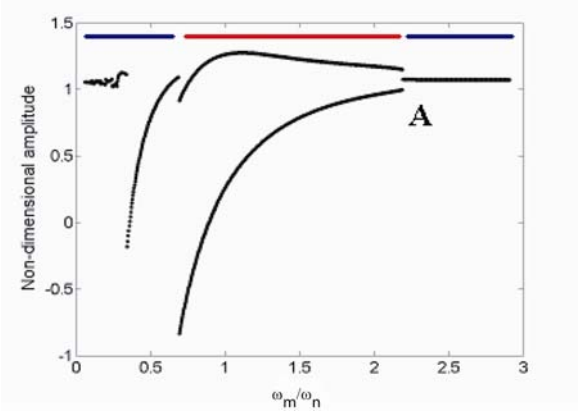

Figure 98: Example of bifurcation diagram.

Note that the points in the diagram does not represents maximum or minimum value of the relative time history.

3. Semi-Amplitude/Frequency diagram: shows semi-amplitude of different solutions with respect to pinion speed (the pinion speed is usually referred as ω_m/ω_n). In this case, the semi-amplitude (maximum minus minimum divided by two) of the time history is calculated for each value of the pinion speed. This semi-amplitude is plotted with respect to pinion speed. Typical results of the semi-amplitude/frequency diagram (see Figure 99) are the dynamics behavior of the gears system at the resonant, parametric and super harmonic frequencies (Nayfeh, 1979).

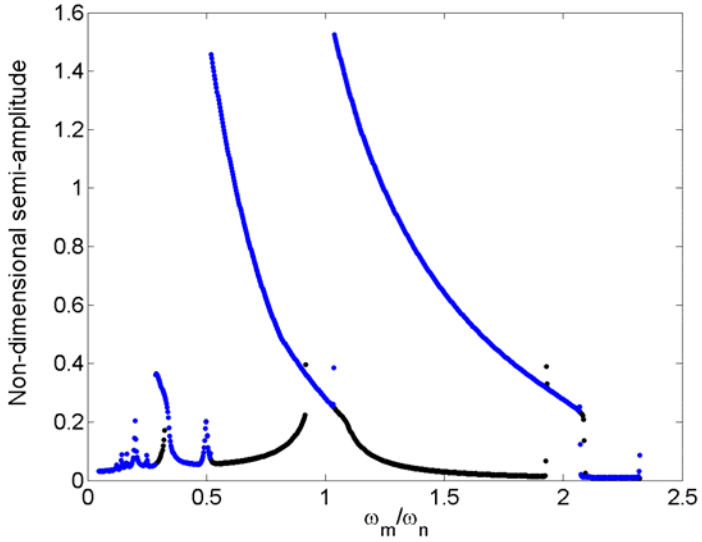

Figure 99: Example of semi-amplitude/frequency diagram.

It is important to clarify that all previous diagrams (bifurcation and semi-amplitude/frequency diagrams) are calculated considering the steady state solution. This means that each values is evaluated neglecting the transient of the dynamics responses.

Since the integrated equations can take into account many non-linear phenomena, the steady state response depends on initial conditions (3.5.2). For this reason when the analysis is performed over a width range of the pinion speed, the following statements must be specified:

1. The speed range of the analysis;
2. The direction of the analysis: it is possible to perform a speed up (SUA) or speed down analysis (SDA);
3. The initial condition for the first analyzed speed.

The bifurcation and semi-amplitude/frequency diagrams are carried out as follows: at the end of the analysis of the system response at a given regime (pinion speed) the final state is recorded; then the rotation speed is changed and a new simulation is carried out using as initial conditions the state of the previous computation. The purpose is to follow as well as possible a solution, in the case of coexisting orbits; if the change of speed is small one suppose that the new orbit is close to the orbit of the previous speed range; therefore, the system response is easily attracted from such orbit.

The orbit is defined as the phase space representation of the solution of ODE system (ordinary differential equations system).

In the following, the accuracy of the direct numerical integration of the non-smooth system is checked by means of comparisons with the existent literature. Subsequently the accuracy of smoothing technique is also proved by comparison with the previous, and the efficiency of the integration algorithms is evaluated.

3.5.1 Validation of Runge-Kutta approach

Let us consider the trilinear system represented by the elastic stiffness presented in Figure 100.

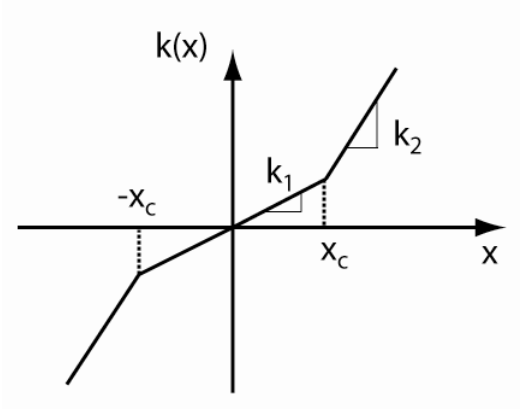

Figure 100: Piecewise linear stiffness (Natsiavas, 1989).

Such a system was deeply analyzed in (Natsiavas, 1989) by means of an analytical procedure. The equation of motion of such system are:

$$m\ddot{x}(t) + c\dot{x}(t) + k(x) = f\sin(\omega t) \tag{3.5.3}$$

where:

$$k(x) = \begin{cases} k_1 x & |x| \le x_c \\ k_2 x + (k_1 - k_2)x_c \operatorname{sgn}(x), & |x| > x_c \end{cases} \tag{3.5.4}$$

Note that in such system the boundary x_c plays the role of clearance b present in equation (3.2.8).

The equation (3.5.3) is now transformed in a nondimensional form $y(t) = x(t)/x_c$

$$\begin{aligned} &\ddot{y}_1 + 2\zeta\tilde{\omega}\dot{y}_1 + \omega_1^2 y_1 = f_0 \sin(\omega t) && |x| \le x_c \\ &\ddot{y}_2 + 2\zeta\tilde{\omega}\dot{y}_2 + \omega_2^2 y_2 = f_0 \sin(\omega t) + \omega_2^2 - \omega_1^2 && |x| > x_c \end{aligned} \tag{3.5.5}$$

where $f_0 = f/(mx_c)$ and $P = f/(m\omega^2 x_c)$.

Simulations are performed by linearyzing equation (3.5.3) or integrating it directly without smoothing functions (non-smooth approach). The following parameters are used in simulations: $\zeta = 0.05$; $k_2 = 4\,k_1$; $\tilde{\omega} = (\omega_1 + \omega_2)/2$; $P = 0.5$.

System (3.5.5) is analyzed with a direct integration code developed for solving systems (3.3.3) and (3.3.7). In Figure 8 results of the present model are compared with the Natsiavas's solution (Natsiavas, 1989). In the figure both nonlinear and linarized models, integrated numerically, are presented. The linear model is accurate below y=1, i.e. below the boundary;

the solution is completely wrong. The direct numerical integration is very close to the solution obtained in (Natsiavas, 1989).

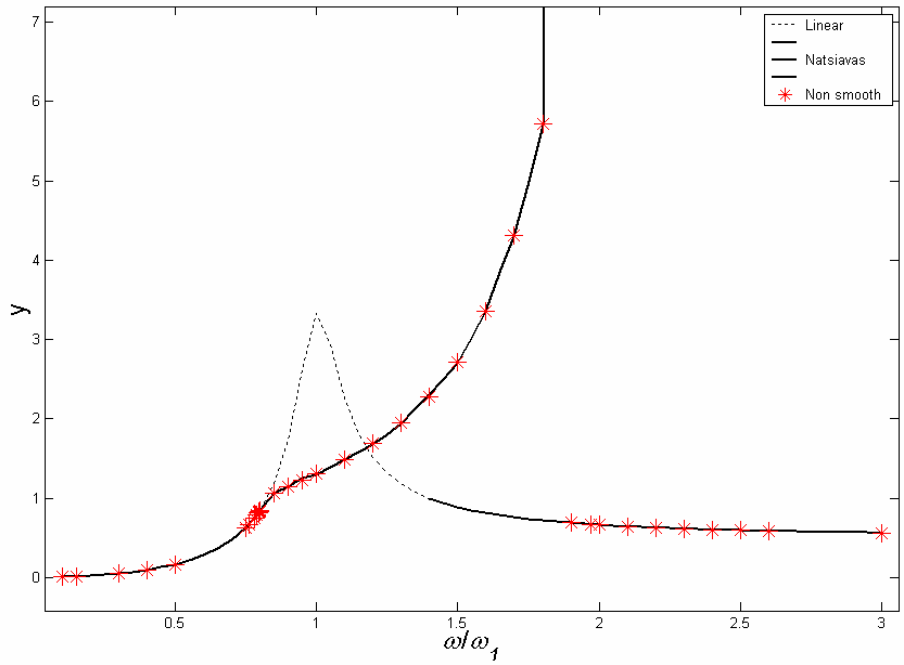

Figure 101: Resonance of system (16): (--) linearized model; (—)(Natsiavas, 1989); (-∗-) present model, direct integration.

3.5.2 Validation of Runge-Kutta and Gear approaches for smoothing system

Let us consider now equations (3.3.3) and (3.3.7): direct integration and smoothing technique are applied in order to check the accuracy of the latter one. Comparisons are carried out through bifurcation diagrams of the Poincaré maps (Nayfeh and Mook, 1979) (Jordan and Smith, 1999). The use of the bifurcation diagram is computationally heavy, but it allows a check of accuracy on a wide parameters range.

The case study is the case study 1 described in Table 2. No profile errors are present, therefore, $e(t)$=0.

Bifurcation diagrams are obtained by varying the excitation frequency (mesh frequency of the gear pair); two cases are considered: increasing frequency and decreasing frequency.

Three approaches are used: direct integration of the non-smooth system; smoothed system integrated by an adaptive step-size Runge-Kutta algorithm; smoothed system integrated by an adaptive step-size Gear algorithm. All methods do not include the back-side effect. Indeed,

even though system (3.3.3) is approximated by a smooth system based on a C^{∞} function given by equation (3.3.7), the new system can be extremely stiff, see e.g. Figure 79 b) and Figure 81 b). The smoothed system is as stiff as the shape parameter α increases.

Figure 102 shows the bifurcation diagram; all methods give almost the same results. Note that the Gear solution completely overlap the Runge-Kutta solution.

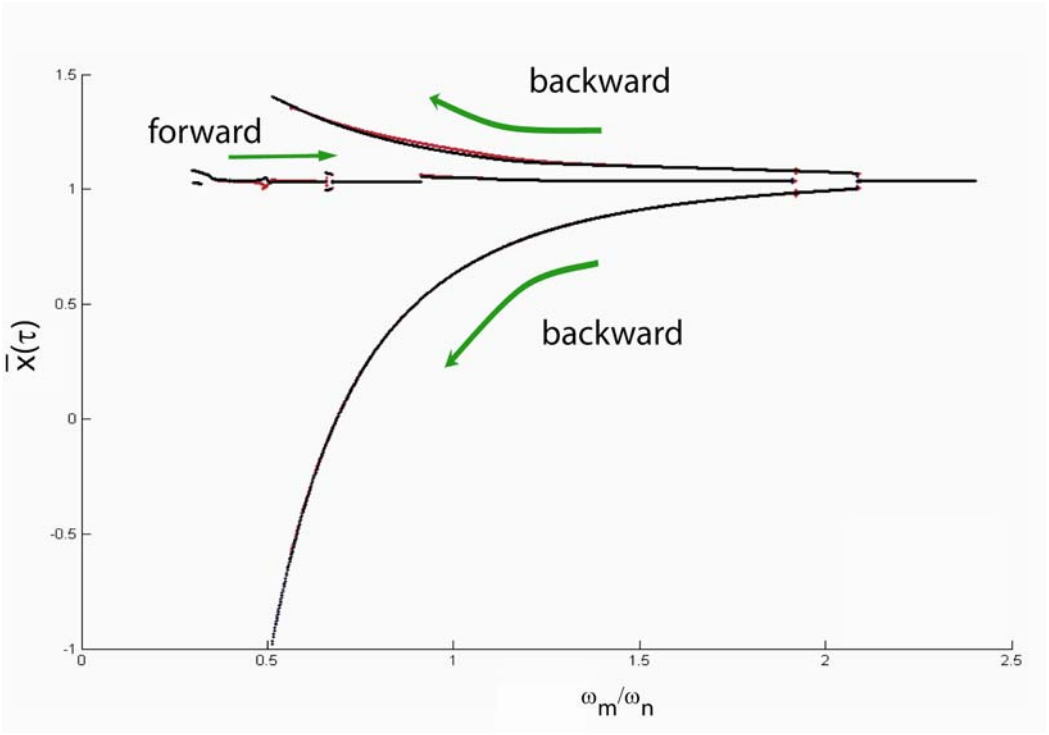

Figure 102: Comparison of numerical integrator using bifurcation diagram: (blue) smoothing, Runge-Kutta integration algorithm; (red) smoothing, Gear integration algorithm; (black) non-smooth system, direct integration.

3.5.3 Validation with experiments

In order to investigate the accuracy of the model with respect to a real system, a comparison with some experimental results is also performed. Kahraman (1997) presented a number of experiments on a physical system with clearance combining parametric and external forcing excitation (Kahraman and Blankenship, 1997). One of the tests concerned a spur gear set with the following geometrical and physical parameters:

	Pinion	**Gear**
Teeth number	50	50
Module [mm]	3	3
Pressure angle [Deg]	20	20
Base diameter [mm]	140.95	140.95
Tooth thickness at pitch diameter [mm]	4.64	4.64
Outer diameter [mm]	156	156
Root diameter [mm]	140.68	140.68
Face width [mm]	20	20
Mass [kg]	2.5161	2.5161
Inertia [kg m^2]	0.0074	0.0074
Young's modulus [MPa]	206000	206000
Poisson's coefficient	0.3	0.3
Center distance [mm]	150	
Backlash [mm]	0.1447	
Backlash ($2b$) on line of action [mm]	0.136	
Backside stiffness phase [rad]	1.594926	
Transmission ratio	1	
Contact ratio	1.75467	
Profile modifications	None	

Table 29: Geometrical data of Kahraman's spur gear set (courtesy of Prof. Kahraman).

The simulation considers no manufacturing error $e(t)$=0 and an approximation for the stiffness function with 6 harmonics. The following values for the normalized stiffness function are obtained:

Normalized stiffness component	**Value**
$\overline{k}_{d,1}$	5.988751 10^{-2}
$\overline{k}_{d,2}$	4.214662 10^{-2}
$\overline{k}_{d,3}$	3.320816 10^{-2}
$\overline{k}_{d,4}$	2.384664 10^{-2}
$\overline{k}_{d,5}$	1.76215 10^{-2}
$\overline{k}_{d,6}$	1.219961 10^{-2}

Phase	**Value [rad]**
φ_1	-3.135189
φ_2	-3.124241
φ_3	-3.111668
φ_4	-3.095101
φ_5	-3.083519
φ_6	-3.082149

Table 30: Stiffness component for the Kahraman case study.

A damping value of $\zeta = 0.01$ and an external torque T_{g1} of 340 Nm is used.

According to finite element results, the natural frequency of the system ω_n results to be equal to 1.983463 10^4 rad/s. Using 15 positions in a mesh cycle the peak to peak value of the mesh stiffness is 6.24172 10^7 N/m and the peak to peak of the static transmission error is 5.34868 μm. The dynamic simulation considers the adaptive step-size Gear algorithm and the hyperbolic tangent smoothing backlash function with an initial position equal to $v(0) = 1.0001$ and an initial speed of $\dot{v}(0) = 0.00001$. The integration tolerance is 10^{-8}.

A semi-amplitude/frequency plot is used to compare the experimental data and the results from the numerical simulation. Figure 103 shows a good agreement between the numerical results and the experimental data.

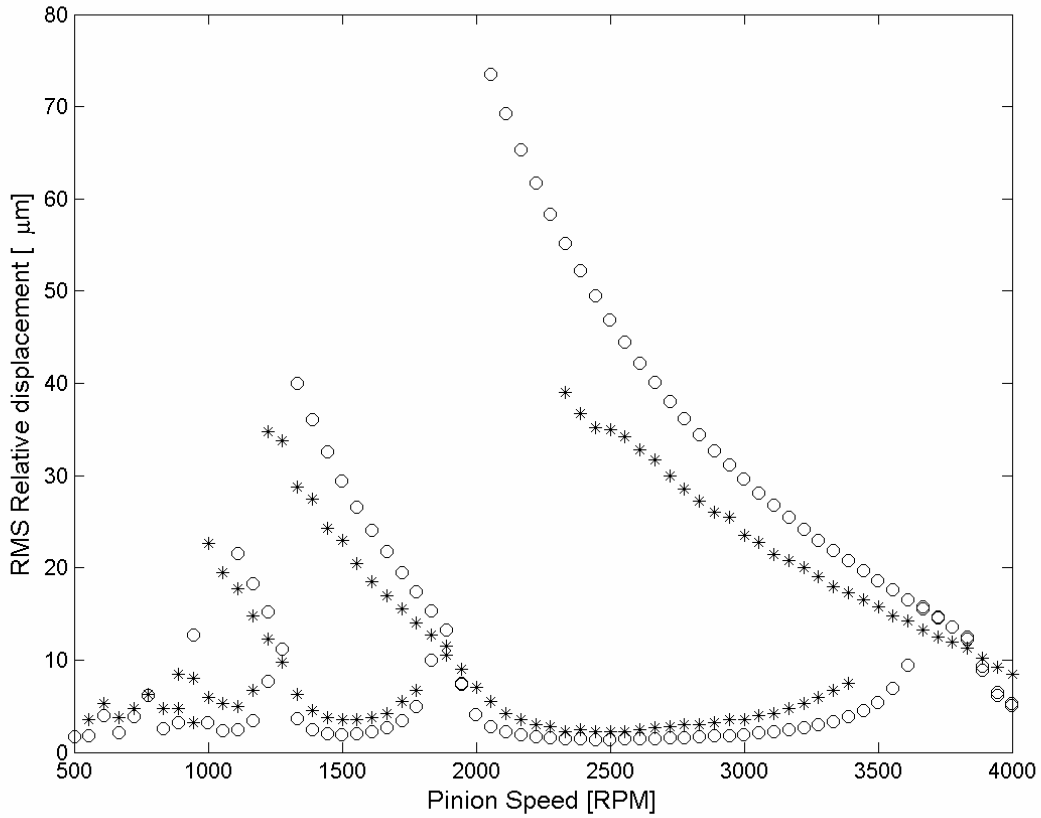

Figure 103: Comparison between numerical simulation and experimental data: (○)Numerical simulation; (*) Kahraman's experimental data (Kahraman and Blankenship, 1997).

3.5.4 Choice of the numerical integrator

Since the previous sections show good behaviors of all numerical techniques, the adopted method has been chosen by the following consideration:

1. The Gear algorithm is preferable because it is suitable for stiff problems (IMSL®, 2003) and results are more reliable;
2. Non-smoothing methods are time consuming with respect to smoothing techniques;
3. Hyperbolic tangent function is time saving with respect to arc-tangent approach;

For these reason the Gear algorithm with the hyperbolic tangent smoothing function will be used in the following. The shape parameter is always set to 10^8.

3.6 Case studies

In this section some case studies are analyzed in order to understand the effect of some parameters on the dynamic behavior of a spur gear pairs.

3.6.1 Case study 1: Spur gear pair without profile modification

The first analysis is performed on the case study 1 (see previous sections). Table 31 shows the geometrical and physical parameters:

Data	**Pinion**	**Gear**
Number of teeth	28	43
Module [mm]	3	3
Pressure angle [Deg]	20	20
Base radius [mm]	39.467	60.610
Theoretical pitch radius [mm]	42	64.5
Thickness on theoretical pitch circle [mm]	6.1151	6.7128
Addendum modification [mm]	1.927	2.748
Face width [mm]	27	22.5
Hob tip radius [mm]	0.9	0.9
Outer diameter [mm]	93.1	139.7
Root diameter [mm]	79.1	126.2
Inner diameter [mm]	40	40
Mass [kg]	0.71681	1.9823
Inertia [kg m^2]	0.0008076	0.0047762
Young's modulus [MPa]	206000	206000
Poisson's coefficient	0.3	0.3
Center distance [mm]	111	
Backlash [mm]	0.3461	
Backlash ($2b$) on line of action [mm]	0.312	
Backside stiffness phase [rad]	1.594232	
Transmission ratio	0.6511	
Contact ratio	1.28565	
Profile modification	None	

Table 31: Complete geometrical data of case study 1 (courtesy of CNH Case New Holland).

The simulation consider a damping value of $\zeta = 0.01$, an external torque T_{g1} of 470 Nm and no manufacturing error $e(t)$=0. The static transmission error is calculated for 15 positions within a mesh cycle, and the approximation for the stiffness function used 7 harmonics.

The evaluated peak to peak value of the mesh stiffness is 1.03906 10^8 N/m, while the peak to peak value of the static transmission error is 11.6457 μm.

The following components for the normalized stiffness function are obtained:

Normalized stiffness component	Value
$\bar{k}_{d,1}$	1.789019 10^{-1}
$\bar{k}_{d,2}$	3.435601 10^{-2}
$\bar{k}_{d,3}$	3.928705 10^{-2}
$\bar{k}_{d,4}$	1.848706 10^{-2}
$\bar{k}_{d,5}$	1.590455 10^{-2}
$\bar{k}_{d,6}$	5.281117 10^{-3}
$\bar{k}_{d,7}$	5.28716 10^{-3}

Phase	Value [rad]
φ_1	-3.074412
φ_2	0.09870295
φ_3	0.1843604
φ_4	-2.739105
φ_5	-2.859687
φ_6	1.135353
φ_7	0.4246241

Table 32: Stiffness components for the case study 1.

According to finite element analysis, the natural frequency of the system ω_n results to be equal to 3.156025 10^4 rad/s.

The dynamic simulation considers the adaptive step-size Gear algorithm and the hyperbolic tangent smoothing backlash function with an initial position equal to $\dot{v}_1(0) = 1.0001$ and an initial speed of $\dot{v}_2(0) = 0.00001$ for the first speed analyzed. The integration tolerance is 10^{-8}.

Figure 104 shows the semi-amplitude/frequency behavior of the spur gear pair for a speed up analysis (SUA) (Figure 104 a)) and a speed down analysis (SDA) (Figure 104 b)).

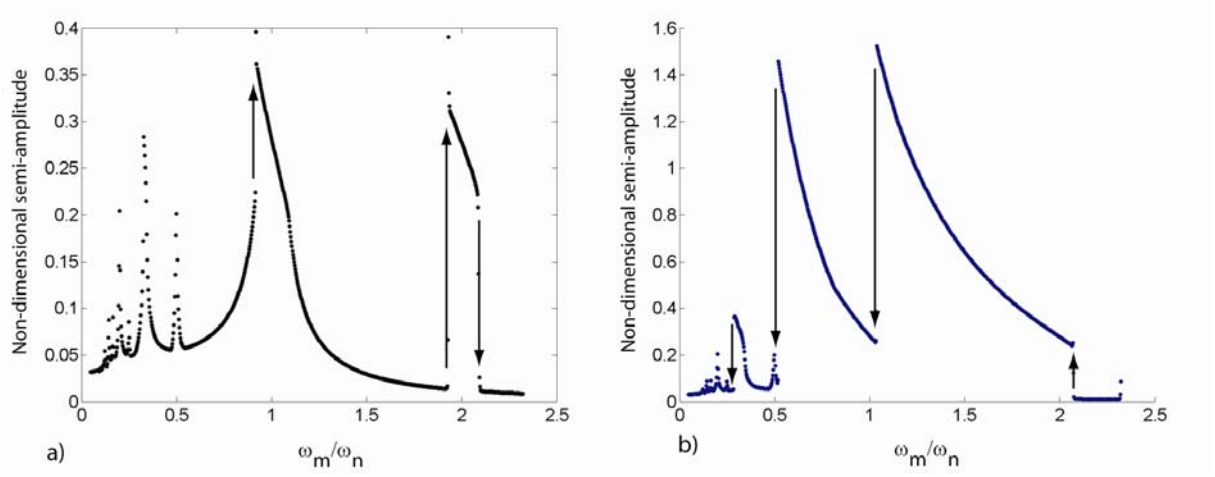

Figure 104: Semi-amplitude/frequency diagram for case study 1: a) SUA analysis (black); b) SDA analysis (blue).

In Figure 105 the previous semi-amplitude/frequency diagrams are overlapped in one complete diagram.

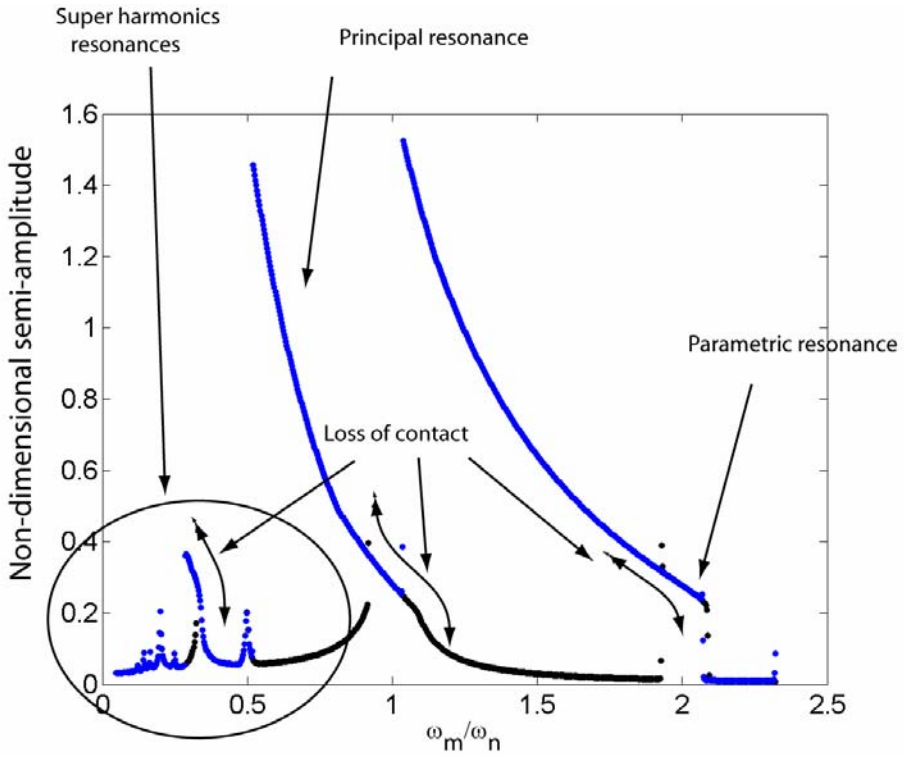

Figure 105: Semi-amplitude/frequency diagram for case study 1: SUA analysis (black); SDA analysis (blue).

The following phenomena are observed:

1. Different dynamic behavior between the SUA and SDA, typical of nonlinear systems;
2. A principal resonance at $\omega_m/\omega_n = 1$;
3. A parametric resonance at $\omega_m/\omega_n = 2$ due to the time variable stiffness;
4. Super harmonics resonances at some frequencies in the range $\omega_m/\omega_n = 0$ - 0.5, due to higher harmonics of the mesh stiffness Fourier expansion and to the nonlinearity;
5. Jumping phenomena at particular resonance frequencies: $\omega_m/\omega_n = 1$ and $\omega_m/\omega_n = 2$ for SUA and $\omega_m/\omega_n = 0.5$, $\omega_m/\omega_n = 1$ and $\omega_m/\omega_n = 2$ for SDA. This typical nonlinear effect results in a sudden change (up or down) of the vibration amplitude while speeding up or speeding down;
6. Softening behavior due to loss of contact at $\omega_m/\omega_n = 0.5$, $\omega_m/\omega_n = 1$ and $\omega_m/\omega_n = 2$. This typical nonlinear effect results in sudden change from the linear behavior with a bending of the semi-amplitude/frequency diagram. Figure 106 clarifies the difference between softening and hardening behavior.

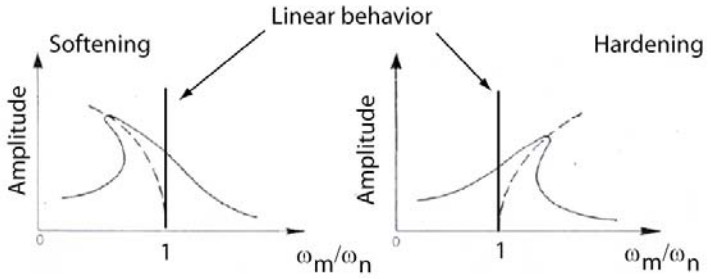

Figure 106: Deviation from linear behavior: softening (left), hardening (right).

Figure 107 shows bifurcation diagrams for SUA and SDA.

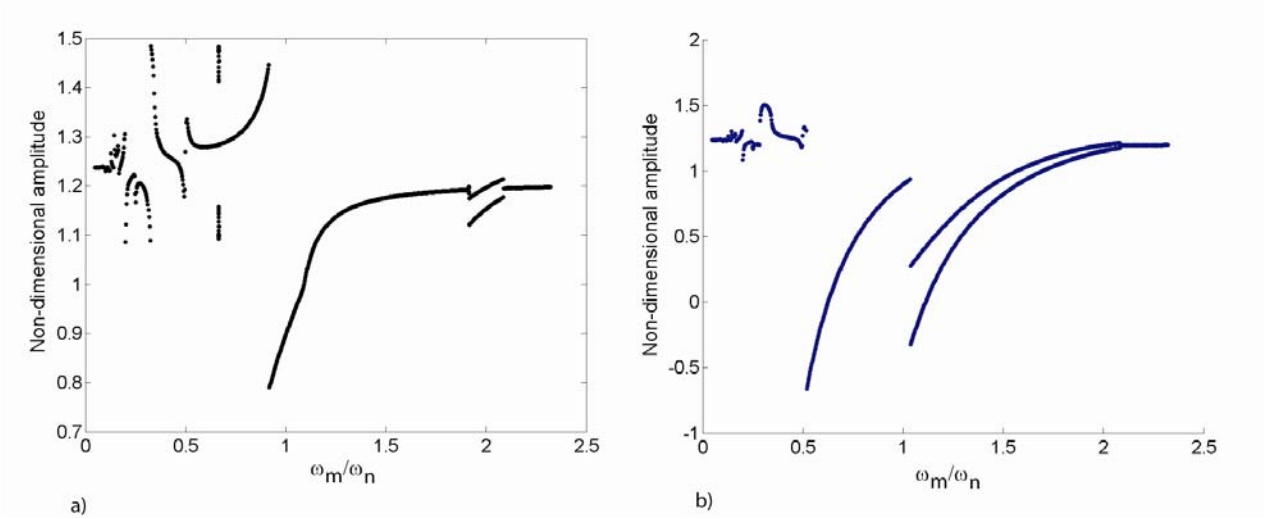

Figure 107: Bifurcation diagram for case study 1: a) SUA analysis (black); b) SDA analysis (blue).

The two diagrams of Figure 107 are overlapped in Figure 108.

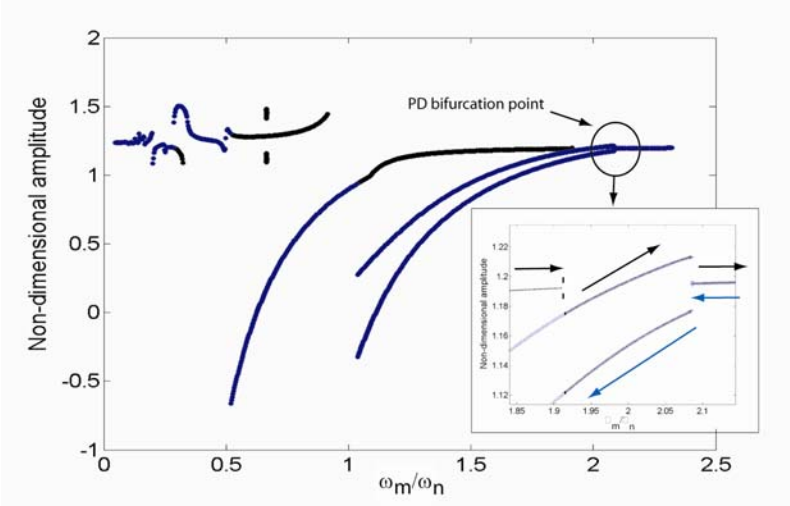

Figure 108: Bifurcation diagram for case study 1: SUA analysis (black); SDA analysis (blue).

Figure 107 and Figure 108 show the presence of a period doubling bifurcation nearby $\omega_m/\omega_n =$ 2, which corresponds to the parametric resonance on the semi-amplitude/frequency diagrams. In order to check the period doubling behavior a time history is plotted for ω_m/ω_n = 2.00072 with $\dot{v}_1(0) = 1.15369$ and $\dot{v}_1(0) = -0.268193$ as initial conditions for the first speed analyzed.

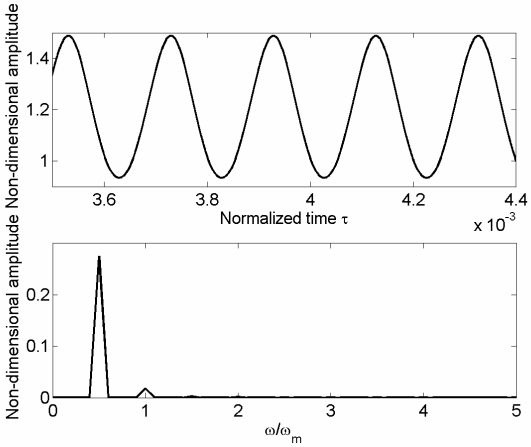

Figure 109: Time history and relative spectrum at ω_m/ω_n = 2.00072 .

The spectrum reflects that in the period doubling frequency range, the steady state response of the system has frequency equal to one half the mesh frequency ω_m.

It is well known that parametrically excited systems undergo to parametric instability and the principal instability region gives rise to 2T response. Here the nonsmoothness of the system influences the bifurcation path, which is generally parabolic for smooth systems. Conversely here a strong jump appears and the bifurcation takes place suddenly.

3.6.2 Case study 2: Spur gear pair with profile modification

The second test is carried out to analyze the effect of profile modifications on the gears dynamics. A new set of gears is considered: case study 2 is equivalent to case study 1 except for the profile modifications described in Table 33:

		Pinion	Gear
Tip relief			
	Type of modification	Linear	Linear
	Roll angle at start of relief [Deg]	30.1569	29.2127
	Magnitude of relief [mm]	0.016	0.018
Root relief			
	Type of modification	Linear	Linear
	Roll angle at start of relief [Deg]	23.4706	25.2079
	Roll angle at end of relief [Deg]	14.4334	20.5764
	Magnitude of relief [mm]	0.016	0.018
Crowning			
	Magnitude [mm]	None	None

Table 33: Profile modifications adopted for case study 2 (courtesy of CNH Case New Holland).

Note that all parameters in Table 33 are calculated according to CNH standard and are designed to improve the static behavior of the gear pair.

The simulation considers a damping value of $\zeta = 0.01$, an external torque T_{g1} of 470 Nm and no manufacturing error $e(t)$=0. The static transmission error is calculated for 15 positions within a mesh cycle, and the approximation for the stiffness function used 7 harmonics. The peak to peak of the mesh stiffness is 3.12098 10^7 N/m while the peak to peak of the static transmission error is 5.10005 μm.

The following components for the normalized stiffness function are obtained (see equation (3.3.6)):

Normalized stiffness component	Value
$\overline{k}_{d,1}$	6.039868 10^{-2}
$\overline{k}_{d,2}$	2.549201 10^{-3}
$\overline{k}_{d,3}$	1.017452 10^{-2}
$\overline{k}_{d,4}$	7.716745 10^{-3}
$\overline{k}_{d,5}$	3.415436 10^{-3}
$\overline{k}_{d,6}$	2.19705 10^{-3}
$\overline{k}_{d,7}$	2.686733 10^{-3}

Phase	Value [rad]
φ_1	-0.02302711
φ_2	-0.9228034
φ_3	3.070796
φ_4	-2.999429
φ_5	-0.8892686
φ_6	0.3613773
φ_7	2.395425

Table 34: Stiffness components for the case study 2.

According to finite element results, the natural frequency of the system ω_n results to be equal to 2.870711 10^4 rad/s. The dynamic simulation considers the adaptive step-size Gear algorithm and the hyperbolic tangent smoothing backlash function with an initial position equal to $\dot{v}_1(0) = 1.0001$ and an initial speed of $\dot{v}_2(0) = 0.00001$ for the first speed analyzed. The integration tolerance is 10^{-8}.

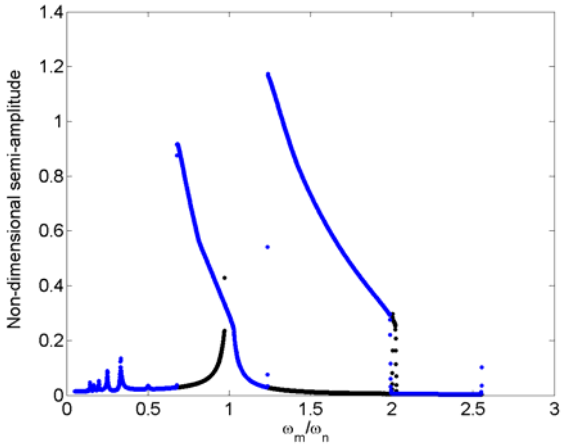

Figure 110: Semi-Amplitude/frequency diagram for case study 2: SUA analysis (black); SDA analysis (blue).

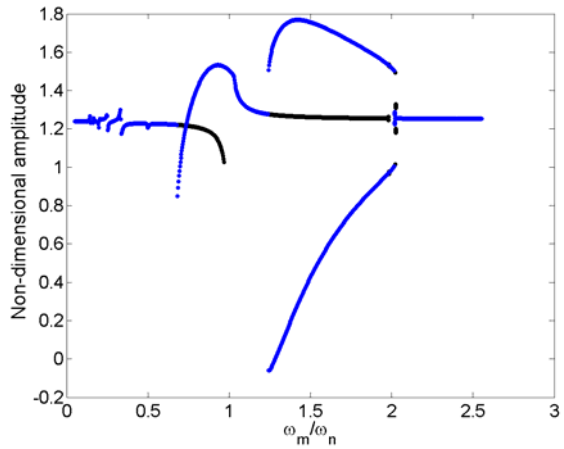

Figure 111: Bifurcation diagram for case study 2: SUA analysis (black); SDA analysis (blue).

The semi-amplitude/frequency and the bifurcation diagrams (Figure 110 and Figure 111) show similar results to case study 1.

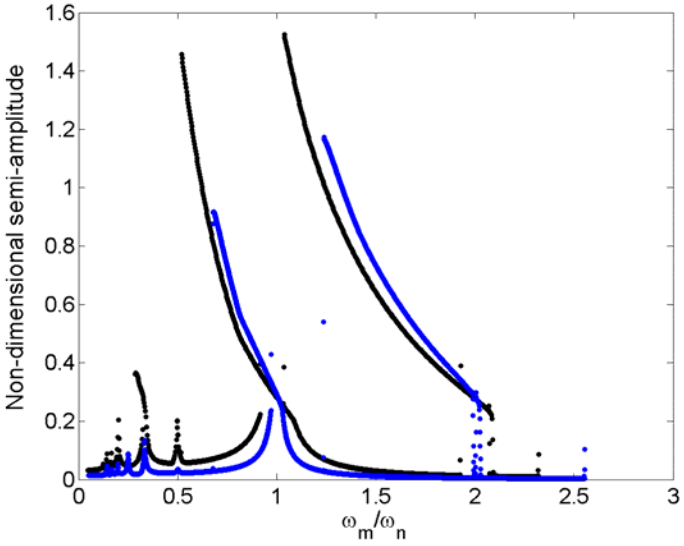

Figure 112: Comparison of semi-amplitude/frequency diagrams: no profile modifications (black); gears with profile modifications (blue).

A direct comparison of the analysis performed on the same gear pair with and without profile modifications, the following considerations can be formulated:

1. The effect of profile modifications decreases the peak to peak of both mesh stiffness and static transmission error of about 56%.
2. The natural frequency of the system changes from 3.156025 10^4 rad/s to 2.870711 10^4 rad/s (decreasing of 9%).
3. The effect of profile modification does not change the main dynamics behavior except for a general decrease of the vibration amplitude as shown trough direct comparison of semi-amplitude in Figure 112.

In conclusion, the profile modifications of Table 33 have a good benefit on the static behavior of the gears pair but lightly improve its dynamics.

3.6.3 Effect of torque on case study 2

The third analysis considers the effect of the torque on the vibrations of the case study 2 gears pair. The following torque values are applied:

	100%	**75%**	**50%**	**25%**
Torque [Nm]	470	352.5	235	117.5

Table 35: Torque value for the case study 2.

The simulation considers a damping ratio of $\zeta = 0.01$ and no manufacturing error $e(t)$=0. The static transmission error is calculated for 15 positions within a mesh cycle, and the approximation for the stiffness function used 7 harmonics. The following values for the normalized stiffness function are obtained:

Normalized stiffness component	Value			
	100%	**75%**	**50%**	**25%**
$\overline{k}_{d,1}$	6.039868 10^{-2}	1.199132 10^{-1}	2.053372 10^{-1}	3.620781 10^{-1}
$\overline{k}_{d,2}$	2.549201 10^{-3}	1.371908 10^{-2}	4.702296 10^{-2}	9.641139 10^{-2}
$\overline{k}_{d,3}$	1.017452 10^{-2}	2.144102 10^{-2}	2.244324 10^{-2}	2.869272 10^{-2}
$\overline{k}_{d,4}$	7.716745 10^{-3}	3.404132 10^{-3}	1.107648 10^{-2}	7.154377 10^{-3}
$\overline{k}_{d,5}$	3.415436 10^{-3}	3.491344 10^{-3}	4.474452 10^{-3}	6.23467 10^{-3}
$\overline{k}_{d,6}$	2.19705 10^{-3}	5.574036 10^{-3}	1.333034 10^{-3}	3.280057 10^{-3}
$\overline{k}_{d,7}$	2.686733 10^{-3}	2.560862 10^{-3}	2.078061 10^{-3}	7.23238 10^{-3}

Table 36: Effect of torque on stiffness components for case study 2.

Phase	Value [rad]			
	100%	**75%**	**50%**	**25%**
φ_1	-0.02302711	-0.0127078	-0.01526997	-0.009202071
φ_2	-0.9228034	-3.023366	3.124581	3.088847
φ_3	3.070796	3.114823	-3.125123	-2.894979
φ_4	-2.999429	-0.4571869	-0.3720098	-0.1799676
φ_5	-0.8892686	-0.6513739	2.947773	0.3490536
φ_6	0.3613773	3.015291	0.5171421	-0.752786
φ_7	2.395425	0.4621283	-2.4227	2.814945

Table 37: Effect of torque on the phases of the stiffness components for case study 2.

The results of Table 38 can be illustrated by a simple histogram:

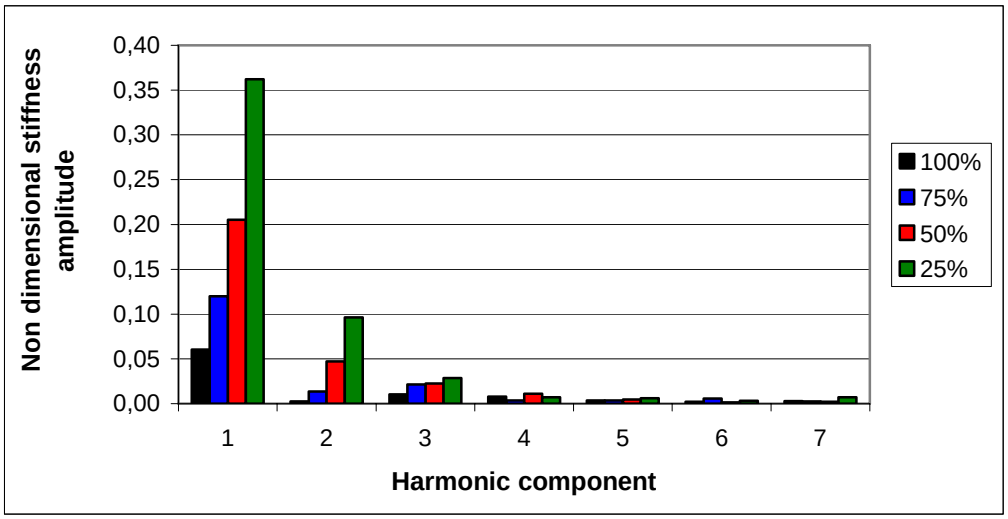

Figure 113: Effect of torque on stiffness components for the case study 2: 100% of nominal (black); 75% of nominal (blue); 50% of nominal (red); 25% of nominal (green).

According to finite element results, the natural frequencies ω_n, the peak to peak value of the mesh stiffness and the peak to peak value of the static transmission error of each cases are:

	ω_n [rad/s]	Peak to peak mesh stiffness [N/m]	Peak to peak STE [µm]
100%	$2.870711\ 10^4$	$3.12098\ 10^7$	5.10005
75%	$2.803574\ 10^4$	$5.70753\ 10^7$	7.93799
50%	$2.710842\ 10^4$	$9.07081\ 10^7$	10.3456
25%	$2.55632\ 10^4$	$1.46854\ 10^8$	13.0259

Table 38: Effect of torque on natural frequency ω_n , mesh stiffness and transmission error for case study 2.

The dynamic simulation considers the adaptive step-size Gear algorithm and the hyperbolic tangent smoothing backlash function with an initial position equal to $\dot{v}_1(0) = 1.0001$ and an initial speed of $\dot{v}_2(0) = 0.00001$ for the first speed analyzed. The integration tolerance is 10^{-8}.

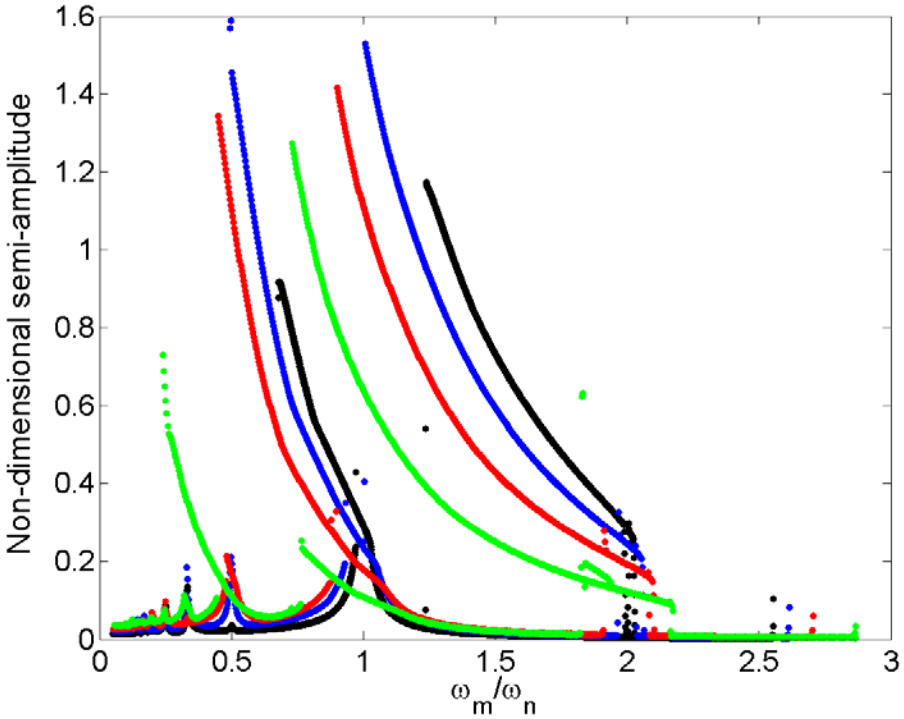

Figure 114: Comparison of semi-amplitude/frequency diagrams for case study 2: 100% of nominal (black); 75% of nominal (blue); 50% of nominal (red); 25% of nominal (green).

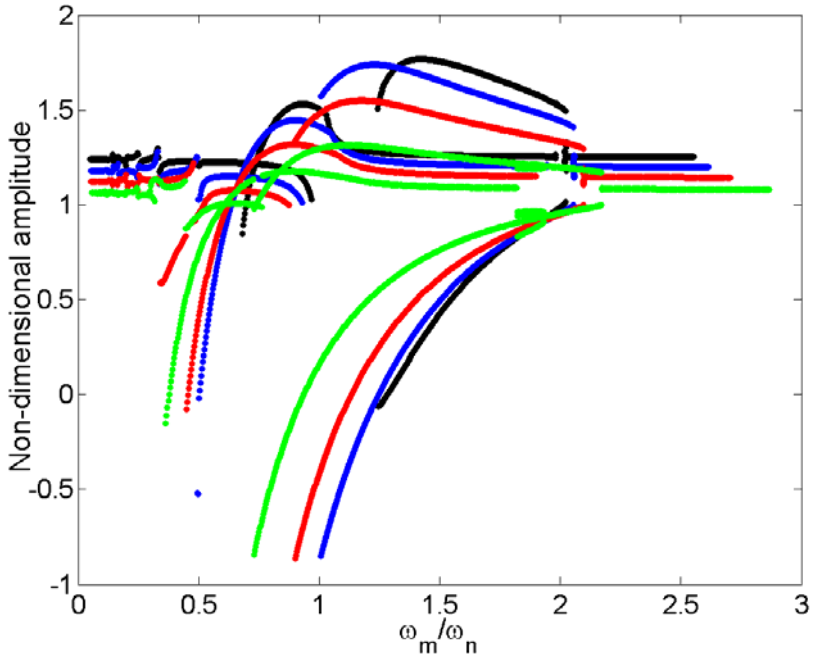

Figure 115: Comparison of bifurcation diagrams (SUA and SDA) for case study 2: 100% of nominal (black); 75% of nominal (blue); 50% of nominal (red); 25% of nominal (green).

The results of analysis can be summarized in five considerations:

1. Decreasing the torque results in a worst value of the peak to peak for both mesh stiffness and STE.
2. The natural frequency of the system decreases with the increase of the torque.
3. Decreasing the torque results in a decreasing of the amplitude of vibration at the high frequencies (principal and parametric resonances) and in a increase at low frequencies (super harmonics resonances). Despite the behavior of amplitudes, the decrease of the torque increases the frequency range at which nonlinear phenomena take place. For example, a more detailed SDA analysis shows that parametric period doubling response occur for a wider range at 25% of the torque with respect to 100%.
4. A time history carried out at ω_m/ω_n = 1.8863, with initial conditions equal to $\dot{v}_1(0) = 1.20756$ and $\dot{v}_1(0) = 0.0483475$ (see Figure 116), shows amplitude modulation, which justify the multiple bifurcations between ω_m/ω_n = 1.8 and ω_m/ω_n = 1.9 in the bifurcation diagram of Figure 115.

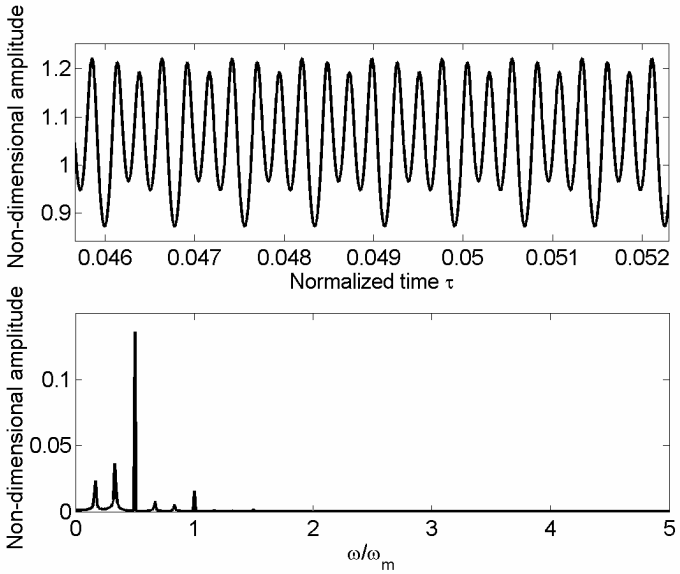

Figure 116: Time history and relative spectrum at ω_m/ω_n = 1.8863.

3.6.4 Effect of damping on case study 2

In order to examine the dynamic effect of the damping ratio ζ, case study 2 is simulated with $\zeta = 0.005$ and compared with previous analysis with $\zeta = 0.01$.

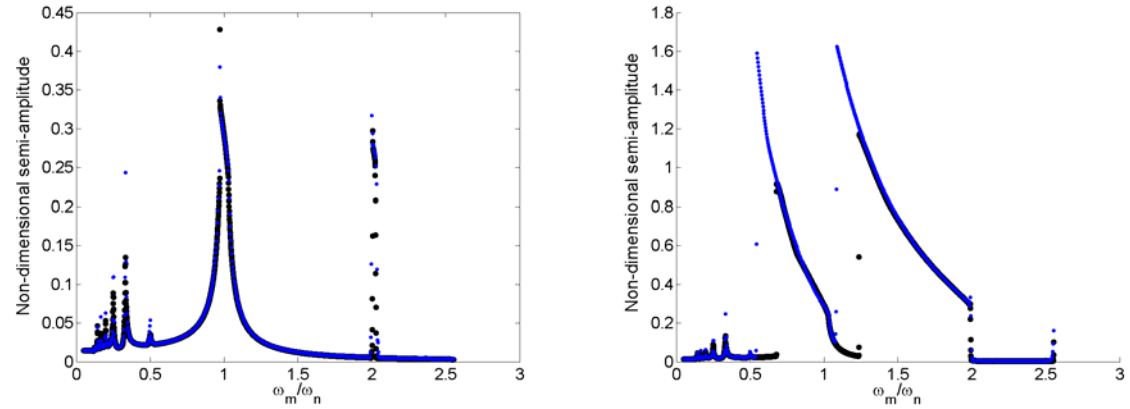

a) b)

Figure 117: Comparison of semi-amplitude/frequency diagrams for ζ = 0.01 (black), ζ = 0.005 (blue): a) SUA analysis; b) SDA analysis.

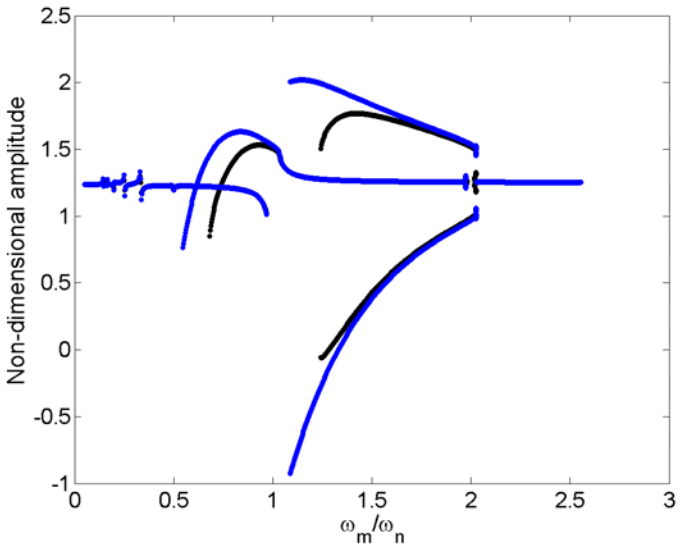

Figure 118: Comparison of bifurcation diagrams (SUA and SDA) for case study 2: ζ = 0.01 (black); ζ = 0.005 (blue).

Figure 117 and Figure 118 show comparison of the semi-amplitude/frequency and bifurcation diagrams. Note that the bifurcation diagram include both SUA and SDA analyses. The simulation shows that a reduction from $\zeta = 0.01$ to $\zeta = 0.005$ of the damping coefficient has a very light effect of on gears dynamics behavior.

3.6.5 Effect of manufacturing errors on case study 2

In this section the effect of manufacturing errors on gears dynamics are investigated.
The approach described in previous sections is applied to case study 2. In effect case study 3 is equivalent to case study 2 except for the introduced profile tolerances described in Table 39.

		Pinion	**Gear**
Involute			
	Tolerance [mm]	0.008	0.008
Tip relief			
	Type of modification	Linear	Linear
	Roll angle at start of relief [Deg]	30.1569	29.2127
	Magnitude of relief [mm]	0.016	0.018
	Tolerance [mm]	0.02	0.02
Root relief			
	Type of modification	Linear	Linear
	Roll angle at start of relief [Deg]	23.4706	25.2079
	Roll angle at end of relief [Deg]	14.4334	20.5764
	Magnitude of relief [mm]	0.016	0.018
	Tolerance [mm]	0.02	0.02
Crowning			
	Magnitude [mm]	None	None

Table 39: "K" chart tolerances for case study 3.

15 points on both pinion and gear, simulate a single-flank machine measurement. These points are used for the analytical reconstruction of the deviation from involute profile along the each teeth. In order to simulate the meshing of the two wheel, 10 point are considered and the combined profile manufacturing error is evaluated according to equation (3.2.28).

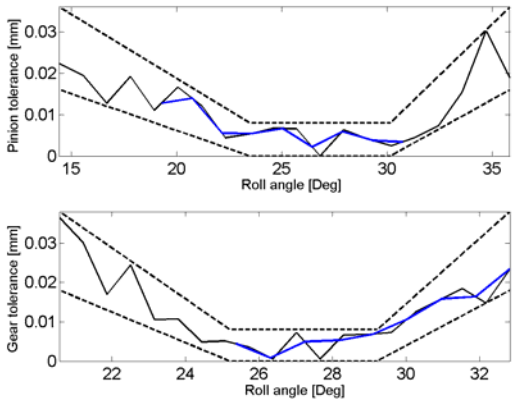

Figure 119: "K" chart for the pinion and the gear of case study 2.

Figure 119 shows the generated deviation from the theoretical involute profile for the first tooth of the pinion and of the gear.

In this example, the FFT of the combined profile error is composed by four harmonics at multiple frequency of the mesh frequency (see Figure 120). The values of amplitudes and phases of each harmonic component is listed in Table 40 according to equation (3.3.2).

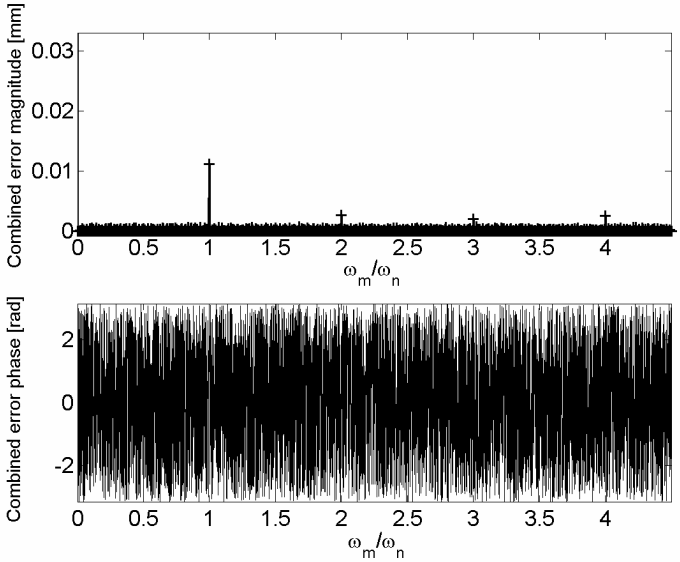

Figure 120: FFT spectrum of the combined profile error.

ω_m/ω_n	Normalized manufacturing error components	Value
1	$\overline{E_1}$	$6.87993\ 10^{-2}$
2	$\overline{E_2}$	1.86928710^{-2}
3	$\overline{E_3}$	$1.753613\ 10^{-2}$
4	$\overline{E_4}$	$1.602615\ 10^{-2}$

Phase	Value [rad]
γ_1	$9.349212\ 10^{-1}$
γ_2	1.987622
γ_3	2.518925
γ_4	2.882258

Table 40: Components of manufacturing profile errors applied to the case study 2.

Figure 121 and Figure 122 show that the general dynamics behavior does not change significantly except for a considerably increase of vibration amplitude at all frequency. This tendency is more evident especially at low speeds where contact loss can also occur.

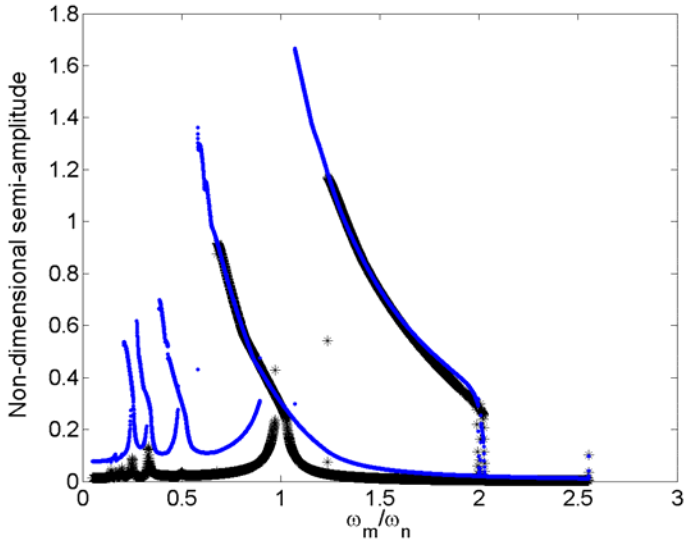

Figure 121: Comparison of semi-amplitude/frequency diagrams for case study 2: no manufacturing errors (black); with manufacturing errors (blue).

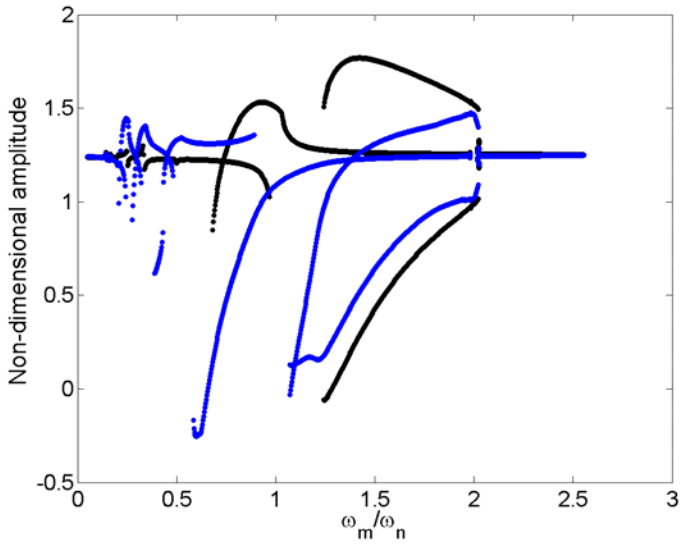

Figure 122: Comparison of bifurcation diagrams for case study 2: no manufacturing errors (black); with manufacturing errors (blue).

3.6.6 Example of chaotic behavior

According to literature the inclusion of manufacturing errors can cause chaotic behavior especially when torque is decreased (Kahraman and Blankenship, 1997).

In order to check if such phenomena can be detected with the present model, a simulation of case study 2 is performed at a very low torque. Two analyses are carried out: the first does not include manufacturing profile errors, the second one include manufacturing errors according to Figure 123 and Table 41.

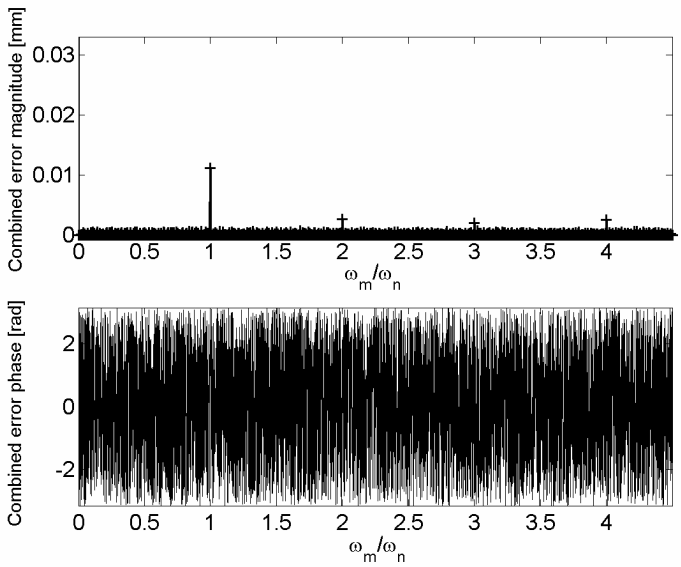

Figure 123: FFT spectrum of the combined profile error.

ω_m/ω_n	Normalized manufacturing error components	Value
1	$\overline{E_1}$	6.733351 10^{-2}
2	$\overline{E_2}$	1.680263 10^{-2}
3	$\overline{E_3}$	1.680263 10^{-2}
4	$\overline{E_4}$	1.379845 10^{-2}

Phase	Value [rad]
γ_1	9.602194 10^{-1}
γ_2	2.010088
γ_3	2.010088
γ_4	2.967895

Table 41: Components of manufacturing profile errors applied to the case study 2.

Using a torque value of 100 Nm, the natural frequency of the system ω_n results to be equal to 2.52129 10^4 rad/s. Using 15 positions in a mesh cycle the peak to peak of the mesh stiffness is 1.59036 10^8 N/m and the peak to peak of the static transmission error is 13.5439 μm.

The normalized stiffness components are listed below:

Normalized stiffness component	Value
$\overline{k}_{d,1}$	4.028604 10^{-1}
$\overline{k}_{d,2}$	1.049323 10^{-1}
$\overline{k}_{d,3}$	3.362532 10^{-2}
$\overline{k}_{d,4}$	6.101244 10^{-3}
$\overline{k}_{d,5}$	1.077443 10^{-2}
$\overline{k}_{d,6}$	3.035402 10^{-3}
$\overline{k}_{d,7}$	8.575266 10^{-3}

Phase	Value [rad]
φ_1	-0.005822678
φ_2	3.093856
φ_3	-2.911356
φ_4	-0.1923082
φ_5	0.2153367
φ_6	-0.8139278
φ_7	2.87615

Table 42: Stiffness component for the case study.

The dynamic simulation considers an initial position equal to $\dot{v}_1(0) = 1.0001$ and an initial speed of $\dot{v}_2(0) = 0.00001$ for the first speed analyzed. The integration tolerance is 10^{-8}.

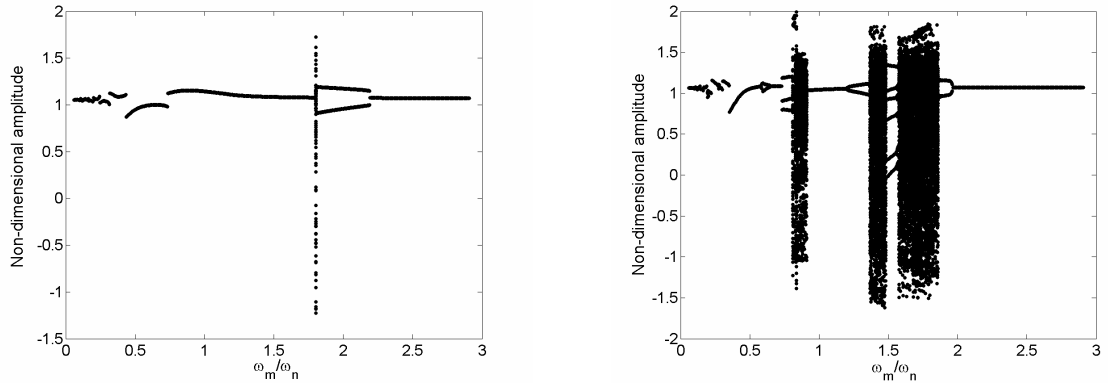

a) b)

Figure 124: Comparison of bifurcation diagrams (SUA): a) no manufacturing errors; b) with manufacturing errors.

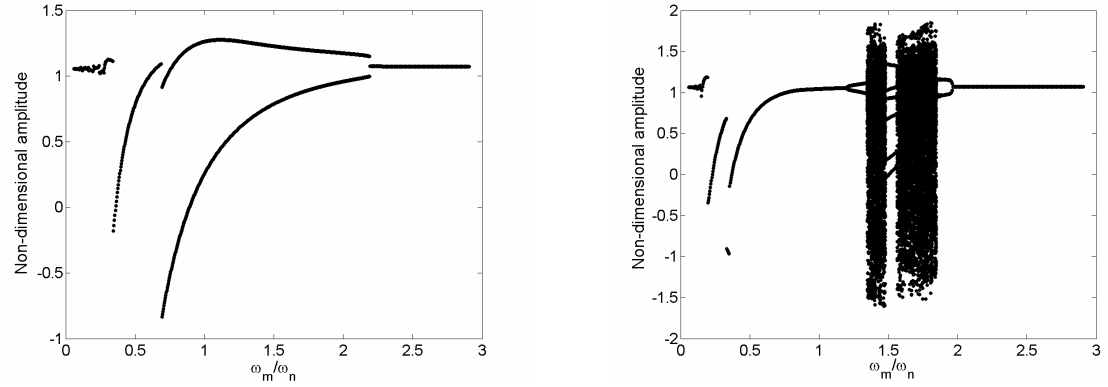

a) b)

Figure 125: Comparison of bifurcation diagrams (SDA): a) no manufacturing errors; b) with manufacturing errors.

Figure 124 and Figure 125 show that the analysis predict chaotic vibration only when manufacturing errors are included into the model. This in agreement to the mentioned Kahraman and Blankenship (1997)experiments.

In addition to the previous analysis a deeper simulation is performed for a time history at $\omega_m/\omega_n = 1.7021$. The initial condition are set to $\dot{v}_1(0) = -0.192391$ and $\dot{v}_2(0) = -0.258668$.

The steady state response, its spectrum (Figure 126) and the phase plane plot confirm the chaotic behavior of the system.

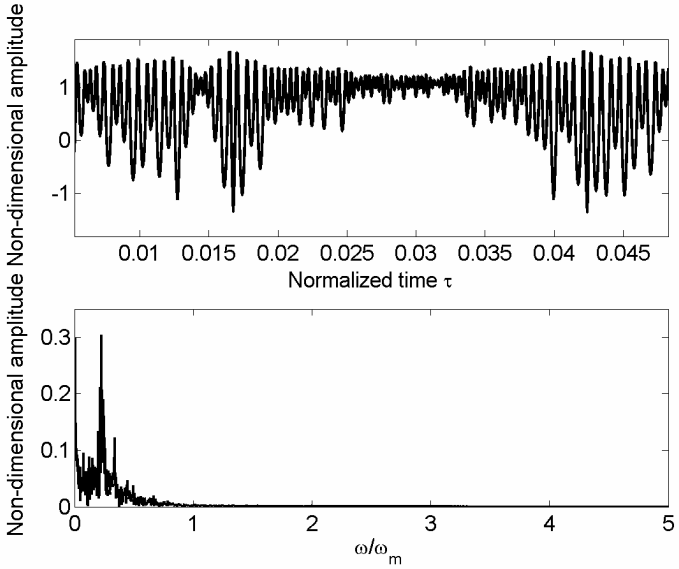

Figure 126: Time history and relative spectrum at $\omega_m/\omega_n = 1.7021$.

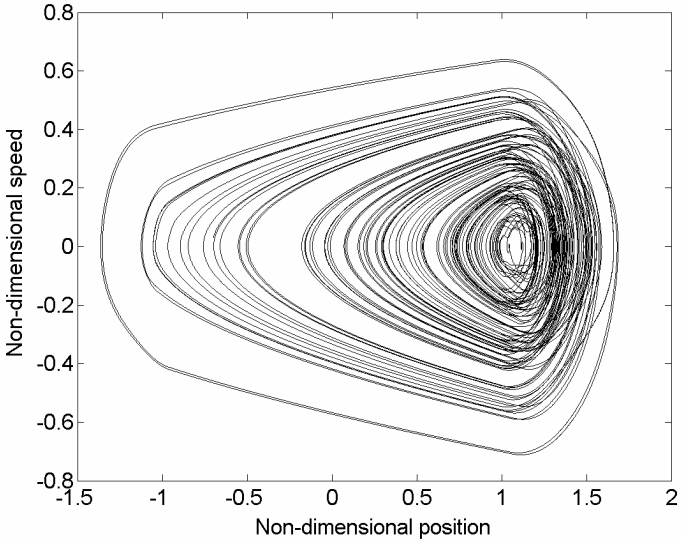

Figure 127: Phase plane plot.

Chapter 4

In this chapter procedures for the optimization of profile modifications are developed to reduce the rotational vibrations of a spur gears pair. Two main approaches are presented.
The first heuristic methodology calculates the peak to peak of the STE for a large range of cases using different values of the profile modification parameters. Maps of the STE are provided with respect to different couple of variables in order to choose the set of them which yield to the minimum peak to peak of the STE and understand manufacturing reliability (robustness). By means of sequential process also the effect of all parameters in the optimization procedure can be monitored. Since the effect of only two parameters at time can be checked, the results of this heuristic method do not yield to a minimum of the objective function but only to an optimum. The second approach is based on genetic algorithms; the basic idea is that the genetic pool of a given population, potentially contains the solution, or a better solution, to the given adaptive problem. The genetic algorithm then creates a population of solutions and applies genetic operators such as "mutation" and "crossover" to evolve the solutions in order to find the best one. Again the final set of profile modifications cannot be considered a minimum but an optimum. The advantages and disadvantages of such method with respect to the heuristic one can be summarized as follows:
Advantages:

1. Small number of iterations to reach the optimum;
2. Control of the procedure performance during calculation.
3. Allows to define a more complex objective function considering the effect of higher harmonics of the STE analytical reconstruction.

Disadvantages:

1. It is not clear the effect of each single parameters along the optimization process;
2. Do not provide robustness information.

Since both methodologies consider objective functions based on the peak to peak of STE and its higher order harmonics, the optimization processes do not automatically improve the dynamic behavior of the gears system. For this reason dynamic simulations are performed to check the effect of the optimum set of profile modification parameters on the gears.
Example of the previous methodology are given on actual gears.

4.1 General approach to optimization

In this work the relationship between gears radiated noise and the transmission error has been clarified and described. For this reason, the literature focuses any attempt to create silent gears, results in controlling and reducing the sources of excitation such as STE, manufacturing errors.

Since it is very difficult to design gears by directly considering the dynamic behavior, most of the common approaches are based on static calculations. The main concepts regards three macro-areas:

1. Macrogeometry: In this case the design process investigates the effect on radiated noise of macro geometrical parameters such as number of teeth, diameters, pressure angle, backlash, and clearance. For example, many authors analyze the effects of involute contact ratio ε_α on both spur and helical gears vibrations ((Sato et al., 1983) (Umezawa, 1985-b)), suggesting values higher then two (HCR high contact ratio gears). In a more detailed work, Kahraman ((Kaharaman and Blankenship, 1996-b), (Kahraman and Blankenship, 1999)) quantified the influence of involute contact ratio ε_α on dynamic transmission error and experimentally validate design guidelines to achieve quite gears. Other related studies ((Arikan, 1996), (Pedrero and Artes, 1996-a), (Pedrero and Artes,1996-b)) gives approximate equations for the relationship between pinion and gear addendum modification factors to have a pre-established contact ratio considering also specific sliding.
2. Surface refinement: Since manufacturing profile errors are a possible source of dynamics excitation, the quality of the teeth can affect gears vibrations. Important aspects such as surface roughness, surfaces refinement and tolerance can play a significant role in reducing radiated noise. The main problem related to increase the surface quality is due to higher manufacturing cost.
3. Microgeometry: In this case the main idea is to intentionally remove material from the gear tooth flanks so that the resulting form is no longer a perfect involute. These modifications (tip and root relief) compensate tooth deflections under load so that the resulting transmission error is minimized for a particular range of operating conditions.

Since macrogeometry modifications can involve a drastical change of the gear pair, and it is practicable only at the first steps of the design process, and surface refinements can involve

higher cost from a manufacturing point of view, the present work will focus its attention only on micro geometrical optimization.

4.1.1 Harris maps

The key point in design the correct profile modifications to reduce gears vibrations, is the calculations of 14 parameters that controls their definitions. In the previous chapter roll angles, magnitudes and type of modification (linear or parabolic) has been defined as the profile modifications parameters.

The literature offers many examples of guidelines to solve this problem but none of them seems to be valid for all applications and load conditions.

In 1940 Walker was the first that consider the tooth deflection in calculation of tooth load. He proposed a trapezoidal tooth cycle from which it was possible to calculate the amount of tip relief and its extension along the tooth profile (Walker, 1940).

The major contribute in this field was given by the Harris in 1958 (Harris, 1958) (Smith, 1999). He introduced the concept of static transmission error applied to profile modifications by developing a particular diagrams called “Harris map”.

Since a general profile modification can be represented as deviation from the theoretical involute profile (see the example of Figure 11), the combined effect of one pair of teeth meshing under no load would be to give a STE of the shape of Figure 128, with about a third of total span following the involute for both profile and generating no error (in Figure 128 the teeth has only tip relief).

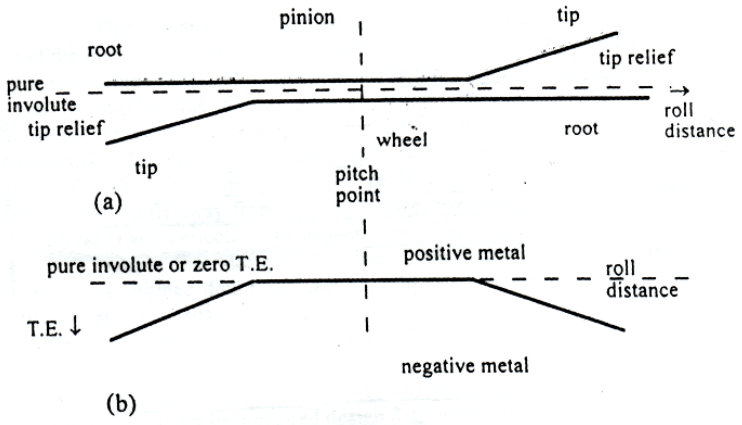

Figure 128: Representation of STE for mating profiles with tip relief in case of no load.

If several pairs of teeth in mesh are putting in succession the obtained effect is the one of Figure 129.

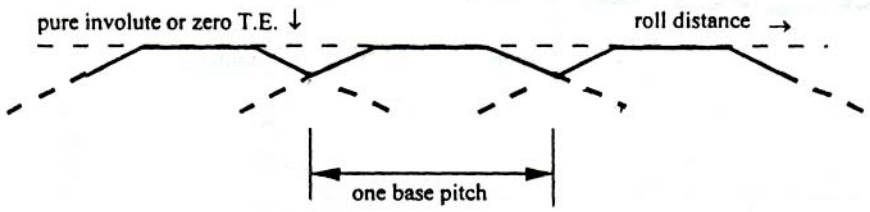

Figure 129: Effect of mating teeth pairs on STE in case tip relief and no-load.

The solid line of Figure 129 represents the STE under no-load conditions during gears rotation. When load is applied there are two regimes (see Figure 130): one around the pitch point where only one pair of teeth are in contact, one near the changeover points where there are two pairs in contact. Since point S corresponds to the HPSTC, the load is shared alternatively between one teeth pair in the involute zone and two teeth pairs in the relief zone between to subsequently points S.

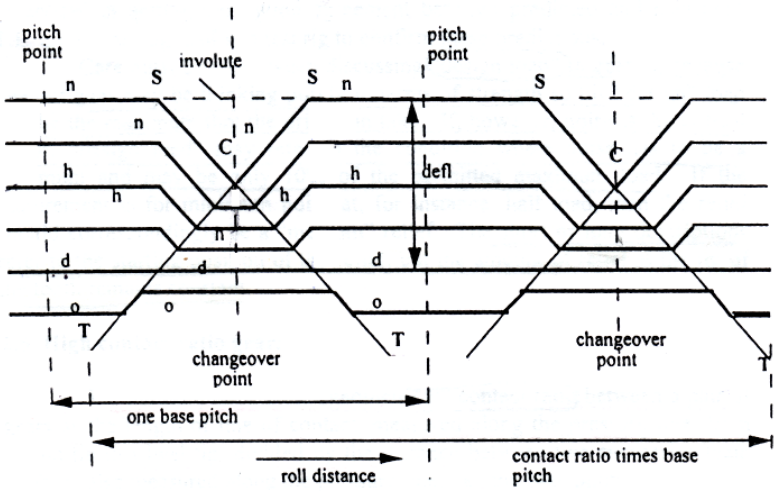

Figure 130: Example of Harris map.

Assuming a constant mesh stiffness, if the combined deflection of the two pairs in contact is equal to the deflection when just one pair is in contact, the STE will have a constant value and no oscillation. Figure 130 shows that at a particular design load (d) the effects of tip relief are exactly cancelled by the elastic deflections. There is a downward deflection away from rigid pure involute position but as the sum of tip relief and deflection is constant, it does not cause vibration. This approach allows to calculate the position of point C and therefore the magnitude of the tip relief once the deflection at the design load is known.

A similar method can be described in case of root relief.

In 1970 Niemann introduced a similar methodology for low load conditions and referred it as "short" relief with respect to Harris "long" relief (Niemann and Baethge, 1970). Note that neither "short" nor "long" relief can give low STE at both high and low load.

Despite the previous techniques, the literature offers other design guidelines for the profile modifications. For example Tavakoli developed a suitable optimization algorithm to minimize any combination of the harmonics of gear mesh frequency components of the static transmission error with different combinations of tip and root relief (Tavakoli and Houser, 1986). Munro et al. (1990) set a theoretical methodology for determining the amount and extent of profile modifications to provide a smooth transmission error curve when the module of the gear is higher than 5 mm. Cai and Hayashi (1992) developed an optimization technique by means of minimization of the equivalent exciting force. Matsumura et al. (1996) and Rouverol (1996) defined new methodologies to eradicate gears noise through profile deviations, respectively for light and high load conditions. Experimental works were made by Kahraman and Blankenship (1999-b) who analyzed the influence of gears linear flank modifications on the torsional vibrations of a spur gears system by means of measured DTE.

4.2 Heuristic method

In the previous sections the influence of profile modifications has been shown with respect to the STE. For this reason the implemented Heuristic method will have the value of peak to peak of the STE as objective function. In simple terms the optimization problem can be summarized as the calculation of a set of tip and root relief for both pinion and gear to achieve the smaller peak to peak value of the STE. The calculation of the peak to peak passes trough the FE methodologies explained in chapters 2 and 3 neglecting manufacturing errors. It is important to remember that the value of the peak to peak is calculated by means of the analytical reconstruction of the STE through the DFT algorithm.

The main problem of such optimization method is that the used of FE yields to an objective function which is not analytically defined. No close form solution can be calculated and no analytical approach such as Hessian matrix, can be applied successfully. In effect the STE depends on the meshing stiffness which is related to the geometry and the elasticity of the gears. Therefore only numerical techniques can guarantee a sufficient accuracy. On the other hand, even the most sophisticated FE codes, such as MSC Marc® or Calyx®, require a big computational effort for a simple STE calculation over a mesh cycle. This forbids the

possibilities of performing a "many cases" analysis in which all combination of the parameters are considered.

In order to reduce the complexity of the problem some assumptions has been supposed, and a sequential iteration method has been developed considering multiple analysis where only two parameters at time are examined (Beghini et al., 2004).

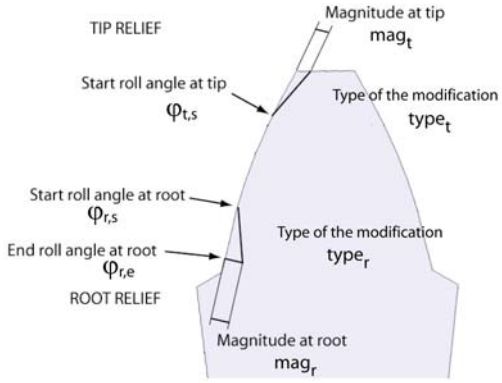

Figure 131: Nomenclature for the profile modification parameters.

According to Figure 131, a set of 7 parameters characterizes the profile modifications on each gear. The type of modification will not be considered as a variable parameter. In effect it depends on the available manufacturing process and it is defined at the beginning of the analysis. Also the end roll angle at root is not variable since it is equal to the start active profile point (SAP). The remaining 4 variable parameters can assume any value inside the following range:

Parameter	From	To
$\varphi_{t,s}$	Pitch point	Tip circle
mag_t	0	50 μm
$\varphi_{r,s}$	Pitch point	SAP
mag_r	0	50 μm

Table 43: Dominium of variable parameters for the heuristic optimization.

For example the start roll angle at tip is defined from the roll angle value at pitch point and the roll angle value at the tip circle. The magnitude can assume a minimum value of 0, which correspond to no relief, and a maximum value of 50 μm, which is in agreement with technological limits.

The sequential iterative approach consists in a set of four different analysis (STEP) where the following couple of variable are changed simultaneously.

	STEP 1	STEP 2	STEP 3	STEP 4
Variable parameter on pinion	$\varphi_{t,s}$	mag_t	$\varphi_{r,s}$	mag_r
Variable parameter on gear	$\varphi_{t,s}$	mag_t	$\varphi_{r,s}$	mag_r

Table 44: Variable parameters for each step.

At each step the range of the relative variable parameters is divided into an arbitrary number of intervals. The peak to peak of the STE is calculated for each different combination of assumed values. In this way a tridimensional surface allows to understand the behavior of the object function with respect to the used variable parameters. Note that the minimum value of such curve, it is not an absolute minimum since each step does not considers the variation of all parameters simultaneously. For this reason, the minimum will be simply referred as an optimum point. A complete optimization analysis allows to obtain a new set of profile modifications from an initial set through calculation of the optimum at each step of analysis (see Figure 132).

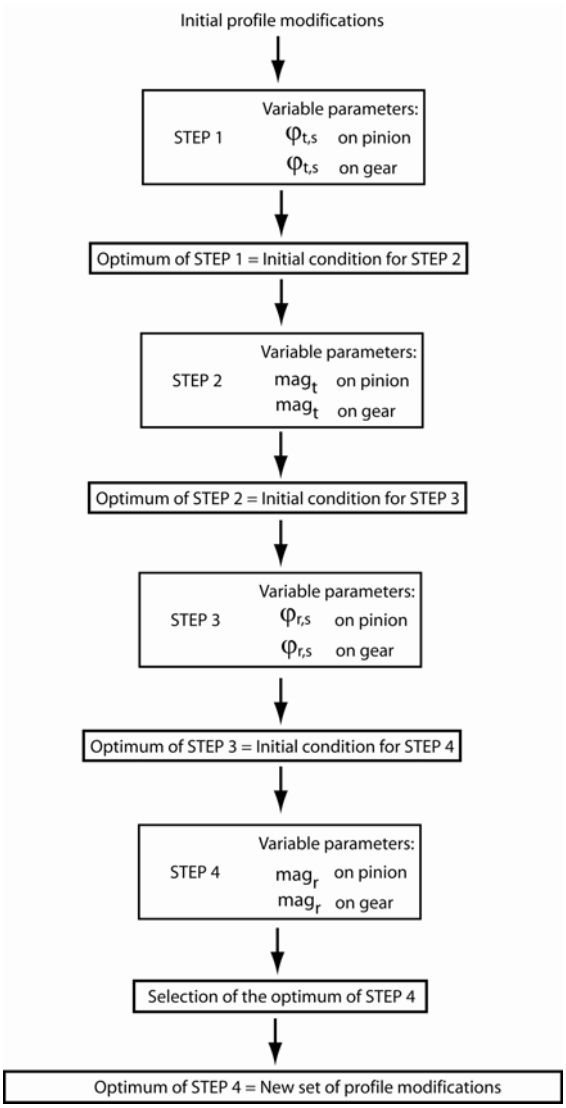

Figure 132: Sequence of the iteration step for the heuristic method.

The optimum of each step will provide the new set of profile modification parameters for the next step. The optimum of the fourth step defines the new set of profile modifications.

As final considerations, the following disadvantages of the heuristic method must be underlined:

1. The final optimum depends from the initial set of profile modifications: this means that different initial conditions can yield to very different results;
2. The final optimum depends on steps order and variables pairs ; Table 44 defines the order of the pairs of variable parameters. A different order of step and variable can yield to very different results;

4.2.1 Manufacturing robustness

One of the main advantages of the heuristic approach is the possibility of control the effect of one parameters on the peak to peak of the STE. For this reason it is possible to assure manufacturing reliability to the optimum set of profile modifications.

Let us considers Figure 133; in this case an example of peak to peak STE surface is given with respect to the variation of the roll start angles at tip. The optimum stands on a flat region which assures manufacturing reliability. A small perturbation of the roll angles in the neighborhood of the optimum, does not affect the value of the STE. This means that the manufacturing process can have larger tolerance on the variable parameters.

The "false optimum" is discarded for the opposite reason. Even if the STE value is small, the sharp variation of the surface can involve high accuracy in the manufacturing process.

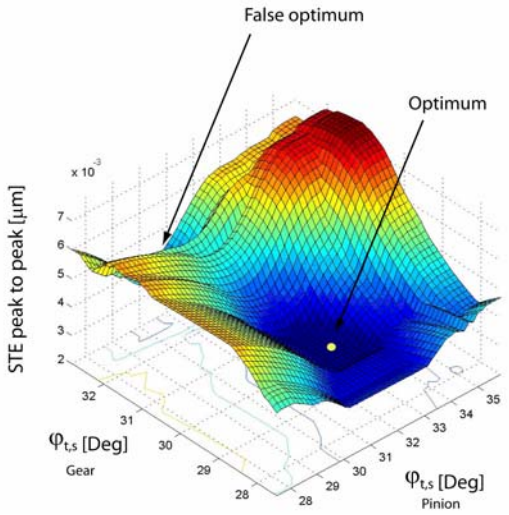

Figure 133: Example of false optimum.

4.2.2 Application of the heuristic method

An application of the developed heuristic method is proposed for case study 2. Therefore the profile modifications shown in Table 33 are used as initial profile modifications for the iteration process. The sequence of the iteration process follows the scheme of Figure 132. For each step the peak to peak value of the STE is calculated for a grid of 1681 possible combination whitin the two relative variable parameters. At each iteration 15 position within a mesh cycle are used to calculate the STE with FE analysis. The peak to peak value of STE, is calculated based on the DFT analytical reconstruction with 7 harmonics.

The following figures show the three-dimensional surface obtained for each step. The chosen optimum is also indicated.

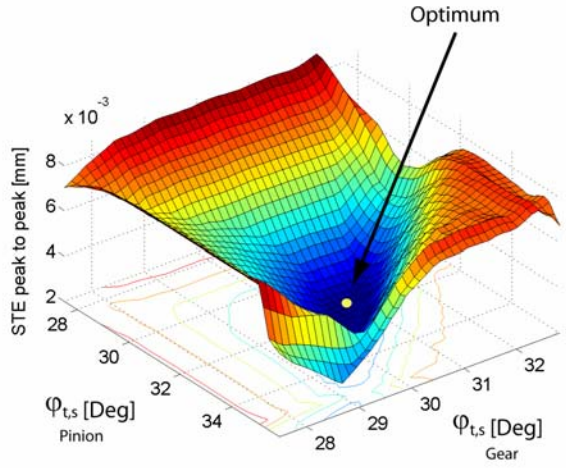

Figure 134: Peak to peak of STE surface for step 1.

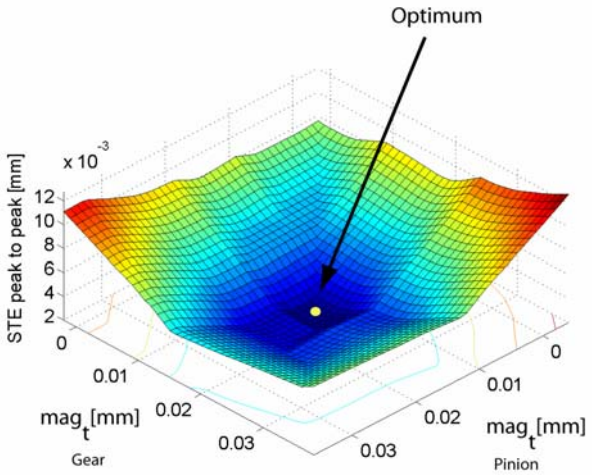

Figure 135: Peak to peak of STE surface for step 2.

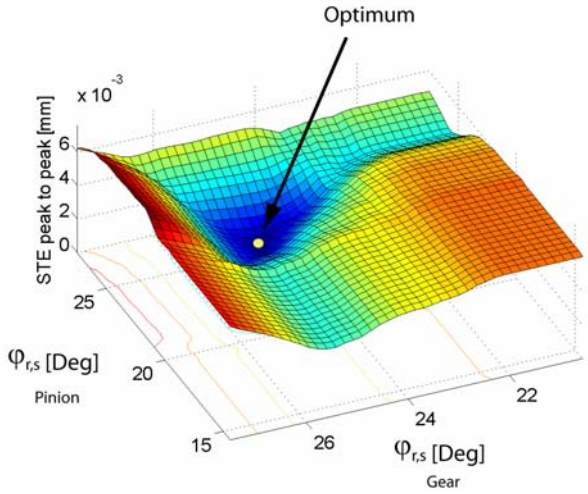

Figure 136: Peak to peak of STE surface for step 3.

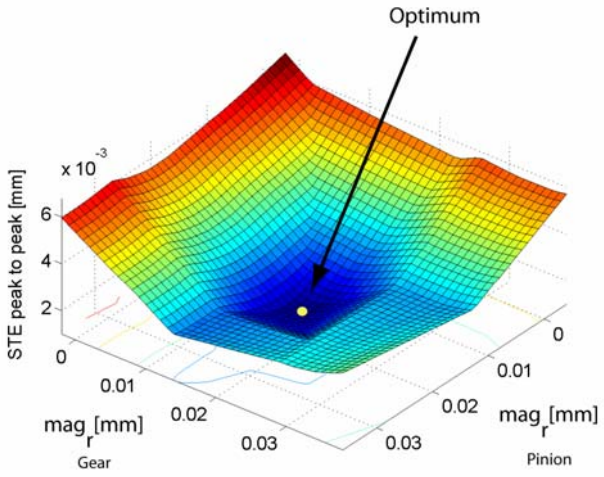

Figure 137: Peak to peak of STE surface for step 4.

The following table summarizes the profile modifications of the chosen optimum at each steps.

	Initial case (case study 2)		**Optimum of STEP 1**		**Optimum of STEP 2**		**Optimum of STEP 3**		**Optimum of STEP 4**	
	Pinion	**Gear**	**Pinion**	**Gear**	**Pinion**	**Gear**	**Pinion**	**Gear**	**Pinion**	**Gear**
Tip relief										
$type_t$	Linear	Linear	Linear	Linear	Linear	Linear	Linear	Linear	Linear	Linear
$\varphi_{t,s}$ [Deg]	30.1569	29.2127	32.2873	30.4219	32.2873	30.4219	32.2873	30.4219	32.2873	30.4219
mag_t [mm]	0.016	0.018	0.016	0.018	0.015	0.017	0.015	0.017	0.015	0.017
Root relief										
$type_r$	Linear	Linear	Linear	Linear	Linear	Linear	Linear	Linear	Linear	Linear
$\varphi_{r,s}$ [Deg]	23.4706	25.2079	23.4706	25.2079	23.4706	25.2079	23.8994	24.7245	23.8994	24.7245
$\varphi_{t,e}$ [Deg]	14.4334	20.5764	14.4334	20.5764	14.4334	20.5764	14.4334	20.5764	14.4334	20.5764
mag_r [mm]	0.016	0.018	0.016	0.018	0.016	0.018	0.016	0.018	0.017	0.018

Table 45: Profile modifications parameters for the optimum at each step.

Values of the peak to peak of the STE and mesh stiffness for each optimum is provided in Table 46.

	Initial case (case study 2)	**Optimum of STEP 1**	**Optimum of STEP 2**	**Optimum of STEP 3**	**Optimum of STEP 4**
Stiffness pk to pk [N/m]	$3.1210\ 10^{7}$	$1.4981\ 10^{7}$	$1.4782\ 10^{7}$	$1.1333\ 10^{7}$	$1.1206\ 10^{7}$
STE pk to pk [μm]	5.10005	2.29845	2.26704	1.7204	1.70299

Table 46: Values of peak to peak for mesh stiffness and STE.

The optimum of step 4 is the final heuristic optimum, and yields a decrease of the peak to peak value of STE of around 64%.

Since the heuristic approach is based on static assumption, the effect of the new profile modification on the dynamics is simulated using the developed vibration model. The simulation considers a torque value of 470 Nm, a damping value of ζ = 0.01 and no manufacturing error $e(t)$=0.

The static transmission error is calculated for 15 positions within a mesh cycle, and the approximation for the stiffness function used 7 harmonics. The following values for the normalized stiffness function are obtained:

Normalized stiffness component	**Value**	
	Case study 2	**Heuristic optimum**
$\overline{k}_{d,1}$	$6.039868\ 10^{-2}$	$2.60938\ 10^{-3}$
$\overline{k}_{d,2}$	$2.549201\ 10^{-3}$	$1.309961\ 10^{-2}$
$\overline{k}_{d,3}$	$1.017452\ 10^{-2}$	$5.389689\ 10^{-3}$
$\overline{k}_{d,4}$	$7.716745\ 10^{-3}$	$8.202505\ 10^{-3}$
$\overline{k}_{d,5}$	$3.415436\ 10^{-3}$	$2.77349\ 10^{-3}$
$\overline{k}_{d,6}$	$2.19705\ 10^{-3}$	$1.018689\ 10^{-3}$
$\overline{k}_{d,7}$	$2.686733\ 10^{-3}$	$1.055638\ 10^{-3}$

Table 47: Values of stiffness components for case study 2 and heuristic optimum.

Phase	Value [rad]	
	Case study 2	**Heuristic optimum**
φ_1	-0.02302711	-0.19126370
φ_2	-0.9228034	-0.18059620
φ_3	3.070796	-3.13598300
φ_4	-2.999429	-2.99123400
φ_5	-0.8892686	-0.07591713
φ_6	0.3613773	-1.97353900
φ_7	2.395425	2.46872500

Table 48: Values of stiffness phases for case study 2 and heuristic optimum.

According to finite element results, the natural frequencies ω_n, increases of 2%.

	ω_n **[rad/s]**
Case study 2	$2.870711\ 10^4$
Heuristic optimum	$2.931195\ 10^4$

Table 49: Values of natural frequencies.

The dynamic simulation considers the adaptive step-size Gear algorithm and the hyperbolic tangent smoothing backlash function with an initial position equal to $\dot{v}_1(0) = 1.0001$ and an initial speed of $\dot{v}_2(0) = 0.00001$ for the first speed analyzed. The integration tolerance is 10^{-8}. Figure 138 shows comparison of the bifurcation diagram scenario for the two cases. The PD bifurcation disappears completely in case of heuristic optimization.

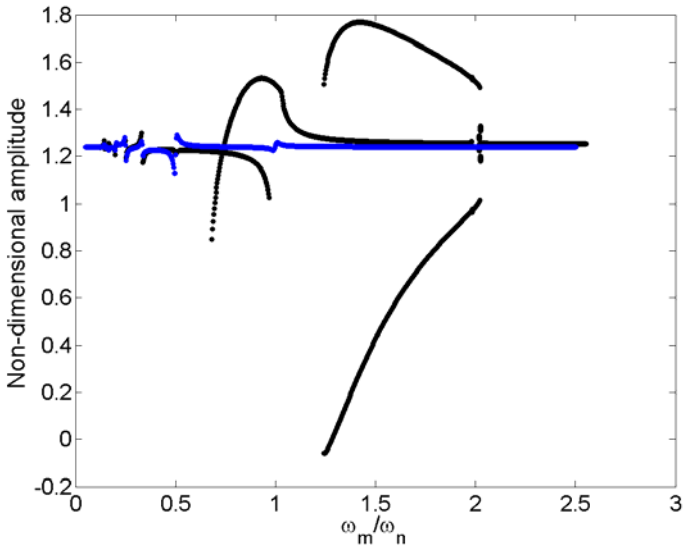

Figure 138: Comparison on bifurcation diagrams: case study 2(black); heuristic optimum (blue).

Figure 139 shows comparison of the semi-amplitude/frequency diagram.

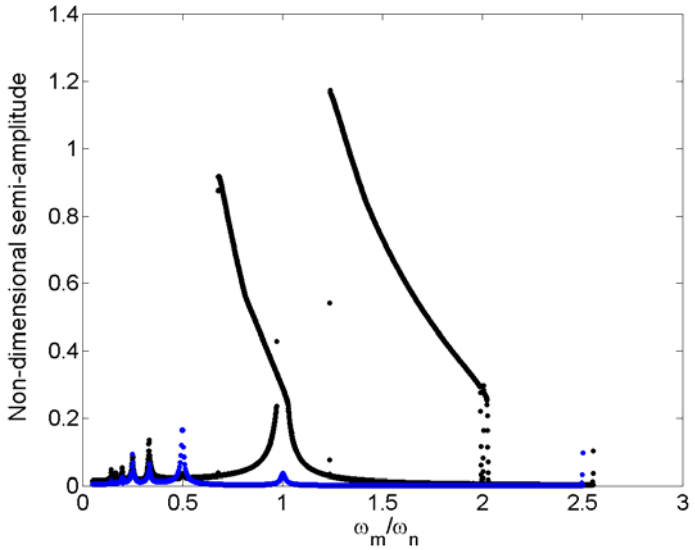

Figure 139: Comparison on semi-amplitude/frequency diagrams: case study 2(black); heuristic optimum (blue).

The heuristic optimization yields to the following effects:

1. Smaller amplitude of vibrations at almost all frequencies;
2. Disappearance of the parametric resonance;
3. Disappearance of loss of contact: the reduction of the vibration amplitude involve no tooth separation and the linearization of dynamics behavior at all resonances.
4. The amplitude of vibration increases at $\omega_m/\omega_n = 0.5$. This is due to an increase of the amplitude of the second harmonic component of the STE. Figure 140 allows to graphically compare the contents of the harmonic components of the two cases.

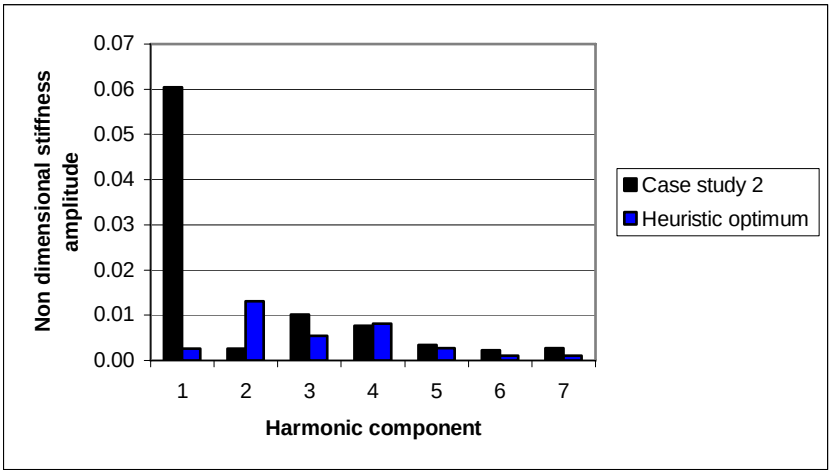

Figure 140: Harmonics contents of the non dimensional mesh stiffness: case study 2 (black); heuristic optimum (blue).

4.3 Genetic optimization method

The basic idea of all genetic optimization techniques is to reproduce numerically the evolution of biological systems. The first work published on this topics is probably due to Fraser (1960). The scientist developed a model to study the gene epistasis phenomena through the evolution of a 15 bit string according to the following phenotype equation:

$$f(a,q,c) = a + q\,a|a| + c\,a^3 \tag{4.3.1}$$

This string was intent to represent the phenotypic expression of a gene. In Fraser's model, 5 bit were used to represents the parameters *a*, *q* and *c*. An initial population was updated by means of a crossover process based on the strings which phenotype expression was within the interval [-1,1]. Fraser also defined the basic terminology used for the genetic approaches (see Table 50).

Genetic	**Genetic algorithm**
Chromosome	String
Genotype: ensemble of all chromosome	Structure
Phenotype: (defined by the iteration of genes)	Solution
Fitness: numerical value associated to the phenotype (describes the probability of surviving of a genetic mutation)	Objective function
Gene: basic element of a chromosome	Elements of a string
Allel: different value of gene	Code (usually a binary code where each gene is a bit)
Locus: position of a gene on the Chromosome (usually different position have the same effect).	Locus: in genetic algorithm each gene is defined by its position
Epistasis: relationship of between character and gene	Multi-variables objective function

Table 50: Genetic and genetic algorithm terminology.

Subsequently Bagley applied genetic algorithms to the game theory in order to simulate Gardener's game "Hexapawn" (Bagley, 1967). This simple game consists in a 3x3 chessboard with 3 white and 3 black pawns (see Figure 141). The game is similar to normal chess, except for the first time movement rule. The ultimate aim of the game is to reach the last rank of the board or to block any opponent movement. Since the black player can always win if the white

player plays first, Bagley implemented an evolutionary algorithm able to predict the correct black movement to win the game.

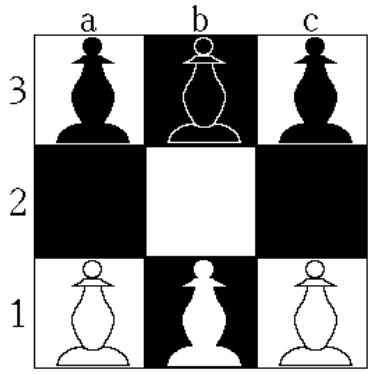

Figure 141: Hexapawn chessboard.

For this purpose, Bagley used a game-tree approach, which contained all functionalities of the modern genetic algorithm, such as: dominance, inversion, diploid string and fitness scaling.

The first application of genetic algorithm to large scale data analysis (data mining) were performed in 1970. For example Caviccio (1970) worked on pattern recognition in order to search object within graphic images.

Hollstien was the first to use genetic approaches to mathematical optimization (Hollstien, 1971). In his work 14 double variable functions are studied with a 8 bit binary code. Different selection and crossover strategies are analyzed and the Grey binary code is introduced in order to improve the efficiency of the algorithm.

The first theory of genetic algorithm was due to Holland in 1975 with the publication of "Adaptation in Natural and Artificial Systems" (Holland, 1975). In the same year De Jong studied how to compare maximum analytical solution with the relative maximum genetic solution by means of convergence tests (De Jong, 1975).

The first engineering application of genetic algorithm was completed by Goldberg in 1989 on the optimization of a gas pipe line and of a reticular beam structures (Goldberg, 1989). Since Goldberg work many other published paper were produced regarding different applications from fluid dynamics to civil engineering, from chemistry to languages.

The only publication existing about genetic approach on spur gear optimization is by Fonseca et al. (2005). Despite the paper seems to be original, lack of important details do not clarify important assumptions and do not allow to repeat the work.

4.3.1 Scheme of a genetic algorithm iteration (SGA)

A genetic algorithm is a optimization method which allows to create a new "better" family of solutions (usually referred as population) from an existing population by means of several genetic iterations. In the simplest approach (SGA) each iteration is constituted by the following three steps:

1. Selection
2. Crossover
3. Mutation

In order to understand if a population is better then another, the concept of fitness is also introduced. As in biologic system, the fitness describes the probability of surviving of a genetic mutation, in engineering applications, it defines the parameters according to which the population will "endure". For example in a maximum problem for a mathematical function, the fitness will corresponds to the value of the function in a certain solution point.

One of the key point in genetic approach is the representation of a solution by mean of binary code strings. For example, let consider the following function (Goldberg, 1989):

$$f(x) = x^2 \quad x = 0,1,...,31 \tag{4.3.2}$$

In this case, the maximum is in x = 31 and 32 integer number constitute the dominium of the function. The dominium can be represented by means of five bits, using a positive binary code.

If the population is composed by four strings, Table 51 shows a possible initial population:

String number	String	*x*	*f(x)*
1	0 1 1 0 1	13	169
2	1 1 0 0 0	24	576
3	0 1 0 0 0	8	64
4	1 0 0 1 1	19	361
		Average	292.5
		Maximum	576

Table 51: Initial population for the genetic algorithm.

Selection

The selection step allows to chose the best string from a given population. One of the simplest selection technique is called "stochastic sampling with replacement" and calculate the probability of selecting a string according to its fitness.

Table 52 reports fitness values and the probability of selection of each string, for the previous example.

String number	String	*x*	*Fitness f(x)*	*p*	Number of selected string number
1	0 1 1 0 1	13	169	0.14	1
2	1 1 0 0 0	24	576	0.49	2
3	0 1 0 0 0	8	64	0.05	0
4	1 0 0 1 1	19	361	0.31	1
		Sum		1.00	4
		Average	292.5		
		Maximum	576		

Table 52: Example of stochastic sampling with replacement.

The fitness *f(x)* corresponds to the value of equation (4.3.2) calculated for the correspondent string value. The probability *p* represents the probability to extract each single string from an equivalent urn in which the number of the contained strings is described in Figure 142. According to this probability the number of selected string described how many time the same string has been extracted when a new population is created.

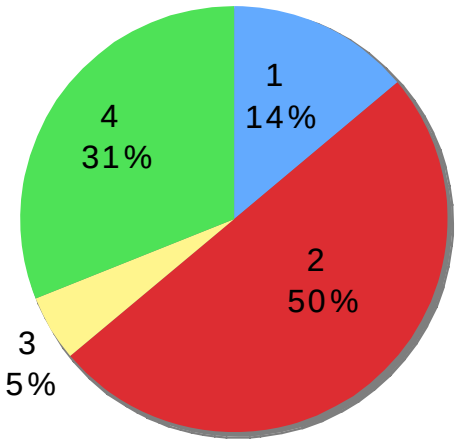

Figure 142: Probability of extraction of each string.

Table 53 shows the new population and the new values of the fitness.

String number	String	*x*	*Fitness f(x)*
1	0 1 1 0 1	13	169
2	1 1 0 0 0	24	576
2	1 1 0 0 0	24	576
4	1 0 0 1 1	19	361
		Media	420.5
		Max	576

Table 53: New population and its fitness.

Note that selection is the only step that involve the calculation of the fitness. In this sense it is the only step which tends to create a "better" population. In effect the average fitness value of increases from 292.5 (Table 52) to 420.5 (Table 53).

Crossover

Once a new population is generated, the strings are randomly grouped by two and, for each pairs of string, a cutting point is randomly selected. The cutting point can be assume a value from 1 to *m*-1 where *m* is the string length. The crossover operation splits each string at the cutting point. The first part of the father's string and the second part of the mother's string combine to form the first child string and, with a similar effect, a second child string is created with the remaining parts.

String number	**String**	**Crossing string number**	**Cutting point**	**New population.**	***x***	**Fitness *f(x)***
1	0 1 1 0 ‖ 1	2	4	0 1 1 0 0	12	144
2	1 1 0 0 ‖ 0	1	4	1 1 0 0 1	25	625
3	1 1 ‖ 0 0 0	4	2	1 1 0 1 1	27	729
4	1 0 ‖ 0 1 1	3	2	1 0 0 0 0	16	256
					Average	438.5
					Maximum	729

Table 54: Example of crossover step.

Table 54 shows the application of the crossing over step to the previous example.

Note that a crossover probability index p_c can be introduced in order to control the number of crossing string pairs and therefore the velocity of variation of the population.

Mutation

Just before the strings are placed into a new population, they have a slight chance of mutating. A mutation is simply a small, random change to one of a bit (allel) of the string. Mutation means flipping the bit from 1 to 0 or 0 to 1. This allows the algorithm to search in all function dominium. In effect if the number of the population is small or the fitness value tends to high an high value, the probability that a bit assumes always a constant value (1 or 0) is high (alleles losing phenomena).

In Table 55, the new population does not contain the string four. Since string four is the only string which contains the allel 1 in position 2, an allel lost occurs. The allel value in position 2

would be always equal to 0, whatever selection or crossover techniques will be used in the following.

String number	String	*p*	Number of selected string number	New population
1	0 1 1 0 1	0.14	1	0 1 1 0 1
2	1 1 0 0 0	0.50	2	1 1 0 0 0
3	0 1 0 0 0	0.05	1	1 1 0 0 0
4	1 0 0 1 1	0.31	0	0 1 0 0 0

Table 55: Alleles losing phenomena.

This results in a restriction of the search dominium from 8 to 16 and from 24 to 31 (see Figure 143).

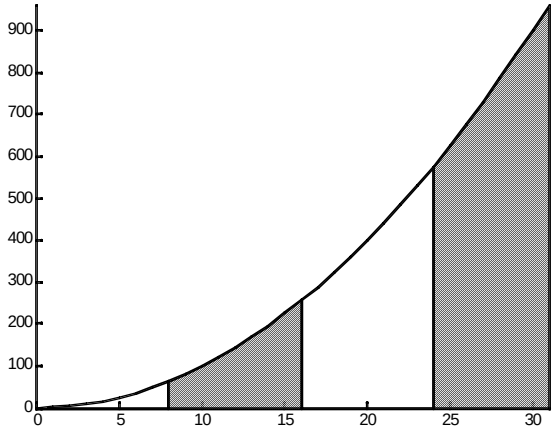

Figure 143: Reduction of the search dominium due to alleles losing phenomena.

The mutation step is controlled by the mutation rate p_m which determines the mutation probability of a single bit.

Once the mutation step is ended, a new population is generated and a full genetic iteration is completed.

4.3.2 Stochastic reminder selection without replacement

Another technique used for the selection step is the "stochastic reminder selection without replacement" developed by Brindle in 1981 (Brindle, 1981).

In this case the population is created by using a combined "deterministic sampling" and "stochastic sampling with replacement" method. Half of the population strings are selected by

means of the "deterministic sampling" and half of them with the "stochastic sampling with replacement".

The first technique consists in selecting a certain number of string of each type from the initial population according to the probability p multiplied by the dimension of the population n. If $p \bullet n$ is real, the number of the chosen string if calculated by rounding-off the $p \bullet n$ value to the smallest integer number. The remaining strings are selected with the "stochastic sampling with replacement" technique but the areas of the diagram in Figure 142, are evaluated using the fraction part of the probability $p \bullet n$.

Table 56 show an example of the combined selection technique.

String number	String	p	$p \bullet n$	Number of selected string number (determ.)	Fraction	Number of selected string number (stoc.)
1	0 1 1 0 1	0.14	0.56	0	0.56	1
2	1 1 0 0 0	0.50	2	2	0	0
3	0 1 0 0 0	0.05	0.2	0	0.2	0
4	1 0 0 1 1	0.31	1.24	1	0.24	0
	Sum	1.00	4.00	3	1.00	1

Table 56: Example of stochastic reminder selection without replacement.

4.3.3 Fitness scaling

During the iteration process the value of the fitness tend progressively toward a specific value (the maximum in the previous example), but at the same time there is a decrease of the difference between the average and the maximum fitness values within the population. Each strings tend to have a specific fitness value and this effect reduce drastically the efficiency of the algorithm in advancing the "best" strings.

Furthermore the fitness value must always have a positive (or negative) value and cannot oscillate within the two possibilities.

Fitness scaling solve both problems by means of a redistribution linear law, like the one in following equation:

$$f' = a f + b \tag{4.3.3}$$

The transformation assures that the maximum value is sufficiently distant from the average value. Coefficients a and b are calculated in order to have:

- The average value of the fitness unaltered;
- The probability of the stochastic sampling with replacement equal to c_{mult}/n. (c_{mult} is the number of string with maximum fitness expected in the population);

Since equation (4.3.3) does not assure that *f'* is always non negative (or non positive) two different cases can be considered:

1. The application of *f'* generates a positive minimum (negative maximum) value of the fitness;
2. The application of *f'* generates both positive and negative fitness values within the population.

In the first case *a* and *b* can be calculated as follows:

$$a = \frac{\overline{f}(1 - c_{mult})}{\overline{f} - f_{\max}} \qquad b = \frac{\overline{f}\left(\overline{f}\, c_{mult} - f_{\max}\right)}{\overline{f} - f_{\max}} \tag{4.3.4}$$

where $\overline{f}$ is the average value of *f*.

In the second case a and b are calculated with the following equation:

$$\begin{cases} a\overline{f} + b = \overline{f} \\ a f_{min} + b = 0 \end{cases} \Rightarrow \quad a = \frac{\overline{f}}{\overline{f} - f_{min}} \qquad b = \frac{\overline{f} f_{min}}{\overline{f} - f_{min}} \tag{4.3.5}$$

The limit condition between the previous two cases is evaluated through the following equation:

$$f'(f_{min}) = a f_{min} + b = 0 \quad \Rightarrow \quad f_{min} = -\frac{b}{a} = \frac{f_{\max} - \overline{f}\, c_{mult}}{1 - c_{mult}} \quad \Rightarrow \quad f_{min} \geq \frac{f_{\max} - \overline{f}\, c_{mult}}{1 - c_{mult}} \tag{4.3.6}$$

4.3.4 Elitism

Elitism consists in saving the "best" string of a population by inserting it in the subsequent. This expedient gives advantages in case of large population by preserving good solution other way deleted.

4.3.5 Online and offline performance

The online and offline parameters allow to control the evolution of the population during iterations. De Jong (1975) defined the online performance r_{ON} as:

$$r_{ON}(j) = \frac{1}{j}\sum_{k=1}^{j} f(x_k) \tag{4.3.7}$$

where *j* is a counter for the number of the string considering all the performed iterations.

The online performance represents the average value of the fitness within the iterations. The online performance is useful for adaptive system where the aim of the analysis is to assure a good behavior of all solutions. Note that the following equation allows to calculate the value of the online performance at string *j* once it is known its value for string *j*-1.

$$r_{ON}(j)=\frac{1}{j}\sum_{k=1}^{j}f(x_k)=\frac{j-1}{j}\left[\frac{1}{j-1}\sum_{k=1}^{j-1}f(x_k)\right]+\frac{f(x_j)}{j}=\frac{j-1}{j}r_{ON}(j-1)+\frac{f(x_j)}{j} \tag{4.3.8}$$

The offline performance is the similar to the online performance except for considering only the string with maximum fitness at each iteration:

$$r_{OFF}(j)=\frac{1}{j}\sum_{k=1}^{j}f_k^* \quad dove \quad f_k^*=\max\left(\{f(x_i):i=1,...,k\}\right) \tag{4.3.9}$$

Since the offline performance results the average of the maximum fitness strings (see equation (4.3.9)), it is the most useful parameter to control the optimization in maximum-minimum problem.

4.3.6 Dominium and binary code

Since the analyzed optimization problem involve a function which depends on a certain number of variable n_{var}, it is important to define how a set of these variables are transformed into a string of bits.

Let us consider a function of three variables x_1, x_2 e x_3 defined as follow:

$$(x_1,x_2,x_3)\in D \quad where \quad D=[-5,5]\times[-10,4]\times[1,7] \tag{4.3.10}$$

It is possible to represent the dominium D with an hyper-rectangles and discretize the dominium such as each point can be described by means of three integer point. Using a binary code and z bits, the dominium of each variables will be divided into 2^z parts. At interval i each integer number h_i will be associated a real number x_i according to:

$$x_i=x_i^1+\frac{x_i^2-x_i^1}{2^z}h_i \quad where \quad \begin{cases} x_i\in\left[x_i^1,x_i^2\right] \\ h_i=0,1,...,\left(2^z-1\right) \end{cases} \tag{4.3.11}$$

Equation (4.3.11) defines the transformation from integer into real. The next step is to convert the integer x_i into a binary s_i and to join all binary numbers to create a string S. The string will be the binary codification of the set x_1, x_2 e x_3.

$$S = s_1 s_2 ... s_{n_{\text{var}}} = a_1 a_2 ... a_m \quad where \quad a_j \in \{0,1\} \quad ; \quad m = \sum_{k=1}^{n_{\text{var}}} z_i$$
$$h_i = \sum_{j=1}^{z_i} a_{i*} 2^{j-1} \quad where \quad i* = \left(\sum_{k=1}^{i-1} z_i \right) + z_i - j + 1 \tag{4.3.12}$$

and where:

$$s_i = a_1 a_2 ... a_m \quad a_j \in \{0,1\}$$
$$h_i = \sum_{j=1}^{m} a_{m-j+1} 2^{j-1} \tag{4.3.13}$$

In the previous example, if the binary string assumes the following expression:

$$S = 1 \quad 0 \quad 0 \quad 1 \quad 1 \left| \right. \quad 1 \quad 0 \quad 1 \left| \right. \quad 0 \quad 1 \quad 1 \tag{4.3.14}$$

the second variable will be:

$$h_2 = 1 \cdot 2^0 + 0 \cdot 2^1 + 1 \cdot 2^2 = 5$$
$$x_2 = -10 + \frac{4 - (-10)}{2^3} 5 = -1.25 \tag{4.3.15}$$

For what concerns the position order of the variables into the string *S*, it is important to evaluate the degree of correlation between the variables. For example the correlation between variable x_1 and variable x_2 can be calculated by deriving the objective function *f* with respect to both variables:

$$\frac{\partial^2 f}{\partial x_2 \partial x_1} \left(x_1, ..., x_{n_{\text{var}}} \right) = 0 \quad \Rightarrow \quad \text{indipendent variables}$$
$$f \left(x_1, ..., x_{n_{\text{var}}} \right) = \sum_{k=1}^{n_{\text{var}}} c_k x_k \quad \Rightarrow \quad \frac{\partial^2 f}{\partial x_i \partial x_j} \left(x_1, ..., x_{n_{\text{var}}} \right) = 0 \quad \forall i, j \tag{4.3.16}$$

If the derivative is equal to zero then the two variables are not correlated. (note that *f* must be of C^1 class). Inorder to assure string variation within the dominium, the string must be built such as not correlated variable are close one each other.

4.3.7 Grey binary code

In order to give an exhaustive overview of genetic approaches it is important to remind that in the common binary codification, two subsequent integer number can differ for a high number of bit. For example 63 and 64 have 7 different bits when a 7 bits binary code is used.

$$0111111 \quad \rightarrow \quad 63$$
$$1000000 \quad \rightarrow \quad 64 \tag{4.3.17}$$

This condition provides very different code for similar values and does not maintains bad conditioned values close one each other. The use of the Grey binary code can avoid this problem.

$$S = s_1 s_2 ... s_{n_{var}} = a_1 a_2 ... a_m \quad where \quad a_j \in \{0,1\} \quad ; \quad m = \sum_{k=1}^{n_{var}} z_i$$
$$h_i = \sum_{j=1}^{z_i} \left(\bigoplus_{k=1}^{z_i - j - 1} a_{i*} \right) 2^{j-1} \quad where \quad i* = \left(\sum_{k=1}^{i-1} z_i \right) + k \tag{4.3.18}$$

Equation (4.3.18) define the new binary codification where the operator $\oplus$ is defined as follow:

$$a_1, a_2 \in \{0,1\} \quad , \quad a_1 \oplus a_2 = \begin{cases} 0 & if \quad a_1 = a_2 \\ 1 & if \quad a_1 \neq a_2 \end{cases} \tag{4.3.19}$$

The operator $\oplus$ is equivalent to a XOR (exclusive OR) operator:

a_1	a_2	c
0	0	0
1	0	1
0	1	1
1	1	0

Table 57: Truth table for XOR operator.

Using Grey code the first 8 integer number can be defined as follows:

0	1	2	3	4	5	6	7
000	001	011	010	110	111	101	100

Table 58: First 8 number with Grey binary code.

4.3.8 Validation of the genetic approach

In order to validate the genetic approach a simple validation procedure has been tested on a maximum-minimum analytical problem.

Let us consider the following function:

$$f(x,y) = \sin(x)\cos(y) \qquad x \in [-5,5] \quad y \in [-5,5] \tag{4.3.20}$$

If the gradient of the function is equalized to zero, the following maximum values can be calculated within the dominium $x \in [-5,5] \quad y \in [-5,5]$.

$$\left[-\frac{\pi}{2}, -\pi\right] \quad \left[-\frac{\pi}{2}, \pi\right] \quad \left[-\frac{3}{2}\pi, 0\right] \quad \left[\frac{\pi}{2}, 0\right] \quad \left[\frac{3}{2}\pi, -\pi\right] \quad \left[\frac{3}{2}\pi, \pi\right] \tag{4.3.21}$$

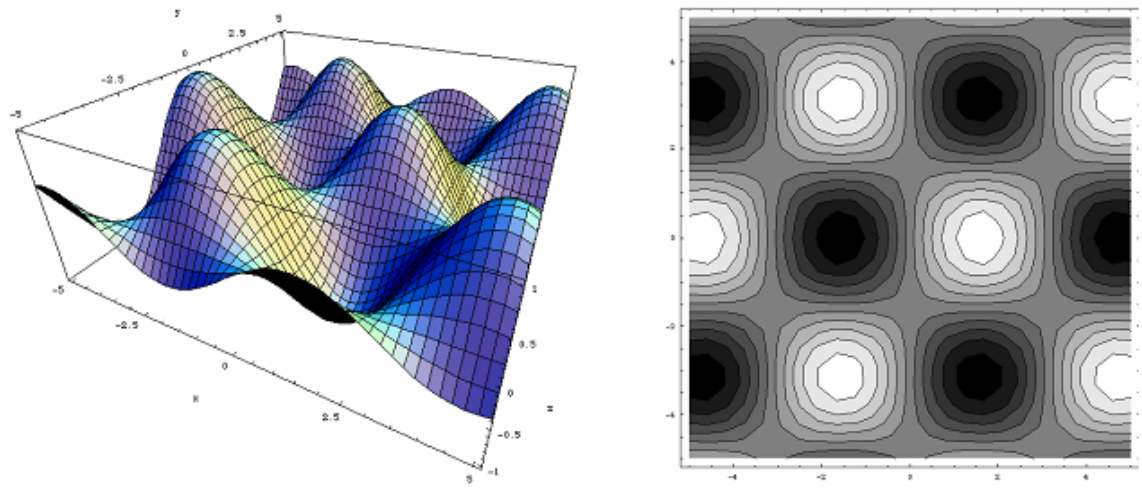

Figure 144: Plots of function f.

The described function can be modulated by means of the following equation:

$$g(x) = -\left(x + \frac{\pi}{2}\right)^2 + \frac{(\pi+10)^2}{4} \tag{4.3.22}$$

Function *g(x)* is a parabola with a maximum in [-π/2 ; -π] and always positive within the dominium of *f(x,y)*. The modulated function has the following expression:

$$\tilde{f}(x,y) = \left[-\left(x + \frac{\pi}{2}\right)^2 + \frac{(\pi+10)^2}{4}\right]\left[-(y+\pi)^2 + (\pi+5)^2\right]\sin(x)\cos(y) \tag{4.3.23}$$

$\tilde{f}(x,y)$ is always positive, has multiple relative maximum and one absolute maximum within the specified dominium; for its properties this function is a suitable function for testing a genetic approach able to find the absolute maximum within the dominium.

Figure 145 shows a plot of the function $\tilde{f}$:

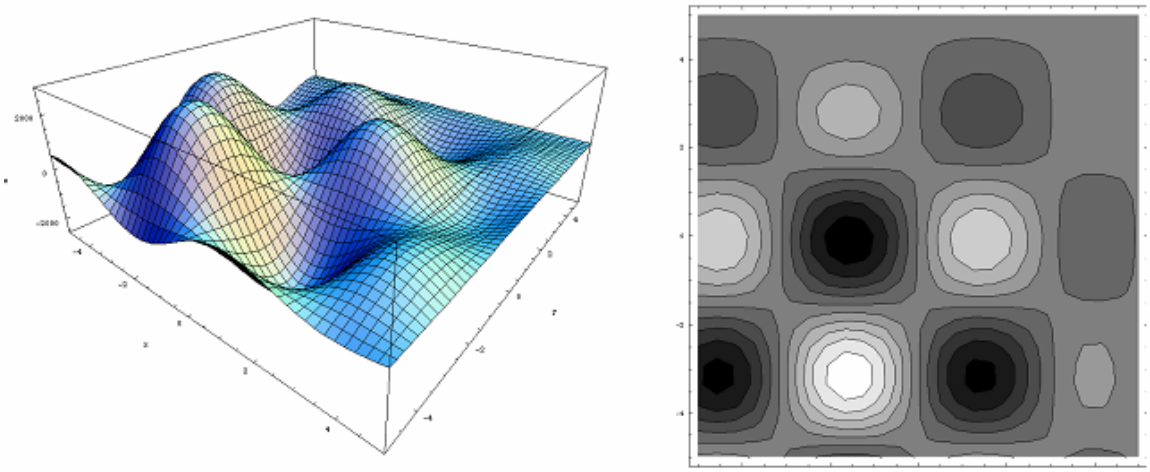

Figure 145: Plots of function $\tilde{f}$.

The absolute maximum corresponds to:

$$\tilde{f}(x,y) = \tilde{f}\left(-\frac{\pi}{2}, -\pi\right) = 2861.90195054543 \tag{4.3.24}$$

Four different genetic algorithms are tested on equation (4.3.23) and the behavior of each is discussed based on online and offline performance. Note that in this case, the fitness corresponds to the value of $\tilde{f}$ for a given string. The following chart lists the characteristic of each algorithm (details on random selection algorithm are provided in the following):

Simulation parameters	**caso1**	**caso2**	**caso3**	**caso4**
Number of bits in the string *m*	32 (16x2)	32 (16x2)	32 (16x2)	32 (16x2)
Number of strings in the population *n*	200	200	200	200
Crossover probability p_c	0.6	0.6	0.6	0.6
Mutation rate p_m	0.033	0.033	0.033	0.033
Multiplier for the fitness scaling c_{mult}	1.5	1.5	1.5	1.5
Number of iteration *niter*	200	200	200	200
Type of genetic algorithm	Stochastic sampling with replacement	Stochastic reminder selection without replacemement	Stochastic reminder selection without replacemement	Random selection
Binary code	Classic	Classic	Grey	-
Elitism	Yes	Yes	Yes	Yes

Table 59: Details of the developed genetic algorithms.

A first analysis is conducted between caso1 and caso2, in order to compare the SGA "stochastic sampling with replacement" and the "stochastic reminder selection without replacemement" approaches.

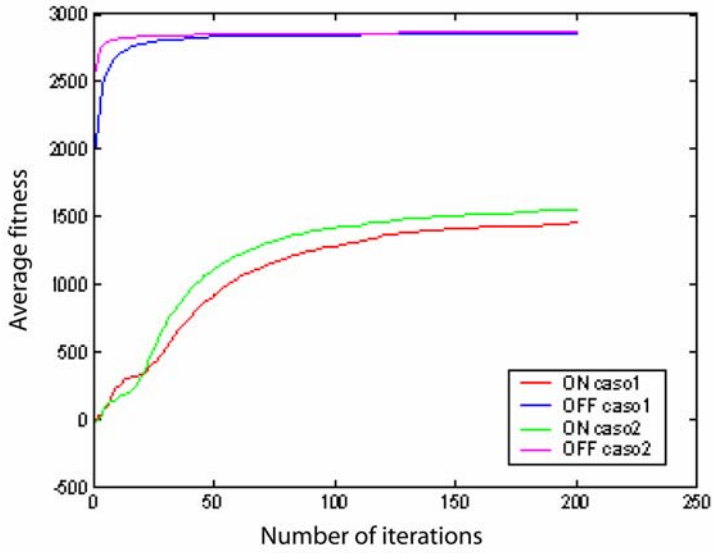

Figure 146: Comparison between caso1 and caso2: caso1 online performance (red); caso1 offline performance (blue); caso2 online performance (green); caso2 offline performance (magenta).

The offline performance shows that the "stochastic reminder selection without replacemement" converges to the maximum value, faster then the SGA. Same results are obtained considering the online performance even if the SGA technique performs better in the first 30 iterations. This comparison results in the choise of the "stochastic reminder selection without replacemement" method for the further analysis.

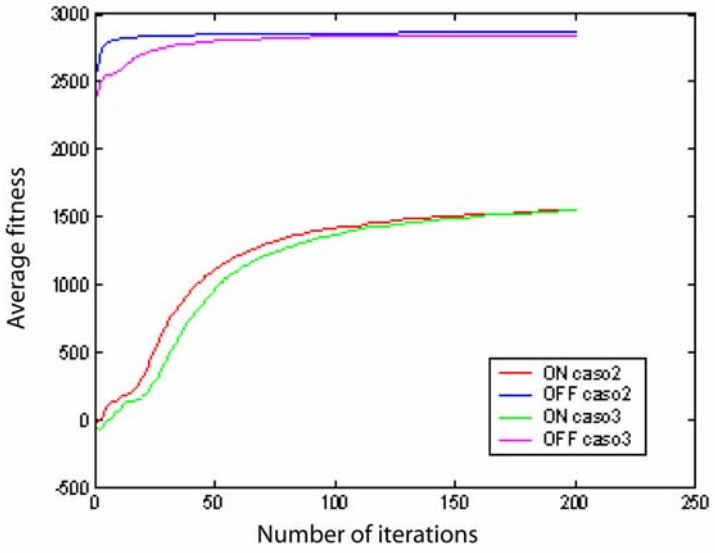

Figure 147: Comparison between caso2 and caso3: caso2 online performance (red); caso2 offline performance (blue); caso3 online performance (green); caso3 offline performance (magenta).

A second test is carried out to analys the effect of the Grey binary code with respect to the classical binary representation. For this reason a similar simulation is performed for caso2 and caso3.

Figure 147 shows that the Grey codification approach does not improve the performances of the genetic algorithm in the case of tested maximum-minimum problem. A probable reason could be related to the analysis parameters listed in Table 59; the values of p_c, p_m and c_{mult} has been chosen according to literature (De Jong, 1975) for a SGA applications. For example it is possible that using an higher mutation ratio can results in a better performance of the Grey code. Indeed the application of the standard binary code is less deterministic, a small change in a bit can cause a large movement within the dominium.

For the present application the standard binary code wil be use in the following application.

Since caso2 have better performance, a plot of the maximum fitness with respect to the iterations are presented for this case:

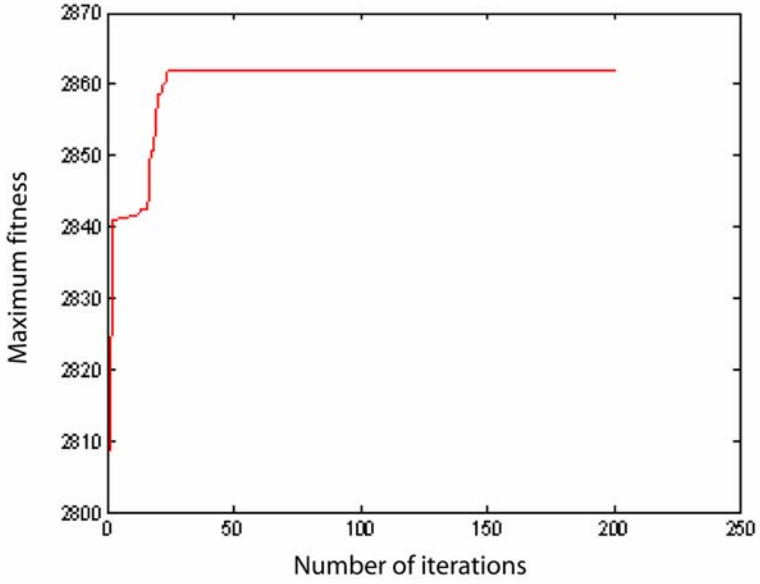

Figure 148: Maximum fitness versus iterations for the caso2.

After 50 iterations the fitness maximum converge to the following value:

Case	Analitycal	Caso2	Difference
Maximu value	2861.90195054543	2861.90163863698	$-1.0899\ 10^{-7}$

Table 60: Coparison of the maximum for function $\tilde{f}$.

Note that the machine precision is of the order 10^{-16}.

The result of Table 58 can be appear not sufficiently accurate. Indeed a complete comparison must also takes into account the discretization of the dominium.

Equation (4.3.25) shows the calculation of discretization step used for both x and y variables:

$$\Delta_x = \Delta_y = \frac{x^2 - x^1}{2^z} = \frac{5-(-5)}{2^{16}} = 1.5294 \cdot 10^{-4} \tag{4.3.25}$$

The coordinates of the maximum point calculated by means of the case2 approach are:

$$(-1.57068741893645, -3.14114595254444) \tag{4.3.26}$$

It is possible to compare these values with the relative analytic value (see equation (4.3.24)); the differences are :

$$(1.089\ 10^{-4},\quad 4.467\ 10^{-4}) \tag{4.3.27}$$

Which have the same order of the discretization step. For this reason previous results must be considered accurated.

A final test is carried out to check the performance of the genetic approach with respect to a purely random technique.
Performing n_{iter} iterations with a population of n strings the number of total strings created by the SGA alghorithm is n^*:

$$n^* = n_{iter}\,(n-1) \tag{4.3.28}$$

Note that equation (4.3.28) takes into account the elitism step which save the best string at each iteration.
The purely random technique will randomly create n^* strings within the dominium and will store the maximum obtained value. Note that each string will have a randomly selection procedure for each bit.

The coordinates of the maximum point calculated by means of the caso4 approach are:

$$(-1.5131609063859, -3.17364766918441) \tag{4.3.29}$$

The differences with respect to the analytical solution are much higher then those obtained for caso2:

$$(0.0576, -0.0321) \tag{4.3.30}$$

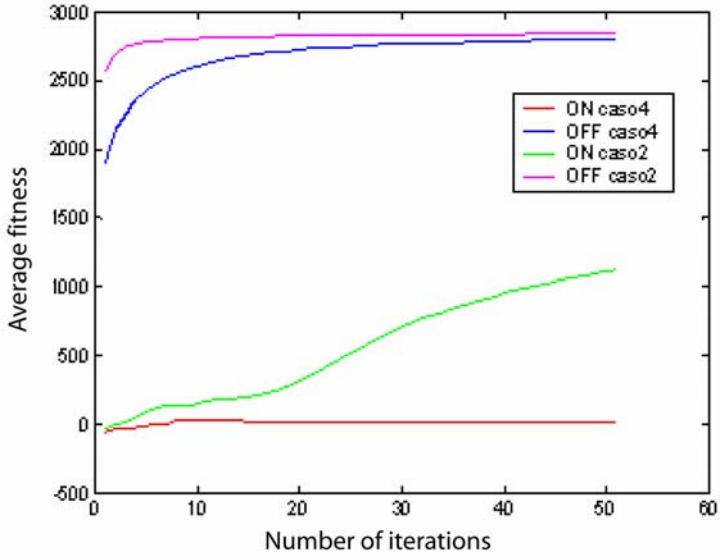

Figure 149: Comparison between caso2 and caso4: caso4 online performance (red); caso4 offline performance (blue); caso2 online performance (green); caso2 offline performance (magenta).

Figure 149 shows the performance comparison between the two cases. The online performance behavior clearly shows how the genetic algorithm is able to recognized the dominium area where the best results are located. For what concern the offline behavior the two results seems to be similar. This is due mainly to the fact that function $\tilde{f}$ depends only by two varables.

4.3.9 Implemented SGA genetic algorithm

In this work a general purpose optimization procedure has been developed based on a SGA genetic algorithm with elitism. The flux diagram of the algorithm can be described as follows:

1. Generation of a random initial population;
2. Calculation of the fitness of each population string;
3. Extraction of the a new population according to fitness
4. Random grouping of population strings;
5. Random cutting and crossing between strings;
6. Application of the bit mutation according to p_m probability.
7. Calculation of the new strings fitness and location of the maximum and minimum fitness within the population;

8. Substitution of the worst string of the new population with the best string of the previous population if the first string has worst fitness then the second one;
9. Repetition of step 3-8 for an arbitrary number of iterations.

All steps has been implemented into a Matlab® code according to the scheme described in Figure 150.

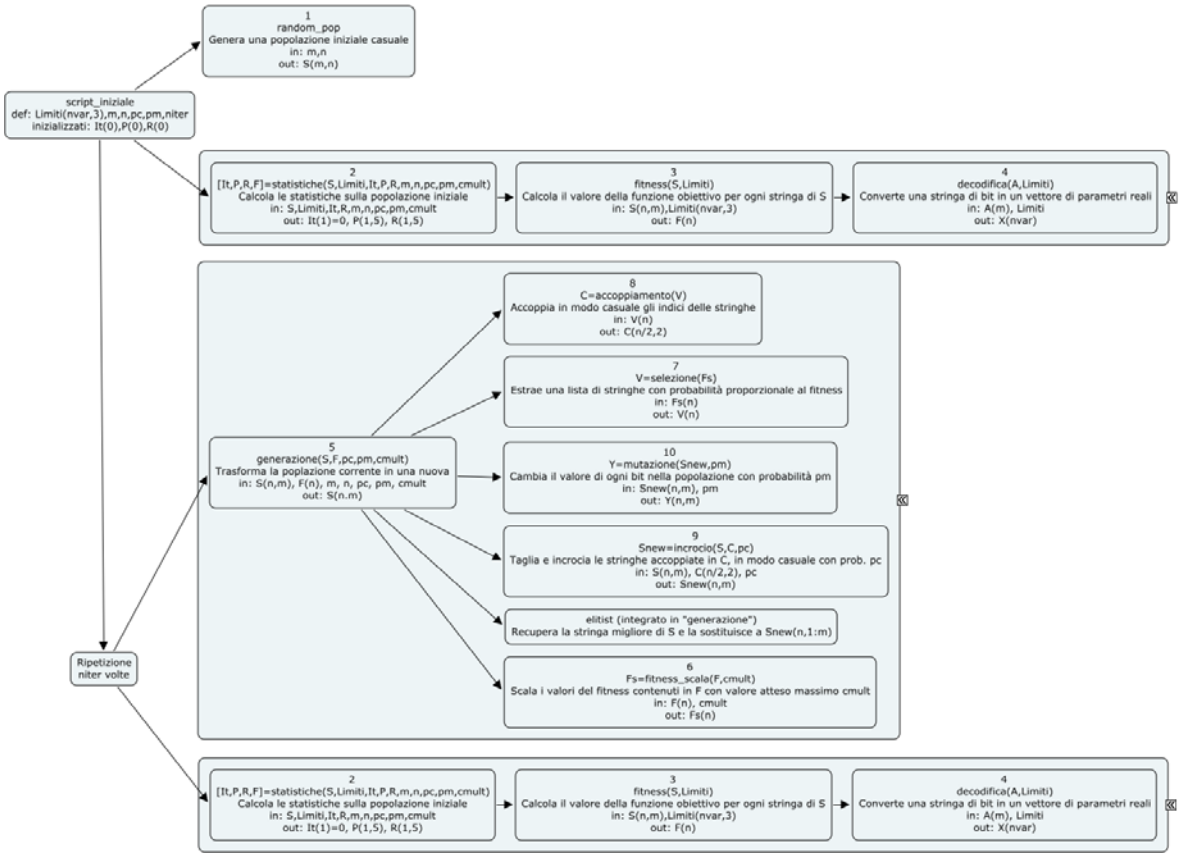

Figure 150: Scheme of the implemented SGA algorithm.

The scheme illustrates the relationships between the previous flux diagram and the hierarchical structure of the Matlab® application.

script_iniziale

"script_iniziale" is the main script of the code. All the parameters of the algorithm and the dominium of the objective function are defined inside this script.

Parameter	**Meaning**
n	Number of string in the population
p_c	Crossover probability
p_m	Mutation rate
c_{mult}	Multiplier for the fitness scaling
nvar	Number of independent variable of the objective function
Limits	Contains dominium and the binary code information (number of bit to represent the variable) of each variables
niter	Number of iteration to be done

Table 61: Parameters defined in script_iniziale.

Note that from these values it is possible to calculate the string length *m* and that the number of string within the population must be even to allow a proper crossover.

statistiche

This function calculate the string fitness for a given population. “statistiche” creates three matrix with the following content:

- R: contains the properties of the population fitness such as maximum, minimum and average fitness values, the online and offline performance and the lost alleles (see Table 62) .
- P: contains the iteration parameters such (see Table 62). In this way it is possible to change some of the parameters after a certain number of iteration. For example after 100 iteration it is possible to replace the last 30 by running 80 new iterations with different value of the mutation probability. This possibility is useful when the algorithm restricts the search dominium.
- It: contains progressive number which allows to record the number of performed iterations.

Column	**1**	**2**	**3**	**4**	**5**
Content	m	n	p_c	p_m	c_{mult}

Table 62: Content of a row of matrix P.

Column	**1**	**2**	**3**	**3**	**4**	**5**
Descrizione	Average fitness	Minimum fitness	Maximum fitness	Online performance	Offline performance	Lost alleles

Table 63: Content of a row of matrix R.

All lost alleles are detected by checking each bit within the strings of the population

fitness

This script contains the definition of the objective function and therefore calculate the fitness for a given string.

fitness_scala

This script executes the scaling process according to equations (4.3.4) or (4.3.5).

decodifica

This script creates string according to equations (4.3.12) and (4.3.13) or according to Grey code.

selezione

This script generates a new population according to the "stochastic sampling with replacement" technique.

incrocio

This script executes the crossing over process.

mutazione

This script executes the crossing over process.

elitism

This script executes the elitism process.

4.3.10 Application of the genetic alghorithm to spur gears pair

In this section some applications of the genetic algorithm are proposed for case study 2.

The used approach is based on a binary codification (classic binary code) of the 10 parameters which control the set of profile modifications on both pinion and gear profiles. Note that all reliefs are considered linear.

The extension of the dominium of each variable is described in Table 64:

Parameter	From	To
$\varphi_{t,s}$	Pitch point	Tip circle
mag_t	0	40 μm
$\varphi_{r,s}$	Pitch point	SAP
mag_r	0	40 μm

Table 64: Dominium of variable parameters for the genetic optimization.

Each dominium is discretized according to Table 65:

Parameter	Number of points	Number of bits
$\varphi_{t,s}$	2048	11
mag_t	64	6
$\varphi_{r,s}$	2048	11
mag_r	64	6

Table 65: Discretization of profile modification variable.

The discretization of Table 65 allows to obtain at least a discretization step of 1 μm on the magnitude and step 1 μm on the roll angle radius (see equation (1.2.6)).

The string has a number of bit equal to the sum The previous table show the number of bit required for the representation of each variable dominium.

The string used for the genetic algorithm, has 68 bits since this number is equal to the total number of bits (*m*) used to represent the variables.

Figure 151 shows the graphical representation of the string. According to theory the order of the variables within the string maintains close the not correlated variables to assure variation within the dominium.

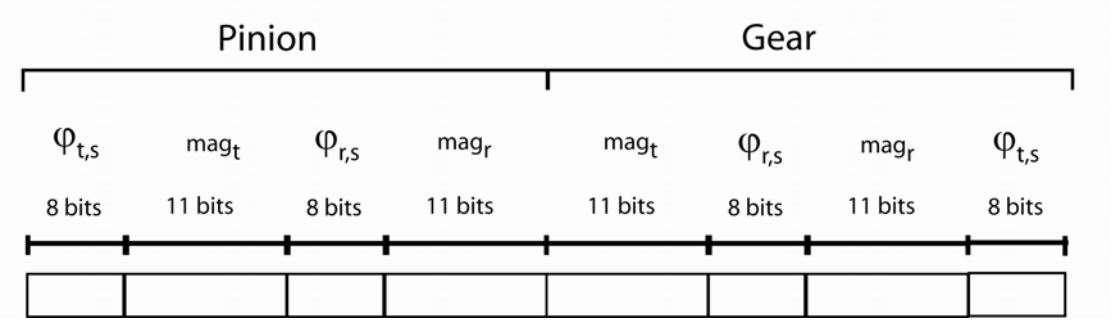

Figure 151: Codification of the profile modification in a string.

Once the string is composed, a calculation of the STE is performed according to previous sections. The number of sample in a mesh cycle is set to 15 and the analytical reconstruction is based on 7 harmonics components.

Four different simulations are performed; each case has a different objective function or a different number of iterations according to Table 66:

Case study	Objective function	Number of iterations
Case D	Minimum peak to peak of STE	100
Case E	Minimize the average of the first 3 harmonic components of STE	100
Case G1000	Minimize the average of the first 7 harmonic components of STE	1000
Case H1000	Minimize the maximum of the first 7 harmonic components of STE	1000

Table 66: Case studies for the genetic otimization approach.

The same simulation parameters are used for all cases (see Table 67):

Number of bits in the string *m*	*68*
Number of strings in the population *n*	*50*
Crossover probability p_c	*0.6*
Mutation rate p_m	*0.033*
Multiplier for the fitness scaling c_{mult}	*1.5*

Table 67: Simulation parameters.

Values for p_c, p_m and c_{mult} are taken from literature (De Jong, 1975).

The simulations provides the following results in terms of profile modifications parameters:

	Case D		**Case E**	
	Pinion	**Gear**	**Pinion**	**Gear**
Tip relief				
$type_t$	Linear	Linear	Linear	Linear
$\varphi_{t,s}$ [Deg]	31.627	30.625	31.619	30.193
mag_t [mm]	0.026032	0.020952	0.019048	0.015238
Root relief				
$type_r$	Linear	Linear	Linear	Linear
$\varphi_{r,s}$ [Deg]	23.035	24.098	24.203	25.056
$\varphi_{t,e}$ [Deg]	14.433	20.576	14.433	20.576
Tip relief	0.0057143	0.0025397	0.011429	0.0063492

Table 68: Resulting profile modifications according to simulations: case D and case E.

	Case G1000		**Case H1000**	
	Pinion	**Gear**	**Pinion**	**Gear**
Tip relief				
$type_t$	Linear	Linear	Linear	Linear
$\varphi_{t,s}$ [Deg]	31.753	30.141	31.472	30.328
mag_t [mm]	0.015238	0.019048	0.026667	0.019682
Root relief				
$type_r$	Linear	Linear	Linear	Linear
$\varphi_{r,s}$ [Deg]	23.187	24.605	21.331	26.564
$\varphi_{t,e}$ [Deg]	14.433	20.576	14.433	20.576
mag_r [mm]	0.010159	0.014603	0.012064	0

Table 69: Resulting profile modifications according to simulations: case G1000 and case H1000.

4.3.11 Results and comparisons

In this section comparison between genetic optima and the heuristic optimum is provided by means of comparison of semi-amplitude/frequency diagrams. All dynamics simulations considers the adaptive step-size Gear algorithm and the hyperbolic tangent smoothing backlash function with an initial position equal to $\dot{v}_1(0) = 1.0001$ and an initial speed of $\dot{v}_2(0) = 0.00001$ for the first speed analyzed. The integration tolerance is 10^{-8}. The applied torque is 470 Nm, the damping $\zeta = 0.01$ and no manufacturing error *e(t)*=0 are included.

The static transmission error is calculated for 15 positions within a mesh cycle, and the approximation for the stiffness function used 7 harmonics.

The following tables shows the harmonic content of the mesh stiffness used for the dynamic simulations:

Normalized stiffness component	**Value**				
	Case D	**Case E**	**Case G1000**	**Case H1000**	**Case Hp**
$\overline{k}_{d,1}$	3.752193 10^{-3}	1.028101 10^{-3}	2.975343 10^{-3}	8.829487 10^{-3}	8.828812 10^{-3}
$\overline{k}_{d,2}$	1.194203 10^{-2}	9.635169 10^{-3}	9.064506 10^{-3}	8.724595 10^{-3}	8.724466 10^{-3}
$\overline{k}_{d,3}$	5.856541 10^{-3}	1.919085 10^{-3}	5.117514 10^{-4}	3.613242 10^{-3}	3.612043 10^{-3}
$\overline{k}_{d,4}$	6.665899 10^{-3}	1.244864 10^{-2}	1.005772 10^{-2}	7.262569 10^{-3}	7.263183 10^{-3}
$\overline{k}_{d,5}$	4.625099 10^{-3}	2.393211 10^{-3}	1.633575 10^{-3}	3.367069 10^{-3}	3.367713 10^{-3}
$\overline{k}_{d,6}$	1.668823 10^{-3}	3.82011 10^{-3}	1.491529 10^{-3}	5.715802 10^{-4}	5.70438 10^{-4}
$\overline{k}_{d,7}$	1.606652 10^{-3}	3.144733 10^{-3}	1.702096 10^{-3}	2.321127 10^{-3}	2.322295 10^{-3}

Table 70: Normalized mesh stiffness components used for the dynamic simulations.

Phase [rad]	**Value**				
	Case D	**Case E**	**Case G1000**	**Case H1000**	**Case Hp**
φ_1	-0.2241531	0.1062465	-0.9378188	-0.04870337	-0.04858557
φ_2	-0.1787807	-0.3990678	-0.07907809	-0.4234867	-0.4236278
φ_3	-2.961203	0.6414558	3.122596	2.887299	2.887213
φ_4	2.867716	-3.064962	-2.978783	-3.14147	3.141568
φ_5	-1.144825	-0.8636339	-0.4594357	-1.073386	-1.073699
φ_6	2.468738	0.0707361	-0.1633323	2.747065	2.746232
φ_7	1.59394	2.885404	2.729787	1.760166	1.760341

Table 71: Harmonic phases of normalized mesh stiffness used for the dynamic simulations.

COMPARISON 1

Figure 152 shows a semi-amplitude/frequency comparison between heuristic optimum, obtained in the previous sections, case D and case E.

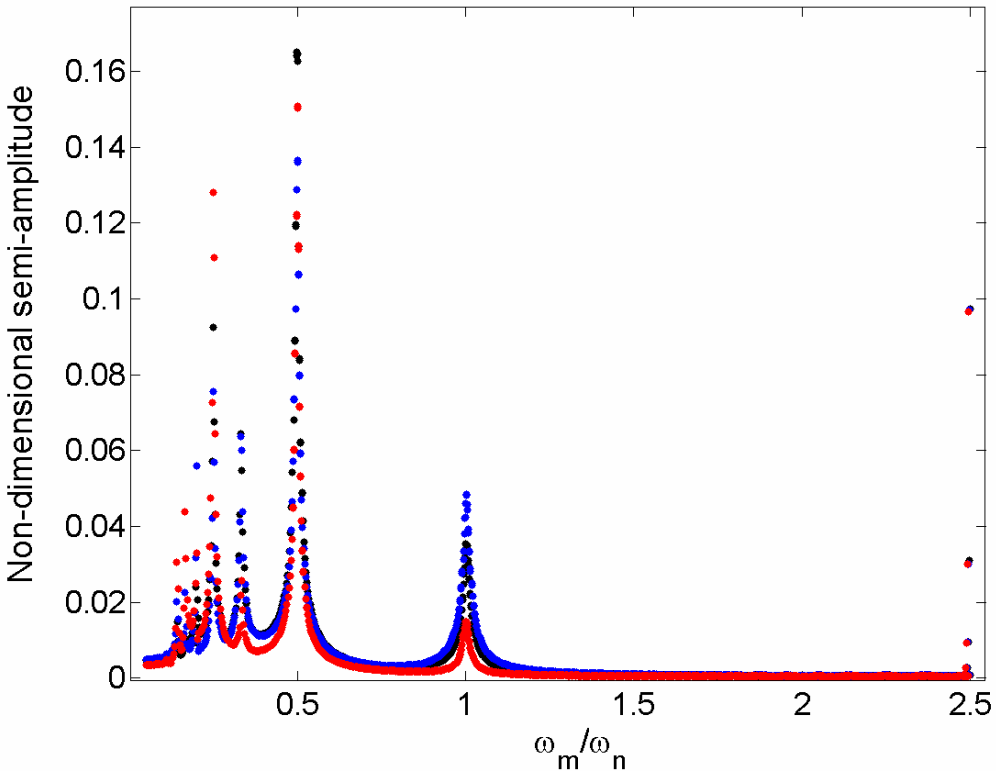

Figure 152: Comparison of semi-amplitude/frequency diagram: heuristic optimum (black); genetic optimization case D (blue); genetic optimization case E (red).

Figure 153 shows the harmonic content of the STE for the heuristic optimum, case D and case E.

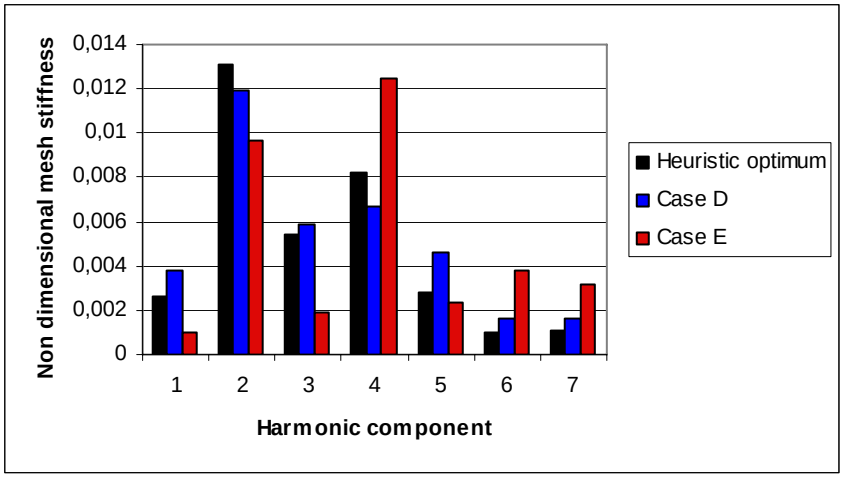

Figure 153: Harmonic content of the STE: heuristic optimum (black); genetic optimization case D (blue); genetic optimization case E (red)

Table 72 shows peak to peak values of the mesh stiffness and of the STE for the heuristic optimum, for case D and for case E.

	Heuristic optimum	**Case D**	**Case E**
Stiffness pk to pk [N/m]	$1.12055\ 10^7$	$1.15468\ E\ 10^7$	$1.45774\ 10^7$
STE pk to pk [μm]	1.70299	1.73964	2.19356

Table 72: Peak to peak values of the mesh stiffness and STE.

The previous diagrams and Table 72 yield to the following considerations:

1. No solution shows parametric resonances;
2. No solution shows non linear effects such as contact loosing or softening behaviors;
3. Despite case D and E has higher peak to peak values, the response at almost all frequencies, is very similar to the one given by the heuristic optimum
4. Case E appears to have the best behaviour at high frequency and the worst at low frequencies. This is the effect of the harmonic content of the STE. Indeed Figure 153 shows that, case E has larger harmonic content for the higher harmonics, which are the excitation source for the super harmonic resonances at low frequencies.
5. Despite case D has not the highest value of the STE peak to peak, it has the higher primary resonance. This is due to the contribution of the first harmonic component.

The previous results clarify that a genetic optimization of the STE, in term of peak to peak value (case D), does not give the best results. When the objective function involve a minimization of the average of the first 3 harmonic components (case E) better results are obtained.

COMPARISON 2

The previous analysis prove that the harmonic content must be controlled as well as the peak to peak value. A second comparison is carried out by considering an objective function which minimize the average value of all the seven harmonic component (case G). Furthermore the number of iteration has been increased to 1000.

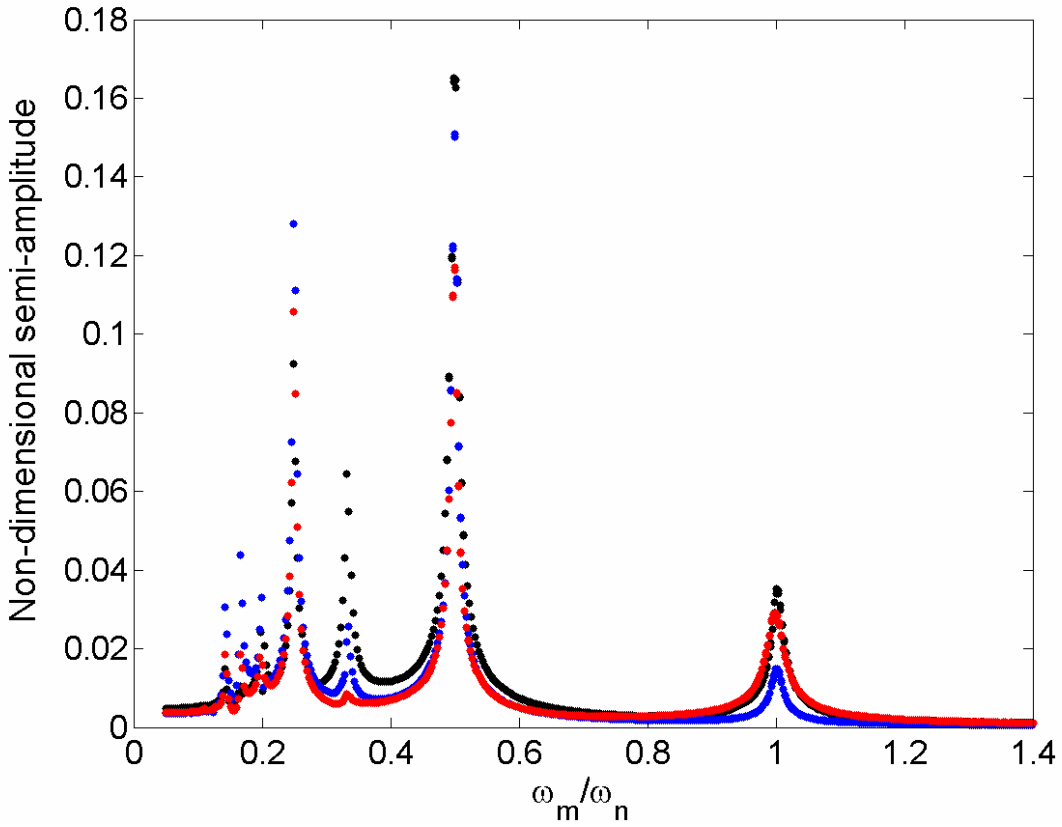

Figure 154: Comparison of semi-amplitude/frequency diagram: heuristic optimum (black); genetic optimization case E (blue); genetic optimization case G1000 (red).

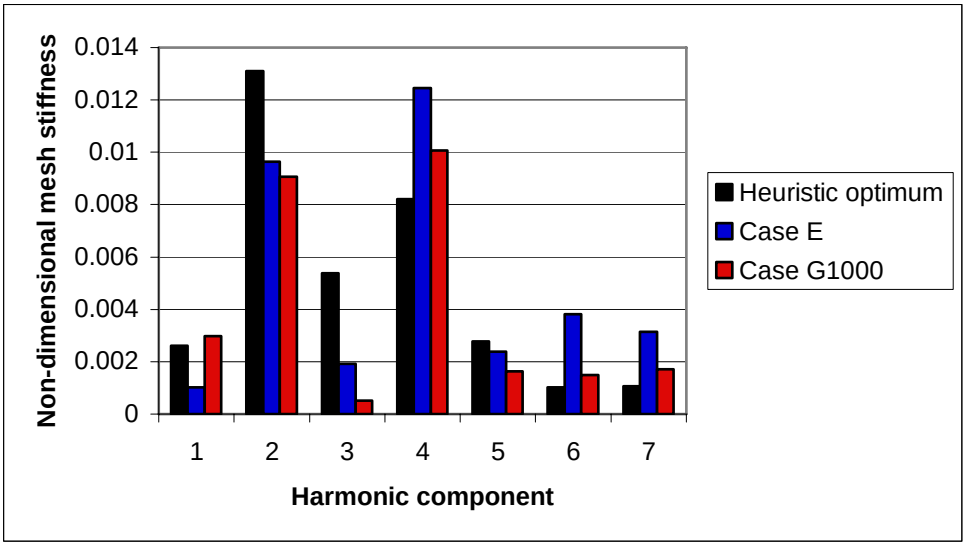

Figure 155: Harmonic content of the STE: heuristic optimum (black); genetic optimization case E (blue); genetic optimization case G1000 (red).

Figure 154 and Figure 155 show respectively the semi-amplitude/frequency diagram and the harmonic content of the STE for the heuristic optimum, case D and case E.

In this simulation case G1000 has an excellent behavior at almost all frequencies, except for the primary and the fourth super harmonic resonances. Table 73 explains, once again, that the minimization of the peak to peak value of the STE does not involve necessarily a lower amplitude of the primary harmonic.

	Heuristic optimum	**Case E**	**Case G1000**
Stiffness pk to pk [N/m]	$1.12055\ 10^7$	$1.45774\ 10^7$	$1.10304\ 10^7$
STE pk to pk [µm]	1.70299	2.19356	1.67044

Table 73: Peak to peak values of the mesh stiffness and STE.

COMPARISON 3

The last comparison considers case G1000 and case H1000. In case G1000, the average of the 7 harmonic components of the STE is minimized, in case H1000 the maximum harmonic component (within the all 7 harmonics) is minimized. Results are compared with the heuristic optimum. The same number of iteration are considered between the two genetic cases.

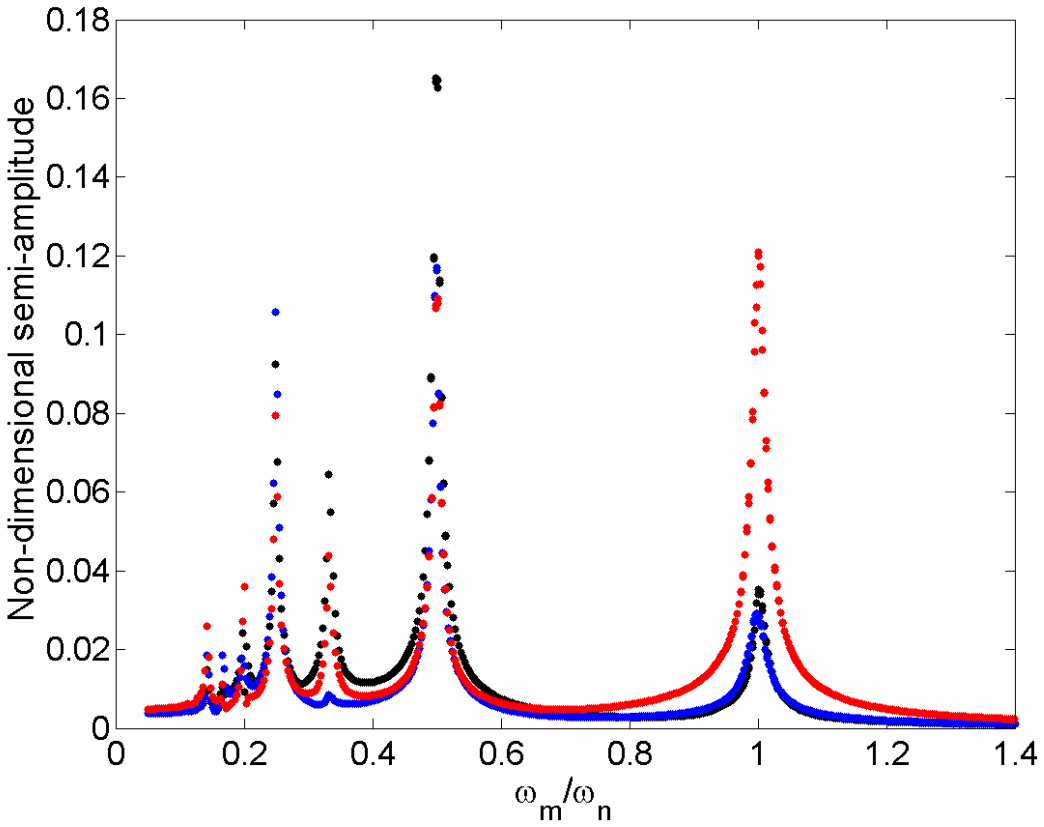

Figure 156: Comparison of semi-amplitude/frequency diagram: heuristic optimum (black); genetic optimization case G1000 (blue); genetic optimization case H1000 (red).

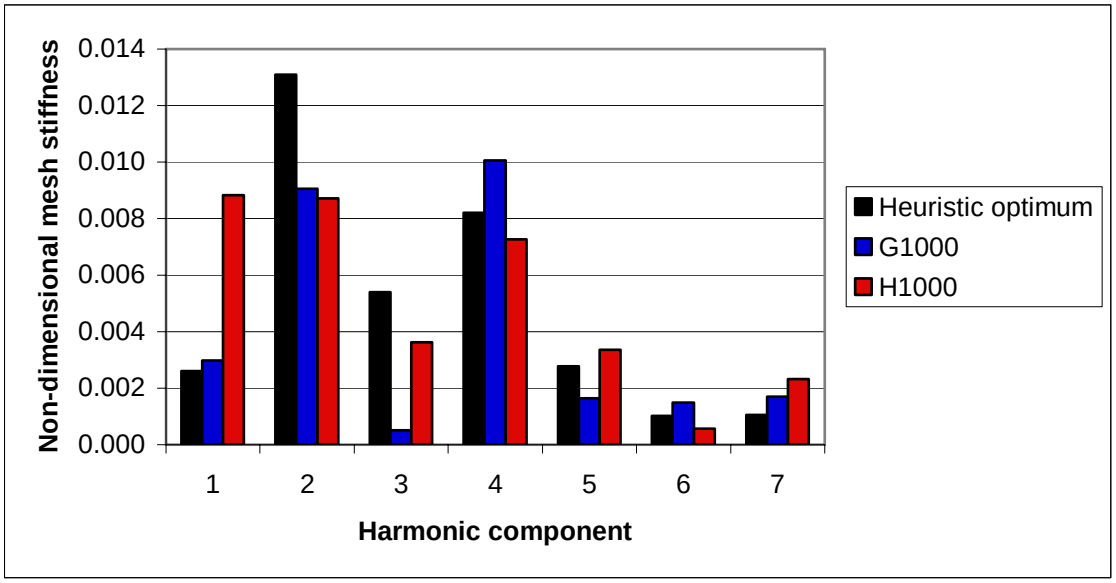

Figure 157: Harmonic content of the STE: heuristic optimum (black); genetic optimization case G1000 (blue); genetic optimization case H1000 (red).

	Heuristic optimum	**Case G1000**	**Case H1000**
Stiffness pk to pk [N/m]	$1.12055\ 10^7$	$1.10304\ 10^7$	$1.20327\ 10^7$
STE pk to pk [μm]	1.70299	1.67044	1.81662

Table 74: Peak to peak values of the mesh stiffness and STE.

Dynamic simulations shows that the best results are obtained for case G1000, which minimize the average values of the seven harmonics.

Despite the implemented genetic algorithms provide better results with respect to heuristic approaches, all previous comparison predict that it is very difficult to minimize all harmonic content. Indeed even if the vibration level decrease for a wide range of frequencies, there is always at least one component which cannot be reduce.

For this reason improvements in the definition of the objective function must be carried out. A starting point, for future work, can be the idea of minimizing the harmonic content of the STE by means of weight averages. This will allows to concentrate the efforts of the algorithm at those particular frequencies that can be dangerous for the system stability.

Conclusion

In the present work the static and dynamic behavior of spur gears systems has been studied.
In Chapter 1 basic fundamentals of spur gear geometry has been provided focusing on macro geometry and mounting parameters. Particular attention has been paid to the description of the tooth profile by means of the theory of meshing. The given formulation is suitable for a industrial application, where gears profiles are defined through the manufacturing process and the cutting tool geometry.
In Chapter 2 an original gear "mesh" generator is described for a pair of spur gears. Routines for the discretization of the involute profile, throcoidal fillet and rim sectors, are presented with some examples. The developed procedure provides an automatic tool capable to generate a FE model of a spur gear pair for an arbitrary number of relative positions of the two wheels. Calculation of the STE for a given number of meshing position within a mesh cycle, are used to test the method. Comparisons with commercial codes show excellent agreement. In the second part of the chapter a unique modeling technique for analyzing complex gears systems, such as multi mesh systems, is described. The presented model take advantage of a new combined semi-analytical FEM solutor Calyx®, which allows to perform static analysis of large gears system with great accuracy. Details of the modeling procedure are provided by means of a compound planetary system example, including bearings effects. Results show the possibility of studying stresses behavior and bearing displacements and reactions during system rotation.
Chapter 3 focuses on the dynamic of a spur gears pair. A single degree of freedom, dynamic model is illustrated which is able to include backlash, damping, variable mesh stiffness and back-side contact effects. Validations of the model are provided by means of comparison with literature and experimental test. Some case studies show the effect of design parameters, such as profile modifications and manufacturing errors. Instability regions and chaotic behavior are also analyzed.
Chapter 4 is completely dedicated to spur gear optimization. Since micro geometry affects the dynamics of gears systems, the main idea is to design a correct set of profile modifications capable to reduce gears vibrations. Two optimization approaches are formulated: the first is based on a heuristic technique, the second one on genetic algorithms. Applications of the two methodologies to actual spur gears pairs and dynamic simulations show how gears vibration

can be reduced. Furthermore advantages and disadvantages of the two approaches are also underlined.

Acknowledgment:

The author thanks: Case New Holland (Italy) for supporting the present research; Advanced Numerical Solutions (USA) for providing the software CALYX®.

References

1. AGMA 913-A98, 1998. Method for Specifying the Geometry of Spur and Helical Gears.
2. AGMA 2001-B88, 1988. Fundamental Rating Factors and Calculation Methods for Involute Spur and Helical Gear Teeth, AGMA Standard.
3. AGMA 2101-C95, 1995. Fundamental Rating Factors and Calculation Methods for Involute Spur and Helical Gear Teeth, Metric version of the AGMA Standard 2001-C95.
4. Almen, O., Straub, J.C., 1937. Durability of Automotive Transmission Gears, SAE.
5. Amabili, M., Rivola, A., 1997. Dynamic analysis of spur gear pairs: steady-state response and stability of sdof model with time-varying meshing damping, Mechanical systems and signal processing, 11(3), 375-390.
6. Andersson, A., Vedmar, L., 2003. A dynamic model to determine vibrations in involute helical gears, Journal of Sound and Vibration, 260, 195-212.
7. Andrisano, A.O., Bertacchi, G., Bonori, G., Faggioni, M., Pellicano, F., Amedei, G., Montanari, P., Seghedoni, C., 2005. Modellazione bidimensionale CAD FEM di coppie d'ingranaggi cilindrici, Proceedings of HTCES2005 Automobili e motori High-Tech, Modena, Italy.
8. Andrisano, A.O., Bertacchi, G., Bonori, G., 2005. Integrated CAM-FEM procedure to create bidimensional spur gear model, Proceedings of XVII INGEGRAF – XV ADM Congreso International Conjuncto, Sevilla, Spain.
9. Arikan, M.A.S., 1996. Effect of Addendum Modification on Spur Gear Dynamic Loads, Proceedings of Power Transmission and Gearing Conference ASME, DE-Vol. 88.
10. Azar, R.C., Crossley, F.R.E., 1977. Digital simulation of impact phenomenon in spur gear system, Journal of Engineering for Industry, 792-798.
11. Bagley, J.D., 1967. The behavior of adaptive systems which employ genetic and correlation algorithms, Ph.D. dissertation, University of Michigan, Ann Arbor, Michigan, USA.
12. Bahgat, B.M., Osman, M.O.M., Sankar, T.S., 1983. On the spur-gear dynamic tooth-load under consideration of system elasticity and tooth involute profile, ournal of Mechanism, Transmission, and Automation in Design, 105, 302-309.

13. Barber, J.R., Gros, K., Oh, S., 2003. Energy considerations in systems with varying stiffness, Journal of Applied Mechaincs, 70, 465-469.
14. Bard, C., 1995. Modélisation du comportement dynamique des transmissions par engranages. Ph.D. Dissertation, Institute National Institut National des Sciences Appliquées de Lyon, France.
15. Beghini, M., Presicce, F., Santus, C., 2004. A method to define profile modification of spur gear and minimize the transmission error, AGMA Technical Paper, 04FTM3.
16. Benton, M., Seireg, A., 1978. Simulation of resonances and instability conditions in pinion-gear systems, Journal of Mechanical Design, 100, 26-32.
17. Bertacchi, G., 2005. Sulla modellazione di ruote dentate, MS dissertation, University of Modena and Reggio Emilia, Modena, Italy.
18. Blankenship, G.W., Kahraman, A., 1995. Steady state forced response of a mechanical oscillator with combined parametric excitation and clearance type non-linearity, Journal of Sound and Vibration, 185(5), 743-765.
19. Brindle, A., 1981. Genetic algorithms for function optimization, Ph.D. dissertation, University of Alberta, Alberta, Canada.
20. Bonori, G., Andrisano, A.O., Pellicano, F., 2004. Stiffness evaluation and vibration in a tractor gear, Proceedings of IMECE 2004, ASME International Mechanical Engineering Congress, Anaheim, CA.
21. Buckingham, E., 1949. Analytical mechanics of gears, Buckingham associates, Inc. Springfield, Vermont, USA. Republished by Dover, New York, USA, 1963.
22. Cai Y., Hayashi, T., 1992. The optimum modification of tooth profile for a pair of spur gears to make its rotational vibration equal to zero, Proceedings of Power Transmission and Gearing Conference ASME, DE-Vol. 43-2, 453-460.
23. Cai Y., Hayashi, T., 1994. The linear approximated equation of vibration of a pair of spur gears (Theory and experiment), Journal of Mechanical Design, 116, 558-564.
24. Cai, Y., 1995. Simulation on the rotational vibration of helical gears in consideration of the tooth separation phenomenon (A new stiffness function of helical involute tooth pair), Journal of Mechanical Design, 117, 460-469.
25. Caviccio, D.J., 1970. Adaptive search using simulated evolution, Ph.D. dissertation, University of Michigan, Ann Arbor, Michigan, USA.
26. Chung, C.H., Steyer, G, Abe, T., Clapper, M., Shah, C., 1999. Gear noise reduction through transmission error control and gear blank dynamic tuning, Proceedings of the 1999 Noise and Vibration Conference, SAE Technical, Paper 1999-01-1766.

27. De Jong, K.A., 1975. An analysis of the behavior of a class of genetic adaptive systems, Ph.D. dissertation, University of Michigan, Ann Arbor, Michigan, USA.
28. de Solla Price, D., 1959. An Ancient Greek Computer, Scientific American, June 1959, 60-67.
29. de Solla Price, D.,1974. Gears from the Greeks - The Antikythera Mechanism, A Calendar Computer from ca. 80 B.C., Transactions of the American Philosophical Society 64, part 7.
30. Drago, R.J., Margasahayam, R., 1987. Stress analysis of planet gears with integral bearings; 3D Finite-Element model development and test validation, MSC NASTRAN World Users' Conference, Los Angeles, California, USA.
31. Drago, R.J., Margasahayam, R., 1987. Finite-Element stress analysis of helicopter planetary gears, 43rd Annual Forum, American Helicopter Society, St. Louis, Missouri, USA.
32. Dudley, D.W., Townsend D.P., 1996. Manuale degli ingranaggi, Tecniche Nuove, Milano.
33. Faires, V.M., Keown, R.M., 1960. Mechanism 5th edition, McGraw-Hill, New York, USA. Republished by Krieger, Malabar, Florida, USA, 1980.
34. Fonseca, D.J., Shishoo, S., Lim, T.C., Chen, D.S., 2005. A genetic algorithm approach to minimize transmission error of automotive spur gears sets, Applied artificial Intelligence, 19(2), 153-179.
35. Fraser, A.S., 1960. Simulation of genetic systems by automatic digital computers. 5-linkage, dominance and epistasis, In O. Kempertone, Biomedical genetics, Macmillan, New York, USA.
36. Funaioli, E., Maggiore, A., Meneghetti, U., 1987. Lezioni di Meccanica Applicata alle Macchine, Patron, Bologna.
37. Gargiulo Jr., E.P., 1980. A simple way to estimate bearing stiffness, Machine design, July 24, 107-110.
38. Gregory, R.W., Harris, S.L., Munro, R.G., 1963-1964. Dynamic behavior of spur gears, Proceedings of the Institution of Mechanical Engineers, 178, 207-218.
39. Goldberg, D.E., 1989. Genetic algorithms in search, optimization & machine learning, Addison-Wesley publishing company, Reading, Massachusetts, USA.
40. Harris, S.L., 1958. Dynamic loads on the teeth of spur gears, Proceedings of the Institution of Mechanical Engineers, 172(2), 87-100.

41. Hayashi, T., Hayashi, I., 1976. The rotational vibration of a spur gear with tooth profile error, Bulletin of Research Laboratory of Precision Machinery and Electronics, Tokyo Institute of Technology, 38, 35-42.
42. Henriot, G., 1987. Ingranaggi - Trattato teorico e pratico, 2nd edition, Tecniche Nuove, Milano.
43. Holland, J.H., 1975. Adaptation in natural and artificial systems, The University of Michigan Press, Ann Arbor, Michigan, USA.
44. Hollstien, R.B., 1971. Artificial genetic adaptation in computer control systems, Ph.D. dissertation, University of Michigan, Ann Arbor, Michigan, USA.
45. Houser, D.R., Bolze, V.M., 1996. Static and dynamic transmission error measurements and predictions for spur and helical gear sets, Power and Transmission and Gearing Conference ASME, DE-Vol.88, 365-372.
46. Hsu, C.S., Cheng, W.-H., 1974. Steady-state response of a dynamical system under combined parametric and forcing excitations, Journal of Applied Mechanics, 371-378.
47. IMSL®, 2003. IMSL Fortran Library User's Guide, MATH/LIBRARY Volume 1 and 2, Visual Numerics Inc., USA.
48. ISO 53, 1998. Cylindrical gears for general and heavy engineering - Standard basic rack tooth profile.
49. ISO 54, 1996. Cylindrical gears for general engineering and for heavy engineering – Modules.
50. ISO 701, 1998. International gear notation – Symbol for geometrical data.
51. ISO 1122-1, 1998. Vocabulary of gear terms - Part 1: Definitions related to geometry.
52. ISO 4462, 1982. Addendum modification of the teeth of cylindrical gears fro speed-reducing and speed-increasing gear pairs.
53. ISO 6336-1, 1996. Calculation of load capacity of a spur and helical gears. Part 1: Basic principles, introduction and general influence factors.
54. ISO 6336-2, 1996. Calculation of load capacity of a spur and helical gears. Part 2: Calculation of surface durability (pitting).
55. ISO 6336-3, 1996. Calculation of load capacity of a spur and helical gears. Part 3: Calculation of tooth bending strength.
56. ISO 6336-5, 1996. Calculation of load capacity of a spur and helical gears. Part 5: Strength and quality of materials.
57. Johnson, D.C., 1958. Excitation of resonant vibrations by gear tooth meshing effects, Proc. Int. Conf. Gearing, 18, Instn Mech. Engrs, London.

58. Johnson, K.L., 1985. Contact Mechanics, Cambridge University Press.
59. Jordan, D.W., Smith, P., 1999. Nonlinear ordinary differential equations, An introduction to dynamical systems, 3rd Edition, OXAM, Ofxord University Press, Oxford, UK.
60. Kahraman, A., Singh,R., 1990. Non-linear dynamics of a spur gear pair, Journal of Sound and Vibrations, 142 (1), 49-75.
61. Kahraman, A., Singh,R., 1992. Dynamics of an oscillator with both clearance and continuous non-linearities, Journal of Sound and Vibrations, 151 (3), 180-185.
62. Kahraman, A., Blankenship, G.W., 1996. Iteractions between commensurate parametric and forcing excitations in a system with clearance, Journal of Sound and Vibrations, 194(3), 317-336.
63. Kahraman, A., Blankenship, G.W., 1996. Gear dynamics experiments, part-II: effectof involute contact ratio, Proceedings of Power Transmission and Gearing Conference, 381-388.
64. Kahraman, A., Blankenship, G.W., 1997. Experiments on nonlinear dynamic behavior of an oscillator with clearance and periodically time-varying parameters, Journal of Applied Mechanics, 64, 217-226.
65. Kahraman A., Blankenship G.W., 1999. Effect of involute contact ratio on spur gear dynamics, Journal of Mechanical Design, 121, 112-118.
66. Kahraman A., Blankenship G.W., 1999. Effect of involute tip relief on dynamic response of spur gear pairs, Journal of Mechanical Design, 121, 313-315.
67. Kim T.C., Rook, T.E., Singh, R., 2003. Effect of smoothening functions on the frequency response of an oscillator with clearance non-linearity. Letter to the Editor Journal of sound and vibration, 263(3), 665-678.
68. Krantz, T.L., 1992. Gear tooth stress measurement of two helicopter planetary stages, NASA Technical Memorandum 105651, Sixth International Power Transmission and Gearing Conference, Phoenix, Arizona, USA.
69. Lewis, W., 1892. Investigation of the Strength of Gear Teeth, Proc. Eng. Club of Philadelphia, October 1892.
70. Lin, J., Parker, R.G., 1999. Analytical characterization of the unique properties of planetary gear free vibration, Journal of Vibration and Acoustics, 121, 316-321.
71. Lin, J., Parker, R.G., 1999. Sensitivity of planetary gear natural frequencies and vibration modes to model parameters, Journal of Sound and Vibration, 228(1), 109-128.

72. Lin, J., Parker, R., 2002. Mesh stiffness variation instabilities in two-stage gear systems, Journal of vibration and acoustics, 124, 68-76.
73. Litvin, F.L., 1989. Theory of Gearing, NASA Publication RP-1212 U.S.A., Washington, DC.
74. Litvin, F.L., 1994. Gear Geometry and Applied Theory, P T R Prentice Hall, Englewood Cliffs, New Jersey 07632.
75. Litvin, F.L., Demenego, A., Vecchiato, D., 2001. Formation by Branches of Envelope to Parametric Families of Surface and Curves, Computer Methods in Applied Mechanics and Engineering, 100, 4587-4608.
76. Love, A.E.H., 1944. A treatise on the mathematical theory of elasticity, Dover Publications, New York.
77. Luo, A.C.J., 2005. A theory for non-smooth dynamic systems on the connectable domains. Communications in Nonlinear Science and Numerical Simulations, 10, 1-55.
78. Lynwander, P., 1983. Gear drive systems design and application, Marcel Dekker Inc., New York & Basel.
79. Maatar, M., Velex, P., Nguyen, T., Octrue, M., Vasseur, J.L., 1995. Experimental and numerical analysis of transmission error in spur gear drives, Machine Vibration, 4, 8-13.
80. Mark, W.D., 1978. Analysis of the vibratory excitation of gear systems: Basic theory, Journal of Acoustic Society of America, 63(5), 1409-1430.
81. Mark, W.D., 1979. Analysis of the vibratory excitation of gear systems. II: Tooth error representation, approximations, and application, Journal of Acoustic Society of America, 66(6), 1758-1787.
82. Mark, W.D., 1989. The generalized transmission error of parallel-axis gears, Journal of Mechanism, Transmission, and Automation in Design, 111, 414-423.
83. Matsumura S., Umezawa, K., Houjoh, H., 1996. Performance diagram of a helical gear pair having tooth surface deviation during transmission on light load, Proceedings of Power Transmission and Gearing Conference ASME, DE-Vol. 88, 161-168.
84. MSC.Marc, 2003. User Manual. Volume A: Theory and User Information Version, Volume B: Element Library Version, Volume C: Program Input, Volume E: Part IV Demostration Problem Contact Advance Topics.
85. Mentat, 2003. Mentat User's Guide.

86. Ming-Haung, T., Ying-Chien, T., 1997. A method for calculating static transmission errors of plastic spur gears using FEM evaluation, Finite Elements in Analysis and Design, 27(4), 345-357.
87. Munro, R.G., 1962. The dynamic behavior of spur gears, Ph.D. dissertation, Cambridge University, Cambridge, UK.
88. Munro, R.G., 1969-1970. Effect of geometrical errors on the transmission of motion between gears, Proceedings of the Institution of Mechanical Engineers, 184 part 30, 79-84.
89. Munro, R.G., Yildirim, N., Hall, D.M., 1990. Optimum profile relief and transmission error in spur gears, Proceedings of Institution of Mechanical Engineers, C404/013, 35-42.
90. Natsiavas, S., 1989. Periodic Response and Stability of Oscillators With Symmetric Trilinear Restoring Force. Journal of Sound and Vibration, 134(2), 315-331.
91. Nayfeh, A..H., Mook, D.T., 1979. Nonlinear oscillations, John Wiley & Sons, New York, USA.
92. Nielsen, T.C., 1960. Latest equations for angular errors in gears.
93. Niemann G., Baethge, J., 1970. Transmission error, tooth stiffness, and noise of parallel axis gears, VDI-Z, 2(4), 2(8).
94. Ognjanovic, M., Subic, A., 1993. Gear quality prediction using vibration analysis, Machine Vibration, 2, 92-100.
95. Olakorede, A., Play, D., 1991. Load sharing, load distribution and stress analysis of cylindrical gears by the Finite Prism Method, Proceedings of the Design Productivity International Conference, Honolulu, Hawaii, USA, 921-927.
96. Ozguven, H.N., Houser, D.R., 1988. Mathematical Models Used in Gear Dynamics – A Review, Journal of Sound and Vibration, 121(3), 383-411.
97. Ozguven, H.N., 1991. A non-linear mathematical model for dynamic analysis of spur gears including shaft and bearing dynamics, Journal of Sound and Vibration, 145(2), 239-259.
98. Parker, R.G., Agashe, V., Vijayakar, S.M., 2000. Dynamic response of a planetary gear system using a finite element/contact mechanics model, Journal of Mechanical Design, 122, 305-311.
99. Parker, R.G., Vijayakar, S.M., Imajo, T., 2000. Nonlinear dynamic response of a spur gear pair: modeling and experimental comparisons, Journal of Sound and Vibration, 237, 435-455.

100. Pedrero, J.I., Artes, M., 1996. Approximate Equation for the Addendum Modification Factors for Tooth Gears with Balanced Specific Sliding, Mechanism and Machine Theory, 31(7), 925-935.

101. Pedrero, J.I., Artes, M., Garcia-Prada, J.C., 1996. Determination of the Addendum Modification Factor for Gears with pre-established Contact Ratio, Mechanism and Machine Theory, 31(7), 937-945.

102. Pfeiffer, F., Kunert, A., 1990. Rattling models from deterministic to stochastic processes, Nonlinear Dynamics, 1,63-74.

103. Press, W.H., 1992. Numerical Recipes in Fortran: the art of scientific computing, Cambridge U.P., UK.

104. Ramamurti, V., Nayak, H.V., Sujata, C., 1998. Static and dynamic analysis of spur and bevel gears using FEM, Mechanism and Machine Theory, 33(8), 1177-1193.

105. Rouverol, W.S., 1996. New modifications eradicate gear noise and dynamic increment at all loads, Proceedings of Power Transmission and Gearing Conference ASME, DE-Vol. 88, 17-21.

106. Ruggieri, G., Righettini, P., 2003. Ruote Dentate con Spostamento di Profilo, McGraw Hill, Milano.

107. Sato, T., Umezawa, K., Ishikawa, J., 1983. Effect of contact ratio and profile correction on gear rotational vibration, Bulletin of Japanese Society of Mechanical Engineering, 26(221), 2010-2016.

108. Sloane, A, 1941. Engineering kinematics, Macmillian, New York, USA. Republished by Dover, New York, USA, 1966.

109. Smith, J.D., 1999. Gear noise and vibration, Marcel Dekker Inc., New York, USA.

110. Strozzi, A., 1998. Costruzione di machine, Pitagora editore, Bologna, Italy.

111. Tavakoli, M.S., Houser, D.R., 1986. Optimum profile modifications for the minimization of static transmission errors of spur gears, Journal of Mechanism, Transmissions, and Automation in Design, 108, 86-95.

112. Theodossiades, S., Natsiavas, S., 2000. Non-linear dynamics of gear-pair systems with periodic stiffness and backlash, Journal of Sound and Vibration, 229(2), 287-310.

113. Timoshenko, S.P., Young, D.H., Weaver, W., 1974. Vibration problems in engineering, 4th edition John Wiley and Sons, New York, USA.

114. Tomlinson, G.R., Lam, J., 1984. Frequency response characteristics of structures with single and multiple clearance-type non-linearity, Journal of Sound and Vibration, 96(1), 111-125.

115. Tuplin, W.A., 1950. Gear tooth stresses at high speed, Proceedings of the Institution of Mechanical Engineers, 16, 162-167.

116. Tuplin, W.A., 1953. Dynamic loads on gears teeth, Machine Design, 25, 203-211.

117. Umezawa, K., Sato, T., Ishikawa, J., 1984. Simulation on rotational vibration of spur gears, Bulletin of Japanese Society of Mechanical Engineering, 27(223), 102-109.

118. Umezawa, K., Sato, Y., Kohno, K., 1984. Influence of gear errors on rotational vibration of power transmission spur gear (1st report, Pressure angle and normal pitch error), Bulletin of Japanese Society of Mechanical Engineering, 27(225), 569-575.

119. Umezawa, K., Sato, Y., 1985. Influence of gear errors on rotational vibration of power transmission spur gear (2nd report Waved form error), Bulletin of Japanese Society of Mechanical Engineering, 28(243), 2143-2148.

120. Umezawa, K., Suzuki, T., Houjoh, H., Sato, T., 1985. Vibration of power transmission helical gears (The effect of contact ratio on the vibration), Bulletin of Japanese Society of Mechanical Engineering, 28(238), 694-700.

121. UNI 8862/2, 1998. Cylindrical gears for general and heavy engineering -- Standard basic rack tooth profile.

122. Valco, M. J., 1992. Planetary Gear Train Ring Gear and Support Structure, Doctoral Dissertation, Cleveland State University.

123. Velex, P., Maatar, M., 1996. A mathematical model for analyzing the influence of shape deviations and mounting errors on gear dynamic behaviour, Journal of Sound and Vibration, 191(5), 629-660.

124. Vilmos, S., 2000. FEM stress analysis in hypoid gears, Mechanism and Machine Theory, 35(9), 1197-1220.

125. Vijayakar, S.M., 1988. Linearization of multibody frictional contact problems, Computers & Structures, 29(4), 569-576.

126. Vijayakar, S.M., 1999. A combined surface integral and finite element solution for a three-dimensional contact problem, International Journal for Numerical Methods in Engineering, 31, 525-545.

127. Vijayakar, S.M., 2003. Calyx Users Manual, Advanced Numerical Solutions, Hilliard, Ohio, USA.

128. Vijayakar, S.M., 2003. Planetary2D User's Manual and Validation Manual, Advanced Numerical Solutions, Hilliard, Ohio, USA.

129. Vijayakar, S.M., 2003. Transmission3D User's Manual, Advanced Numerical Solutions, Hilliard, Ohio, USA.

130. Vijayakar, S.M., 2004. Helical3D Users Manual, Advanced Numerical Solutions, Hilliard, Ohio, USA.

131. Vijayakar, S.M., 2005. Helical3D Validation Manual, Advanced Numerical Solutions, Hilliard, Ohio, USA.

132. Walker, H., 1938. Gear tooth deflection and profile modification, The engineer, 14, 409-412.

133. Walker, H., 1940. Gear tooth deflections and profile modifications, Engineer 170, 102-104.

134. Wang, C.C., 1978. Rotational vibration with backlash: Part 1, Journal of Mechanical Design, 100, 363-373.

135. Wang, C.C., 1981. Rotational vibration with backlash: Part 2, Journal of Mechanical Design, 103, 387-409.

136. Wolfram, S., 1999. The Mathematica Book, 4th edition, Wolfram Media/Cambridge University Press.

137. Yang, D.C.H., Sun, Z.S., 1985. A rotary model of spur gear dynamics, Journal of Mechanism, Transmission, and Automation in Design, 107, 529-535.

138. Yang, D.C.H., Lin, J.Y., 1987. Hertzian damping, tooth friction and bending elasticity in gear impact dynamics, Journal of Mechanism, Transmission, and Automation in Design, 109, 189-196.

…during my fellowship at Ohio State University, I had a memorable conversation about complexity of human being with a friend of mine…since we were working and "hopefully" studying gears systems, we had a lot of fun on comparing people to gears...in some way the conversation was a revealing conversation!!!...indeed not all people are "meshing" properly when connected...from a "dynamics" point of view, people can be really unstable, noisy, or having chaotic behaviors...furthermore is not difficult having people's "failures" for bending fatigue…gears do exactly the same!!!

I think this strange similarity has been unconsciously in my mind for all these three years…since my adviser, professor Andrisano, decided that I was going to become a "gear-guy"…the strange fact is that only now I realize that my understanding of the complexity of gear system went parallel to those of the human being.

Since my perception of humankind is a "bit" changed in the last three years, I have thousand of new reasons to thanks professor Franceso Pellicano, who has been at the same time a GREAT teacher and a GREAT friend (and I know it is not easy!!!).

I would like to thank my colleagues (Doctors and Ph.D. students) at the University of Modena and Reggio Emilia…Andrea Baldini, Gabriele Bertacchi, Giorgio Scagliarini, Giulia Catellani, Marcello Faggioni e Barbara Zardin, the engineers Jacopo De Martin, Francesco Lami and Marco Barbieri and "The" technician Enrico Salardi.

Many thanks also to unforgettable friends: Krishna Taminnana, Haris Ligata and Vijay Ambarisha, and to the professors: Robert Parker and Ahmet Kahraman at the Ohio State University.

A particolar thank also to Doctor Marco Gabiccini of the University of Pisa who introduced me in the unbelivable world of "not cylindrical" gears…thank you to be a friend of mine.

Last but not least…a great thank to Doctor Sandeep Vijayakar…who taught me what expertise, hard work, humility and patience can do!!!

A final thank to professors Andrisano and Strozzi who supported me during the Ph.D activity.

Many many many many many many warmly thanks also to my family for simply being MY family!!!!

Thank you also to my friends: Chiara, Christian, Enrica, Marcello and Mirco…a big hug to all of you!!!

...and to people who have not been mentioned because it is time to print....THANKS!!!